Bayesian Approach to Investigating Supersymmetric Models

by

Andrew Fowlie

September 2013

Submitted in conformity with the requirements
for the degree of Ph.D.
Department of Physics
Sheffield University

Supervised by Prof. Leszek Roszkowski

Abstract

Bayesian Approach to Investigating Supersymmetric Models

Andrew Fowlie

With Bayesian statistics, constrained and phenomenological supersymmetric models are examined and compared with the strongest contemporary experimental results, including the Higgs discovery, Large Hadron Collider (LHC) searches for supersymmetry, dark matter relic density measurements, rare decays and electroweak precision tests. Preliminary introductions to relevant supersymmetry phenomenology, Bayesian statistics and algorithms, and comprehensive descriptions of likelihood functions for experimental results are provided. Likelihood functions for searches for supersymmetry at the LHC are built at the event-level from Monte-Carlo simulations, including CMS $35\,\text{pb}^{-1}$, $1.1\,\text{fb}^{-1}$ and $4.4\,\text{fb}^{-1}$ searches. Five studies of different supersymmetric models, including the Constrained Minimal Supersymmetric Standard Model (CMSSM), the Non-Universal Higgs Model, the Non-Universal Gaugino Model and phenomenological MSSM models, and for different states of knowledge, including hypothetical benchmark scenarios, and pre- and post-Higgs discovery, are comprehensively presented. Credible regions for model parameters, Bayesian evidences, best-fit points and p-values are calculated in each study. We demonstrate that the CMSSM's soft-breaking masses could be determined from LHC searches with $100\,\text{fb}^{-1}$ at $\sqrt{s} = 14\,\text{TeV}$ for a specific favourable choice of parameters consistent with all current constraints. The favoured soft-breaking scale in the CMSSM increases to $M_\text{SUSY} \sim 1\,\text{TeV}$ with stau-coannihilation and $M_\text{SUSY} \sim 3\,\text{TeV}$ with A-funnel annihilation. Agreement with the anomalous magnetic moment of the muon (δa_μ) is difficult in the CMSSM, and, without δa_μ, $\mu < 0$ is insignificantly preferred. The CMSSM struggles to simultaneously agree with experimental results — its p-value is ostensibly significant. In our pMSSM model with nine free parameters, if the mass of the lightest neutralino is between $200\,\text{GeV}$ and $500\,\text{GeV}$, agreement with δa_μ and electroweakino searches at the LHC is possible.

Acknowledgements

I am grateful to my advisor, Prof. Roszkowski for his expertise and guidance, and must thank my collaborators, especially Yue-Lin Sming Tsai and Malgorzata Kazana, for their hard work and help. I also thank Prof. Winstanley, Prof. van de Bruck and my colleagues at Sheffield University. Lastly, I thank my family, for supporting me during my studies and while I wrote this thesis.

Andrew Fowlie, 2013.

Contents

Page

1 Theory 1

List of Figures

Figure Page

1 Theory

2 Statistics

3 Likelihoods

3.1 Physicality

3.3 Dark matter

3.4 Higgs mass

3.6 Direct collider searches

3.7 *B*-physics

3.8 Anomalous magnetic moment of the muon

4 Results

4.1 Introduction . . . .

4.2 Low-mass golden decay . . . .

4.3 High-mass golden decay . . . .

4.4 CMSSM with α_T 1 fb^{-1} . . . .

4.5 CMSSM with Razor 4.4 fb^{-1} and Higgs discovery . . . .

4.6 pMSSM dark matter and collider signatures . . . .

List of Tables

Table Page

1 Theory

2 Statistics

3 Likelihoods

4 Results

A Experimental constraints

B Priors

Chapter 1

Theory

This thesis charts the changing status of supersymmetry (SUSY) during an historic period in high-energy physics — the early years of the Large Hadron Collider (LHC) and its discovery of the Higgs boson. Whilst the Standard Model [1–4] describes most phenomena with extraordinary precision, technical and conceptual problems and puzzles suggest that it might be extended by supersymmetry. With Bayesian statistics, we investigate the best regions of supersymmetric models' parameter spaces, and the models' viabilities, considering various experimental results, including those from the LHC. We review supersymmetry, our Bayesian methodology and relevant experimental results.

1.1 SUSY motivation

The motivations for supersymmetry [5–7] are manifold; we review an incomplete selection of the three strongest arguments [8].

1.1.1 The hierarchy problem

The "hierarchy problem" is a technical problem concerning the hierarchy between the electroweak scale $M_{\text{EW}} \sim 10^3\,\text{GeV}$ and the Planck scale $M_{\text{P}} \sim 10^{19}\,\text{GeV}$, at which gravity is relevant. Although the existence of this hierarchy is itself a problem [9–11], the "hierarchy problem" is that in the Standard Model this hierarchy is destroyed by quantum corrections to the electroweak scale.

The destruction of the hierarchy is facilitated by the Standard Model's scalar field; scalar fields are pathological in a quantum field theory without a supersymmetry [40]. The Standard Model's scalar potential,

$$V(\phi) = m_\phi^2 \phi^2 + \lambda \phi^4, \tag{1.1}$$

results in electroweak symmetry breaking via the famous Higgs mechanism. The predicted electroweak scale is $v^2 = -m_\phi^2/\lambda$. From μ-decay, we know that $v \approx 246\,\mathrm{GeV}$.

Consider the quantum loop corrections to fermion and scalar masses in the Standard Model in Fig. 1.1.1. The fermions' masses are protected by chiral symmetry in the massless limit via the mass insertion in Fig. 1.1.1a,

$$\delta m_f \sim m_f \ln\left(\frac{M_\mathrm{P}}{m_f}\right), \tag{1.2}$$

where M_P is the Standard Model's ultraviolet cutoff; the scale at which gravity becomes important. The gauge bosons' masses are similarly protected by their gauge symmetries. The scalar, however, has no gauge or chiral symmetry to protect its mass [40]; the quantum loop in Fig. 1.1.1b is quadratic in the Planck scale,

$$\delta m_\phi^2 \sim M_\mathrm{P}^2. \tag{1.3}$$

Our expression for the electroweak scale including quantum loop corrections,

$$\begin{aligned} m_\phi^2 + \delta m_\phi^2 &= -\lambda v^2, \\ m_\phi^2 + M_\mathrm{P}^2 &\approx -\lambda\,(246\,\mathrm{GeV})^2 \end{aligned} \tag{1.4}$$

requires a miraculous cancellation between the tree-level scalar mass, its corrections and the quartic coupling. Were we to interpret the Standard Model as the "ultimate," fundamental theory, we could renormalise the scalar mass and remove the quadratic corrections via counterterms. The hierarchy problem is that quantum corrections drag the electroweak scale to the highest mass scale in the theory; it is a sensitivity to new physics, which must truncate the loop corrections or else require an incredible degree of cancellations.

There are three contributions to the one-loop quantum corrections to the scalar mass in Eq. 1.4: gauge couplings, Yukawa couplings and the scalar's self-interaction from the quartic coupling in the scalar potential,

$$m_\phi^2 + \frac{1}{16\pi^2}\left[C_W g^2 + C_\phi \lambda - \sum_f C_f y_f^2\right] M_\mathrm{P}^2 = -\lambda\,(246\,\mathrm{GeV})^2\,, \tag{1.5}$$

where the C's are numerical coefficients. We would like the loop corrections in brackets to sum to zero, though not by a miraculous cancellation, but naturally. We might try:

- Introducing extra scalar fields for each fermionic degree of freedom with couplings $\lambda_s = -y_f^2$; the original Yukawa couplings cancel with these new scalar field couplings if the extra scalars' masses equal the fermions' masses.
- Introducing extra fermionic fields for each boson with identical gauge couplings; the original quartic and gauge couplings cancel if the quartic coupling and the gauge couplings are suitably related.

This prescription is "supersymmetry;" supersymmetry relates bosonic and fermionic degrees of freedom and couplings in such a way that the electroweak scale is stable from quantum loop corrections [29]. By utilising the difference in sign between fermionic and bosonic loops, supersymmetry protects the scalar's mass. Other solutions to this problem exist, including strong dynamics [12], extra dimensions [13] and conformal symmetries [14].

1.1.2 Dark matter

"Dark matter" is an experimental motivation for supersymmetry. The evidence that non-luminous, non-baryonic matter pervades the Universe with substantial abundance — "dark matter" — is overwhelming [15–18]. This evidence stems from independent techniques to infer the mass of luminous and non-luminous matter:

- An early example of such an inference was that of Zwicky (1933) [19]; he found that the mass of the Coma cluster from the virial theorem was substantially greater than that of the luminous matter, and posited the existence of dark matter within the cluster.

- Luminous matter is concentrated at the centre of galaxies. Within individual galaxies, in the absence of dark matter, stars ought to orbit with "Keplerian" velocity curves — their rotation velocities ought to decrease with their distance from the galactic centre. The observed velocity curves, however, are constant with distance from the galactic centre, indicating the presence of dark matter within galaxies, evenly-distributed with distance from the galactic centre.

- "Lensing" is a modern technique to infer dark matter, independently from kinematic techniques. From general relativity, geodesics — and hence light rays — ought to be bent by matter. If dark matter is present between us and a bright galaxy, the light from the galaxy ought to be distorted [20]. This distortion was observed, indicating dark matter between galaxies, with substantial mass. "Micro-lensing," however, was not observed at a sufficient rate, indicating the absence of a substantial number of non-luminous baryonic objects in the Universe [21].

- Cosmology, independently, indicates dark matter; the Universe's large-scale structure requires neutral matter so that structure can conglomerate before recombination [22]. Furthermore, dark and baryonic matter behave differently in cosmology; because baryonic matter couples with light, its "photon-baryon fluid" causes fluctuations in the cosmic microwave background (baryon acoustic oscillations).

- Recent compelling evidence for non-baryonic dark matter is from collisions between galaxy clusters; the "bullet" cluster resulted from such a collision. A cluster's baryonic mass is dominated by its intergalactic gas. During collisions between galaxy clusters, this gas is heated, and we observe its location from its X-ray radiation. Lensing of light by the bullet cluster ought to occur at these locations. The mass distributions inferred from X-ray radiation and from lensing, however, disagree, suggesting that the majority of the matter in the bullet cluster is dark matter [23].

In summary, experiments with a variety of techniques and distance-scales within the Universe are in concordance and find overwhelming evidence for dark matter which is approximately 80% of the Universe's mass density, 20% of its energy density, non-baryonic, electrically neutral, weakly interacting, and cold. Supersymmetry with R-parity (forthcoming, Sec. 1.5) includes a particle that satisfies these desiderata; no such particle exists in the Standard Model.

1.1.3 Gauge coupling unification

A popular proposal is that the Standard Model gauge groups are embedded in a single, simple Lie group, which is spontaneously broken down to the known Standard Model semi-simple product gauge group (grand unification) [24,25]. Because this model is described by a single non-Abelian group, all quantum numbers are discrete eigenvalues and charges, including hypercharge, are quantised. The grand unified theory (GUT) has a single gauge coupling, common to its subgroups, but, after symmetry breaking, the subgroups' couplings deviate as heavy gauge bosons decouple from the renormalisation group evolution. This explains the different subgroup couplings observed at low energies. Because the couplings differ considerably at low energy but their running is logarithmic, we anticipate that the GUT scale must be high.

This proposal, unfortunately, fails in the Standard Model. When the Standard Model gauge couplings are ran from their measured infrared values to the ultraviolet, they fail to unify. However, including supersymmetric particle content in the group flow at $\lesssim 10\,\text{TeV}$ results in unification at $M_{\text{GUT}} \sim 10^{16}\,\text{GeV}$, because the loop coefficients are suitably altered by an additional Higgs doublet [26]. The qualitative behaviour of the couplings is unaffected, only $\text{SU}_\text{c}(3)$ has asymptotic freedom.

1.2 SUSY algebra

We consider the SUSY algebra, that is, the SUSY transformations, their generators and their commutation and anti-commutation rules. The Coleman-Mandula theorem [27] forbids conserved charges with non-trivial Lorentz transformations. A simplified argument considers a $1 + 2 \to 3 + 4$ scattering process with Poincaré invariance, in which one attempts to construct an additional tensor symmetry generator. We find a no-go theorem; we cannot construct such a generator, because the additional symmetry prohibits non-trivial scattering. We find, however, that the no-go theorem is evaded if the new charges transform as spinors and modify

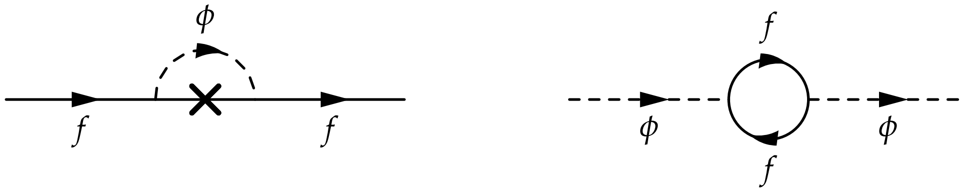

(a) *Fermion mass correction with mass insertion.*

(b) *Scalar mass correction from a fermion loop.*

(c) *Scalar mass correction from a boson loop.*

(d) *Scalar mass correction from a quartic self-interaction.*

Figure 1.1.1: *(a) Scalar one-loop correction to fermion mass and one-loop corrections to the scalar mass in the Standard Model from (b) fermions, (c) bosons and (d) a quartic self-interaction.*

spin by half a unit [42],

$$Q_\alpha \mid j\rangle = \mid j \pm 1/2\rangle. \tag{1.6}$$

Because spin is not modified in a $1+2 \to 3+4$ scattering process, the Coleman-Mandula argument is stopped.

The symmetry's charges and thus their anti-commutator must commute with the Hamiltonian, the generator of time translations,

$$[Q_\alpha, H] = [\{Q_\alpha, Q_\beta\}, H] = 0, \tag{1.7}$$

where Q_α is a two-component left-handed Weyl spinor with undotted left-handed spinor index $\alpha = 1, 2$. Because, by its symmetry, the anti-commutator has three independent components, we suspect it transforms as vector. Combined with our knowledge that it commutes with the Hamiltonian from Coleman-Mandula type arguments, we suspect that

$$\{Q_\alpha, Q_\beta\} \sim P^\mu, \tag{1.8}$$

where P^μ, the four-momentum generator of space-time translations, is the only available conserved four-vector. We later find that this informal reasoning is slightly wrong.

We construct a simple toy Lagrangian (the Wess-Zumino model [5]) with a Weyl spinor and a complex scalar,

$$\mathcal{L}_{\text{Wess-Zumino}} = -\partial^\mu\phi^*\partial_\mu\phi - i\psi^\dagger\bar{\sigma}^\mu\partial_\mu\psi. \tag{1.9}$$

where $\bar{\sigma}^\mu$ are two-by-two matrices $(\mathbb{1}, -\sigma_i)$ where σ_i are two-by-two Pauli matrices.

The Weyl spinor, ψ, has two (four) on-shell (off-shell) degrees of freedom and the complex scalar, ϕ, has two degrees of freedom. We know from Eq. 1.6 and from our motivations that SUSY transformations ought to relate bosons with fermions. In fact, the infinitesimal transformations are [41]:

$$\begin{aligned}
\delta\phi &= \epsilon^\alpha\psi_\alpha, \\
\delta\phi^* &= \epsilon^{\dagger\dot{\alpha}}\psi^\dagger_{\dot{\alpha}}, \\
\delta\psi_\alpha &= i\sigma^\mu_{\alpha\dot{\alpha}}\epsilon^{\dagger\dot{\alpha}}\partial_\mu\phi, \\
\delta\psi^\dagger_{\dot{\alpha}} &= -i\epsilon^\alpha\sigma^\mu_{\alpha\dot{\alpha}}\partial_\mu\phi^*,
\end{aligned} \tag{1.10}$$

where ϵ is an infinitesimal Weyl spinor that parameterises the transformation.

The Wess-Zumino Lagrangian is invariant under these transformations (to within a total derivative). The algebra, however, only closes on-shell, that is, if we use the Euler-Lagrange equations of motion. This is not surprising — the number of off-shell bosonic degrees of freedom and the number of off-shell fermionic degrees of freedom were not equal. To remedy this, we introduce an "auxiliary" complex scalar field F, with transformations that close the algebra and with zero (two) on-shell (off-shell) degrees of freedom. From the Noether procedure, we find the conserved charges and their algebras [41]:

$$\begin{aligned} \{Q_\alpha, Q^\dagger_{\dot\beta}\} &= 2\sigma^\mu_{\alpha\dot\beta} P_\mu, \\ \{Q_\alpha, Q_\beta\} &= 0, \\ [Q_\alpha, P^\mu] &= 0. \end{aligned} \tag{1.11}$$

This algebra differs from that which we anticipated in Eq. 1.8.

The Wess-Zumino model, with a complex scalar, Weyl fermion and an auxiliary complex scalar to close the algebra, is a "chiral supermultiplet" representation of the algebra. Our ultimate goal is to "supersymmetrise" the Standard Model, but chiral supermultiplets cannot contain gauge bosons. Gauge bosons live in a "gauge supermultiplet." The gauge supermultiplet contains gauge bosons A^a_μ, where the adjoint index $a = 1, \ldots, N^2 - 1$ for $\mathrm{SU}(N)$, and a Weyl fermion (gaugino) λ^a, with transformations in the Wess-Zumino gauge [41]:

$$\begin{aligned} \delta A^a_\mu &= \frac{1}{\sqrt{2}}(\epsilon^\dagger_{\dot\alpha} \bar\sigma^{\alpha\dot\alpha}_\mu \lambda^a_\alpha + \lambda^{\dagger a}_{\dot\alpha} \bar\sigma^{\alpha\dot\alpha}_\mu \epsilon_\alpha), \\ \delta\lambda^a_\alpha &= \frac{i}{2\sqrt{2}} \sigma^\mu_{\alpha\dot\alpha} \bar\sigma^{\alpha\dot\alpha}_\mu \epsilon_\alpha F^a_{\mu\mu} + \frac{1}{\sqrt{2}} \epsilon_\alpha D^a. \end{aligned} \tag{1.12}$$

The gauge boson has two (three) on-shell (off-shell) degrees of freedom and the gaugino has two (four) on-shell (off-shell) degrees of freedom. Similarly to the chiral supermultiplet, the gauge supermultiplet requires an auxiliary real scalar field D^a to close the algebra.

1.3 SUSY Lagrangian

In Sec. 1.1 and Sec. 1.2, we discussed our motivations for constructing SUSY theories and their underlying algebras; we now construct a full supersymmetric Lagrangian in left-handed Weyl spinors. The kinetic and gauge interactions for a scalar, a Weyl fermion and a gauge boson are:

$$\mathcal{L}_{\text{scalar}} = -D^\mu \phi^* D_\mu \phi, \tag{1.13}$$

$$\mathcal{L}_{\text{fermion}} = -i\psi^\dagger \bar{\sigma}^\mu D_\mu \psi, \tag{1.14}$$

$$\mathcal{L}_{\text{gauge}} = -\frac{1}{4} F^a_{\mu\nu} F^{\mu\nu}_a, \tag{1.15}$$

where $F^a_{\mu\nu}$ is a field-strength tensor with adjoint index $a = 1, \ldots, N^2 - 1$, and D_μ is a covariant derivative, including relevant gauge interactions.

In addition, the auxiliary fields, F and D, have kinetic pieces,

$$\mathcal{L}_{\text{aux}} = F^* F + \frac{1}{2} D^a D_a, \tag{1.16}$$

where D_a must not be confused with the covariant derivative D_μ. The auxiliary fields are ultimately eliminated by their trivial equations of motion.

We are, however, permitted interactions between the scalars and the fermions in the chiral supermultiplets and gauge interactions between the scalar and fermion within a chiral supermultiplet and gauginos, in addition to the gauge interactions in the covariant derivatives. The permitted supersymmetric interactions between scalars and fermions are generalised by the "superpotential," W, a holomorphic polynomial in the scalar fields, with a maximum operator dimension of three for renormalisable interactions,

$$W = L^i \phi_i + \frac{1}{2} M^{ij} \phi_i \phi_j + \frac{1}{6} y^{ijk} \phi_i \phi_j \phi_k, \tag{1.17}$$

where the Latin indices represent distinct fields and not, e.g., weak isospin indices. This must, of course, respect Standard Model gauge symmetries. Because the Standard Model has no gauge singlets, the linear term is forbidden in minimal models. The quadratic and cubic terms are permitted only if the combination of scalars is a singlet. The superpotential's functional derivatives specify new interactions,

$$\mathcal{L}_{\text{chiral int}} = \left(-\frac{1}{2} W^{ij} \psi_i \psi_j + W^i F_i \right) + \text{c.c.}, \tag{1.18}$$

where only for the superpotential superscripts and subscripts indicate functional differentiation with respect to the scalar field with that index, e.g.,

$$W^i = \frac{\delta W}{\delta \phi_i}. \tag{1.19}$$

The superpotential includes Yukawa interactions for Standard Model fields in the $W^{ij}\psi_i\psi_j$ terms. It does not, however, specify their values.

The superpotential contributes additional interactions via so-called F-terms. The Euler-Lagrange equation for the auxiliary field F is trivial; it contains no derivatives, and hence F is a non-propagating, unphysical field. We find $F_i = -W_i^*$, resulting in interactions from Eq. 1.16 and Eq. 1.18,

$$\begin{aligned}\mathcal{L}_{F\text{-terms}} = F_i^* F^i + W_i F^i + W_i^* F^{i*} &= -W^i W_i^* \\ &= -M_{ik}^* M^{kj} \phi^{*i}\phi_j - \frac{1}{2} M^{in} y_{jkn}^* \phi_i \phi^{*j} \phi^k \\ &- \frac{1}{2} M_{in}^* y^{jkn} \phi^{*i} \phi_j \phi_k - \frac{1}{4} y^{ijn} y_{kln}^* \phi_i \phi_j \phi^{*k} \phi^{*l}.\end{aligned} \tag{1.20}$$

In the Standard Model, gauge interactions result from replacing the derivative with the covariant derivative, $\partial_\mu \to D_\mu$, but this substitution cannot generate interactions between gaugino fields (or gauge supermultiplet auxiliary fields) and scalar or fermion fields. The additional supersymmetric, gauge invariant and renormalisable interactions are:

$$\mathcal{L}_{\text{gauge int}} = -\sqrt{2} g_a \left(\phi^* T_a \psi\right) \lambda^a - \sqrt{2} g_a \lambda^{\dagger a} \left(\psi^\dagger T_a \phi\right) + g_a \left(\phi^* T_a \phi\right) D^a, \tag{1.21}$$

where supersymmetry requires that the couplings are the Standard Model gauge couplings, and T_a are the generators associated with a field's adjoint index a. The fields ϕ and ψ must belong to the same chiral supermultiplet and must transform in the fundamental representation of the gauge group with generators T^a. We eliminate D^a by its trivial equation of motion, $D^a = -g(\phi^* T^a \phi)$, resulting in D-terms from Eq. 1.16 and Eq. 1.21,

$$\mathcal{L}_{D\text{-terms}} = \frac{1}{2} D^a D_a - D^a D_a = -\frac{1}{2} D^a D_a = \frac{1}{2} g_a^2 (\phi^* T^a \phi)^2, \tag{1.22}$$

where a sums the adjoint index of every Standard Model gauge group and g_a is the associated gauge coupling (although $a = 1, \ldots, N^2 - 1$ for each gauge group $\mathrm{SU}(N)$, g_a only represents one of the three gauge group couplings).

To check that a Lagrangian is supersymmetric, we check that $\delta\mathcal{L} = 0$ modulo a total derivative from our transformation laws in Eq. 1.10 and Eq. 1.12. This laborious procedure is simplified with "superspace" formalism, in which regular spacetime x_μ is extended with spinor dimensions $\{x_\mu, \theta_\alpha, \bar{\theta}_{\dot{\beta}}\}$ that have Grassman algebra [26, 28, 29]. Supersymmetric invariance is manifest in constructions in superspace.

A "superfield" is an expansion in θ_α and $\bar{\theta}_{\dot{\beta}}$. Because θ_α and $\bar{\theta}_{\dot{\beta}}$ are Grassman numbers, a superfield terminates at $\theta\theta\bar{\theta}\bar{\theta}$. The co-efficients in a superfield's Grassman expansion are identified with fields in chiral and gauge supermultiplets. The chiral and gauge superfields are irreducible representations of the supersymmetry algebra. The superpotential in Eq. 1.17 can be rewritten in chiral superfields, $\hat{\Phi}$;

$$\hat{W} = L^i \hat{\Phi}_i + \frac{1}{2} M^{ij} \hat{\Phi}_i \hat{\Phi}_j + \frac{1}{6} y^{ijk} \hat{\Phi}_i \hat{\Phi}_j \hat{\Phi}_k. \tag{1.23}$$

Because $\hat{W}$ is a chiral superfield, its F-term transforms as a total derivative under a supersymmetry transformation. In fact, the F-term of $\hat{W}$ in Eq. 1.23 is W in Eq. 1.17.

1.4 SUSY breaking

Unbroken SUSY posits a "mirror" of the Standard Model. Because, however, we observe no e.g., massless photino or gluino, supersymmetry must be broken. If SUSY is to solve the hierarchy problem, the breaking scale cannot be much greater than the electroweak symmetry breaking scale.

Electroweak symmetry breaking would simultaneously break supersymmetry, because Higgs VEVs in F-terms (Eq. 1.20) and D-terms (Eq. 1.22) induce mass splittings between superpartners. The linear algebra is such, however, that some sparticles would be lighter than their Standard Model superpartners. We need an additional mechanism for supersymmetry breaking at a mass scale heavier than the electroweak scale for phenomenologically viable sparticle masses.

Supersymmetry is spontaneously broken if, although the Lagrangian respects SUSY, the vacuum breaks SUSY,

$$Q_\alpha \left|0\right\rangle \neq 0. \tag{1.24}$$

With Eq. 1.11, we find that if SUSY is broken by the vacuum,

$$\langle 0 | H | 0 \rangle = \langle 0 | V | 0 \rangle > 0. \tag{1.25}$$

Unfortunately, SUSY breaking in the scalar potential cannot work, because there are no singlet fields for F-term breaking and D-term breaking would break colour or electromagnetism. The "supertrace" theorem demonstrates that if SUSY is broken by tree-level renormalisable interactions, within a supermultiplet,

$$m^2_{\phi_1} + m^2_{\phi_2} = 2m^2_{\psi}. \tag{1.26}$$

SUSY must, therefore, be broken radiatively from a "hidden sector" [41]. An interaction mediates SUSY breaking from this "hidden sector" to our "visible sector." Because experiments restrict flavour changing neutral currents, the interactions ought to be approximately flavour blind, as depicted in Fig. 1.4.1. Gravity and gauge interactions are popular choices for the interactions [30].

These breaking masses must be "soft" — by "softly" breaking supersymmetry, by the non-renormalisability theorem [29], no quadratic corrections to the electroweak scale are reintroduced, though logarithmic corrections are introduced. The soft-breaking operators must have dimension three or less.

1.5 The MSSM

The "Minimal Supersymmetric Standard Model" (MSSM) supersymmetrises the Standard Model with minimal additional fields and with minimal additional interactions [31,32]. The MSSM includes explicit soft-breaking masses, but posits no mechanism for supersymmetry breaking; it is phenomenological. We define the MSSM by its superpotential and by the structure of its soft-breaking terms. The MSSM has two Higgs-doublets — a necessity in supersymmetry to prevent a chiral anomaly (a single higgsino would result in $\text{Tr}(Q) \neq 0$) and for Yukawa interactions for up-type and down-type quarks (the superpotential must be holomorphic — the $i\tau H^*$ construction of the Standard Model, with the correct hypercharge for coupling with down-type quarks, is forbidden). The literature in MSSM weak-scale phenomenology is vast; see e.g., [33–44].

The particles in the MSSM's chiral and gauge supermultiplets are listed in Table 1.5.1 and Table 1.5.2 respectively, in left-handed Weyl spinors and in interaction eigenstates. We denote the right-handed chiral supermultiplets by bars, e.g., $\bar{u}$, and the superparticle within a supermultiplet with a tilde, e.g., $\tilde{\bar{u}}$. Supermultiplets and Standard Model content within a supermultiplet should be distinguished by context. The superparticle fields and their Standard Model partners transform in identical representations of the Standard Model gauge groups. The MSSM contains minimal particle content — it does not include right-handed neutrinos.

The MSSM superpotential is

$$W_{\text{MSSM}} = \tilde{\bar{u}} \boldsymbol{y_u} \tilde{Q} H_u - \tilde{\bar{d}} \boldsymbol{y_d} \tilde{Q} H_d - \tilde{\bar{e}} \boldsymbol{y_e} \tilde{L} H_d - \mu H_u H_d, \tag{1.27}$$

where the Yukawa matrices differ from those in the Standard Model, because the MSSM has two Higgs-doublets, and μ, the bilinear, is the only dimensionful coupling. The Yukawa matrices are divided by factors of $\sin\beta$ and $\cos\beta$ relative to the Standard Model Yukawa couplings. Requiring perturbativity in the t- and b-Yukawa couplings below the GUT scale results in $1.2 \lesssim \tan\beta \lesssim 63$.* Because the superpotential must be holomorphic, the $i\tau H^*$ transformation, present in the Standard Model's Yukawa interaction for the down-type quarks, is forbidden; we instead introduce a second Higgs doublet.

The MSSM superpotential omits the lepton and baryon number violating operators

$$\begin{aligned} W_{\Delta L=1} &= \lambda^{ijk} \tilde{L}_i \tilde{L}_j \tilde{\bar{e}}_k + \lambda'^{ijk} \tilde{L}_i \tilde{Q}_j \tilde{\bar{d}}_k + \mu'^{i} \tilde{L}_i H_u, \\ W_{\Delta B=1} &= \lambda''^{ijk} \tilde{\bar{u}}_i \tilde{\bar{d}}_j \tilde{\bar{d}}_k. \end{aligned} \tag{1.28}$$

In the Standard Model, lepton and baryon number violating operators are forbidden by an accidental symmetry. If λ' and λ'' were present, the proton would decay at a rate much faster than that which is observed. In the MSSM, the operators in Eq. 1.28 are forbidden by "R-parity:" a discrete $\mathbb{Z}_2$ symmetry with a multiplicatively conserved quantum number,

$$P_R = (-1)^{3(B-L)+2s}. \tag{1.29}$$

With this prescription, Standard Model particles have even parity ($P_R = 1$) and

---

* The definition of $\tan\beta$ is forthcoming; see Eq. 1.35.

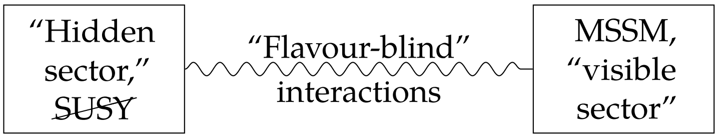

Figure 1.4.1: *Schematic of flavour-blind interactions transmitting supersymmetry breaking from a "hidden sector" to the MSSM.*

	Supermultiplet	Spin-$\frac{1}{2}$	Spin-0
Quarks and squarks	Q	$Q = (u_L, d_L)^T$	$\tilde{Q} = \left(\tilde{u}_L, \tilde{d}_L\right)^T$
	$\bar{u}$	$\bar{u} = u_R^\dagger$	$\tilde{\bar{u}} = \tilde{u}_R^*$
	$\bar{d}$	$\bar{d} = d_R^\dagger$	$\tilde{\bar{d}} = \tilde{d}_R^*$
Leptons and sleptons	L	$L = (\nu, e_L)^T$	$\tilde{L} = (\tilde{\nu}, \tilde{e}_L)^T$
	$\bar{e}$	$\bar{e} = e_R^\dagger$	$\tilde{\bar{e}} = \tilde{e}_R^*$
higgsinos and Higgs	H_u	$\tilde{H}_u = \left(\tilde{H}_u^+, \tilde{H}_u^0\right)^T$	$H_u = \left(H_u^+, H_u^0\right)^T$
	H_d	$\tilde{H}_d = \left(\tilde{H}_d^0, \tilde{H}_d^-\right)^T$	$H_d = \left(H_d^0, H_d^-\right)^T$

Table 1.5.1: *The interaction eigenstates in chiral supermultiplets in the MSSM in left-handed Weyl spinors.*

	Spin-1	Spin-$\frac{1}{2}$
Gluon and gluino	g	$\tilde{g}$
W-bosons and winos	$W^{i=1,2,3}$	$\tilde{W}^{i=1,2,3}$
B-boson and bino	B	$\tilde{B}$

Table 1.5.2: *The interaction eigenstates in gauge supermultiplets in the MSSM.*

their superpartners have odd parity ($P_R = -1$). This discrete symmetry could be a subgroup of a broken symmetry; it is phenomenologically and theoretically motivated.

R-parity has an astounding cosmological implication; in conjunction with conservation of energy, it prohibits decays of the lightest supersymmetric particle (LSP). The LSP's potential decays to Standard Model particles are forbidden by R-parity and its potential decays to an odd number of superparticles and Standard Model particles are forbidden by conservation of energy. With an R-parity, the LSP is, therefore, stable and, if it is weakly interacting, could be dark matter. If the LSP is electrically charged in the MSSM, the model is forbidden.

In the MSSM, the neutral sparticles are neutralinos and sneutrinos. Sneutrinos, however, cannot be all of the dark matter. Sneutrinos would scatter with nucleons via a Z-boson in the t-channel [45]. If sneutrinos dominated the local density of dark matter, they would have been detected in dark matter direct detection searches (forthcoming in Sec. 3.3.4). The neutralino, however, could be all of the dark matter or a subdominant component of dark matter.

Within the approximation that the Yukawa matrices are dominated by the entries from the third families, we can approximate the MSSM superpotential;

$$\begin{aligned} W_{\text{MSSM}} \approx{} & y_t \left(\tilde{\bar{t}}\tilde{t}H_u^0 - \tilde{\bar{t}}\tilde{b}H_u^+\right) - y_b \left(\tilde{\bar{b}}\tilde{t}H_d^- - \tilde{\bar{b}}\tilde{b}H_d^0\right) - y_\tau \left(\tilde{\bar{\tau}}\tilde{\nu}_\tau H_d^- - \tilde{\bar{\tau}}\tilde{\tau}H_d^0\right) \\ & + \mu \left(H_u^+ H_d^- - H_u^0 H_d^0\right). \end{aligned} \tag{1.30}$$

In the MSSM, we include explicit soft-breaking masses, though posit no mechanism for their origin or their scale. The soft-breaking Lagrangian in the MSSM is minimal, in that in omits non-analytic scalar-cubed couplings $\phi^*\phi\phi$. Without loss of generality,

$$\begin{aligned} \mathcal{L}_{\text{soft}} ={} & -\frac{1}{2}\left(M_3\tilde{g}\tilde{g} + M_2\tilde{W}\tilde{W} + M_1\tilde{B}\tilde{B} + \text{c.c.}\right) \\ & - \left(\tilde{\bar{u}}\boldsymbol{a_u}\tilde{Q}H_u - \tilde{\bar{d}}\boldsymbol{a_d}\tilde{Q}H_d - \tilde{\bar{e}}\boldsymbol{a_e}\tilde{L}H_d + \text{c.c.}\right) \\ & - \tilde{Q}^\dagger\boldsymbol{m^2_Q}\tilde{Q} - \tilde{L}^\dagger\boldsymbol{m^2_L}\tilde{L} + \tilde{\bar{u}}\boldsymbol{m^2_{\bar{u}}}\tilde{\bar{u}}^\dagger + \tilde{\bar{d}}\boldsymbol{m^2_{\bar{d}}}\tilde{\bar{d}}^\dagger + \tilde{\bar{e}}\boldsymbol{m^2_{\bar{e}}}\tilde{\bar{e}}^\dagger \\ & - m^2_{H_u}H_u^*H_u - m^2_{H_d}H_d^*H_d - \left(bH_uH_d + \text{c.c.}\right). \end{aligned} \tag{1.31}$$

The breaking parameters are matrices in quark and lepton family space, which could be complex, though must be Hermitian. Whilst such explicit masses break supersymmetry, because only part of each supermultiplet is granted a mass, electroweak symmetry is preserved. These parameters have an implicit scale dependence; their behaviour is determined by their beta-functions (forthcoming, Sec. 1.5.5).

1.5.1 The MSSM particle spectrum

Sparticles in the MSSM receive contributions to their masses from electroweak symmetry breaking and supersymmetry breaking, including contributions that mix sparticles' interaction eigenstates in mass eigenstates.

Squarks and sleptons

The left- and right-handed squarks* receive contributions to their masses from electroweak symmetry breaking via diagonal soft-breaking masses (Eq. 1.31), diagonal F-term Yukawa couplings (Eq. 1.20), resulting in contributions equal to Standard Model quark masses, diagonal D-terms (Eq. 1.22), Δ,† off-diagonal soft-breaking trilinears (Eq. 1.31) after electroweak symmetry breaking and off-diagonal F-terms after electroweak symmetry breaking. For the top-squark,

$$\boldsymbol{M}^2_{\tilde{t}} = \begin{pmatrix} m^2_{\tilde{Q}_3} + M_t^2 + \Delta_{\tilde{u}_L} & v(a_t^* \sin\beta - \mu y_t \cos\beta) \\ v(a_t \sin\beta - \mu^* y_t \cos\beta) & m^2_{\tilde{\bar{u}}_3} + M_t^2 + \Delta_{\tilde{u}_R} \end{pmatrix}. \tag{1.32}$$

Because off-diagonal elements are proportional to the Yukawa couplings (if a_t is assumed to be proportional to y_t), left- and right-handed squarks are significantly mixed only for third-generation squarks and sleptons. In fact, we neglect mixing for first- and second-generation squarks and sleptons. The diagonal contribution equal to the Standard Model mass is present for all squarks and sleptons, but only important for the top-squark.

The left- and right-handed sleptons are mixed in a similar fashion. For the

---

* A scalar's "handedness" is the chirality of its fermionic superpartner.

† The D-term contribution to any sfermion's mass is $\Delta = M_Z^2 \cos 2\beta (T_3 - Q) \sin^2\theta_W$ where θ_W is the Weinberg angle, Q is the sfermion's electric charge and T_3 is the sfermion's weak isospin.

τ-slepton,

$$M^2_{\tilde{\tau}} = \begin{pmatrix} m^2_{\tilde{L}_3} + \Delta_{\tilde{e}_L} & v(a^*_\tau \cos\beta - \mu y_\tau \sin\beta) \\ v(a_\tau \cos\beta - \mu^* y_\tau \sin\beta) & m^2_{\tilde{\bar{e}}_3} + \Delta_{\tilde{e}_R} \end{pmatrix}. \tag{1.33}$$

We diagonalise these mass matrices to obtain the physical states, which are linear superpositions of left- and right-handed states. This mixing, however, is neglected for the first- and second-generation squarks and sleptons, for which the physical states are identical to the interaction states. Because squark and slepton mixing in the third-generation splits the mass eigenvalues, the lightest top-squark and the lightest τ-slepton are often the lightest squark and slepton, respectively.

Higgs bosons

Supersymmetry requires two Higgs-doublets, so the structure of its scalar potential is more complicated than that of the Standard Model. The quartic Higgs coupling in the MSSM results from D-terms in Eq. 1.22, $\lambda = 1/8(g^2 + g'^2)$, where g and g' are the $\mathrm{SU}_L(2)$ and $\mathrm{U}_Y(1)$ gauge couplings respectively (as was required to cancel quadratic corrections to the Higgs mass in Sec. 1.1.1), unlike in the Standard Model, in which it is an unspecified free parameter. The quadratic Higgs couplings are $|\mu|^2$ from F-terms (Eq. 1.20), and $m^2_{H_{u,d}}$ and b from the soft-breaking masses. We sum quadratic and quartic terms to obtain the neutral scalar potential

$$\begin{aligned} V =& (|\mu|^2 + m^2_{H_u})|H^0_u|^2 + (|\mu|^2 + m^2_{H_d})|H^0_d|^2 - (bH^0_u H^0_d + \text{c.c.}) \\ &+ 1/8(g^2 + g'^2)(|H^0_u|^2 - |H^0_d|^2). \end{aligned} \tag{1.34}$$

In the MSSM, the electroweak symmetry-breaking mechanism is that the MSSM's two Higgs-doublets receive VEVs, v_u and v_d, related to the Standard Model VEV by $v^2 = v^2_u + v^2_d$ by the gauge bosons' masses. We parameterise the VEVs by

$$\begin{aligned} \tan\beta &= \frac{v_u}{v_d}, \\ v_u &= v \sin\beta, \\ v_d &= v \cos\beta. \end{aligned} \tag{1.35}$$

The fermion masses in the MSSM from electroweak symmetry breaking are, for example,

$$\begin{aligned} M_t &= y_t v_u = y_t v \sin\beta \Rightarrow y_t = \frac{M_t}{v\sin\beta} = \frac{y_t^{\text{SM}}}{\sin\beta}, \\ m_b &= y_b v_d = y_b v \cos\beta \Rightarrow y_b = \frac{m_b}{v\cos\beta} = \frac{y_b^{\text{SM}}}{\cos\beta}. \end{aligned} \tag{1.36}$$

The Yukawa couplings in the MSSM superpotential are those in the Standard Model, though scaled so that Standard Model masses are those measured. Because we want the Yukawa couplings to be perturbative up to the GUT scale, neither $\sin\beta$ nor $\cos\beta$ can be small; consequently, it must be that $1.2 \lesssim \tan\beta \lesssim 63$.

Prior to electroweak symmetry breaking, the Higgs doublets have 8 real degrees of freedom. When electroweak symmetry is broken, the three broken generators "eat" three degrees of freedom, resulting in three massive gauge bosons and in five massive Higgs bosons: light and heavy CP-even Higgs, h and H, a CP-odd Higgs, A and a charged Higgs, $H^\pm$. The lightest Higgs is an admixture of neutral H_u^0 and H_d^0, mixed by an angle α, that results from diagonalising a mass matrix. Within the "decoupling regime," in which $m_A \gg M_Z$, we obtain $\alpha \approx \beta - \pi/2$ and the lightest Higgs h couples with Standard Model fields identically to the Higgs in the Standard Model. At tree-level, its mass is $m_h \lesssim M_Z|\cos 2\beta|$, but it receives significant contributions from self-energy diagrams, particularly those involving top squarks or quarks. Including one-loop corrections,

$$m_h^2 \approx M_Z^2\cos^2 2\beta + \frac{3}{4\pi^2}\sin^2\beta\, y_t^2\left[\ln\left(\frac{M_{\text{SUSY}}^2}{M_t^2}\right) + \left(\frac{X_t^2}{M_{\text{SUSY}}^2}\right)\left(1 - \frac{X_t^2}{12M_{\text{SUSY}}^2}\right)\right], \tag{1.37}$$

where

$$X_t = a_t - \mu\cot\beta \tag{1.38}$$

is proportional to the off-diagonal element of the stop mass matrix (and hence stop mixing) in Eq. 1.32 and

$$M_{\text{SUSY}} = \sqrt{m_{\tilde{t}_1} m_{\tilde{t}_2}} \tag{1.39}$$

is the SUSY breaking scale. Despite these corrections, $m_h \lesssim 135\,\text{GeV}$, if the SUSY scale is less than ~ 1 TeV [41].

Because the loop corrections are logarithmic in the SUSY breaking scale, the

SUSY breaking scale must be increased exponentially if it is to result in moderate increases in Higgs mass. For a given M_{SUSY}, we can maximise the Higgs mass by fine-tuning the parameter X_t,

$$\frac{\partial m_h^2}{\partial X_t^2} \approx \frac{3}{4\pi^2} \sin^2\beta\, y_t^2 \frac{1}{M_{\text{SUSY}}^2} \left(1 - \frac{X_t^2}{6M_{\text{SUSY}}^2}\right) = 0, \Rightarrow X_t = \pm\sqrt{6}\, M_{\text{SUSY}}. \quad (1.40)$$

We refer to this as "maximal mixing"; we have fine-tuned stop mixing, via X_t, to maximise the Higgs mass (though stop mixing itself is not maximised). The maximal mixing condition in Eq. 1.40 is modified at higher orders.

The mass spectrum for the five Higgs bosons at tree-level is

$$m_A^2 = 2\mu^2 + m_{H_u}^2 + m_{H_d}^2, \quad (1.41)$$

$$m_{H^\pm}^2 = m_A^2 + M_W^2, \quad (1.42)$$

$$m_{h,H}^2 = \frac{1}{2}\left(m_A^2 + M_Z^2 \mp \sqrt{\left(m_A^2 - M_Z^2\right) + 4M_Z^2 m_A^2 \sin^2 2\beta}\right), \quad (1.43)$$

evaluated with running soft-breaking mass parameters at the electroweak scale. Notice that the CP-odd pseudoscalar Higgs mass is approximately degenerate with the charged Higgs mass, and that the CP-odd pseudoscalar Higgs mass, charged Higgs mass and heavy Higgs mass are approximately degenerate in the decoupling regime.

Neutralinos and charginos

The masses for the neutral wino, the bino and the neutral higgsinos result in a rich phenomenology. After electroweak symmetry breaking, these interaction eigenstates share quantum numbers and are "mixed" by off-diagonal mass terms:

$$\mathcal{L}_{\text{neutralino mass}} = -\frac{1}{2}\left(\psi^0\right)^T \boldsymbol{M}_{\chi^0} \psi^0 + \text{c.c.}, \quad (1.44)$$

where $\left(\psi^0\right)^T = \left(\tilde{B}, \tilde{W}^3, \tilde{H}_u, \tilde{H}_d\right)$ and

$$\begin{aligned}\boldsymbol{M}_{\chi^0} &= \begin{pmatrix} M_1 & 0 & -g'v_d/\sqrt{2} & g'v_u/\sqrt{2} \\ \cdot & M_2 & gv_u/\sqrt{2} & -gv_d/\sqrt{2} \\ \cdot & \cdot & 0 & -\mu \\ \cdot & \cdot & \cdot & 0 \end{pmatrix} \\ &= \begin{pmatrix} M_1 & 0 & -M_Z \sin\theta_W \cos\beta & M_Z \sin\theta_W \sin\beta \\ \cdot & M_2 & M_Z \cos\theta_W \cos\beta & -M_Z \cos\theta_W \sin\beta \\ \cdot & \cdot & 0 & -\mu \\ \cdot & \cdot & \cdot & 0 \end{pmatrix},\end{aligned} \tag{1.45}$$

with parameters at the electroweak scale. The diagonal elements are soft-breaking masses in Eq. 1.31, the off-diagonal μ elements result from chiral interactions from the superpotential (Eq. 1.18) and the off-diagonal M_Z elements result from gauge interactions in Eq. 1.21 after electroweak symmetry breaking.

The physical mass eigenstates that diagonalise Eq. 1.45 are called neutralinos,

$$\boldsymbol{M}_{\chi^0} \chi_i^0 = m_{\chi_i^0} \chi_i^0. \tag{1.46}$$

The neutralinos are orthonormal combinations of the neutral wino, the bino and the neutral higgsinos, labelled $\chi^0_{i=1,\ldots,4}$, $\chi_1^0 \equiv \chi$, with masses $m_\chi < m_{\chi_2^0} < m_{\chi_3^0} < m_{\chi_4^0}$. In the MSSM with gaugino mass unification, the bino mass at the electroweak scale is approximately half that of the wino,

$$M_1 \approx 0.5 M_2. \tag{1.47}$$

In the MSSM, if $M_1, M_2 \ll |\mu|$, the lightest neutralino is approximately bino-like in its composition with $m_\chi \approx M_1$, the second lightest is approximately wino-like with $m_{\chi_2^0} \approx 2m_\chi$, and the heavier neutralinos are even and odd (with respect to interchanging up- and down-type neutral higgsinos) admixtures of up- and down-type neutral higgsinos. The neutralinos' masses in this regime are approximately

$$\begin{aligned} m_{\chi^0_{1,2}} &\approx M_{1,2} - \frac{M_Z^2 \sin^2\theta_W (M_{1,2} + \mu \sin 2\beta)}{\mu^2 - M_{1,2}^2}, \\ m_{\chi^0_{3,4}} &\approx |\mu| + \frac{M_Z^2 (\operatorname{sgn}\mu \mp \sin 2\beta)(\mu \pm M_1 \cos^2\theta_W \pm M_2 \sin^2\theta_W)}{2(\mu \pm M_1)(\mu \pm M_2)}. \end{aligned} \tag{1.48}$$

Similarly to the neutral gauginos and neutral higgsinos, the charged wino and the charged higgsino interaction eigenstates are mixed in so-called charginos. The winos rewritten in the W-boson mass eigenstates are

$$\tilde{W}^{\pm} = \frac{1}{\sqrt{2}}\left(\tilde{W}^1 \mp i\tilde{W}^2\right), \tag{1.49}$$

$$\tilde{W}^0 = \tilde{W}^3. \tag{1.50}$$

The wino soft-breaking Lagrangian is

$$\begin{aligned}\mathcal{L}_{\text{soft}} &\supset -\frac{1}{2}M_2\tilde{W}\tilde{W} + \text{c.c.} \qquad (1.51)\\ &= -\frac{1}{2}M_2(\tilde{W}^1\tilde{W}^1 + \tilde{W}^2\tilde{W}^2 + \tilde{W}^3\tilde{W}^3) + \text{c.c.}\\ &= -\frac{1}{2}M_2(\tilde{W}^0\tilde{W}^0 + \tilde{W}^+\tilde{W}^- + \tilde{W}^-\tilde{W}^+) + \text{c.c..}\end{aligned}$$

The first term contributes to the neutralino mass matrix in Eq. 1.45 and the second and third terms contribute to the chargino mass matrix,

$$\mathcal{L}_{\text{chargino mass}} = -\frac{1}{2}\left(\psi^{\pm}\right)^T \boldsymbol{M}_{\chi^{\pm}}\psi^{\pm} + \text{c.c.}, \tag{1.52}$$

where $\left(\psi^{\pm}\right)^T = \left(\tilde{W}^+, \tilde{H}_u^+, \tilde{W}^-, \tilde{H}_d^-\right)$ and

$$\boldsymbol{M}_{\chi^{\pm}} = \begin{pmatrix} 0 & X^T \\ X & 0 \end{pmatrix}, \tag{1.53}$$

with

$$X = \begin{pmatrix} M_2 & gv_u \\ gv_d & \mu \end{pmatrix} = \begin{pmatrix} M_2 & \sqrt{2}\sin\beta M_W \\ \sqrt{2}\cos\beta M_W & \mu \end{pmatrix}. \tag{1.54}$$

The diagonal μ element results from chiral interactions from the superpotential (Eq. 1.18) and the off-diagonal M_W elements result from gauge interactions in Eq. 1.21 after electroweak symmetry breaking.

We rewrite Eq. 1.52 as

$$\mathcal{L}_{\text{chargino mass}} = -\frac{1}{2}\left(\phi^T X^T \eta + \eta^T X \phi\right) + \text{c.c.}, \tag{1.55}$$

where $(\psi^{\pm})^T = \left(\phi^T, \eta^T\right)$. We rotate our physical states to interaction eigenstates,

$$\chi^+ = V\phi, \tag{1.56}$$

$$\chi^- = U\eta, \tag{1.57}$$

where $\chi^{\pm}$are our physical states, positive and negative charginos,

$$\begin{aligned}\mathcal{L}_{\text{chargino mass}} = &-\frac{1}{2}\left(\chi^+\right)^T \left[\left(XV^{-1}\right)^T U^{-1}\right]\chi^- \\ &-\frac{1}{2}\left(\chi^-\right)^T \left[\left(X^T U^{-1}\right)^T V^{-1}\right]\chi^+ + \text{c.c.}.\end{aligned} \tag{1.58}$$

We require that masses are diagonal,

$$\left(XV^{-1}\right)^T U^{-1} = \left(X^T U^{-1}\right)^T V^{-1} = \begin{pmatrix} m_{\chi_1^{\pm}} & 0 \\ 0 & m_{\chi_2^{\pm}} \end{pmatrix}, \tag{1.59}$$

and that U and V are unitary, so that probability is conserved. We find that

$$VX^TXV^{\dagger} = UXX^TU^{\dagger} = \begin{pmatrix} m^2_{\chi_1^{\pm}} & 0 \\ 0 & m^2_{\chi_2^{\pm}} \end{pmatrix}, \tag{1.60}$$

i.e., positively charged (negatively charged) charginos are two eigenvectors of the symmetric X^TX (XX^T) matrix. Negative charginos are orthonormal combinations of $\tilde{W}^-$ and $\tilde{H}_d^-$ and positive charginos are orthonormal combinations of $\tilde{W}^+$ and $\tilde{H}_u^+$. Whilst the i-th positive and i-th negative charginos are different admixtures of wino and higgsino, their masses are degenerate.

Within the regime $M_2 \ll |\mu|$, the composition of the lighter charginos is predominantly charged wino, and that of the heavier chargino is predominantly charged higgsino, and their masses are approximately:

$$\begin{aligned} m_{\chi_1^{\pm}} &\approx M_2 - \frac{M_W^2(M_2 + \mu \sin 2\beta)}{\mu^2 - M_2^2}, \\ m_{\chi_2^{\pm}} &\approx |\mu| + \frac{\operatorname{sgn}\mu M_W^2(M_2 + \mu\sin 2\beta)}{\mu^2 - M_2^2}. \end{aligned} \tag{1.61}$$

If M_2 and $|\mu|$ in Eq. 1.54 are much larger than M_W or if $\tan\beta = 1$, because

$X \approx X^T$, the positive and negative chargino compositions are approximately identical.

Unlike the other wino and bino gauginos, the gluino cannot mix in a mass state, because it is a colour octet of the unbroken $\mathrm{SU_c}(3)$ gauge symmetry. The gluino's soft-breaking mass M_3 has a strong scale dependence; its physical mass in the CMSSM is

$$m_{\tilde{g}} \approx 2.7 m_{1/2}. \tag{1.62}$$

The gluino is frequently the heaviest sparticle in the CMSSM.

1.5.2 The CMSSM

The soft-breaking MSSM Lagrangian in Eq. 1.31 includes an exorbitant number of parameters: 105 parameters that cannot be rendered trivial by field rotations and that have no equivalent in the Standard Model. We want to construct a simpler, tractable model. Because experiments constrain flavour-changes in, for example, $\mu \to e\gamma$ and kaon mixing, we neglect soft-breaking masses that are off-diagonal in flavour space that could induce such changes. Because experiments constrain CP-violation in electric dipole moments, we neglect CP-violating phases in the soft-breaking Lagrangian.

We finally assume that the gauginos and scalars have common soft-breaking masses at the GUT scale,

$$\begin{aligned} m_{1/2} &= M_1 = M_2 = M_3, \\ m_0^2 \mathbb{1} &= m_{H_u}^2 \mathbb{1} = m_{H_d}^2 \mathbb{1} = \boldsymbol{m_Q^2} = \boldsymbol{m_L^2} = \boldsymbol{m_{\bar{u}}^2} = \boldsymbol{m_{\bar{d}}^2} = \boldsymbol{m_{\bar{e}}^2}, \end{aligned} \tag{1.63}$$

and that the trilinear couplings are equal to their respective Yukawa couplings multiplied by a common trilinear mass, which limits flavour-changing in quarks and leptons:

$$\begin{aligned} A_0 \boldsymbol{y_u} &= \boldsymbol{a_u}, \\ A_0 \boldsymbol{y_d} &= \boldsymbol{a_d}, \\ A_0 \boldsymbol{y_e} &= \boldsymbol{a_e}. \end{aligned} \tag{1.64}$$

We define the "Constrained Minimal Supersymmetric Standard Model" (CMSSM) as the MSSM with relations Eq. 1.63 and Eq. 1.64 imposed. The CMSSM's parameters are Yukawa couplings and μ in the superpotential, m_0, $m_{1/2}$, A_0 and a bilinear soft-breaking mass in the soft-breaking Lagrangian and the Standard Model gauge group couplings.

Electroweak symmetry breaking requires particular relations between soft-breaking and superpotential parameters; that the scalar potentials for H_u and H_d are minimised imposes

$$b = \frac{1}{2}\left[\tan 2\beta\left(m_{H_u}^2 - m_{H_d}^2\right) - M_Z^2\right], \tag{1.65}$$

$$\mu^2 = \frac{1}{2}\left[\tan 2\beta\left(m_{H_u}^2 \tan\beta - m_{H_d}^2 \cot\beta\right) - M_Z^2\right], \tag{1.65$'$}$$

where $M_Z^2 = \left(g^2 + g'^2\right) v^2/2$. We choose to trade μ^2 and b for M_Z and $\tan\beta$ via these relations. This is a convenience; within the "natural" b-μ^2 parameterisation, we might struggle to satisfy Eq. 1.65. Within the "pragmatic" $\tan\beta$-M_Z parameterisation, we axiomatically satisfy Eq. 1.65. The sign of μ, $\operatorname{sgn}\mu$, however, remains ambiguous. Rewriting Eq. 1.65, we obtain an expression for M_Z,

$$\frac{1}{2}M_Z^2 = -\mu^2 + \frac{m_{H_d}^2 - m_{H_u}^2 \tan^2\beta}{\tan^2\beta - 1}. \tag{1.66}$$

The CMSSM's input parameters in our "pragmatic" parameterisation are

$$m_0,\, m_{1/2},\, A_0,\, \tan\beta,\, \operatorname{sgn}\mu. \tag{1.67}$$

The value of M_Z (see Sec. 3.2.5) and the Standard Model fermion masses are* experimentally measured with high precision, and we neglect these in our parameterisation. The Standard Model, however, has "nuisance" parameters that are experimentally measured with limited precision (see Sec. 3.2), and which we consider unknown input parameters: the top-quark mass, the bottom-quark mass, the fine-structure constant and the strong coupling,

$$M_t,\, m_b(m_b)^{\overline{MS}},\, 1/\alpha_{\text{em}}(M_Z)^{\overline{MS}},\, \alpha_s(M_Z)^{\overline{MS}}. \tag{1.68}$$

The soft-breaking parameters in Eq. 1.67 are running parameters with an implicit scale dependence within the dimensional reduction renormalisation scheme

---

* With the exception of the top-quark mass and the bottom-quark mass, forthcoming.

with modified minimal subtraction ($\overline{DR}$). The common dimensional *regularisation* scheme breaks supersymmetric Ward identities. The soft-breaking parameters are defined at the GUT scale: the scale at which the extrapolated gauge couplings unify, typically $M_{\text{GUT}} \sim 10^{16}\,\text{GeV}$. The unification relations are broken by the renormalisation group evolution of the soft-breaking parameters. The CMSSM is a framework that can accommodate specific models at the Planck scale, including minimal supergravity (mSUGRA), in which supersymmetry is a local symmetry, related by the commutation relations of its generators to the generator of local space-time translations, i.e., gravity. Gravitational interactions transmit supersymmetry breaking from a hidden sector. The universality and unification of soft-breaking masses is a minimal assumption, resulting in CMSSM boundary condition

1.5.3 Other MSSM-type models

The CMSSM imposes stringent boundary conditions on the soft-breaking masses in the MSSM. We investigate tractable models in which these conditions are relaxed:

- In the "Non-Universal Higgs Model" (NUHM), the soft-breaking Higgs masses do not unify with a common scalar mass, because the Higgs' supermultiplets differ from those of the leptons and quarks, and because the Higgs, squarks and sleptons might belong to different representations of a GUT group. The NUHM has additional m_{H_u} and m_{H_d} soft-breaking input parameters.
- In the "Non-Universal Gaugino Model" (NUG), we permit the gaugino soft-breaking masses to differ from each other; the NUG has two additional parameters, because $m_{1/2}$ is replaced by M_1, M_2 and M_3.

We also consider phenomenological MSSM (pMSSM) models in which soft-breaking masses are defined at the scale $M_{\text{SUSY}} = \sqrt{m_{\tilde{t}_1} m_{\tilde{t}_2}}$, rather than at the GUT scale. We eliminate soft-breaking masses by assuming *ad hoc* degeneracies between parameters at the SUSY scale:

- Our 9 parameter pMSSM (p9MSSM) is defined by

$$M_2,\, M_3,\, m_{\tilde{Q}_3},\, m_{\tilde{L}_3},\, A_t,\, A_\tau,\, m_A,\, \mu,\, \tan\beta. \tag{1.69}$$

- Our 12 parameter pMSSM (p12MSSM) is defined by

$$M_2,\ m_{\tilde{L}_{1,2,3}},\ m_{\tilde{\bar{e}}_{1,2,3}},\ m_{\tilde{Q}_{1,2,3}},\ m_{\tilde{\bar{u}}_{1,2,3}},\ m_{\tilde{\bar{d}}_{1,2,3}},\ A_{u,c,t},\ A_{d,s,b},\ A_{e,\mu,\tau},\ m_A,\ \mu,\ \tan\beta, \tag{1.70}$$

  with separately degenerate up-type, down-type and slepton trilinears and a gaugino mass unification relation applied at the SUSY scale.

- Our 14 parameter pMSSM (p14MSSM) drops the unification of gaugino masses, resulting in additional M_1 and M_3 parameters.

- Finally, a popular pMSSM — the p19MSSM [46] — is defined by

$$\begin{gathered} M_1,\ M_2,\ M_3, \qquad (1.71)\\ m_{\tilde{Q}_{1,2}},\ m_{\tilde{Q}_3},\ m_{\tilde{\bar{u}}_{1,2}},\ m_{\tilde{\bar{u}}_3},\ m_{\tilde{\bar{d}}_{1,2}},\ m_{\tilde{\bar{d}}_3},\\ m_{\tilde{L}_{1,2}},\ m_{\tilde{L}_3},\ m_{\tilde{\bar{e}}_{1,2}},\ m_{\tilde{\bar{e}}_3},\\ A_t,\ A_b,\ A_\tau,\ A_{f\neq t,b,\tau}=0,\\ \mu,\ m_A,\ \tan\beta. \end{gathered}$$

1.5.4 Singlet extensions of the MSSM

Although I will not investigate extensions of the MSSM, I introduce singlet extensions of the MSSM for completeness. The MSSM superpotential in Eq. 1.27 contains a single dimensionful parameter, μ, that must be $\sim M_{\text{SUSY}}$ for electroweak symmetry breaking (Eq. 1.66). *A priori,* however, the μ parameter knows nothing of supersymmetry breaking; why should it be small compared with e.g., M_{P}? This is considered unnatural [47]. A popular solution is that μ is generated spontaneously [48,49]. The μ-term in the MSSM superpotential in Eq. 1.27 is replaced by a gauge singlet scalar S,

$$W = W_{\text{MSSM}}|_{\mu=0} + \lambda S H_u H_d, \tag{1.72}$$

where λ is a dimensionless parameter. The original μ-term is forbidden by a discrete $\mathbb{Z}_3$ symmetry. Electroweak symmetry breaking generates an effective μ-term, $\mu_{\text{eff.}} = \lambda\langle S\rangle$, because the gauge singlet scalar S obtains a non-zero VEV. Singlet extensions include an extra scalar and fermionic singletino, resulting in a fifth neutralino and a tree-level contribution to the mass of the lightest Higgs.

The superpotential in Eq. 1.72 is, however, problematical, because it is invariant under a global $U_{\text{PQ}}(1)$ symmetry [50]. After electroweak symmetry breaking, it would result in a massless axion. Three singlet extensions of the MSSM that solve this problem are:

- The "Next-to-Minimal Supersymmetric Standard Model" [48,49] (NMSSM) with superpotential

  $$W = W_{\text{MSSM}}|_{\mu=0} + \lambda S H_u H_d + \frac{1}{3}\kappa S^3. \tag{1.73}$$

  The κ-term explicitly breaks the $U_{\text{PQ}}(1)$ symmetry.

- The "$U(1)'$ Supersymmetric Standard Model" [51] ($U(1)'$SSM), in which the $U_{\text{PQ}}(1)$ symmetry is gauged, resulting in a massive Z' boson after electroweak symmetry breaking.

- The "E_6 Supersymmetric Standard Model" [52] (E_6SSM), a GUT in which the Standard Model gauge groups are embedded in the exceptional E_6 Lie group. The $U_{\text{PQ}}(1)$ symmetry is gauged and is a remnant of the broken E_6. The E_6SSM requires extra fields to complete the fundamental 27 representation of E_6. The E_6 group is motivated by string theory and the extra fields cancel anomalies present in the $U(1)'$SSM.

1.5.5 Renormalisation group equations for soft-breaking masses

To minimise missing orders in the electroweak symmetry breaking condition in Eq. 1.66, which is a boundary condition for the CMSSM parameters, we calculate the supersymmetric mass spectrum with soft-breaking parameters at the scale M_{SUSY}. This requires renormalisation group (RG) equations, which are found from the renormalisation scale μ-independence of physical quantities (via the independence of unrenormalised vertex functions [53]). If only the third-generation Yukawa couplings are significant, at one loop the β-functions and anomalous dimensions γ are relatively simple. The soft-breaking gaugino masses evolve as

$$\frac{\mathrm{d}M_i}{\mathrm{d}t} = \frac{1}{8\pi^2} b_i g_i^2 M_i, \tag{1.74}$$

where i indicates the gauge group, $t = \ln(\mu/\mu_0)$ with μ_0 a reference scale and, for MSSM-type models, $b_i = (33/5, 1, -3)$. These functions are similar in structure to the β-functions for the gauge couplings at one-loop (the gauge couplings do not, however, unify with only one-loop β-functions as foreshadowed in Sec. 1.1.3),

$$\beta_{g_i} = \frac{1}{16\pi^2} b_i g_i^3. \tag{1.75}$$

Consequently, $\frac{\mathrm{d}M_i/g_i^2}{\mathrm{d}t} = 0$ and M_i/g_i^2 is a renormalisation group invariant. If the gaugino masses are unified at M_{GUT} to $m_{1/2}$, as they are in the CMSSM, at the electroweak scale they are approximately:

$$\begin{aligned} M_1 &\approx 0.4 m_{1/2}, \qquad (1.76)\\ M_2 &\approx 0.8 m_{1/2},\\ M_3 &\approx 2.7 m_{1/2}. \end{aligned}$$

The RG equations for the soft-breaking scalar masses are of the form

$$\frac{\mathrm{d}m_\phi^2}{\mathrm{d}t} = \frac{1}{16\pi^2}\left[B_t Z_t + B_b Z_b + B_\tau Z_\tau - 8\sum_i C_i(\phi) g_i^2 M_i^2 + B_Y Y_\phi g_1^2 S\right], \tag{1.77}$$

where Y_ϕ is the hypercharge of field ϕ, $C_i(\phi)$ is the Casimir invariant for the field ϕ, which is dependent on the field's representation under the gauge group i, the B's are numerical coefficients, $S = \mathrm{Tr}(Y_{\phi_k} \boldsymbol{m}^2_{\boldsymbol{\phi}_k})$ and the Z's are

$$\begin{aligned} Z_t &= 2|y_t|^2(m_{H_u}^2 + m_{\tilde{Q}_3}^2 + m_{\tilde{\bar{u}}_3}^2) + 2|a_t|^2, \qquad (1.78)\\ Z_b &= 2|y_b|^2(m_{H_d}^2 + m_{\tilde{Q}_3}^2 + m_{\tilde{\bar{d}}_3}^2) + 2|a_b|^2,\\ Z_\tau &= 2|y_\tau|^2(m_{H_d}^2 + m_{\tilde{L}_3}^2 + m_{\tilde{\bar{e}}_3}^2) + 2|a_\tau|^2. \end{aligned}$$

The Yukawa couplings and trilinears, and thus these factors, are important for only third-generation scalars and for the Higgs. The RG equations for the MSSM scalars are given by the coefficients in Table 1.5.3 in conjunction with the general formula Eq. 1.77. Fig. 1.5.1 illustrates the evolution of the soft-breaking masses from M_{GUT} to M_{SUSY}. The quadratic couplings in the Higgs potential, $\mu^2 + m_0^2$, bifurcate and the up-type Higgs quadratic coefficient runs negative at M_{SUSY}, triggering electroweak symmetry breaking (radiative electroweak symmetry breaking).

ϕ	B_t	B_b	B_τ	(C_3, C_2, C_1)	B_Y
$\tilde{Q}_{1,2}$	0	0	0	$(4/3, 3/4, 1/60)$	6/5
$\tilde{\bar{u}}_{1,2}$	0	0	0	$(4/3, 0, 4/15)$	6/5
$\tilde{\bar{d}}_{1,2}$	0	0	0	$(4/3, 0, 1/5)$	6/5
$\tilde{L}_{1,2}$	0	0	0	$(0, 3/4, 3/20)$	6/5
$\tilde{\bar{e}}_{1,2}$	0	0	0	$(0, 0, 3/5)$	6/5
H_u	3	0	0	$(0, 3/4, 3/20)$	3/5
H_d	0	3	1	$(0, 3/4, 3/20)$	-3/5
$\tilde{Q}_3$	1	1	0	$(4/3, 3/4, 1/60)$	1/5
$\tilde{\bar{u}}_3$	2	0	0	$(4/3, 0, 4/15)$	-4/5
$\tilde{\bar{d}}_3$	0	2	0	$(4/3, 0, 1/5)$	2/5
$\tilde{L}_3$	0	0	1	$(0, 3/4, 3/20)$	-3/5
$\tilde{\bar{e}}_3$	0	0	2	$(0, 0, 3/5)$	6/5

Table 1.5.3: *MSSM RG equation coefficients for Eq. 1.77. The C_i are the Casimir invariants, except for the Higgs, in which case they are the Casimir invariants scaled by* $1/4$.

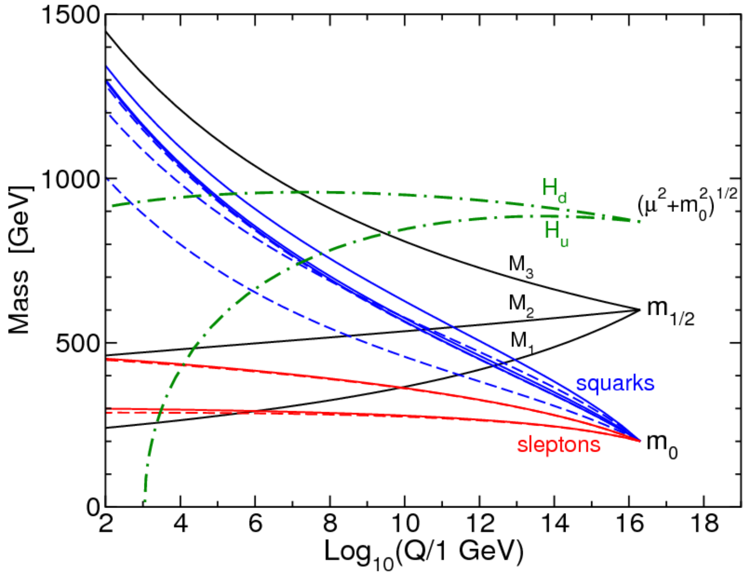

Figure 1.5.1: *The RG evolution of the MSSM soft-breaking masses from Ref. [41].*

Chapter 2

Statistics

We wish to compare the predictions of MSSM-type models with experimental data in a formal, probabilistic manner, to find the “best” regions of their parameter spaces, and, perhaps, to exclude or favour particular models with a meaningful, well-defined test. For this we require a statistical methodology. There are two classes of statistical methodologies (and hybrids), built upon complementary interpretations of probability.

A “frequentist” methodology defines a probability as the frequency with which an event occurs, in the limit of an infinite number of identical experiments [54]. This is problematical: we cannot realise either the limit, an infinite number of experiments, or that the experiments are identical. Nevertheless, this axiom is the foundation of the frequentist interpretation of probability.

A Bayesian methodology, in contrast, defines probability as a (numerical) measure of the plausibility of a proposition, and is built upon Bayes’ theorem [55],

$$P\left(A|B\right) \equiv \frac{P\left(A,B\right)}{P\left(B\right)} = \frac{P\left(B|A\right) \times P\left(A\right)}{P\left(B\right)}, \tag{2.1}$$

where P is a probability and A and B are propositions. We manipulate Eq. 2.1 by writing $B \to B, C$;

$$
\begin{aligned}
P\left(A|B,C\right) &= P\left(B,C|A\right) \times P\left(A\right) \times \frac{1}{P\left(B,C\right)} \\
&= P\left(B,C|A\right) \times P\left(A\right) \times \frac{1}{P\left(B|C\right)P\left(C\right)} \\
&= P\left(B,C|A\right) \times \frac{P\left(A\right)}{P\left(C\right)} \times \frac{1}{P\left(B|C\right)} \\
&= P\left(B,C|A\right) \times \frac{P\left(A|C\right)}{P\left(C|A\right)} \times \frac{1}{P\left(B|C\right)} \\
&= \frac{P\left(B,C|A\right)}{P\left(C|A\right)} \times P\left(A|C\right) \times \frac{1}{P\left(B|C\right)} \\
&= \frac{P\left(B|A,C\right) \times P\left(A|C\right)}{P\left(B|C\right)}.
\end{aligned}
\tag{2.2}
$$

If A and B are continuous variables, however, we rewrite Eq. 2.2 with probability density functions (pdf);

$$
p\left(A|B,C\right) = \frac{p\left(B|A,C\right) \times p\left(A|C\right)}{p\left(B|C\right)}, \tag{2.3}
$$

where p is a pdf. If we have a model M with parameters $x_1, \ldots, x_N$, for which we have obtained experimental data D, the Bayesian posterior pdf (henceforth posterior) for the model's parameters is given by Bayes' theorem in the form in Eq. 2.3;

$$
\begin{aligned}
\underbrace{p\left(x_1, \ldots, x_N|D,M\right)}_{\text{Bayesian posterior}} &= \frac{p\left(D|x_1, \ldots, x_N, M\right) \times p\left(x_1, \ldots, x_N|M\right)}{p\left(D|M\right)} \\
&\equiv \frac{\overbrace{\mathcal{L}\left(x_1, \ldots, x_N\right)}^{\text{Likelihood}} \times \overbrace{\pi\left(x_1, \ldots, x_N\right)}^{\text{Prior}}}{\underbrace{\mathcal{Z}}_{\text{Evidence}}},
\end{aligned}
\tag{2.4}
$$

where $\mathcal{L}$ is the likelihood, π is the prior pdf, our prior belief in the hypothesis, and $\mathcal{Z}$ is the evidence. The posterior, $p\left(x_1, \ldots, x_N|D,M\right)$, does not imply that $x_1, \ldots, x_N$ are random variables.

The likelihood is $p\left(D|x_1, \ldots, x_N, M\right)$ as a function of $x_1, \ldots, x_N$ — it is the probability of measuring a particular outcome of an experiment given the theory that governs the experiment as a function of the theory's parameters. The likelihood is not a pdf. If $p\left(D|x_1,\ldots,x_N,M\right)$ is interpreted as a function of the outcomes or data, it is called the sampling distribution (which is a pdf). In contrast, a prime advantage of Bayesian statistics is that the posterior reflects the plausibility of the proposition of interest. The prior is our beliefs on the plausibility of the proposition before the experimental data (discussed in detail in Sec. 2.5). The evidence reflects the viability of the model, though individual evidences lack meaning, and so evidences must be compared.

We review the relevant Bayesian and frequentist statistical quantities and tests, with emphasis on parameter inference and model comparison. The Bayesian and frequentist objects are identical in purpose but have conceptual differences in their interpretation and meaning.

2.1 Posteriors and likelihoods

We wish the quantify whether a region of a model's parameter space is in agreement with experiments and, in the Bayesian methodology, our prior beliefs about the model's parameter space. This requires that we calculate the posterior density function in the Bayesian methodology and the likelihood in the frequentist methodology.

The posterior and the likelihood, though, are functions of all of the model's parameters. This is inconvenient — we often wish to examine only a subset of the model's parameters, typically either one or two, so that the objects can be visualised.

The posterior density, however, is problematical in that, as a pdf, it is dependent on the model's parameterisation. If we changed the parameterisation of the pdf, it would be altered by a Jacobian. It would be desirable, then, if statistics derived from the posterior were independent of this choice of parameterisation.*

We can make use of the posterior's properties as a pdf and integrate or marginalise parameters which are of no interest, resulting in a marginalised poste-

---

* Strictly speaking, we ought to require only that "decisions" are not dependent on our parameterisation, for example, whether to reject a model, or whether to build a new experiment.

rior pdf for only the desired subset of parameters, that is,

$$p\left(x_{N+1},\ldots,x_M|D\right) = \int p\left(x_1,\ldots,x_M|D\right) \prod_{i=1}^{N} \mathrm{d}x_i \tag{2.5}$$

where p is a pdf and the first N parameters $(x_1, \ldots, x_N)$ were marginalised.

In contrast, the likelihood is "profiled" — parameters of no interest are set to the values for which the likelihood is maximised. The profile likelihood is

$$\mathcal{L}\left(x_{N+1},\ldots,x_M\right) = \max_{x_1,\ldots,x_N} \mathcal{L}\left(x_1,\ldots,x_M\right), \tag{2.6}$$

where the first N parameters $(x_1, \ldots, x_N)$ were profiled. The desirable feature of this method is that it facilitates an application of Wilkes's theorem in determining confidence intervals (forthcoming, Sec. 2.2), though it lacks meaning, since the profile likelihood is not a sampling distribution.

These procedures are contrasted in Fig. 2.1.1. It illustrates that marginalisation results in modes in posterior distributions that are not present in the profile likelihood.

It is unfortunate that the quantity $-2\ln\mathcal{L}$ is often synonymous with χ^2,

$$-2\ln\mathcal{L} = \chi^2 \tag{2.7}$$

This is strictly true, though, only if $\mathcal{L}$ is Gaussian. I will, however, repeat this misnomer, but beware that χ^2 defined in this way are not necessarily χ^2-distributed (forthcoming, Sec. 2.2).

The notation is henceforth such that marginalisation of the posterior and profiling of the likelihood and χ^2 are implicit. Missing arguments are either marginalised or profiled.

2.1.1 Derived quantities

We often want posterior densities and profile likelihoods as functions of derived quantities that are functions of the model's parameters, rather than the model's parameters themselves. Fortunately, this is trivial. The profile likelihood is not a pdf, and can be written as a function of derived quantities. Because the posterior density is a pdf, we check its transformation. Suppose we transform our

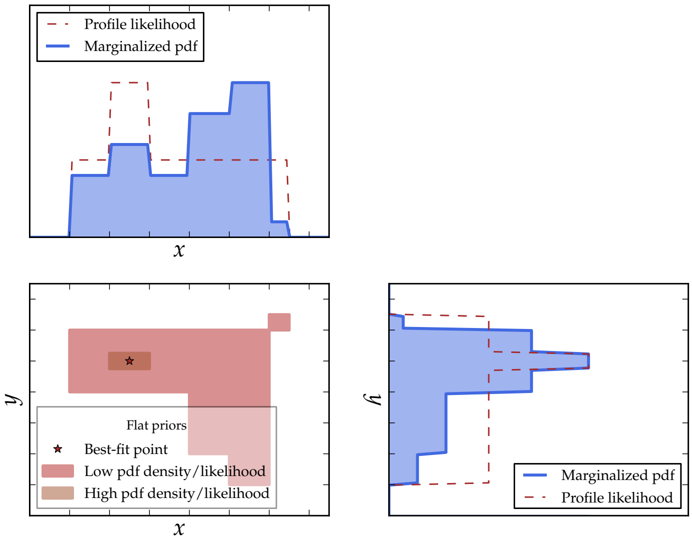

(a) *Marginalised pdf and profile likelihood contrasted in a simple two-dimensional example.*

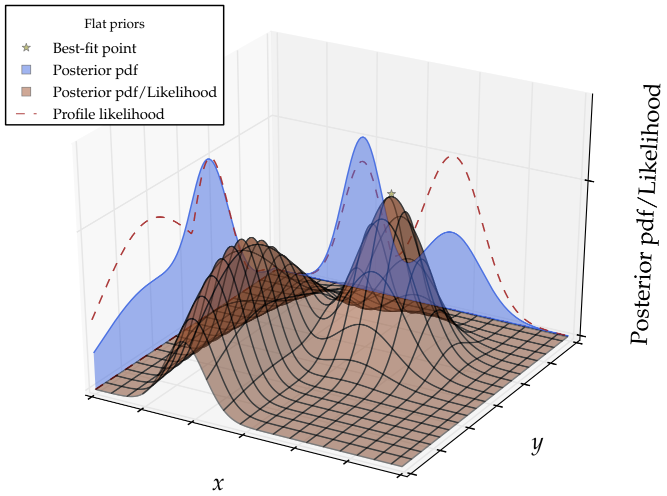

(b) *Marginalised pdf and profile likelihood contrasted in a three-dimensional example.*

Figure 2.1.1: *Marginalised pdf and profile likelihood contrasted. The two-dimensional plots show posterior pdf, or equivalently, with flat priors, the likelihood. The one-dimensional plots show marginalised pdf in blue and profile likelihood in red. The best-fit point, marked with a star, equivalent, with flat priors, to the MAP in the two-dimensional plots, does not correspond to the MAP in the one-dimensional plots. Modes are present in the marginalised posterior that are not present in the profile likelihood, as a result of marginalisation. The distributions are normalised so that their maximum values are unity.*

parameters,

$$x_1, \ldots, x_N \to f_1(x_1, \ldots, x_N), \ldots, f_N(x_1, \ldots, x_N), \tag{2.8}$$

where the functions f_i define a well-behaved change of variables. We can write, without loss of generality, that

$$\begin{aligned} p\left(f_1' | D\right) &= \int p\left(f_1 | D\right) \delta\left(f_1 - f_1'\right) \, \mathrm{d}f_1 \\ &= \int p\left(f_1, \ldots, f_N | D\right) \delta\left(f_1 - f_1'\right) \prod_{i=1}^{N} \mathrm{d}f_i \\ &= \int p\left(x_1, \ldots, x_N | D\right) \delta\left(f_1(x_1, \ldots, x_N) - f_1'\right) \prod_{i=1}^{N} \mathrm{d}x_i. \end{aligned} \tag{2.9}$$

Our posterior densities transform trivially to a derived quantity; we integrate our densities whilst fixing our derived quantity via the delta function, without invoking complicated Jacobians.

2.2 Confidence intervals and credible regions

We wish to find intervals in parameter space which we believe contain the true parameters. We construct either frequentist confidence intervals, which reflect properties of the method — we can be sure that method captures the true parameters with a particular frequency and the interval is constructed "in the data," or Bayesian credible regions, which reflect our degree of belief in the region and are constructed "in the model."

Confidence intervals have a "frequentist" definition — a $(1-\alpha)$ confidence interval for a parameter will contain the parameter's true value at a frequency of $(1-\alpha)$, were the experiment repeated identically ad infinitum. Conversely, the interval will not contain the true value at a frequency of α. This violates the "likelihood principle:" that information is in the data alone, rather than pseudo-data. Confidence intervals may be found from likelihoods via an application of Wilkes's theorem, that asymptotically

$$\chi^2\left(x_1, \ldots, x_N\right) - \chi^2_{\text{Min}} \sim \chi^2_N, \tag{2.10}$$

where χ^2_N is a χ^2-distribution with N degrees of freedom, where N is the dimension of the confidence interval and $x_1, \ldots, x_N$ are the parameters of interest. A χ^2-distribution with N degrees of freedom is how $\chi^2 = \sum_i^N (x_i - \mu_i)^2/\sigma_i^2$ is distributed if x_i follow Gaussian distributions with means μ_i and variances σ_i^2.

We find the critical $\Delta\chi^2$ values — the values of χ^2 for which there is only an α probability of obtaining a $\Delta\chi^2$ that large or larger. We apply a profile likelihood test (PL):

$$\begin{aligned}&\text{If } \chi^2 \left(x_1, \ldots, x_N\right) - \chi^2_{\text{Min}} > \Delta\chi^2_{\text{Crit}},\ x_1, \ldots, x_N \text{ outside } (1-\alpha) \text{ confidence interval,}\\ &\text{If } \chi^2 \left(x_1, \ldots, x_N\right) - \chi^2_{\text{Min}} \leq \Delta\chi^2_{\text{Crit}},\ x_1, \ldots, x_N \text{ inside } (1-\alpha) \text{ confidence interval.}\end{aligned} \tag{2.11}$$

The $\Delta\chi^2_{\text{Crit}}$ values are such that

$$\mathrm{F}\left(\Delta\chi^2_{\text{Crit}}, N\right) = 1 - \alpha, \tag{2.12}$$

where F is a cumulative χ^2-distribution with N degrees of freedom. We are typically interested in $(1-\alpha) = 68\%$ or 95% with $N = 1$ or 2, these $\Delta\chi^2_{\text{Crit}}$ values are listed in Table 2.2.1. The χ^2-distribution is illustrated in Fig. 2.2.1.

Confidence intervals found in this way are not necessarily contiguous but they are unique, always include the best-fit point, and may be of any dimension. If our model had a single parameter, we could find our confidence interval via a Neyman or Feldman-Cousins construction.

In our Bayesian methodology, we again make use of the posterior's properties as a pdf, and find its credible regions — regions that contain $(1-\alpha)$ of our posterior. These regions, though, are not unique, and credible regions are chosen via a choice of so-called "ordering rule." As noted in Sec. 2.1, it would be desirable if our statistical measures were invariant under reparameterisations.

For a $(1-\alpha)$ one-dimensional credible region, we choose an equal-tail-probabilities ordering rule (ETP), in which $\alpha/2$ of the posterior is below the region and $\alpha/2$ of the posterior is above the region,

$$\int\limits_{-\infty}^{L} p\left(x|D\right)\,\mathrm{d}x = \int\limits_{U}^{\infty} p\left(x|D\right)\,\mathrm{d}x = \alpha/2. \tag{2.13}$$

These one-dimensional regions from U to L are invariant under reparameterisa-

Dimension of interval, N	Confidence level, $(1-\alpha)$	$\Delta\chi^2_{\mathrm{Crit}}$
1	68%	0.99
	95%	3.84
2	68%	2.28
	95%	5.99

Table 2.2.1: *The critical* χ^2 *values,* $\Delta\chi^2_{\mathrm{Crit}}$*, for constructing one-dimensional and two-dimensional* 68% *and* 95% *confidence intervals.*

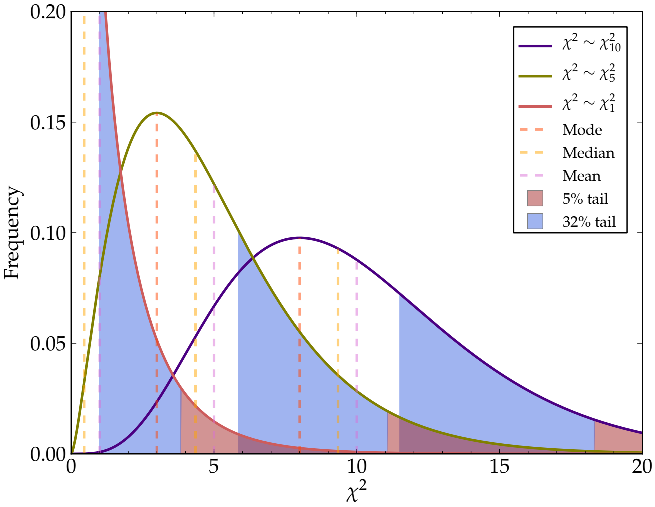

Figure 2.2.1: χ^2*-distributions with* 1, 5 *and* 10 *degrees of freedom, showing* 32% *and* 5% *tails, mode, mean and median.*

tions, always include the median (but not necessarily the mode or the best-fit point, forthcoming, Sec. 2.3) and are contiguous. If we were to choose $x = f(y)$, the limits U and L for x would change trivially to $f^{-1}(U)$ and $f^{-1}(L)$ for y. This prescription, however, is ill-suited to distributions in which a posterior mode is at the edge of the prior distribution.

Unfortunately, this construction cannot be readily generalised to higher dimensions. We choose a different ordering rule for two-dimensional credible regions: the credible region is the smallest region R (in the "pragmatic" parameterisation) that contains $(1 - \alpha)$ of the posterior,

$$\int_R p\left(x_1, x_2 | D\right) \, \mathrm{d}x_1 \, \mathrm{d}x_2 = 1 - \alpha. \tag{2.14}$$

These highest posterior density (HPD) multidimensional regions are not invariant under reparameterisations, not necessarily contiguous, and always include the mode (but not necessarily the best-fit point, forthcoming, Sec. 2.3). Although, of course, integrals are invariant under reparameterisations, the domain of this integral is parameterisation dependent, because the size of a region of parameter space depends on parameterisation. I know of no multidimensional ordering rule with entirely satisfactory properties. One, then, should be careful in interpreting two-dimensional credible regions (and pdfs), because they change non-trivially under reparameterisations.

2.3 Posterior means and best-fit points

We want to present a single point in the model's parameter space which summarises the results of a statistical analysis. These "best estimates" ought to be invariant under reparameterisations (suppose x^B is declared to be the best estimate of x, it would be desirable if the best estimate for $y = \mathrm{f}\left(x\right)$ was $\mathrm{f}\left(x^B\right)$, but this is difficult to achieve), consistent (asymptotically equal the parameter's true value as more experiments are performed), and unbiased (with a finite number of experiments, its expectation should be equal to the parameter's true value).

Since the posterior is a pdf, we can calculate the expectation value for each parameter — the "posterior mean,"

$$\bar{x} = \int x \times p\left(x|D\right)\,\mathrm{d}x. \tag{2.15}$$

The resulting posterior mean might, however, lie outside the credible region, particularly if the posterior is multimodal, in which case it may lie between two modes, may have a large χ^2 or may even be unphysical. The posterior mean does not satisfy our invariance criteria for a best estimate; if we were to choose $x = \mathrm{f}\left(y\right)$, $\bar{x} \neq \mathrm{f}\left(\bar{y}\right)$, but it is consistent and axiomatically unbiased.

The reader might wonder why a point with maximum posterior density is not identified (maximum a posteriori probability or MAP) — as mentioned previously, densities are parameterisation dependent, violating our invariance criteria. We could choose the posterior median, which is parameterisation invariant in that if we were to choose $x = \mathrm{f}\left(y\right)$, $\mathrm{Me}\left(x\right) = \mathrm{f}\left(\mathrm{Me}\left(y\right)\right)$.

We choose the posterior mean as our best estimator, since, despite it failing parameterisation invariance, it has a meaningful interpretation as the expectation of a parameter and is representative of distributions with more than one mode or large tails, unlike the mode. Clearly, constructing a best estimator from the posterior is challenging — perhaps this is no surprise, since the result of Bayesian inference is the posterior pdf, the distribution itself. Technically, it is recognised that our estimator ought to minimise the expected "loss function" — a function that measures the cost of wrongly estimating a parameter. If we were, for example, building an expensive experiment from our analysis, we would construct an appropriate loss function to find our best estimator [56].

We also present the point with the smallest $\chi^2 = \chi^2_{\mathrm{Min}}$ — the "best-fit" point (or equivalently the maximum likelihood estimator or MLE). The best-fit point has a special significance in frequentist statistics — it is from the best-fit point that the confidence intervals are constructed, and χ^2_{Min} is the test statistic for judging the model. The best-fit point satisfies our parameterisation invariance criteria and consistency, but might be biased, because, with limited data, the best-fit point for a parameter might not coincide with the posterior mean (expectation) for that parameter.

2.4 Evidences and *p*-values

The Bayesian probability of a model M given data D can be written via Bayes' theorem (Eq. 2.1),

$$P\left(M|D\right) = p\left(D|M\right) \times P\left(M\right) / p\left(D\right), \tag{2.16}$$

where P is a probability and p is a pdf. This probability is proportional to our prior belief regarding the model, $P\left(M\right)$. This is meaningful if we consider a ratio of probabilities for models M_a and M_b, eliminating $p\left(D\right)$ and permitting only relative prior belief in a model,

$$\underbrace{P\left(M_a|D\right) / P\left(M_b|D\right)}_{\text{Posterior odds}} = \underbrace{p\left(D|M_a\right) / p\left(D|M_b\right)}_{\text{Bayes-factor}} \times \underbrace{P\left(M_a\right) / P\left(M_b\right)}_{\text{Prior odds}}. \tag{2.17}$$

The Bayes-factor indicates how our prior odds ought to change because of the data, resulting in our posterior odds. The Bayes-factor is, in fact, a ratio of evidences found from parameter inferences in the models in the denominator in Eq. 2.4.

Individual evidences are meaningless — it is necessary to compare against a reference model with a Bayes-factor. If the Bayes-factor is greater than (less than) one, the model in the numerator (denominator) is favoured. The interpretation of Bayes-factors is somewhat subjective, though a popular choice is the Jeffreys' scale, Table 2.4.1, to ascribe qualitative meanings to Bayes-factors. Prior odds are somewhat subjective and there might exist a spectrum of assigned prior odds amongst investigators. All investigators, however, will make identical conclusions from the posterior odds, if the Bayes-factor is sufficiently large.

The Bayes-factor quantitatively incorporates a principle of economy widely-known as Occam's razor [58] and in physics as "fine-tuning" or "naturalness" [59–61]. It is insightful to consider the evidence $\mathcal{Z} = p\left(D|M\right)$ a function of the data normalised to unity, i.e., as a sampling distribution [62,63]. Natural models "spend" their probability mass near the obtained data — a large fraction of their parameter space agrees with the data. Complicated models squander their probability mass away from the obtained data. This is illustrated in Fig. 2.4.1. Whilst it might be that a model is complicated because it has many parameters, and so makes a range of predictions for the data, a model with many parameters can be simple. Simple models are falsified by experiments more easily than complicated models, because they make sharper predictions. It might be said that Bayesian statistics reifies Occam's razor, "fine-tuning" and "naturalness" arguments. "Naturalness" is no longer a nebulous, aesthetic criterion; it is formalised and justified by Bayesian statistics [64].

The frequentist test is a χ^2 test: we assume that the χ^2_{Min} has a particular distribution (its sampling distribution) were the experiments repeated ad infinitum, and calculate the p-value — the probability of obtaining a χ^2 as large or larger than the observed χ^2_{Min}:

$$p\text{-value} = 1 - \mathrm{F}\left(\chi^2_{\text{Min}}, N\right), \tag{2.18}$$

where F is a cumulative χ^2-distribution with N degrees of freedom. We assume that the distribution is χ^2_N, where N, the number of degrees of freedom, is the number of contributions to the χ^2 minus the number of parameters that were fitted to achieve χ^2_{Min}. This assumption is reasonable if and only if the contributions to the χ^2 are approximately Gaussian and the parameter space completely maps the observables space. It could, in principle, be checked via Monte Carlo — we could repeat the following procedure many times: draw pseudo-experimental data from the sampling distributions (assuming that the best-fit point is true), fit the model's parameters, and note the χ^2_{Min} achieved, and lastly plot a histogram of the χ^2_{Min}. This, however, is completely unfeasible, because of the CPU time required to fit the model's parameters.

One solution is to treat the pseudo-experimental data as a "perturbation," and re-minimise the χ^2 only in the vicinity of the observed best-fit point. The feasibility of this, though, is not clear.

An easier but less robust check is to check only the sampling distribution of the χ^2 at the best-fit point, rather than the distribution of χ^2_{Min}. The procedure is identical, except that the parameters are not refitted. We expect the result will be χ^2-distribution with a number of degrees of freedom equal to the number of contributions to the χ^2, i.e., we do not check whether subtracting the number of fitted parameters to account for fitting is reasonable, only that the contributions to the χ^2 are approximately Gaussian.

We will consider p-values of less than 5% to be significant. This is aggressive; we have a appreciable chance of a type-II error.* One might wonder whether a

---

* A type-II error is that an hypothesis is wrongly rejected by chance.

Grade	Bayes-factor, B	Interpretation
0	$K > 1$	Favours hypothesis in numerator.
1	$1 > K > 10^{-0.5}$	Barely worth mentioning.
2	$10^{-0.5} > K > 10^{-1}$	Substantial.
3	$10^{-1} > K > 10^{-1.5}$	Strong.
4	$10^{-1.5} > K > 10^{-2}$	Very strong.
5	$K < 10^{-2}$	Decisive.

Table 2.4.1: *The Jeffreys' scale for interpreting Bayes-factors [57], which are ratios of evidences. We assume that the favoured model is in the denominator, though this could be readily inverted.*

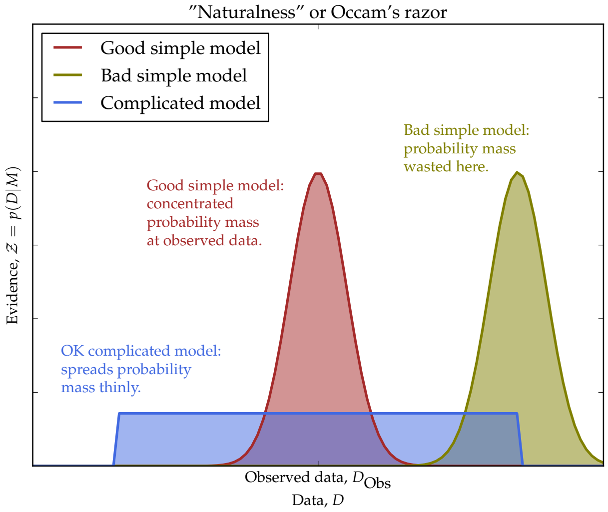

Figure 2.4.1: *Illustration of the evidence, interpreted as a sampling distribution, originally from Ref. [63]. The observed evidence is the evidence evaluated at the observed data. The blue line shows a model that concentrates its probability mass at the observed data: it is a good, simple model. The green line shows a model that concentrates its probability mass away from the observed data: it is a bad, simple model. The red line shows a model that thinly spreads its probability mass around the observed data: it is an OK, complicated model. The complicated model might achieve a maximum likelihood greater than that of the good, simple model, but the simple model is favoured by the Bayes-factor.*

prior effect has crept into our frequentist statistics; our choice of critical p-value might depend on our prior belief in an hypothesis, even if we, of course, choose critical p-value before the analysis.

2.5 Prior choices and effects

A common criticism of Bayesian methodologies is that the results depend on one's choice of priors, for which there is no objectively unique correct choice, though there are certainly bad choices. Bayesian methodologies manipulate our prior beliefs in a consistent manner, but give no clue as to what they ought to be. Even "flat" priors, priors that equally weight linear intervals in the "pragmatic" parameterisation, are a choice: we have no choice but to choose. A "sensible" prior choice is non-informative; a prior which does not strongly influence the posterior. Our prior choices were motivated by either our state of knowledge or by pragmatism. If our conclusions, evidences or posteriors are dependent on our choices of non-informative priors, it indicates that the data (in the likelihood) is too weak on which to draw robust conclusions.

Because we decide that our prior beliefs for our models' parameters are not correlated, our prior pdf can be factorised,

$$\pi\left(x_1, \ldots, x_N\right) = \prod_{i=1}^{N} \pi\left(x_i\right). \tag{2.19}$$

Here we make use of the relation,

$$p\left(A, B|C\right) = p\left(A|C\right) \times p\left(B|C\right) \times \frac{p\left(A|B, C\right)}{p\left(A|C\right)}. \tag{2.20}$$

Because we decide that the priors are independent, the fraction in Eq. 2.20 is trivially equal to unity. This can be applied recursively for an arbitrary number of parameters.

If we are ignorant of the magnitude of a parameter, our priors must not favour particular orders of magnitude. The "log" prior is a scale invariant Jeffreys' prior: it equally weights each decade or logarithmic interval. Flat priors, on the other hand, weight each decade ten times more than the last, e.g., a flat prior for x over the range $0 - 100$ will weight $10 - 100$ ten times more than $0 - 10$. This is an example of "pile-up."* We are ignorant of the magnitudes of m_0 and $m_{1/2}$ in the CMSSM, so we choose log priors.

Starting from our requirement that the prior for a scale parameter is scale invariant,

$$\pi\left(\lambda x\right)\,\mathrm{d}\lambda x = \pi\left(x\right)\,\mathrm{d}x, \tag{2.21}$$

we find that $\pi(x) \propto 1/x$, which gives $\pi(\log x) = $ constant. The base of the logarithm is of no consequence; the kernel for a log prior is independent of its base and the prior pdf is normalised to unity, so the height and shape of a log prior are independent of its base.*

The trilinear parameter, A_0, is problematical: it is scale, and we are ignorant of its magnitude, but it may be positive or negative, or zero, contrary a scale parameter. We choose a flat prior for A_0 for these pragmatic reasons. We are not ignorant of the magnitude of $\tan\beta$ — from LEP, we know that $\tan\beta > 2$ and, if the top-quark Yukawa coupling is perturbative, we must have $\tan\beta < 63$. We choose a flat prior for $\tan\beta$. A flat prior for x is $\pi(x) \propto$ constant. The difference between flat and log priors for $\tan\beta$ is small, because we know its magnitude.

We adopt two numerically equivalent approaches for the nuisance parameters (Eq. 1.68):

1. Our nuisance priors are informative, Gaussian priors, representing the best experimental estimates of the parameters. This choice maximises the efficiency of our scanning algorithm. In this case, the likelihood does not include nuisance experiments — the profile likelihood might be distorted by discrepant values of the nuisance parameters.

2. Our nuisance priors are flat (since we are not ignorant of the scale of these parameters), and the nuisance experimental data is included in the likelihood function.

The "volume effect," common in the literature, is nothing more than marginalisation. This "effect" is identified when marginalisation favours regions of parameter space with a large volume of high posterior density. This is noticeable with flat priors, for which prior probability "piles up" at infinity, or large values. When posteriors from flat priors are marginalised, the marginalised "piled up"

---

* Similarly, log priors "pile-up" prior probability at zero.

* The kernel of a distribution is its shape, irrespective of normalisations.

prior probability results in preferences in the marginalised posterior. This, in my opinion, is not a fault, though it might not reflect our prior beliefs, in which case, we should choose different priors.

The potential difference in posterior pdf resulting from our choice of priors is illustrated in Fig. 2.5.1. Fig. 2.5.1a shows that, with a sharp likelihood, the choice of priors is moot. Fig. 2.5.1b, however, shows that with a broad, weak likelihood, the posterior pdf is dominated by the prior, rather than the likelihood.

A final remark: it is possible, though not desirable, to include "prior" beliefs as a multiplicative component of the likelihood. This would, in general, damage the efficiency of one's algorithm (Sec. 2.6). We would like to include physicality (forthcoming, Sec. 3.1) in our priors. It is, however, difficult to construct a function to sample from only physical parts of the parameter space (in general, a numerical algorithm requires the sampling distribution, rather than the prior distribution itself). Consequently, we include physicality in the likelihood.

2.6 Algorithms

The statistical quantities so far discussed must, of course, be calculated numerically. This is challenging — the model's parameter space is large and its distributions are multimodal and non-trivial. The first thought might be a grid-scan, in which one evaluates the likelihoods and priors at each point on a grid that spans the whole parameter space in the "pragmatic" parameterisation. This, though, has drawbacks: it is computationally inefficient, particularly if the dimension of the parameter space is large, and it might miss narrow modes in the posterior distribution and likelihood (though this is less important for the posterior than the likelihood, because a narrow mode might be insignificant after marginalisation).

In Ref. [204], a Markov chain Monte Carlo [65] Metropolis algorithm [66] is constructed for the CMSSM. In Markov chain algorithms, the algorithm "steps" through points in a model's parameter space. The algorithm's next point is dependent on only its current point — a chain of such points is a Markov chain. The Metropolis algorithm is [67]:

1. Begin at a point in the parameter space, x^n.

2. Consider a potential "step" to a new point in the parameter space, y^n, where $y^n \sim q(y^n|x^n)$, the proposal distribution.

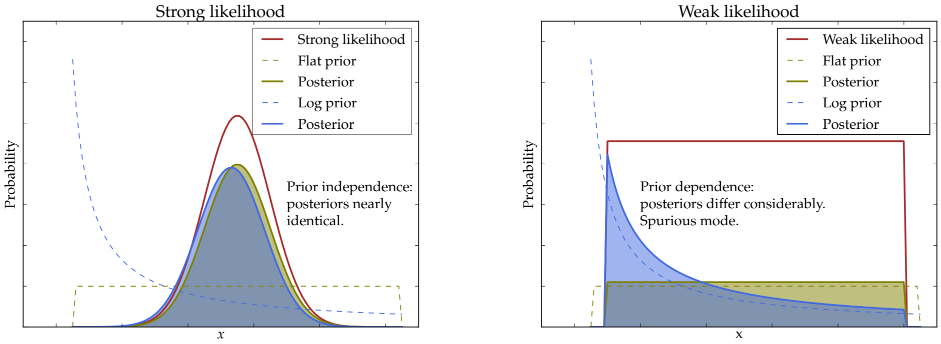

(a) *Posterior distributions resulting from flat and log priors, in the case of a strong likelihood. The posterior distributions are nearly identical to each other and to the likelihood.*

(b) *Posterior distributions resulting from flat and log priors, in the case of a weak likelihood. The posterior distributions are quite different from each other.*

Figure 2.5.1: *The potential difference in posterior pdf resulting from our choice of priors, in two cases: a strong likelihood, Fig. 2.5.1a, and a weak likelihood, Fig. 2.5.1b. The pdfs are normalised so that they integrate to unity. The profile likelihood normalisation is arbitrary.*

3. The next point is

$$x^{n+1} = \begin{cases} y^n \text{ with probability } \rho(x^t, y^t), \\ x^n \text{ with probability } 1 - \rho(x^t, y^t), \end{cases} \tag{2.22}$$

where

$$\rho(x, y) = \min\left\{1, \frac{p\,(y|D)}{p\,(x|D)}\right\} \tag{2.23}$$

is the acceptance probability.

The acceptance probability permits with a specified probability steps to points with a posterior, $p\,(x^n|D)$, smaller than that of the current point. Steps to points with a posterior larger than that of the current point are compulsory. The density of the sequence x^n converges to the posterior.

We, instead, use a Monte Carlo algorithm tailored to Bayesian statistics, called nested sampling [68] and implemented in the `MultiNest` computer package [69, 70]. This algorithm is vastly more efficient than a grid-scan, and slightly more efficient than traditional Markov chain algorithms in finding posterior distributions, including the Metropolis algorithm.

Nested sampling is primarily for evidence calculation, but posterior distributions can be inferred from the calculation. This calculation is, a priori, slow, because one must integrate over the whole parameter space. The insight in nested sampling is that the algorithm finds contours of iso-likelihood that enclose a prior volume which can be approximated from the Monte Carlo nature of the algorithm itself. The evidence is, from Eq. 2.4,

$$\mathcal{Z} = p\,(D|M) = \int \mathcal{L}\,(x_1, \ldots, x_N) \times \pi\,(x_1, \ldots, x_N) \prod_{i=1}^{N} \mathrm{d}x_i. \tag{2.24}$$

We consider, instead, prior volume with a likelihood greater than λ, $X(\lambda)$,

$$\begin{aligned} \mathrm{d}X &= \pi\,(x_1, \ldots, x_N) \prod_{i=1}^{N} \mathrm{d}x_i \\ X\,(\lambda) &= \int_{\mathcal{L}(x_1,\ldots,x_N)>\lambda} \mathrm{d}X. \end{aligned} \tag{2.25}$$

We can now rewrite Eq. 2.24 as a one-dimensional integral,

$$\mathcal{Z} = \int_0^1 \mathcal{L}\left(X\right)\, \mathrm{d}X, \tag{2.26}$$

where $\mathcal{L}\left(X\right)$ is the inverse of Eq. 2.25; it is the likelihood which encloses a prior volume of X, rather than the prior volume enclosed by a likelihood λ. Numerically, if we can evaluate $\mathcal{L}\left(X\right)$ for values of X, we can find the evidence with numerical integration,

$$\mathcal{Z} = \sum \frac{1}{2}\left[\mathcal{L}\left(X_i\right) + \mathcal{L}\left(X_{i+1}\right)\right] \times \left(X_i - X_{i+1}\right) = \sum \frac{1}{2}\mathcal{L}\left(X_i\right) \times \left(X_{i-1} - X_{i+1}\right) \tag{2.27}$$

where we have a used a trapezium rule.

We perform this numerical integration with the nested sampling algorithm in Table 2.6.1. This algorithm is illustrated in Fig. 2.6.1.

We must calculate X_i: the prior volume enclosed by $\mathcal{L}_i$ in the i-th iteration of the algorithm. Let

$$X_i = t_i X_{i-1}. \tag{2.28}$$

Because $X_0 = 1$, recursively,

$$X_i = \prod t_i. \tag{2.29}$$

Our N live points in the i-th iteration are sampled uniformly from the prior volume enclosed by $\mathcal{L} > \mathcal{L}_{i-1}$, X_{i-1}, though themselves enclose a prior volume X_i with $\mathcal{L} > \mathcal{L}_i$. Each live point corresponds to a likelihood that encloses a fraction of the volume enclosed at that iteration, f. These fractions are uniformly distributed on $[0, 1]$. The fraction t_i is the largest of these fractions, which corresponds to the live point with the smallest likelihood, because it encloses the largest fraction. The pdf for t_i is the probability density that a live point has $f = t_i$ multiplied by the probability that $N - 1$ of our live points have f less than t_i;

$$\begin{aligned} p\left(t_i\right) &= p\left(1 \text{ live point has } f = t_i\right) \times p\left(N-1 \text{ live points have } f < t_i\right) \\ &= Np\left(f = t_i\right) \times t_i^{N-1} \\ &= N \times t_i^{N-1}, \end{aligned} \tag{2.30}$$

where $p\left(f = t_i\right)$ is a pdf equal to unity, because it is a uniform distribution on $[0, 1]$.

Nested sampling algorithm

```
1. Set our counter $i = 0$.
2. Draw a specified number, $N$, "live points" from the model's prior distribution,
   subject to no constraints (or equivalently subject to $\mathcal{L} > \mathcal{L}_0 = 0$).
   The live points are evenly distributed within a prior volume $X_0 = 1$.
3. Add one to our counter; $i = i + 1$.
4. Identify the live point with the smallest likelihood, and note its likelihood as $\mathcal{L}_i$.
5. Remove this point from the "live points" — this point is henceforth an inactive replaced point.
6. Draw a new live point from the model's prior distributions, subject to the constraint $\mathcal{L} > \mathcal{L}_i$.
   The live points are evenly distributed within a prior volume $X_i = \exp(-i/N)$.
7. Calculate the evidence found so far.
8. If stopping conditions are satisfied, then exit.
9. Return to step 3.
```

Table 2.6.1: *The nested sampling algorithm, without ellipsoidal sampling, from Ref. [68].*

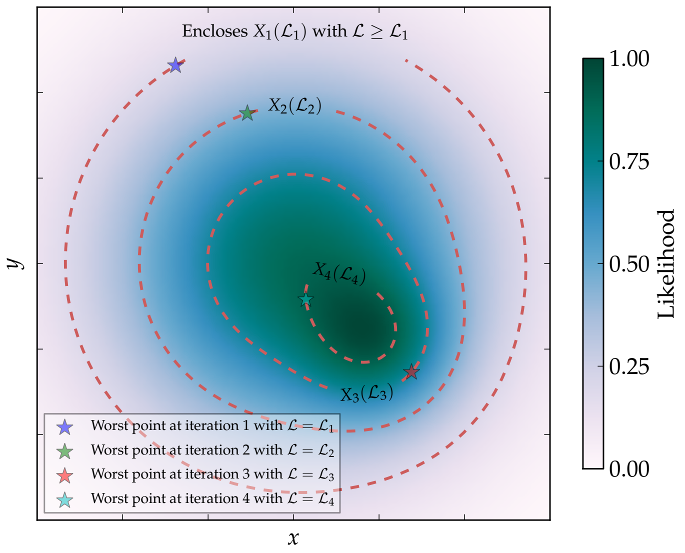

(a) *The model's parameter space, showing the likelihood function, the worst point found at each iteration of the nested sampling algorithm, and the prior volumes enclosed by the worst points.*

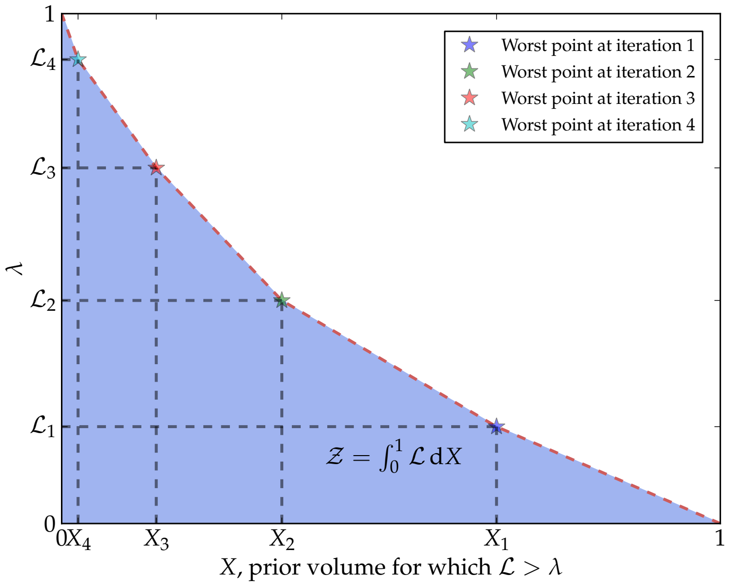

(b) *The worst likelihoods found at each iteration of the nested sampling algorithm against the prior volume they enclose. The area under the graph is the evidence.*

Figure 2.6.1: *An illustration of the nested sampling algorithm with four replacements applied to a two-dimensional model with a Gaussian likelihood and with flat priors, from Ref. [68].*

We approximate $X_i = \exp \mathbf{E}(\ln X_i)$, because $\ln X$, rather than X, dominates the geometrical exploration. We find that $\mathbf{E}(\ln t_i) = -1/N$ and that, consequently,

$$X_i = \exp \mathbf{E}(\ln X_i) = \exp \mathbf{E}(\textstyle\sum \ln t_i) = \exp(-i/N). \tag{2.31}$$

This is the genius of the nested sampling algorithm; we can find the prior volumes from the Monte Carlo nature of the algorithm, rather than from a time-consuming exploration of the whole parameter space.

The algorithm stops once it has determined the evidence to sufficient precision. The largest remaining contribution to the evidence is $\delta\mathcal{Z} = \mathcal{L}_{\text{Max}} X_i$. The algorithm stops once $\ln\left((\delta\mathcal{Z} - \mathcal{Z})/\mathcal{Z}\right)$ is less than a specified tolerance.

The posterior is a by-product of the evidence calculation. We can ascribe a posterior weight to each final live point and each inactive point,

$$p_i = \mathcal{L}_i w_i / \mathcal{Z}, \tag{2.32}$$

where i runs from 1 to the number of live points, N, plus the number of replacements, M, and the weights, w_i are

$$w_i = \begin{cases} \frac{1}{2}\left(X_{i-1} - X_{i+1}\right), & \text{for } M \text{ replaced points} \\ X_M/N, & \text{for } N \text{ final live points.} \end{cases} \tag{2.33}$$

The replaced points have a prior volume equal to the width of their iso-likelihood contour and the final live points share the remaining prior volume. We recall that likelihood is a function of our model parameters $x_1, \ldots, x_N$, and so too, then, are the posterior weights in Eq. 2.32. We construct the posterior pdf numerically by histogramming our points, with each point weighted by its posterior. We perform integrations for marginalisation by histogramming only with respect to parameters of interest. We can readily calculate all other aforementioned statistical quantities numerically, from the posterior pdf and likelihood.

The algorithm has two important parameters: its tolerance and its number of live points. The number of live points ought to be large enough to cast at least one live point into a "basin of attraction" for each mode in the distribution — it can be thought of as analogous to a scan "resolution." The tolerance ought to be small enough so that each mode is explored in sufficient detail — it can be thought of as analogous to a scan "depth."

The algorithm's performance for recovering likelihoods and finding χ^2_{Min} is poor. To accurately find these frequentist quantities, one must tweak the algorithm's parameters and stopping conditions, to explore the model's parameter space in greater detail.

Chapter 3

Likelihoods

We now introduce the important observables to which we fit our model's parameters. We detail the supersymmetric contributions to the observables, the experiments which measure the observables and their public results, and how we construct our likelihood functions from the results. The likelihoods are a key ingredient in our statistical analysis. We assume that our likelihoods are independent. This is reasonable, because the experiments are disjoint and have negligible correlated systematic errors. From Eq. 2.20, we can factorise the K likelihoods,

$$\mathcal{L}\left(D_1, \ldots, D_K | x_1, \ldots, x_N\right) = \prod_{i=1}^{K} \mathcal{L}\left(D_i | x_1, \ldots, x_N\right). \tag{3.1}$$

We interpret experimental errors δx listed as $x \pm \delta x$ to be 68% confidence intervals, with Gaussian likelihoods in which δx corresponds to 1σ. If two errors are listed, $x \pm \delta a \pm \delta b$, the errors are statistical and systematic respectively, and we combine them in quadrature. We frequently include PDG [71] averages. Their averaging procedure is such that the combined result is

$$\bar{x} \pm \delta\bar{x} = \frac{\sum w_i x_i}{\sum w_i} \pm \frac{1}{\sqrt{\sum w_i}}, \tag{3.2}$$

$$w_i = \frac{1}{(\delta x_i)^2}. \tag{3.3}$$

This error is adjusted, however, if the resulting χ^2 is large, because that indicates that an error is underestimated. Occasionally, experiments measure a set of correlated parameters, for example, branching ratios. In these cases, PDG perform a constrained fit to the experimental data to combine data.

Typically, our likelihood functions are Gaussian;

$$\mathcal{L} = \exp\left[-\frac{(x-\mu)^2}{2\sigma^2}\right], \tag{3.4}$$

where μ is the mean experimental measurement, σ is its 1σ error and x is our model's prediction for the measured quantity. Because we are interested in the kernel, we neglect the normalisation, such that $-2\ln\mathcal{L} = \chi^2$.

Our model's predictions, however, are imperfect. From an experiment, we know the likelihood of obtaining data given our model's "true" prediction, that could be obtained in only a perfect calculation. We find the likelihood of obtaining data given our model's imperfect calculation with conditional probability,[*]

$$p\left(D|x_{\text{Calc}}\right) = \int p\left(D|x_{\text{True}}\right) \times p\left(x_{\text{True}}|x_{\text{Calc}}\right)\, \mathrm{d}x_{\text{True}}, \tag{3.5}$$

where x_{Calc} is our model's imperfect calculation and x_{True} is our model's unknown "true" prediction. If we believe that our uncertainty is Gaussian with theoretical error τ,

$$p\left(x_{\text{True}}|x_{\text{Calc}}\right) = \exp\left[-\frac{\left(x_{\text{Calc}} - x_{\text{True}}\right)^2}{2\tau^2}\right], \tag{3.6}$$

the familiar result from Eq. 3.5 is that the theoretical and experimental errors are added in quadrature,[†] i.e., $\sigma^2 \to \sigma^2 + \tau^2$ in Eq. 3.4.

3.1 Physicality

Our models' parameter spaces contain regions that are "unphysical;" regions in catastrophic conflict with theoretical principles or experiments, or in which we cannot perform calculations. These potential physicality problems are listed in Table 3.1.1. The common physicality problems are incorrect electroweak symmetry breaking or that a scalar particle is tachyonic. The occurrence of these problems in

---

[*] Note that $p\left(D|x_{\text{True}}, x_{\text{Calc}}\right) = p\left(D|x_{\text{True}}\right)$.

[†] We neglect a complication; if our theoretical error is a function of the calculated value, the normalisation factor is also a function of the calculated value. This affect, however, is moot if $\sigma/\mu \ll 1$.

the CMSSM parameter space is illustrated in Fig. 3.1.1. One might expect that we preclude unphysical regions of our parameter space via our prior distributions. It is, however, difficult to construct such priors, because they would include non-trivial correlations amongst a model's parameters. Unphysical regions of parameter space are forbidden via the likelihood; they are assigned zero likelihood. For simplicity, we also exclude regions in which the neutralino is not the LSP, which would violate strict limits on long-lived charged particles, in this way.

3.2 Nuisance parameters

3.2.1 Top mass

The mass of the top quark was the pen-ultimate parameter to be measured in the Standard Model. Quark mass is a conceit; unlike leptons, quarks are confined in hadrons in quantum chromodynamics (QCD). We must carefully define our notion of top-quark mass, with reference to quantum field theory and particular renormalisation schemes. We use the top quark pole mass, defined as the pole in the top quark propagator in a perturbative regime.

Top-quark mass is measured from $t\bar{t}$ production and its subsequent decay $t\bar{t} \to W^+b^-W^-b^+$. Experiments at the Tevatron [73] and the LHC [74] select events with b-tags and leptonic, hadronic or semi-leptonic WW-decays. The top mass is measured by fitting its mass to reconstructed kinematic distributions, with a Monte-Carlo event generator. The Particle Data Group (PDG) averaged top-quark mass from such measurements at the LHC and the Tevatron is [71]

$$M_t = 173.5 \pm 0.6 \pm 0.8\,\text{GeV}, \tag{3.7}$$

where the errors are the one-sigma statistical error followed by the one-sigma systematic error. Alarmingly, despite the high precision in this measurement, it is not clear how to interpret the top-quark mass in the Monte-Carlo event generator. PDG interpreted it as a pole mass, with the caveat that this interpretation might have an associated systematic error of $\sim 1\,\text{GeV}$ [75]. Well-defined measurements, in which the top-quark mass is extracted in a defined renormalisation scheme, are now being performed from measurements of the top-quark pair production cross section, but are uncompetitive in precision.

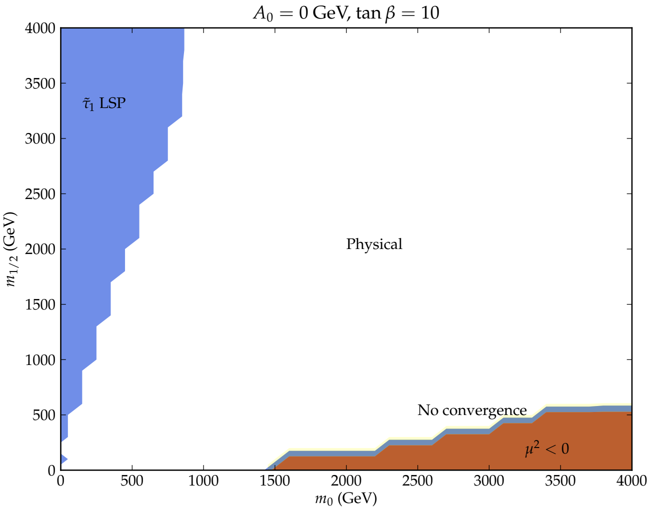

Figure 3.1.1: *Unphysical regions of the CMSSM's* $(m_0, m_{1/2})$ *plane for* $\tan\beta = 10$ *and* $A_0 = 0$ *GeV.*

Physicality problems
1. Desired accuracy cannot be reached
2. Landau pole in renormalisation group evolution of gauge couplings
3. Landau pole in Yukawa coupling; infra-red quasi-fixed point breached
4. No radiative electroweak symmetry breaking; m_3^2 has the wrong sign
5. No radiative electroweak symmetry breaking; μ^2 has the wrong sign
6. Tachyonic sfermion
7. Cannot calculate ρ or determine gauge couplings
8. Higgs minimum is in fact a saddle point; potential unbounded from below
9. M_{GUT} is too high
10. Higgs mass calculation non-perturbative
11. Lightest neutralino is not the LSP

Table 3.1.1: *The potential physicality problems from Ref. [72]. If a point has one or more of these problems, it is unphysical.*

We use the PDG prescription and interpret generator mass as pole mass, but ignore their caveat, and add their statistical and systematic errors in quadrature to obtain

$$M_t = 173.5 \pm 1.0\,\text{GeV}, \tag{3.8}$$

where the error is a combined one-sigma error. Our likelihood (or prior) for the top mass is a Gaussian with this mean and standard deviation.

3.2.2 Bottom mass

We use the bottom mass in the $\overline{MS}$ scheme. The bottom mass in the $\overline{MS}$ scheme is related to the physical mass by

$$M_b = (1 + 0.09 + 0.05 + 0.03) \times m_b(m_b)^{\overline{MS}}, \tag{3.9}$$

where the coefficients are orders in α_s. This sequence is converging slowly; the corrections have similar magnitudes. A potential systematic error is introduced by extracting $m_b(m_b)^{\overline{MS}}$ from an intermediate measurement of M_b or the bottom mass in a different renormalisation scheme. The choice of scale, $\mu = m_b^{\overline{MS}}$, is a convention, which might be suboptimal, in that it might not minimise higher-order coefficients in Eq. 3.9.

The precision in measurements of the bottom mass owes to experimental results from so-called B-meson (an anti-bottom quark and an up quark) factories, and from advances in relating bottom quark measurements to masses in particular schemes. The experiments (CLEO [76], BaBar [77], Belle [78] and DELPHI [79]) infer M_b from the measured energy spectra of the products of B-meson decays, predominantly $B \to X_c \ell \nu$, where X_c is a hadronic system with a charm quark. The PDG averaged bottom-quark mass, with results converted to the $\overline{MS}$ scheme and combined, is

$$m_b(m_b)^{\overline{MS}} = 4.18 \pm 0.03\,\text{GeV}. \tag{3.10}$$

This error includes errors from such conversions. Our likelihood (or prior) for the bottom mass is a Gaussian with this mean and standard deviation.

3.2.3 Strong coupling

The quantum chromodynamic $\mathrm{SU_c}(3)$ coupling strength $\alpha_s = g_s^2/4\pi$ (where g_s is the strong coupling) is a running parameter, with a scale dependence controlled by its β-function. We use α_s in the $\overline{MS}$ scheme at the conventional scale M_Z. The running of α_s to M_Z can introduce a systematic error, because the β-function is known to a finite order in perturbation theory.

The strong coupling is measured in several processes, including deep-inelastic scattering, τ-decay and high-energy hadron collisions. PDG evolved these measurements of α_s to a common scale (M_Z) with its β-function and averaged the resulting values,

$$\alpha_s(M_Z)^{\overline{MS}} = 0.1184 \pm 0.0007. \tag{3.11}$$

This does not include an error from the variation of the bottom-quark mass. Our likelihood (or prior) for $\alpha_s(M_Z)^{\overline{MS}}$ is a Gaussian with this mean and standard deviation.

3.2.4 Fine-structure constant

The remaining nuisance parameter is the fine-structure constant α_{em}; the coupling strength of the unbroken electromagnetic $\mathrm{U_{em}}(1)$ interaction, which is a running parameter. We use the reciprocal of the fine-structure constant in the $\overline{MS}$ scheme at the conventional scale M_Z. The fine-structure constant is measured at low-energy, where it approaches a fixed-point, from the anomalous magnetic moment of the electron and the quantum Hall effect, and ran to the desired scale. The PDG combination of such results is

$$1/\alpha_{\mathrm{em}}(M_Z)^{\overline{MS}} = 127.916 \pm 0.015, \tag{3.12}$$

which is found with $\alpha_s(M_Z)^{\overline{MS}} = 0.120$. Our likelihood (or prior) for $1/\alpha_{\mathrm{em}}(M_Z)^{\overline{MS}}$ is a Gaussian with this mean and standard deviation.

3.2.5 Mass of the Z-boson

The mass of the Z-boson was precisely measured by LEP [80–83] in electron-positron collisions with centre-of-mass energies $\sqrt{s} \sim M_Z$. "On-peak" collisions measured production cross sections, whereas "off-peak" collisions measured the shape of the Z-resonance, parameterised by the Z-boson's mass and decay-width.

The Z-boson mass was extracted from this data with no model dependent assumptions, for example, the mass and decay width were assumed to be independent parameters. PDG averaged such measurements, obtaining

$$M_Z = 91.1876 \pm 0.0021\,\text{GeV}. \tag{3.13}$$

This is a relative precision of approximately one part in fifty-thousand. We approximate this precision to absolute precision — M_Z is an input parameter fixed to its experimental measurement.

3.3 Dark matter

The experimental evidence for dark matter is now considered to be overwhelming. The MSSM includes a weakly interacting massive particle (WIMP); an ideal candidate for dark matter. The χ is this WIMP [84,85]; its decay is forbidden by R-parity and by kinematics. We consider three dark matter experiments. The Wilkinson Microwave Anisotropy Probe (WMAP) [22, 86] and PLANCK [87] are the most important; the relic density of dark matter is inferred from the cosmic microwave background (Sec. 3.3.3). The XENON100 direct detection experiment (Sec. 3.3.4) is important in parts of the MSSM parameter space; its null results forbid large scattering cross sections between neutralinos and protons (Sec. 3.3.4).

3.3.1 Relic density calculation

The neutralino could be a relic of the early Universe with a substantial abundance that explains the dark matter phenomena in Sec. 1.1.2. The early Universe cooled and expanded from M_P through symmetry breaking transitions, including transitions breaking GUT, SUSY and electroweak symmetries [88]. Because interactions were faster than the Universe's expansion, the Universe was approximately in thermal equilibrium [26]. If a particle's interactions dropped with temperature, however, such that they were slower than the Universe's expansion, the particle would "freeze-out" of thermal equilibrium at a temperature $T_\text{F.O.}$. This was the fate of the neutralino [89].

We find a Boltzmann rate equation for the neutralino density [90];

$$\frac{\mathrm{d}n_\chi}{\mathrm{d}t} = -3Hn + \left\langle \sigma\left(\chi\chi \to X_i X_j\right) v_{\text{Møller}} \right\rangle \left(n_\chi^2 - n_{\chi,\text{Eq.}}^2\right), \tag{3.14}$$

where n is a number density, $\langle\cdot\rangle$ is a thermal average, σ is the neutralino annihilation cross section, H is the Hubble constant and $v_{\text{Møller}}$ is the Møller velocity,

$$v_{\text{Møller}} \equiv c\frac{\sqrt{(p_\mu q^\mu)^2 - m_p^2 m_q^2 c^4}}{p_\mu q^\mu} = \frac{\sqrt{(\vec{v}-\vec{u})^2 - (\vec{v}\times\vec{u})^2/c^2}}{1 - \vec{v}\cdot\vec{u}/c^2}, \tag{3.15}$$

defined such that the interaction rate is Lorentz invariant. In the non-relativistic limit, $v_{\text{Møller}}$ reduces to $|\vec{u}-\vec{v}|$. Because in thermal equilibrium the density of states is approximately Boltzmann, the thermal average is

$$\langle \sigma v_{\text{Møller}} \rangle = \frac{\int \sigma v_{\text{Møller}} e^{-E_p/k_B T} e^{-E_q/k_B T} \mathrm{d}^3\boldsymbol{p}\mathrm{d}^3\boldsymbol{q}}{\int e^{-E_p/k_B T} e^{-E_q/k_B T} \mathrm{d}^3\boldsymbol{p}\mathrm{d}^3\boldsymbol{q}}. \tag{3.16}$$

For insight, the result is split into an effective cross section multiplied by a statistical weight [91], each a function of energy. Note that although an annihilation would remove two neutralinos, the cross section is divided by two because the neutralino is a Majorana particle [89].

The neutralino abundance is expressed as a fraction of the Universe's critical density [26],

$$\Omega h^2 \equiv \frac{\rho_\chi}{\rho_{\text{CRITICAL}}} h^2, \tag{3.17}$$

where ρ_χ is the density of neutralinos, ρ_{CRITICAL} is the critical density of the Universe, the precise density required for the spatial geometry of the Universe to be flat in the Friedmann equation, and $h \sim 0.7$ is the Hubble constant divided by $100\,\text{kms}^{-1}\text{Mpc}^{-1}$.*

With approximate expressions for freeze-out, we find that [89]

$$\Omega_\chi h^2 \simeq \frac{3\times 10^{-26}\text{cm}^3\text{s}^{-1}}{\left\langle \sigma\left(\chi\chi \to X_i X_j\right) v_{\text{Møller}} \right\rangle}, \tag{3.18}$$

which is dependent on the neutralino's mass in only its denominator.

---

* Multiplying by the Hubble constant squared removes the uncertainly otherwise present in the critical density.

Three phenomena that affect $\langle \sigma v_{\text{Møller}} \rangle$ in Eq. 3.16 and thus the relic density are [92]:

- Resonances from s-channel diagrams in which the cross section spikes at, e.g., $\sqrt{s} = m_A$, the pseudoscalar Higgs mass. In equilibrium, from Boltzmann statistics, $\langle s \rangle \simeq 4m_\chi^2 + 6m_\chi T$. If the resonance's spike is near $\langle s \rangle$, it is critical to relic density. Because typically $T_{\text{F.O.}} \ll m_\chi$, the resonance is relevant if $m_\chi \simeq 0.5 m_A$.
- Coannihilation with a second particle species with mass m. The thermal average in Eq. 3.16 results in an approximate Boltzmann suppression factor for coannihilation [93],

  $$\langle \sigma v_{\text{Møller}} \rangle \propto e^{-(m-m_\chi)/k_B T_{\text{F.O}}}. \tag{3.19}$$

  Coannihilation is important if $m \approx m_\chi$, i.e., if the their densities are similar in thermal equilibrium from Boltzmann statistics. In `MicrOMEGAs`, coannihilation is included if $m/m_\chi < 1.55$ [93]. Coannihilation reduces the relic density if the second species annihilates faster than the neutralino.
- Thresholds in the cross section — final states forbidden at e.g., $\sqrt{s} < 2m_f$. Thresholds imply that $\langle \sigma v_{\text{Møller}} \rangle_{T_{\text{F.O.}}} > \langle \sigma v \rangle_{T \to 0}$.

We review dark matter annihilation for Majorana neutralinos.

3.3.2 Dark matter annihilation

The neutralino is a Majorana fermion. Majorana fermion annihilation to fermions is "helicity suppressed." The Majorana fermions' spins could be asymmetric, $S = 0$, or symmetric, $S = 1$. At threshold, $\sqrt{s} = 2m_\chi$, however, their orbital angular momentum is $L = 0$. Because the Majorana fermions' spatial wavefunction is symmetric with $L = 0$ (orbital parity is $(-1)^L$), their spin wavefunction must be asymmetric, $S = 0$. The outgoing fermions, however, result from a chiral interaction. If the fermions are massless, their helicities are parallel, $S = 1$. Because orbital angular momentum is perpendicular to helicity, orbital angular momentum in the outgoing fermions cannot balance momentum. This $L = 0$ partial wave annihilation is possible, if the outgoing fermions are massive, because fermion mass permits a fermion to "helicity flip." It is, however, "helicity suppressed" by a factor $\propto m_f^2$.

The orbital angular momentum $L > 0$ partial waves are possible, in which case the Majorana fermions' spins are symmetric, $S = 1$, if L is odd. The $L > 0$ partial waves, however, are "p-wave suppressed" by a factor v^{2L}, with v, the relative velocity between the Majorana fermions, typically $\sim 10^{-3}c$ [94]. In general, then, neutralino annihilation is "helicity suppressed" in the $L = 0$ partial wave and p-wave suppressed in the $L > 0$ partial waves. For a substantial annihilation rate, we desire an $L = 0$ partial wave without helicity suppression.

With scalar Yukawa-type couplings to outgoing fermions, we avoid helicity suppression, because scalars couple opposite chiralities. If the Yukawa is responsible for fermion masses, however, its coupling is suppressed by $\propto y_f^2$, similar to genuine helicity suppression. In the MSSM, the Yukawa couplings can be enhanced by $\tan\beta$. The pseudoscalar and scalar Majorana couplings contain subtleties. The parity of the Majorana fermions' is $P = (-1)^{L+1}$. The $P = -1$ pseudoscalar coupling, therefore, is the $L = 0$ partial wave, while the $P = +1$ scalar coupling is the $L = 1$ partial wave. Only the pseudoscalar coupling could, therefore, avoid helicity and p-wave suppression, because it couples opposite chiralities in the $L = 0$ partial wave [95].

In the CMSSM, the dark matter relic abundance is reduced by distinct annihilation mechanisms, including:

- "Stau-coannihilation" (Fig. 3.3.1a), in which $m_\chi \approx m_{\tilde{\tau}_1}$. It occurs for $m_{1/2} \gtrsim m_0$. The neutralino composition is bino-like. That $m_\chi \approx m_{\tilde{\tau}_1}$ insures that in thermal equilibrium the density of neutralinos and staus is similar. Staus and neutralinos annihilate via t-channel and s-channel diagrams, predominantly via an s-channel stau-tau-bino $(\phi^* T_a \psi)\,\lambda^a$ vertex in Eq. 1.21.

- "Focus-point" [96, 97] (Fig. 3.3.1b), in which the neutralino's higgsino-component is relevant because $\mu \lesssim M_1, M_2$ and neutralinos annihilate to WW via a t-channel chargino. It occurs for $m_0 \gg m_{1/2}$, so that μ is small. Annihilation is via a higgsino-charged higgsino-gauge boson gauge interaction in the covariant derivative in Eq. 1.14. Because higgsino-like neutralinos annihilate too quickly, focus-point neutralino composition is predominantly bino with a higgsino admixture.

- "A-funnel" resonance (Fig. 3.3.1c), in which neutralinos annihilate via an

s-channel pseudoscalar Higgs resonance because $|2m_\chi - m_A| \lesssim \Gamma_A$, the pseudoscalar's width. It occurs for $m_{1/2} \lesssim m_0$ and $\tan\beta \gtrsim 30$, so that $2m_\chi \sim m_A$ [98] and so that Γ_A is large [99]. Annihilation is via a Higgs-higgsino-gaugino $(\phi^* T_a \psi)\, \lambda^a$ vertex in Eq. 1.21 — the neutralino composition must be an admixture of gaugino and higgsino. Because its second vertex is a Yukawa pseudoscalar coupling between fermions with opposite chiralities, the diagram Fig. 3.3.1c avoids helicity suppression and p-wave suppression. In fact, neutralinos with a significant higgsino-like component annihilate too quickly via the A-funnel. In the A-funnel, therefore, neutralinos are bino-like and the s-channel is fractionally off-resonance.

- Light/heavy Higgs resonance, in which neutralinos annihilate via an s-channel scalar resonance, with the light or heavy scalar Higgs, with $2m_\chi \approx m_h$ or $2m_\chi \approx m_H$. Annihilation is via a Higgs-higgsino-gaugino $(\phi^* T_a \psi)\, \lambda^a$ vertex in Eq. 1.21. In contrast with the A-funnel, this mechanism is p-wave suppressed by the Majorana-scalar coupling. The heavy Higgs resonance, with $2m_\chi \approx m_H$, struggles to sufficiently reduce neutralino relic density. If present, the heavy Higgs resonance occurs near the A-funnel, because $m_A \approx m_H$. The light Higgs resonance region occurs at $m_{1/2} \sim 100\,\text{GeV}$, so that $m_\chi \sim 50\,\text{GeV}$, with $m_0 \gg m_{1/2}$, so that m_h is heavier than LEP's lower limit. For the light Higgs resonance, the neutralino must be bino-like (though with non-zero higgsino composition), because a light higgsino-like neutralino would imply a light higgsino-like chargino, which violates LEP bounds.

- Z-resonance, in which neutralinos annihilate via an s-channel Z-boson resonance, with $2m_\chi \approx M_Z$. Annihilation is via a higgsino-higgsino-Z-boson or a wino-wino-Z-boson gauge interaction in the covariant derivative in Eq. 1.14. Because the Z-boson is CP-even, this mechanism is p-wave suppressed, and unless the final state is WW, it is also helicity suppressed. The neutralino cannot, however, be higgsino-like, because it would violate LEP chargino bounds. Because the wino couples strongly with the Z-boson, the neutralino's composition can be predominantly bino with a wino component.

- "Bulk" (Fig. 3.3.1d), in which neutralinos annihilate to fermions via a t-channel sfermion. Annihilation is via two sfermion-fermion-gaugino

> $(\phi^* T_a \psi)\,\lambda^a$ vertices in Eq. 1.21. Diagram Fig. 3.3.1d is helicity suppressed. In the $L = 0$ partial wave, the annihilating neutralinos are $S = 0$. Because a gauge interaction couples fermions with identical chiralities, in the massless limit, the outgoing fermions have $S = 1$. The diagram is permitted by a helicity flip, because fermions are massive, or at high-energies (p-wave suppression), because at high-energies the incoming Majorana neutralinos could have $S = 1$.

Because stau-coannihilation and higgsino-like annihilation to WW invoke t-channel sparticles in $\langle\sigma v\rangle_{T_{\text{F.O.}}}$, $\langle\sigma v\rangle_{T_{\text{F.O.}}}$ decreases if sparticle masses increase and the relic density increases if sparticle masses increase. Ultimately, if t-channel annihilation is significant, $\Omega_\chi h^2$ measurements limit sparticle masses, and, because sparticles must be heavier than the neutralino, the neutralino mass [100].

3.3.3 Relic density measurements

The WMAP spacecraft is in a triangular Lagrange point in the Sun and Earth's gravitational fields [101]. WMAP measured the power spectrum of anisotropies in the cosmic microwave background and reported posterior mean values, best-fit values and 68% ETP credible regions for parameters of the ΛCDM model, the so-called Standard Model of cosmology, with flat priors, including the relic density of cold dark matter, $\Omega_{\text{CDM}} h^2$. WMAP was succeeded by a similar experiment, PLANCK [87]. The latest PLANCK result is that

$$\zeta \equiv \Omega_{\text{CDM}} h^2 = 0.1199 \pm 0.0027. \tag{3.20}$$

Our likelihood function for ζ is Gaussian; however, we include a theoretical error in the MSSM ζ calculation. We distinguish between the true value of ζ for the model, with a perfect calculation, and the calculated ζ for the model, with an imperfect calculation, containing approximations. From Ref. [102,103], we know that this theoretical error can be as large as a 10% fraction of ζ in the focus-point region,

$$p\left(\zeta_{\text{True}} | \zeta_{\text{Calc}}\right) = \exp\left[-\frac{\left(\zeta_{\text{True}} - \zeta_{\text{Calc}}\right)^2}{2 \times 0.01^2 \zeta_{\text{Calc}}^2}\right]. \tag{3.21}$$

We combine these expressions via conditional probability in Eq. 3.5 and arrive at our likelihood for ζ; a Gaussian with theoretical and experimental errors added in quadrature. This likelihood, and its broadening by the theoretical error in the calculation, is shown in Fig. 3.3.2.

3.3.4 Direct detection

XENON100 is a terrestrial "direct detection" experiment — XENON100 is sensitive to elastic scattering between nuclei in its detector and dark matter. The detector, by virtue of the Sun's motion in the galactic rest frame, experiences a "WIMP wind," with a relative velocity that is modulated annually by the Earth's rotation around the Sun, and from a direction that is modulated diurnally by the Earth's rotation around its axis [104]. The WIMP wind itself depends on the distribution and velocity distribution of dark matter in our galaxy. We consider only the strongest negative result from direct detection experiments, which is from XENON100 [105], and ignore conflicting results from DAMA/LIBRA [106–108], which observes an annual modulation with a significance of 8.9σ.

XENON100 is a noble liquid detector made of liquid xenon which scintillates and ionises in scattering events. XENON100 distinguishes signal events from background events from the time that elapses between scintillation and ionisation. XENON100 cannot measure the direction from which an event originated, but it can fully locate the scattering event within the detector. This enables XENON100 to reject "double strike" events — events that occur in close temporal and spatial proximity within the detector, which are likely to be slow neutrons scattering several times within the detector [109].

In one-hundred days of operation, XENON100 detected 3 events; statistically insignificantly more than their expectation of 1.8 ± 0.6 events [105]. This null result constrained WIMP mass and WIMP scattering cross sections with nucleons in the XENON100 detector. The publicly available results, however, were limited to a 90% CL exclusion contour in the WIMP mass and WIMP scattering cross section plane, reproduced in Fig. 3.3.3. We crudely constructed a likelihood function from this exclusion contour, by approximating the 90% exclusion contour by a 100% exclusion contour, i.e., our likelihood is constant below the exclusion contour and zero above it. There is, however, a significant theoretical error in the calculated scattering cross section, estimated to be a $\sim$ 100% fraction of the calculated cross section [110] (see Sec. 4.6). We incorporate this uncertainty via Eq. 3.5, resulting in

(a) *Stau-coannihilation.*

(b) *Focus-point, higgsino-like neutralino.*

(c) *A-funnel, pseudoscalar Higgs resonance.*

(d) *"Bulk" region, sfermion exchange.*

Figure 3.3.1: *Feynman diagrams for dominant mechanisms by which neutralinos annihilate in the MSSM in the early Universe, labelled by interaction eigenstates.*

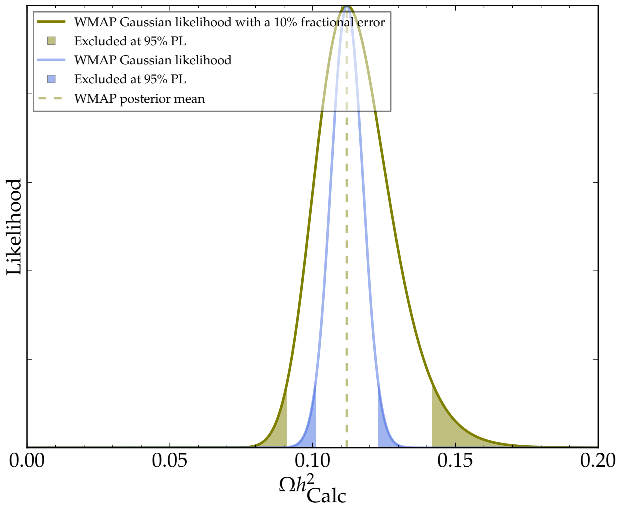

Figure 3.3.2: *Likelihood from WMAP's relic density measurement, illustrating the effect of a fractional theoretical error.*

our likelihood function on the WIMP mass and calculated WIMP scattering cross section plane (Fig. 3.3.3).

3.3.5 Indirect detection

The possible long-lived dark matter annihilation products are photons, neutrinos, electrons and positrons, and protons and anti-protons. Because we expect the rate of annihilation to be proportional to ρ_χ^2, searches target regions or objects in which we expect dark matter to be abundant, including [88]:

- Our galactic halo and centre, because from simulations we expect that $\rho_\chi \propto r^{-\alpha}$;
- Our Sun, because it might capture dark matter in elastic collisions. Other than photons, only neutrinos could escape our Sun's gravitational field; and
- Low-luminosity galaxies beyond our galaxy, including dwarf spheroidal galaxies.

Because electrons and protons are deflected by electromagnetic fields, searches target particular objects with photons or neutrinos. To minimise backgrounds, searches target positrons and anti-protons, rather than electrons and protons. The relevant prediction is $\langle \sigma v \rangle_{T\to 0}$, i.e., the thermally averaged cross section in the zero temperature limit.

3.4 Higgs mass

The historic discovery of a Standard Model-like Higgs particle and its contemporaneous mass measurement at the LHC was preceded by strict lower limits on the Standard Model Higgs boson's mass from LEP [111], upper limits on its mass from the Tevatron [112] and by indirect constraints on its mass from electroweak precision data [113,114]. We consider only direct measurements; because we already include electroweak precision data in our analysis, to include indirect Higgs mass measurements from electroweak precision data would be to "double-count" this data in our analysis. The Higgs mass measurements are summarised in Ref. [115].

The exclusion limits are applicable to only a Standard Model Higgs boson, because Higgs bosons with suppressed couplings could have evaded direct searches,

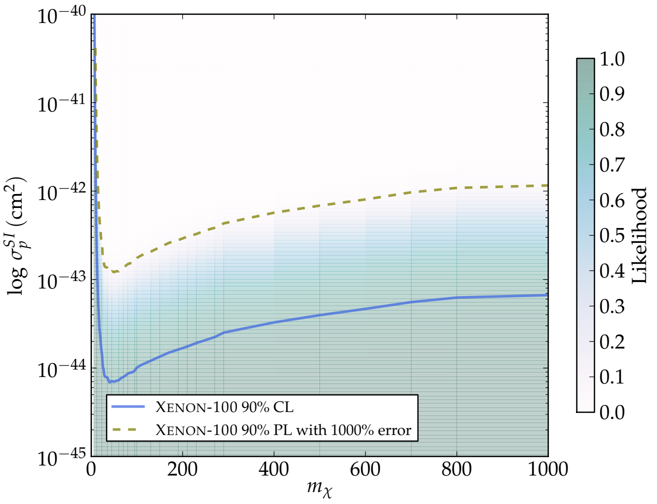

Figure 3.3.3: *Likelihood from XENON100 direct detection experiment, showing* 90% *exclusion contours from XENON100 and from our likelihood, which incorporates a large fractional error.*

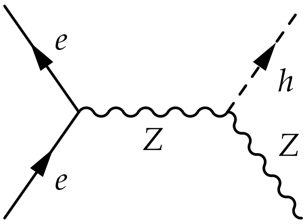

Figure 3.4.1: *Feynman diagram for Higgs-strahlung — the dominant Higgs production mechanism at LEP in association with a Z-boson.*

and Higgs bosons with enhanced couplings would struggle to evade searches. We assume that the lightest MSSM Higgs is Standard Model-like, in that the constraints for Standard Model Higgs bosons apply to the lightest MSSM Higgs boson, without reinterpretation. We consider constraints on only the Higgs boson's mass, and neglect measurements of its couplings. We, furthermore, neglect the upper limit on the Higgs bosons mass from the Tevatron, since it is higher than that which can be achieved in our supersymmetric models.

3.4.1 LEP

The LEP experiments searched for Higgs bosons from Higgs-strahlung production in association with a Z-boson in electron-positron collisions at centre-of-mass energies of less than and equal to 209 GeV [111]. This production mechanism is illustrated in Fig. 3.4.1. LEP was sensitive to Standard Model Higgs bosons with masses of less than $\sim 115\,\text{GeV}$, which would decay dominantly to $b\bar{b}$ and $\tau\tau$ (see Fig. 3.4.2). LEP searched for these decays in combination with a Z-decay to leptons, quarks or neutrinos, but it found no significant evidence of Standard Model Higgs boson production. The combined exclusion from the LEP experiments (ALEPH [116], DELPHI [117], L3 [118] and OPAL [119]) was that $m_h < 114.4\,\text{GeV}$ is excluded at 95% CL_s [111].

There were, however, statistically insignificant hints in the LEP results. LEP saw an excess of events at 115 GeV which was consistent with a Standard Model Higgs, but had an appreciable chance (9%) of being a fluctuation in the background, and an excess at 98 GeV which had a small chance (2%) of being a fluctuation in the background, but was much weaker than that expected from a Standard Model Higgs boson.

Prior to the LHC's historic discovery, we included only this LEP upper limit in our likelihood. It is, however, difficult to extract a likelihood from the public

LEP results, because the pertinent quantity in their analysis was a likelihood ratio, rather than a likelihood. Nevertheless, from the sharp behaviour of their CL_s test statistic, we can infer that their likelihood is sharp, and so approximate it to a step-function,

$$p\left(\mathrm{LEP}|m_h^{\mathrm{True}}\right)=\begin{cases}1 & m_h^{\mathrm{True}}\geq 114.4\,\mathrm{GeV}\\ 0 & \text{otherwise.}\end{cases} \tag{3.22}$$

This is a likelihood function — we cannot easily approximate or parameterise LEP's sampling distribution, i.e., we cannot interpret Eq. 3.22 as a function of the data. We distinguish between the "true" Higgs mass from a perfect calculation and the "calculated" Higgs mass from the realised, approximate calculation. There is an appreciable uncertainty in interpreting the calculated Higgs mass, calculated to a finite order in perturbation theory, with a hypothetical "true" Higgs mass calculation, estimated to be $\tau = 2\,\mathrm{GeV}$ [121]. Our belief is that the true Higgs mass is most likely to be the calculated Higgs mass, but that there is an appreciable and equal probability that it is less than or greater than the calculated Higgs mass, which diminishes asymptotically. A Gaussian distribution conveniently captures these properties;

$$p\left(m_h^{\mathrm{True}}|m_h^{\mathrm{Calc}}\right)=\exp\left[-\frac{\left(m_h^{\mathrm{True}}-m_h^{\mathrm{Calc}}\right)^2}{2\tau^2}\right]. \tag{3.23}$$

We combine Eq. 3.22 and Eq. 3.23 via Eq. 3.5. The result is a convolution of a step function with a Gaussian; a non-analytic function, which can be expressed in error functions,

$$\mathcal{L}_{\mathrm{LEP}}=p\left(\mathrm{LEP}|m_h^{\mathrm{Calc}}\right)=1/2\left[1-\mathrm{erf}\left(\frac{114.4\,\mathrm{GeV}-m_h^{\mathrm{Calc}}}{\sqrt{2}\tau}\right)\right]. \tag{3.24}$$

This function is plotted in Fig. 3.4.3.

3.4.2 LHC

Last year (2012), the ATLAS [122] and CMS [123] experiments at the LHC discovered a Higgs boson produced in pp collisions at centre-of-mass energies of $\sqrt{s}=7\,\mathrm{TeV}$ and $\sqrt{s}=8\,\mathrm{TeV}$. The search was conducted at a breathless pace; prior to their discovery, CMS [124–128] and ATLAS [129–132] regularly reported con-

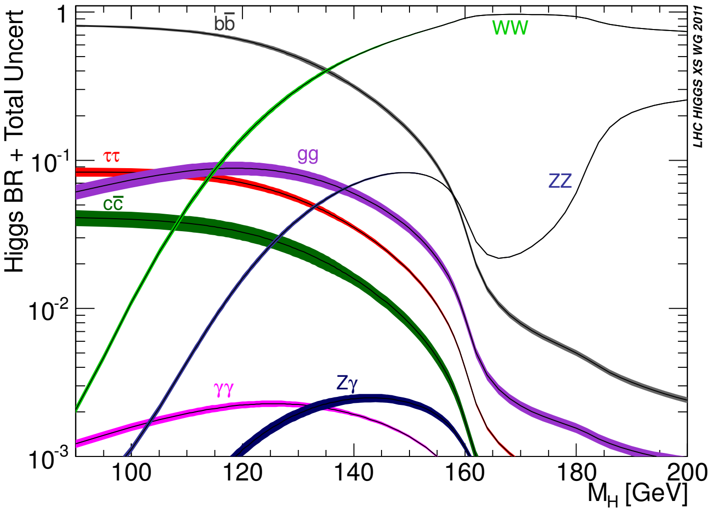

Figure 3.4.2: *Standard Model Higgs boson branching fractions as a function of mass, with theoretical uncertainties indicated by line width, taken from Ref. [120].*

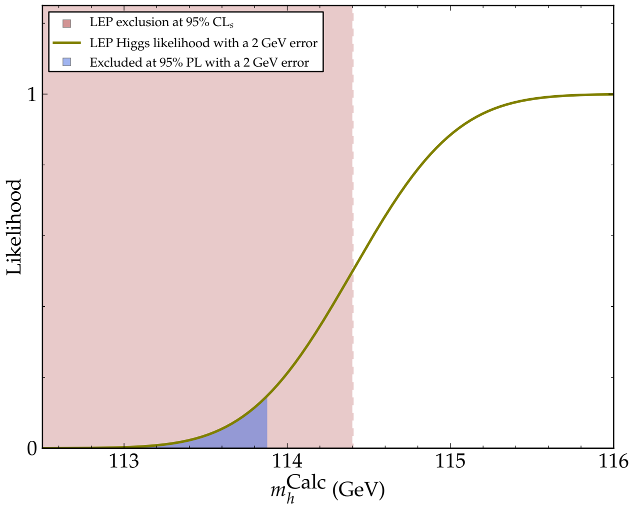

Figure 3.4.3: *Our likelihood from LEP Standard Model Higgs searches as a function of the calculated, rather than true, Higgs mass, including a* 2 *GeV error in the Higgs mass calculation.*

straints on the Standard Model Higgs mass which usurped previous constraints. Our analysis was conducted during the frantic historic moments immediately preceding and succeeding their discovery, and included publicly available Higgs constraints that were soon surpassed. Whilst these constraints are now an historical footnote, and their detail might seem arcane, it is necessary that they are described. The results quoted were contemporary with this work and were since updated by CMS and ATLAS.

At centre-of-mass energies of $\sqrt{s} = 7\,\text{TeV}$ and $\sqrt{s} = 8\,\text{TeV}$, a proton's valence quarks are engulfed by sea quarks and sea gluons. Collisions between sea quarks and sea gluons, rather than valence quarks, dominate Higgs boson production. The four dominant Higgs boson production mechanisms at the LHC are gluon fusion, vector boson fusion, Higgs-strahlung and $t\bar{t}$ fusion (see Fig. 3.4.4) [133]. Standard Model Higgs boson production is on-shell, because the Standard Model Higgs boson has a narrow width.

In the MSSM, the lightest Higgs boson's mass must be less than $\sim 135\,\text{GeV}$ if $M_{\text{SUSY}} \lesssim 1\,\text{TeV}$ [41] and heavier than the LEP lower bound. In this permitted window, the Higgs boson decays through many decay modes (see Fig. 3.4.2). The LHC experiments cannot distinguish the gg and $c\bar{c}$ decay modes from Standard Model QCD backgrounds. Whilst the WW^* off-shell, $b\bar{b}$ and $\tau\tau$ decay modes contributed to the Higgs discovery, the discovery was primarily in the "golden" ZZ^* off-shell and $\gamma\gamma$ decay modes. The decay modes are further categorised by their Higgs production mechanism into disjoint "channels."

CMS, for example, saw excesses in each decay mode, with a nugatory chance of being a fluctuation in the background (6.9σ* [134]), and excesses in the golden decay modes with a combined significance of 5.8σ.

The "golden channels" are $h \to ZZ^* \to 4\ell$ and $h \to \gamma\gamma$ — they can be entirely reconstructed, because they have no missing energy in their final states. CMS and ATLAS inferred the Higgs mass from these high-sensitivity channels. So that their mass estimate is model-independent, CMS do not assume Standard Model Higgs couplings, rather; CMS perform a simultaneous scan of mass, "signal strength modifiers" for $gg \to h \to \gamma\gamma$, $qq \to h \to \gamma\gamma$ and $h \to ZZ^* \to 4\ell$, and nuisance parameters. They report a best-fit Higgs mass and a 68% PL interval for the Higgs

---

[*] In ATLAS and CMS, p-values are converted to "significances" with a one-sided Gaussian tail convention. This significance corresponds to a p-value of 3×10^{-12}.

(a) *Higgs-strahlung with associated W production.*

(b) *Gluon fusion, dominated by top-quarks loops.*

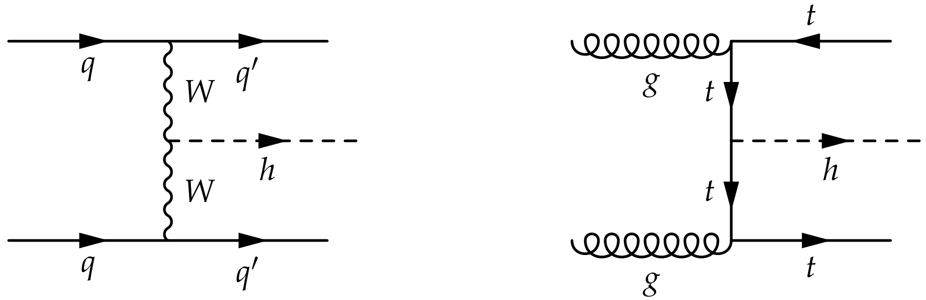

(c) *Vector-boson fusion.*

(d) *$t\bar{t}$.*

Figure 3.4.4: *Feynman diagrams for dominant Standard Model Higgs production mechanisms at the LHC.*

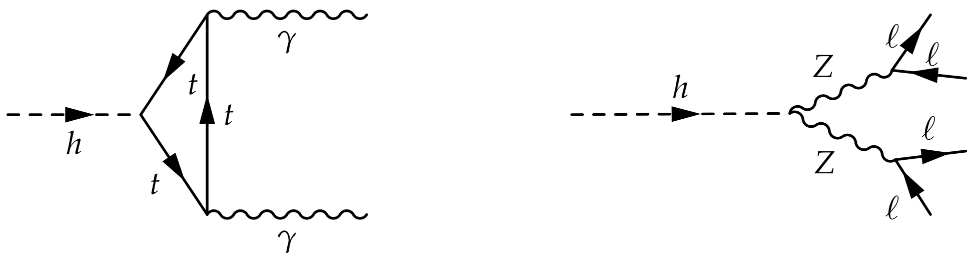

(a) *The diphoton mode, mediated by a top-quark or W-boson loop.*

(b) *The off-shell ZZ^*-mode, illustrated with subsequent leptonic Z-decays to a four-lepton final state.*

Figure 3.4.5: *Feynman diagrams for the dominant Standard Model Higgs decay modes at the LHC.*

mass of

$$m_h = 125.8 \pm 0.4 \pm 0.4\,\text{GeV}. \tag{3.25}$$

The Standard Model Higgs boson is compatible with this mass measurement; a measurement without floating signal strength modifiers agrees with this result to within 0.1 GeV.

CMS also observed insignificant discrepancies in signal strength modifier with respect to the Standard Model, which, by definition, predicts unity for these quantities. The $\gamma\gamma$ signal strength was enhanced, with a best-fit value of 1.43, but compatible with unity within one standard deviation. CMS saw, however, no evidence against the Standard Model Higgs sector; the p-value that these discrepancies are fluctuations in the Standard Model is 0.46. Permitted Higgs couplings are investigated in Ref. [135–137].

ATLAS report similar results; their model independent mass measurement from the golden channels is [138]

$$m_h = 125.2 \pm 0.3 \pm 0.6\,\text{GeV}. \tag{3.26}$$

Their results [138], however, contained a puzzle. The Higgs masses inferred independently from $\gamma\gamma$ and from ZZ^* were $126.6 \pm 0.3 \pm 0.7\,\text{GeV}$ and $123.5 \pm 0.8 \pm 0.3\,\text{GeV}$, respectively. This inconsistency had a p-value, a probability of an inconsistency as large or larger than that observed assuming that the Higgs mass is identical in each channel, of $\lesssim 1\%$ (its precise value depends on whether one uses Monte Carlo simulations or asymptotic formulae). Various explanations, including two Higgs bosons with nearly degenerate masses [139], systematic errors, and chance, have been posited.

Our analyses were performed during the discovery. Before either experiment had achieved a significant result, ATLAS [127] and CMS [124] excluded at 95% CL$_s$ Standard Model Higgs boson masses outside the intervals:

$$\begin{gathered}\text{ATLAS 95\% CL}_s,\ m_h^{\text{True}}(\,\text{GeV}) \in \{117.5, 118.5\} \text{ or } m_h^{\text{True}} \in \{122.5, 129\} \\ \text{CMS 95\% CL}_s,\ m_h^{\text{True}}(\,\text{GeV}) \in \{115, 127.5\}\end{gathered} \tag{3.27}$$

We approximated the likelihood from these experiments with box-car functions, taking the smallest allowed 95% regions,

$$p\left(\text{LHC}|m_h^{\text{True}}\right)=\begin{cases}1: m_h^{\text{True}}\,(\text{GeV})\in\{117.5,118.5\}\\ 1: m_h^{\text{True}}\,(\text{GeV})\in\{122.5,127.5\}\\ 0: \text{elsewhere.}\end{cases}\tag{3.28}$$

We did not attempt to combine the statistical significances of the ATLAS and CMS results in this crude procedure, and approximated the intervals as 100%, rather than 95%, intervals. We incorporated the significant theoretical error in the MSSM Higgs mass calculation via Eq. 2.20, which resulted in our likelihood;

$$\begin{aligned}\mathcal{L}_{\text{Pre-LHC}}&=p\left(\text{LHC}|m_h^{\text{Calc}}\right)\qquad(3.29)\\&=\text{erf}\left(m_h^{\text{Calc}}-117.5\,\text{GeV}/\sqrt{2}\tau\right)-\text{erf}\left(m_h^{\text{Calc}}-118.5\,\text{GeV}/\sqrt{2}\tau\right)+\\&\quad\text{erf}\left(m_h^{\text{Calc}}-122.5\,\text{GeV}/\sqrt{2}\tau\right)-\text{erf}\left(m_h^{\text{Calc}}-127.5\,\text{GeV}/\sqrt{2}\tau\right).\end{aligned}$$

We ignored statistically insignificant discrepancies in signal strength modifier or measured signal strengths within the permitted mass windows. This function (plotted in Fig. 3.4.6) has a ridge at $m_h = 118\,\text{GeV}$ corresponding to the lower permitted mass window from CMS; however, this window is disfavoured by the convolution, because their is an appreciable chance that m_h^{Calc} inside the lighter window corresponds to m_h^{True} outside this permitted window (the width of this window is less than the theoretical error τ).

We were fortunate in our analysis; we anticipated the discovery of a Standard Model-like Higgs boson with a mass of 125 GeV, as indicated at that moment by the statistically insignificant publicly available results in Ref. [124, 127]. We estimated that its mass would be measured with a Gaussian error of $\sigma = 2\,\text{GeV}$ — we slightly underestimated the precision and mass. We combined this hypothetical measurement with a theory error in the Higgs mass calculation via Eq. 3.5. Our likelihood in this hypothetical scenario was approximately that which was later realised by the ATLAS and CMS experiments, and, as such, we identified this scenario and its results with reality;

$$\mathcal{L}_{\text{Post-LHC}}=p\left(\text{LHC}|m_h^{\text{Calc}}\right)=\exp\left[-\frac{\left(125\,\text{GeV}-m_h^{\text{Calc}}\right)^2}{2\left(\tau^2+\sigma^2\right)}\right].\tag{3.30}$$

We again ignored measurements (hypothetical or real) of Higgs couplings in our likelihoods. Updated CMS measurements of Higgs signal strengths with $5.1\,\text{fb}^{-1}$ of integrated luminosity at $\sqrt{s} = 7\,\text{TeV}$ and $19.6\,\text{fb}^{-1}$ of integrated luminosity $\sqrt{s} = 8\,\text{TeV}$ [140] are shown in Fig. 3.4.7. The measurements agree with the Standard Model; the p-value is 0.65.

3.5 Electroweak precision observables

Electroweak precision observables are loosely defined as "unfolded" observables measured with high, $\lesssim 1\%$ relative precision with which one can test the Standard Model or MSSM at beyond the leading-order [141]. We consider loop contributions to the W-boson and Z-boson unrenormalised self-energies,

$$\Sigma^{W,Z}_{\mu\nu}(q) = \left(-g_{\mu\nu} + \frac{q_\mu q_\nu}{q^2}\right)\Sigma^{W,Z}(q^2) + \ldots, \tag{3.31}$$

where $\Sigma^{W,Z}(q^2)$ is the transverse self-energy [142]. In fact, our electroweak precision observables are characterised by

$$\Delta\rho \equiv \frac{\Sigma^Z(0)}{M_Z^2} - \frac{\Sigma^W(0)}{M_W^2}. \tag{3.32}$$

3.5.1 Mass of the W-boson

With our $\Delta\rho$ parameter in Eq. 3.32, sparticle loops in the Z-boson and W-boson self-energies, predominantly stop loops [143], shift the W-boson mass by approximately [142]

$$\delta M_W \approx \frac{1}{2} M_W \frac{\cos^2\theta_W}{\cos^2\theta_W - \sin^2\theta_W}\Delta\rho. \tag{3.33}$$

The mass of the W-boson was precisely measured at LEP by DELPHI [144], OPAL [145], L3 [146] and ALEPH [147] and at the Tevatron by CDF [148] and DØ [149]. At LEP, W-bosons were produced in pairs from electron-positron collisions, with subsequent leptonic and hadronic W-decays. The mass was inferred by reconstructing the decay products. At the Tevatron, W-bosons were produced in combination with initial state hadronic radiation in $q'\bar{q} \to XW$. The transverse mass and transverse momentum distributions were measured from the products

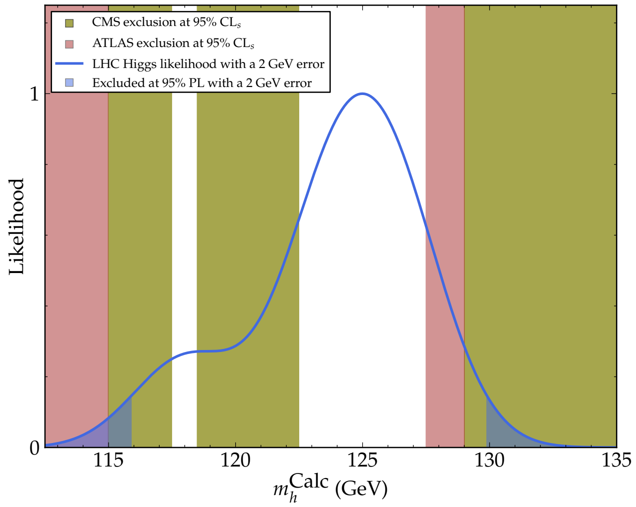

Figure 3.4.6: *Our likelihood from the LHC Standard Model Higgs searches as a function of the calculated, rather than true, Higgs mass, including a 2 GeV error in the Higgs mass calculation, prior to its Higgs discovery.*

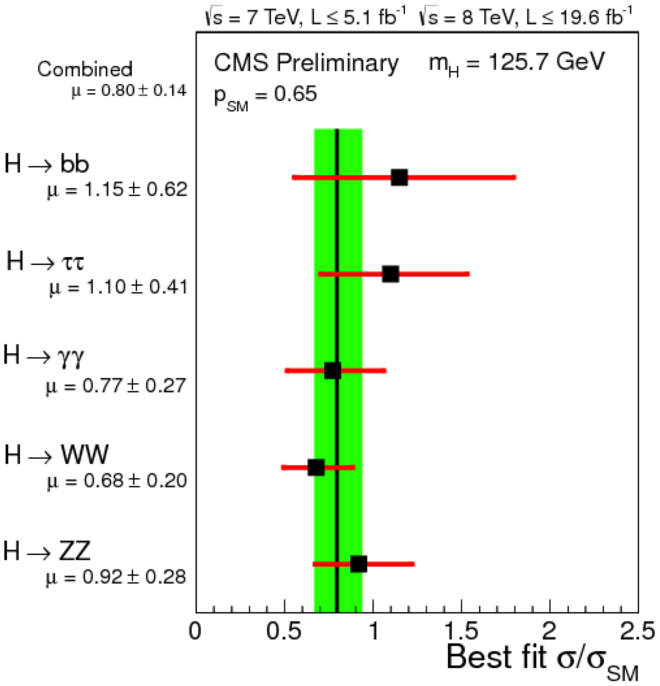

Figure 3.4.7: *CMS measurements of Higgs signal strengths for separate Higgs decay channels from Ref. [140]. The black squares are the best-fitting signal strengths and the red lines indicate the combined statistical and systematic* 1σ *errors. The vertical line and green band is the combined measurement,* $\sigma/\sigma_{SM} = 0.80 \pm 0.14$.

of the subsequent W-decay, from which the mass of the W-boson was extracted, by fitting "templates" to these distributions, which were functions of the W-mass.

The PDG average of such measurements is [71]

$$M_W = 80.385 \pm 0.015\,\text{GeV}. \tag{3.34}$$

We assume that the likelihood is Gaussian, and include a 0.015 GeV theoretical error in the W-mass calculation [150] via Eq. 3.5.

3.5.2 Weak-mixing angle

The weak-mixing angle is defined, at the tree-level, by the relation [151]

$$e = g \sin\theta_W = g' \cos\theta_W, \tag{3.35}$$

resulting, via electroweak symmetry breaking, in the tree-level relation

$$\sin^2\theta_W = 1 - \frac{M_W^2}{M_Z^2}. \tag{3.36}$$

This "Sirlin" definition is the weak-mixing angle in the on-shell renormalisation scheme in all orders. The quantity $\sin^{2,l}_{\text{Eff}}\theta_W$, the leptonic effective weak mixing angle, differs from the on-shell mixing angle by $\lesssim 1\%$.

Similarly to the W-boson mass, loop contributions shift $\sin^{2,l}_{\text{Eff}}\theta_W$ by approximately [142]

$$\delta\sin^{2,l}_{\text{Eff}}\theta_W \approx \frac{-\cos^2\theta_W \sin^2\theta_W}{\cos^2\theta_W - \sin^2\theta_W}\Delta\rho. \tag{3.37}$$

The PDG combination of measurements of $\sin^{2,l}_{\text{Eff}}\theta_W$ from the Tevatron and LEP is [71]

$$\sin^{2,l}_{\text{Eff}}\theta_W = 0.23146 \pm 0.00012. \tag{3.38}$$

We assume that the likelihood from this combination is Gaussian and include a theoretical error in the $\sin^{2,l}_{\text{Eff}}\theta_W$ calculation in the MSSM of 0.00015 [150] via Eq. 3.5.

3.6 Direct collider searches

Superparticles, if they exist and are sufficiently light, ought to be produced in particle collisions. If R-parity is conserved, as it is in the MSSM, this production results in pairs of the lightest neutralino, χ, which cannot be detected, resulting in missing energy in the event. If the collider is a hadron collider, however, because the initial longitudinal momentum is unknown, only missing transverse energy, $\not{E}_T$, is measured. A general final state from superparticle production in the MSSM is n leptons, m jets, and $\not{E}_T \geq 2m_\chi$; however, there are significant Standard Model background processes with missing energy from W-boson or Z-boson decays to neutrinos. Experiments discriminate background events from signal events via kinematic "cuts." Historically, the first of such direct searches was the UA1 [152] experiment, but we considered only results from direct searches at LEP [153–157], the Tevatron [158–161] and the LHC.

3.6.1 LEP

LEP experiments, including ALEPH, DELPHI, OPAL and L3, searched for supersymmetry in electron-positron collisions with centre-of-mass energies of $\sqrt{s} \leq 208\,\text{GeV}$; the null results of which were combined by the LEP SUSY working group into 95% CL lower limits on superparticle masses [162]. Superparticles could have been produced in pairs via an s-channel Z-boson or photon, or via a t-channel gaugino or sfermion. We constructed a likelihood from the 95% LEP sparticle mass limits [158–161,163]

$$\begin{aligned}
m_\chi &\geq 50\,\text{GeV}, \\
m_{\chi^\pm} &\geq 94\,\text{GeV}, \\
m_{\tilde{e}_R} &\geq 100\,\text{GeV}, \\
m_{\tilde{\mu}_R} &\geq 95\,\text{GeV}, \\
m_{\tilde{\tau}_1} &\geq 87\,\text{GeV}, \\
m_{\tilde{t}_1} &\geq 95\,\text{GeV}, \\
m_{\tilde{b}_1} &\geq 95\,\text{GeV}.
\end{aligned} \tag{3.39}$$

Our likelihood included a 5% Gaussian fractional error in the calculated sparticle masses, estimated from the scale and scheme dependence of the calculated masses in Ref. [164], via Eq. 3.5.

3.6.2 Tevatron

The Tevatron collided protons and anti-protons at centre-of-mass energies of $\sqrt{s} = 1.96\,\text{TeV}$ in its search for supersymmetry and the Higgs boson [165]. The Tevatron experiments searched for supersymmetry via distinct signatures with minimal Standard Model backgrounds [166,167]. The direct production of a chargino and a neutralino might have had such a signature, because it might result in a trilepton final state with missing transverse energy, via Fig. 3.6.1. The direct production of squarks or gluinos could have resulted in final states with multiple jets, no leptons and missing transverse energy, or a same-sign dilepton signal from gluino decays via a chargino. Because Tevatron searches for supersymmetry observed no statistically significant signals, the Tevatron excluded superparticles with masses below particular thresholds at 95% CL [158–161];

$$\begin{aligned} m_{\tilde{q}} &\geq 375\,\text{GeV}, \\ m_{\tilde{g}} &\geq 289\,\text{GeV}. \end{aligned} \tag{3.40}$$

We constructed a likelihood from these limits that included a 5% Gaussian fractional error in the calculated sparticle masses, estimated from the scale and scheme dependence of the calculated masses in Ref. [164], via Eq. 3.5.

3.6.3 LHC

During our research, the ATLAS and CMS experiments searched for supersymmetry at the LHC at $\sqrt{s} = 7\,\text{TeV}$ and $\sqrt{s} = 8\,\text{TeV}$. Because they observed no statistically significant excesses of events over the expected Standard Model backgrounds, ATLAS and CMS excluded light squarks and gluinos. We interpret their results within the CMSSM in Chap. 4.

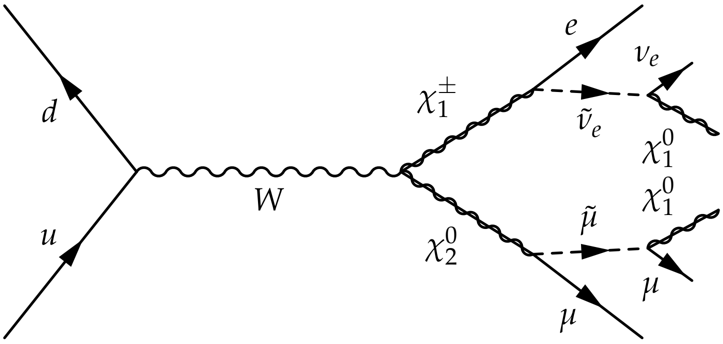

Figure 3.6.1: *Feynman diagram for a trilepton final state from direct gaugino production at a hadron collider; the final state is a same-flavour lepton pair, a third lepton and missing energy.*

3.7 *B*-physics

B-physics is the study of *b*-flavoured hadrons, particularly their weak or rare decays [168]. We are interested in rare decays that could be "crystal balls" for new physics. The Standard Model forbids tree-level flavour-changing neutral currents; these currents are permitted only via loops, and are suppressed by their additional orders of couplings. Ordinarily, loop-level supersymmetric contributions would be minuscule compared with the tree-level Standard Model contributions, but in rare decays such tree-level contributions are forbidden.

3.7.1 $b \to s\gamma$

The decay $\overline{B} \to X_s\gamma$, where X_s is a strange-flavoured hadron and $\overline{B}$ is a $\bar{d}b$ meson, is mediated by a flavour-changing neutral current in $b \to s\gamma$, which is suppressed by loops in the Standard Model. The loop-level supersymmetric contributions might be significant. The dominant Standard Model and supersymmetric diagrams (assuming MFV) that contribute to $b \to s\gamma$ are shown in Fig. 3.7.1 [169]. The sum of such diagrams is proportional to CKM-matrix elements and is schematically [29]

$$\text{BR}\,(b \to s\gamma) \propto \frac{|V_{ts}^* V_{tb}|^2}{|V_{cb}|^2}\left[\text{SM contr.} + H^\pm \text{ contr.} - \frac{\operatorname{sgn}\mu\, M_t^2 \tan\beta}{M_\text{SUSY}^2}\right]^2, \tag{3.41}$$

where the contributions in brackets are Standard Model, charged Higgs and approximate supersymmetric contributions, respectively. This approximation, however, is a gross simplification. The $\text{BR}\,(b \to s\gamma)$ behaviour with $\tan\beta$ is complicated by mass insertions. If particular diagrams dominate $\text{BR}\,(b \to s\gamma)$, supersymmetric contributions can be proportional to $\cot\beta$ or A_0.

The branching ratio $\text{BR}\,(b \to s\gamma)$ was measured in *B*-factories, including CLEO [170], BaBar [171] and Belle [172]. Because of the detector's finite resolution, the energy of the photon in the $\overline{B}$ rest frame was required to be greater than a specified threshold. This mitigates infrared divergences in $\text{BR}\,(b \to s\gamma)$. The PDG average of such measurements for $E_\gamma \geq 1.6\,\text{GeV}$ [71],

$$\text{BR}\,(b \to s\gamma) = 3.60 \pm 0.23 \times 10^{-4}, \tag{3.42}$$

slightly differs from the Heavy Flavor Averaging Group (HFAG) average [173,174],

$$\mathrm{BR}\,(b \to s\gamma) = 3.43 \pm 0.21 \pm 0.07 \times 10^{-4}, \tag{3.43}$$

because they average slightly different experimental data.

The Standard Model prediction at NNLO, $\mathcal{O}(\alpha_s^2)$ is [175]

$$\mathrm{BR}\,(b \to s\gamma) = 3.15 \pm 0.23 \times 10^{-4}. \tag{3.44}$$

This uncertainty includes non-perturbative, parametric and higher-order uncertainties. Whilst the Standard Model prediction is in agreement with the averaged measurements to within 1.4 standard deviations (we add theoretical and experimental errors in quadrature), this insignificant discrepancy hints that it may be enhanced by new physics.

We include either the PDG or HFAG $\mathrm{BR}\,(b \to s\gamma)$ average in our likelihood, with a Gaussian, including a 0.21×10^{-4} [175] theory error in the MSSM $\mathrm{BR}\,(b \to s\gamma)$ calculation via Eq. 3.5.*

3.7.2 $B_s \to \mu^+\mu^-$

The decay $B_s \to \mu^+\mu^-$, where B_s is an $s\bar{b}$ meson, is a rare decay in the Standard Model. Standard Model tree-level flavour-changing neutral currents are forbidden, and loop-level diagrams (Fig. 3.7.2a and Fig. 3.7.2b) are "helicity suppressed" [176]. The B_s is a pseudoscalar, which, in the Standard Model, might decay to two fermions via an electroweak interaction that separates chiralities. Angular momentum conservation in such a decay requires a "helicity flip," via a mass insertion and suppresses this decay. The supersymmetric diagram (Fig. 3.7.2c), in contrast, is mediated via Yukawa interaction that mixes chiralities, and is not suppressed in this way. The supersymmetric contributions to $B_s \to \mu^+\mu^-$ could have been a "smoking gun" signal for supersymmetry in experimental searches; however, supersymmetric contributions can interfere destructively. In the large $\tan\beta$ limit of the MSSM, we neglect the light Higgs contribution in Fig. 3.7.2c because its down-type Yukawa coupling is not enhanced [177], and approximate $m_H \approx m_A$, resulting in an approximate relation between $\mathrm{BR}\,(B_s \to \mu^+\mu^-)$, $\tan\beta$

---

* Our theoretical error for $\mathrm{BR}\,(b \to s\gamma)$ in the MSSM is chosen to be equal to that in the Standard Model in Ref. [207].

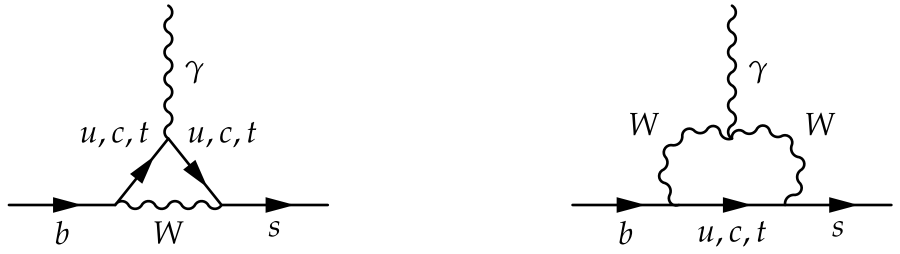

(a) *Standard Model loop contribution facilitated by quark mixing in the CKM matrix.*

(b) *Standard Model loop contribution facilitate by quark mixing in the CKM matrix, with $WW\gamma$ interaction.*

(c) *"Supersymmetrised" (a), via a chargino.*

(d) *"Supersymmetrised" (b), via a chargino.*

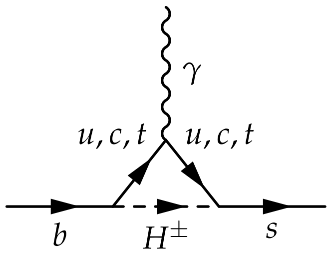

(e) *Charged-Higgs contribution, present in two-Higgs doublet models, including the MSSM.*

Figure 3.7.1: *Leading-order Feynman diagrams for the rare decay $b \to s\gamma$ in the Standard Model and in the MSSM. Gluino loops (not shown) also contribute to $b \to s\gamma$ at leading order. $b \to s\gamma$ requires at least one mass insertion (not indicated), depending on whether the chargino is a higgsino or wino, which introduces factors of μ, m_b, M_2, A_0 or M_Z [169].*

and m_A [178]

$$\mathrm{BR}\left(B_s \to \mu^+\mu^-\right)^{\mathrm{SUSY}} \propto \tan^6\beta \left(\frac{M_{\mathrm{SUSY}}}{m_A}\right)^4. \tag{3.45}$$

The Standard Model prediction for $\mathrm{BR}\left(B_s \to \mu^+\mu^-\right)$ calculated in Ref. [179] is

$$\mathrm{BR}\left(B_s \to \mu^+\mu^-\right)^{\mathrm{SM}} = 3.23 \pm 0.27 \times 10^{-9}. \tag{3.46}$$

This prediction requires adjustments so that it exactly matches what is measured in experiments, including removal of direct-emission photons, and flavour averaging. Because the B_s meson is a flavour eigenstate, rather than a mass eigenstate, the branching ratio is flavour-averaged time-integrated over B_s to $\overline{B}_s$ oscillations [179],

$$\left\langle \mathrm{BR}\left(B_s \to \mu^+\mu^-\right)\right\rangle_{[t]} = \frac{1}{2}\int_0^t \mathit{\Gamma}(B_s(t') \to \mu^+\mu^-) + \mathit{\Gamma}(\overline{B}_s(t') \to \mu^+\mu^-)\,\mathrm{d}t', \tag{3.47}$$

where $\langle\cdot\rangle$ represents a flavour-average, $[t]$ represents time-integration and, e.g., $\mathit{\Gamma}(B_s(t') \to \mu^+\mu^-)$ is the decay distribution at proper time t' for a flavour eigenstate B_s at $t' = 0$.

The LHC experiment LHCb searched for the $B_s \to \mu^+\mu^-$ decay [180–182]. Their adjusted Eq. 3.46 Standard Model prediction for $\mathrm{BR}\left(B_s \to \mu^+\mu^-\right)$ for their experiment was [182]

$$\left\langle \mathrm{BR}\left(B_s \to \mu^+\mu^-\right)\right\rangle_{[t]}^{\mathrm{SM}} = 3.54 \pm 0.30 \times 10^{-9}. \tag{3.48}$$

The experiment accrued sufficient data to observe $B_s \to \mu^+\mu^-$ at a statistically significant rate and measure [182]

$$\mathrm{BR}\left(B_s \to \mu^+\mu^-\right) = 3.2^{+1.5}_{-1.2} \times 10^{-9}, \tag{3.49}$$

which is in agreement with the adjusted Standard Model prediction in Eq. 3.48.

We include the $\mathrm{BR}\left(B_s \to \mu^+\mu^-\right)$ measurements in our likelihood, including a 14% [204] theory error in the MSSM $\mathrm{BR}\left(B_s \to \mu^+\mu^-\right)$ calculation via Eq. 3.5.*

---

* This 14% theoretical error arises from adding in quadrature a 10% parametric uncertainty from the B_s decay constant and a 10% uncertainty from missing higher orders.

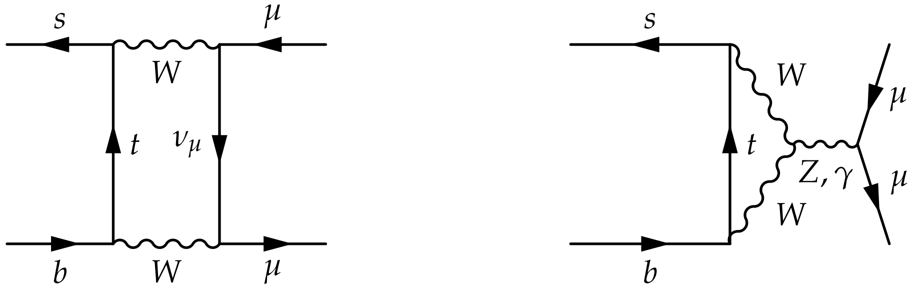

(a) *Standard Model box diagram, which is helicity suppressed. In two-Higgs doublet models, including the MSSM, there is an additional similar diagram in which a W-boson is replaced by a charged Higgs.*

(b) *Standard Model penguin diagram, which is helicity suppressed. In two-Higgs doublet models, including the MSSM, there is an additional scalar diagram in which a W-boson is replaced by a charged Higgs, and the Z, γ is replaced by a neutral Higgs.*

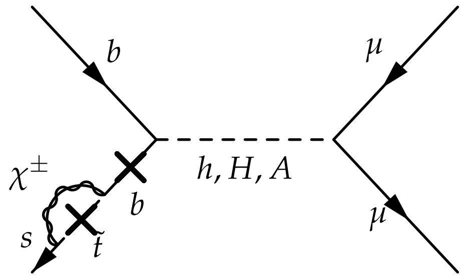

(c) *An MSSM contribution, which avoids helicity suppression, because the $\mu\mu$ vertex is a Yukawa interaction, rather than a chiral weak interaction.*

Figure 3.7.2: *Leading-order Feynman diagrams for the rare decay $B_s \to \mu^+\mu^-$ in the Standard Model and in the MSSM.*

3.7.3 $B_u \to \tau\nu$

The B_u meson ($u\bar{b}$) may decay leptonically at tree-level in the Standard Model via a W-boson [183]; $B_u \to \tau\nu$ (Fig. 3.7.3a). This decay is helicity suppressed because the B_u meson is a pseudoscalar; B_u dominantly decays to a τ, rather than a e or μ, because it is heavier than e or μ. The branching ratio $\text{BR}\,(B_u \to \tau\nu)$ is proportional to the $|V_{ub}|^2$ element of the CKM-matrix. The CKM-fitter collaboration [184] calculate that

$$\text{BR}\,(B_u \to \tau\nu)^{\text{SM}} = 1.68 \pm 0.31 \times 10^{-4}. \tag{3.50}$$

This branching ratio is altered in the MSSM by a tree-level s-channel diagram with a charged Higgs boson (Fig. 3.7.3b). Because the couplings in this diagram are Yukawa, it is not helicity suppressed, and the branching ratio may be enhanced by approximately [185]

$$\text{BR}\,(B_u \to \tau\nu)^{\text{MSSM}} = \text{BR}\,(B_u \to \tau\nu)^{\text{SM}} \times \left[1 - \tan^2\beta \left(\frac{m_{B_u}}{m_{H^\pm}}\right)^2\right]^2. \tag{3.51}$$

This factor enhances the branching ratio if

$$\tan\beta > \sqrt{2}\frac{m_{H^\pm}}{m_{B_u}} \approx \frac{m_{H^\pm}}{4\,\text{GeV}}. \tag{3.52}$$

This decay was measured in B-factory experiments at CLEO [186], Belle [187] and BaBar [188]. The experiments collide electrons with positrons at centre-of-mass energies close to the $\Upsilon(4s)$ ($b\bar{b}$) resonance, $\sqrt{s} = 10.58\,\text{GeV}$. The $\Upsilon(4s)$ meson decays into B_u-$\overline{B}_u$ pairs. Any $\overline{B}_u$ decay is a "tag" from which the $\Upsilon(4s)$ decay is inferred; a $B_u \to \tau\nu$ decay is measured from the opposite side of the event. The Heavy Flavor Averaging Group average of such measurements [189],

$$\text{BR}\,(B_u \to \tau\nu) = 1.67 \pm 0.30 \times 10^{-4}, \tag{3.53}$$

is in agreement with the Standard Model prediction. We combine this measurement with a 0.38×10^{-4} theoretical error in the $\text{BR}\,(B_u \to \tau\nu)$ calculation [207] via Eq. 3.5 to construct our Gaussian likelihood.*

---

* The theoretical error 0.38×10^{-4} in Ref. [207] results from combining parametric uncertainties in CKM matrix elements, the B_u meson lifetime and the B_u meson decay constant.

3.7.4 ΔM_{B_s}

The B_s ($s\bar{b}$) and $\overline{B}_s$ ($\bar{s}b$) mesons are flavour eigenstates; the B_s mixes with its antiparticle $\overline{B}_s$, resulting in a light $\overline{B}_{s,l}$ mass eigenstate and a heavy $\overline{B}_{s,h}$ mass eigenstate [190]. Flavour eigenstates participate in interactions, either B_s or $\overline{B}_s$, but oscillate in time, in a quantum mechanical superposition, between $\overline{B}_s$–B_s. Off-diagonal elements in the mixing matrix [191], which are induced by the diagrams in Fig. 3.7.4, cause this mixing. The diagrams are flavour-changing neutral currents, which are forbidden in the Standard Model at tree-level. The frequency of this oscillation is the difference in mass between the $\overline{B}_{s,h}$ and $\overline{B}_{s,l}$ states, ΔM_{B_s}, in units in which $\hbar = 1$. The Standard Model prediction is that [191]

$$\Delta M_{B_s} = 17.3 \pm 1.5\,\text{ps}^{-1}. \tag{3.54}$$

Because it is so small, historically, experiments struggled to measure ΔM_{B_s} with statistical significance [192]. The Tevatron's D∅ [193] and LHCb [194] experiments, however, measured ΔM_{B_s}. These experiments observe the production and subsequent decay of a B_s or a $\overline{B}_s$, which, between its production and decay, oscillates between $\overline{B}_s$–B_s. The final flavour and initial flavour are inferred from its decay products and information in the opposite side of the event, respectively. The time between production and decay is calculated from the distance between the primary vertex and the decay vertex. The oscillation frequency ΔM_{B_s} is fitted to these measurements.

The PDG average of such ΔM_{B_s} measurements is [71]

$$\Delta M_{B_s} = 17.69 \pm 0.08\,\text{ps}^{-1}. \tag{3.55}$$

We include the PDG ΔM_{B_s} average in our likelihood with a Gaussian, including a $2.40\,\text{ps}^{-1}$ theory error in the MSSM ΔM_{B_s} calculation [207] via Eq. 3.5.*

---

* Ref. [207] states that this $2.40\,\text{ps}^{-1}$ theory error is that in the Standard Model from the UTfit collaboration. The electronic link cited in Ref. [207] is, however, ambiguous. The UTfit collaboration lists $2.60\,\text{ps}^{-1}$ in Ref. [195].

(a) *Standard Model tree-level* $B_u \to \tau\nu$ *via W-boson.*

(b) *MSSM* $B_u \to \tau\nu$ *contribution via a charged Higgs.*

Figure 3.7.3: *Tree-level Feynman diagrams for the rare decay* $B_u \to \tau\nu$ *in the Standard Model and the MSSM.*

(a) *Standard Model box diagram.*

(b) *Standard Model box diagram.*

(c) *An MSSM box diagram with a chargino.*

(d) *An MSSM box diagram with a gluino.*

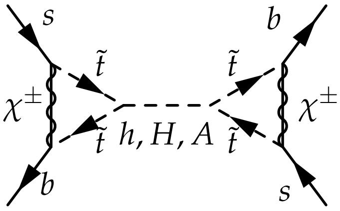

(e) *An MSSM double-penguin diagram with charginos. There is a similar MSSM double-penguin diagram with gluinos (not shown).*

Figure 3.7.4: *Dominant Feynman diagrams contributing to $\overline{B}_s$–B_s in the Standard Model and the MSSM.*

3.8 Anomalous magnetic moment of the muon

The anomalous magnetic moment of the muon is one of the most precisely measured observable in high-energy physics [196], with a precision of approximately one part per million from the Brookhaven National Laboratory [197]. Particles with spin, including the muon, have intrinsic magnetic moments,

$$\vec{\mu} = g_\mu \left(\frac{e}{2m_\mu} \right) \vec{S}. \tag{3.56}$$

The tree-level prediction is that $g_\mu = 2$ from the equations of motion for a muon in an external electromagnetic field. Were this the case, the spin and the muon's direction would precess identically in a magnetic field. Deviations from this prediction constitute the anomalous magnetic moment of the muon,

$$a_\mu = \frac{1}{2} \left(g_\mu - 2 \right), \tag{3.57}$$

and originate from higher-order corrections and, possibly, new physics. The Brookhaven National Laboratory measured a_μ by circulating polarised muon beams around a torus in a uniform magnetic field. The difference between the angular frequencies with which muons circulate the torus and with which their spins precess is proportional to a_μ. The muons decay leptonically and the electrons are emitted predominantly in the directions of the muons' spins, from which a_μ is determined. The Muon $(g-2)$ Collaboration's final measurement was [71,197]

$$a_\mu = 11659208.9 \pm 5.4 \pm 3.3 \times 10^{-10}. \tag{3.58}$$

The higher-order corrections are computed from the full QED Lagrangian with a classical external contribution to the photon field [198]. The one-particle irreducible Feynman diagrams with external muons and a photon are summed to a high-order in a perturbative expansion in the fine-structure constant.

Contributions to a_μ mediate helicity-flipping (because a_μ misaligns a muon's spin and momentum) and would be forbidden were the muon massless, because the Standard Model has a chiral symmetry before electroweak symmetry is broken [198]. The amplitudes for helicity-flipping are, consequently, proportional to the muon mass, and contributions to the anomalous magnetic moment of the muon are proportional to the transition probability, that is, the muon mass squared. This is precisely why this observable is a "crystal ball" for new physics; the muon is heavy and anomalous contributions might be tangible. The contributions for the muon are $(m_\mu/m_e)^2 \sim 40,000$ times larger than for the electron.

Within the MSSM, there are additional diagrams, originating from the muon Yukawa coupling, that contribute. The dominant Standard Model and MSSM diagrams are drawn in Fig. 3.8.1. There are, however, higher-order Standard Model hadronic light-by-light contributions (Fig. 3.8.1b), which cannot be reliably calculated. These contributions are instead measured in auxiliary experiments that measure hadronic cross sections in electron-positron collisions [199]. An approximate one-loop expression for δa_μ in the MSSM [196] is

$$\delta a_\mu^{\text{MSSM}} = a_\mu^{\text{MSSM}} - a_\mu^{\text{SM}} \approx 13 \times 10^{-10} \left(\frac{100\,\text{GeV}}{m_{\tilde{\mu}}} \right)^2 \tan\beta \,\text{sgn}\,\mu \tag{3.59}$$

We use the Standard Model prediction for a_μ compiled in Ref. [71],

$$a_\mu^{\text{SM}} = 116591802 \pm 2 \pm 42 \pm 26 \times 10^{-11}, \tag{3.60}$$

where the errors are electroweak, lower-order hadronic and higher-order hadronic, from which the measured result is subtracted [71],

$$\delta a_\mu = a_\mu - a_\mu^{\text{SM}} = 287 \pm 80 \times 10^{-11}, \tag{3.61}$$

where all errors are added in quadrature. The discrepancy from zero is 3.6 standard deviations. The probability of obtaining such a discrepant result by chance is 3×10^{-4}.* This is a "harbinger" for new physics, which contributes to the anomalous magnetic moment of the muon [200], ameliorating the discrepancy. Historically, precise calculations of hadronic and weak contributions shrunk this discrepancy from 8 standard deviations [196]. The disagreement is reduced to 2.4σ if we use $\tau\tau$, rather than electron-positron, measurements of hadronic light-by-light contributions in the Standard Model prediction [71].

Because the anomalous magnetic moment is a form-factor in a dressed QED vertex, rather than a transition probability, there is no interference between contributions, and we can separately calculate the MSSM contribution to a_μ. We approximate our likelihood for δa_μ to a Gaussian, and incorporate a 1×10^{-10}

---

* Assuming that the associated likelihood is Gaussian.

theoretical error the MSSM δa_μ calculation [142] via Eq. 3.5,[*]

$$\mathcal{L}_{\delta a_\mu} = \exp\left[-\frac{\left(\delta a_\mu^{\mathrm{Calc}} - \delta a_\mu\right)^2}{2\left(\sigma^2 + \tau^2\right)}\right]. \tag{3.62}$$

---

[*] In Ref. [142], δa_μ with two-loops is $\sim 2\%$ different from δa_μ with one-loop, from which we estimate that the theory error is 1×10^{-10}.

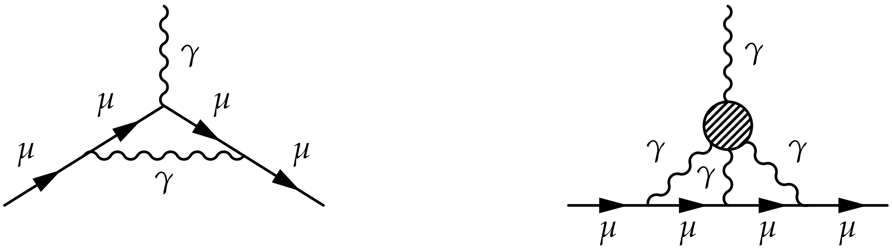

(a) *Leading-order (Schwinger).*

(b) *Hadronic light-by-light.*

(c) *Leading-order weak, via W-boson.*

(d) *Leading-order weak, via Z-boson or Higgs.*

(e) *Leading-order MSSM, via chargino.*

(f) *Leading-order MSSM, via neutralino.*

Figure 3.8.1: *Leading-order Feynman diagrams that contribute to the anomalous magnetic moment of the muon in the MSSM, plus the incalculable hadronic light-by-light contribution.*

Chapter 4

Results

4.1 Introduction

4.1.1 History

We briefly recapitulate the status of the CMSSM prior to the beginning of this work and LHC operations. This work is similar to that in Ref. [201–222], Ref. [223], which examines the NUHM, Ref. [224–232], which contain a frequentist, rather than Bayesian, analysis, and Ref. [233–274] in which pMSSM models are considered.

Indeed, many studies attempted to assess the CMSSM's compatibility with indirect experimental evidence and identify its most likely regions of parameter space, and, whilst results differed quantitatively, results were qualitatively similar. Ref. [207], representative of the literature, showed that the CMSSM was compatible with existing constraints including the $(g-2)_\mu$ anomaly in particular regions of its parameter space, characterised by the mechanism by which the neutralino annihilates [201] (see Sec. 3.3.2). These regions are schematically illustrated in Fig. 4.1.1. Ref. [207], however, stressed that results were dependent on the choice of priors for the CMSSM parameters.

4.1.2 Computer codes

For our likelihood functions, we calculated relevant quantities with publicly available computer programs:

- With `SOFTSUSY` [72], we ran soft-breaking masses from M_{GUT} to M_{SUSY} with the RG, and calculated sparticle and Higgs masses and mixing angles. The Higgs mass is calculated to two-loops. From its scale and scheme dependence, its error is estimated to be $\sim 2\,\text{GeV}$ [121]. The sparticle masses are calculated to one-loop but include various approximations; their error is estimated to be $\sim 10\%$ [275,276].
- With `MicrOMEGAs` [93], we calculated the relic density, with an approximate 10% fractional error [102,103], and σ_p^{SI}.
- With `FeynHiggs` [277–280], we calculated our electroweak precision observables, $\sin^2\theta_{\text{eff}}$ and M_W, and ΔM_{B_s}.
- With `SuperIso` [281, 282], we calculated $\text{BR}\,(B_u \to \tau\nu)$, $\text{BR}\,(b \to s\gamma)$, $\text{BR}\,(B_s \to \mu^+\mu^-)$ and δa_μ.

Note, however, that in our CMSSM $1\,\text{fb}^{-1}$ study, we calculated δa_μ, $\text{BR}\,(B_s \to \mu^+\mu^-)$ and $\text{BR}\,(b \to s\gamma)$ with `MicrOMEGAs`, and $\text{BR}\,(B_u \to \tau\nu)$ and ΔM_{B_s} with `B-Decay` [204,283].

We returned the product of our likelihood functions to `MultiNest`, our scanning algorithm. We linked `MultiNest` with the aforementioned publicly available computer programs with a modified version of `SuperBayeS` [204,284] in our CMSSM $1\,\text{fb}^{-1}$ study (Sec. 4.4) and low-mass golden decay study (Sec. 4.2), `SuperPy` [285] in our high-mass golden decay study (Sec. 4.3), and `BayesFits` [219] in our CMSSM $4.4\,\text{fb}^{-1}$+Higgs (Sec. 4.5) and p9MSSM (Sec. 4.6) studies.

4.2 Low-mass golden decay

The results in this section were published in Ref. [286].

4.2.1 Hypothetical mass measurements at ATLAS SU3

To evaluate prospects for discovering supersymmetry, it was convenient to identify various "benchmark" points in the MSSM's parameter space [287], with dis-

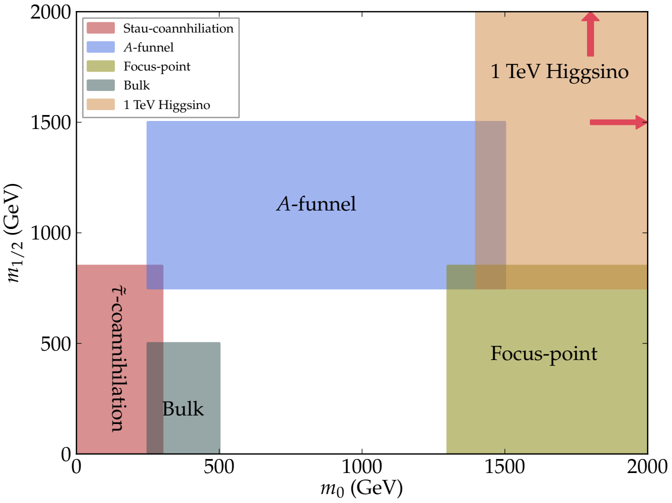

Figure 4.1.1: *Sketch of permitted regions on the CMSSM's $(m_0, m_{1/2})$ plane characterised by the neutralino annihilation mechanism.*

tinct phenomenologies and signals. One such benchmark was ATLAS SU3 [288] (Table 4.2.1); a low-mass scenario in the "bulk" region of the CMSSM, which is excluded by direct searches at the LHC (Sec. 3.6).

Were this scenario realised in nature, the mass spectrum (Table 4.2.2) would be such that sparticle decay in LHC experiments would exhibit a "golden-decay;" a decay chain from which experiments can extract the masses of all sparticles in the decay chain [289]. The golden decay begins from a squark, produced in a pair, with a gluino, or from a gluino, and results in a final state with opposite-sign same-flavour leptons, at least one jet and missing transverse energy, illustrated in Fig. 4.2.1,

$$\tilde{q} \to \chi_2^0 q \to \tilde{\ell}\ell q \to \chi\ell\ell q. \tag{4.1}$$

The sleptons that contribute in the ATLAS SU3 scenario are right-handed selectrons and smuons. The final state from the opposite side of the golden decay (the final state from the sparticle with which the squark in the golden decay was produced) includes missing transverse energy from a second neutralino and contaminates the golden decay with combinatorial misidentifications. This decay is spoilt if the χ_2^0 branching fractions to electron and muon lepton-slepton pairs is subdominant, if the squark branching fraction to gluinos is dominant, or if the sparticles masses are not such that

$$m_\chi < m_{\tilde{\ell}_R} < m_{\chi_2^0} < m_{\tilde{q}}. \tag{4.2}$$

The required branching fractions imply that $m_{\tilde{q}} < m_{\tilde{g}}$, suppressing the $\tilde{q} \to q\tilde{g}$ decay mode.

This final state exhibits four kinematic "endpoints;" distinct features that arise in histograms of the invariant masses of combinations of the leptons and jet. We considered the endpoints in the invariant masses of the dilepton pair ($m_{\ell\ell}$), the jet and either lepton ($m_{\ell,\text{low}}$ and $m_{\ell,\text{high}}$), and the jet and both of the leptons ($m_{\ell\ell q}$). Because experiments cannot ascertain the origin of the leptons, the highest (lowest) lepton-jet invariant mass in an event populates the $m_{\ell,\text{high}}$ ($m_{\ell,\text{low}}$) distribution. The positions of the endpoints can be predicted from the conservation of four-momentum, and the shapes of the endpoints can be predicted from spin-correlations or from Monte-Carlo simulations. The dilepton pair's invariant mass distribution is a sawtooth; because the intermediate slepton is a scalar, the angular separation between the leptons is uniformly distributed in its cosine. The

CMSSM parameter	ATLAS SU3 point
$m_{1/2}$	300 GeV
m_0	100 GeV
$\tan\beta$	6.0
A_0	-300 GeV
$\operatorname{sgn}\mu$	+

Table 4.2.1: *CMSSM parameter values at the ATLAS SU3 benchmark point.*

Sparticle	Mass (GeV)				
χ	117.9	$\tilde{e}_L$, $\tilde{\mu}_L$	230.8	$\tilde{d}_L$	666.2
χ_2^0	223.4	$\tilde{e}_R$, $\tilde{\mu}_R$	157.5	$\tilde{d}_R$	639.0
χ_3^0	463.8	$\tilde{\nu}_e$,$\tilde{\nu}_\mu$	217.5	$\tilde{u}_R$	660.3
χ_4^0	479.9	$\tilde{\tau}_1$	152.2	$\tilde{u}_R$	644.3
$\chi_1^\pm$	224.4	$\tilde{\tau}_2$	232.4	$\tilde{b}_1$	599.0
$\chi_2^\pm$	476.4	$\tilde{\nu}_\tau$	216.9	$\tilde{b}_2$	636.6
$\tilde{g}$	717.5			$\tilde{t}_1$	446.9
				$\tilde{t}_2$	670.9

Table 4.2.2: *The sparticle mass spectrum in the CMSSM at the ATLAS SU3 benchmark point, calculated with* ***`SOFTSUSY`***.

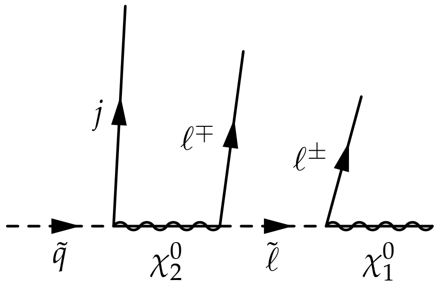

Figure 4.2.1: *Feynman diagram for the "golden decay" from which experiments can extract the masses of all sparticles in the decay chain.*

predictions for the endpoints are [290]

$$\begin{aligned}
\max m^2_{\ell\ell} &= \frac{\left(m^2_{\chi^0_2} - m^2_{\tilde{\ell}}\right)\left(m^2_{\tilde{\ell}} - m^2_{\chi}\right)}{m^2_{\tilde{\ell}}}, \qquad (4.3)\\
\max m^2_{\ell,\text{near}} &= \frac{\left(m^2_{\tilde{q}} - m^2_{\chi^0_2}\right)\left(m^2_{\chi^0_2} - m^2_{\tilde{\ell}}\right)}{m^2_{\chi}},\\
\max m^2_{\ell,\text{far}} &= \frac{\left(m^2_{\tilde{q}} - m^2_{\chi^0_2}\right)\left(m^2_{\tilde{\ell}} - m^2_{\chi}\right)}{m^2_{\tilde{\ell}}},\\
\max m^2_{\ell,\text{low}} &= \min\left(\max m^2_{\ell,\text{near}}, \max m^2_{\ell,\text{far}}\right),\\
\max m^2_{\ell,\text{high}} &= \max\left(\max m^2_{\ell,\text{near}}, \max m^2_{\ell,\text{far}}\right),\\
\max m^2_{\ell q} &= \max\left[\frac{\left(m^2_{\tilde{q}} - m^2_{\chi^0_2}\right)\left(m^2_{\chi^0_2} - m^2_{\chi}\right)}{m^2_{\chi^0_2}}, \frac{\left(m^2_{\tilde{q}} - m^2_{\tilde{\ell}}\right)\left(m^2_{\tilde{\ell}} - m^2_{\chi}\right)}{m^2_{\tilde{\ell}}},\right.\\
&\qquad\left.\frac{\left(m^2_{\tilde{q}}m^2_{\tilde{\ell}} - m^2_{\chi}m^2_{\chi^0_2}\right)\left(m^2_{\chi^0_2} - m^2_{\tilde{\ell}}\right)}{m^2_{\tilde{\ell}}m^2_{\chi^0_2}}\right]
\end{aligned}$$

where the expressions are maximised with respect to the angular separations of the leptons and jet, and

$$\begin{aligned}
m_{\tilde{q}} &= \frac{1}{4}\left(m_{\tilde{u}_R} + m_{\tilde{u}_L} + m_{\tilde{d}_R} + m_{\tilde{d}_L}\right), \qquad (4.4)\\
m_{\tilde{\ell}} &= \min\left[m_{\tilde{e}_R}, m_{\tilde{e}_L}, m_{\tilde{\mu}_R}, m_{\tilde{\mu}_L}, m_{\tilde{\tau}_R}, m_{\tilde{\tau}_L}\right].
\end{aligned}$$

Because the first-generation squarks have the largest production cross sections at the LHC, and because typical CMSSM mass hierarchies permit third-generation squarks to decay to lighter third-generation squarks and a gauge-boson, the squark mass in our analysis is the average of such squarks [289]. The golden decay is dominated by the lightest slepton, regardless of the helicity of its superpartner, because the pertinent neutralino interaction could be bino, wino or higgsino.

From measurements of these four endpoints, an experiment could extract the masses of the four sparticles. These measurements would, however, be correlated, and, in an experiment with a finite integrated luminosity, have substantial statistical errors from the limited numbers of events populating the distributions. This was considered by calculating a covariance matrix describing the sampling distribution; from repeated Monte-Carlo pseudo-experiments in the ATLAS SU3 scenario with $1\,\text{fb}^{-1}$, Ref. [288] calculated the distributions of the extracted masses, and their covariances. This procedure incorporates statistical errors, but, because the systematic nuisance parameters were fixed in the Monte-Carlo, excludes systematic errors, which are negligible [209].

The covariance matrix, calculated in the basis

$$M = (m_\chi, m_{\chi_2^0} - m_\chi, m_{\tilde{q}} - m_\chi, m_{\tilde{\ell}} - m_\chi), \tag{4.5}$$

in units GeV^{-2} is [209]

$$C = \begin{pmatrix} 3.72\times10^3 & 53.4 & 1.92\times10^3 & 1.075\times10^2 \\ \cdot & 3.6 & 29.0 & -1.3 \\ \cdot & \cdot & 29.0 & -1.3 \\ \cdot & \cdot & \cdot & 14.1 \end{pmatrix}. \tag{4.6}$$

We approximated this sampling distribution to a multivariate Gaussian, and this sampling distribution to our likelihood function. This assumed that, in the vicinity of the ATLAS SU3 parameter point, the covariance matrix was approximately constant, and that, further away from the ATLAS SU3 parameter point, the covariance matrix is moot, because the likelihood is negligible. Our multivariate Gaussian likelihood function was

$$\mathcal{L}_{\text{ATLAS SU3}} = \exp\left[-\frac{1}{2}(M - M_{\text{ATLAS SU3}})C^{-1}(M - M_{\text{ATLAS SU3}})^T\right], \tag{4.7}$$

where $M_{\text{ATLAS SU3}}$ is the "Asimov" data set — M evaluated in the ATLAS SU3 benchmark scenario, and M is a function of the model's parameters.

4.2.2 Scans

In this scenario, we investigated whether, from golden decay measurements, one would be able to reconstruct the Lagrangian parameters of 5 models (CMSSM, NUG, NUHM, p12MSSM and p14MSSM models defined in Sec. 1.5.3), and whether, with Bayesian evidence, a model would be preferred by the pseudo-data. A similar analysis was conducted in gauge and anomaly mediated SUSY breaking models in Ref. [291]. To understand the impact that the WMAP-5 [292] experiment would have in our scenario, we added a likelihood describing a hypothetical measurement of dark matter abundance from WMAP,

$$\mathcal{L}_{\text{ATLAS SU3}} = \exp\left[-\frac{\left(\Omega h^2_{\text{ATLAS SU3}} - \Omega h^2\right)^2}{2((0.1\Omega h^2)^2 + \sigma^2)}\right], \tag{4.8}$$

that is, with a mean $\Omega h^2_{\text{ATLAS SU3}} = 0.2332$, rather than its measured value, an error $\sigma = 0.0062$, the true WMAP-5 experimental error [292], and a 10% theoretical error in the Ωh^2 calculation. $\Omega h^2_{\text{ATLAS SU3}}$ exceeded and was in statistically significant disagreement with the WMAP-5's contemporary measurement, $\Omega h^2 = 0.1099 \pm 0.0062$ [292]. ATLAS SU3, however, represented points with the correct relic density. One could, for example, slightly increase the neutralino's higgsino component by increasing $\tan\beta$, enhancing neutralino annihilation via Fig. 3.3.1b and suppressing the relic density.

Whilst ATLAS SU3 is a CMSSM benchmark point, it is equivalent to points within our five models, in that such points result in identical sparticle mass spectra. In the NUHM, ATLAS SU3 is as it was in the CMSSM but with $m_{H_d} = m_{H_u} = m_0$, in the NUG, $M_1 = M_2 = M_3 = m_{1/2}$, and in the pMSSM models, ATLAS SU3 soft-breaking parameters were ran from the GUT to the SUSY scale with the RG, and soft-breaking masses that were degenerate at the SUSY scale in our pMSSM models were averaged.

To understand our priors, we calculated the models' posterior densities with logarithmic and linear priors for soft-breaking masses, and with only the physicality conditions in Sec. 3.1. As discussed in Sec. 2.5, numerically, the physicality conditions are included in our likelihood, rather than our priors, and induce nontrivial correlations amongst our model's parameters. The posterior density with only physicality conditions reflects the *de facto* priors; that is, the priors including physicality conditions. Because our pMSSM models have many parameters, posterior density is prior dependent, and to understand the posterior density we must understand our priors. Table B.2 in Appendix B shows the priors for the five models. Our priors covered a low-mass $\lesssim 1$ TeV region — covering larger soft-breaking masses would be redundant, because in our scenario ATLAS discovered $\ll 1$ TeV sparticles — and nuisance parameters within their 3σ experimental intervals.

In summary, we find posterior densities for five models (CMSSM, NUG, NUHM, p12MSSM and p14MSSM) with three likelihoods

1. Physicality conditions only;
2. Physicality conditions and ATLAS SU3 golden decay;
3. Physicality conditions, ATLAS SU3 golden decay and simulated WMAP-5 relic density,

and with two prior choices: logarithmic and linear priors for soft-breaking masses. Our likelihoods are listed in Appendix A.

4.2.3 CMSSM

Because it is the most economical of our five models, the CMSSM ought to be the easiest model in which to recover the ATLAS SU3 Lagrangian parameters. We consider credible regions for the planes $(m_0, m_{1/2})$ and $(A_0, \tan\beta)$ in Fig. 4.2.2 with logarithmic priors for soft-breaking masses. We show posterior mean and best-fit estimators for the reconstructed parameters, which should be compared with the ATLAS SU3 Lagrangian parameters.

Fig. 4.2.2a shows *de facto* priors for the CMSSM — the likelihood vetoes unphysical points, but is otherwise unity (case 1). By marginalisation, it is easiest to find physical points within the credible regions. The unphysical region in which the $\tilde{\tau}_1$ is the LSP is visible at $m_{1/2} \gg m_0$ on the $(m_{1/2}, m_0)$ plane. Larger $m_{1/2}$ is disfavoured, because its logarithmic prior is proportional to $1/m_{1/2}$. Larger m_0, however, is not disfavoured, despite its logarithmic prior, because larger m_0 insures sparticles are not tachyonic, regardless of substantial off-diagonal mass matrix elements. Very small m_0, $m_{1/2} \lesssim 50\,\text{GeV}$ is plagued by physicality problems, including tachyonic tau-sneutrinos. The tau-sneutrinos soft-breaking mass after RG running is smaller than its negative D-term contribution.

Larger A_0 is disfavoured, because it splits mass eigenvalues such that sparticles are tachyonic or such that $\tilde{\tau}_1$ is the LSP. The asymmetry in A_0 results from its β-function and from our choice of $\operatorname{sgn}\mu = 1$. The β-function is positive — $A_{t,b,\tau}(M_{\text{SUSY}})$ are less than A_0. The Higgs mixing parameter μ cancels large positive A_0 if $\operatorname{sgn}\mu = 1$, because the off-diagonal mass matrix elements are (Eq. 1.38):

$$X_t = a_t - \mu \cot\beta.$$

By these two facts, $|X_t|$ with positive A_0 is smaller than that with negative A_0. Because tachyonic sparticles occur if $|X_t|$ is large, positive A_0 is preferred. Physicality prefers $\tan\beta \lesssim 50$ and $\tan\beta \lesssim 10$ with extreme A_0 (Fig. 4.2.2a), so that the off-diagonal mass matrix elements are small.

We included a likelihood from ATLAS pseudo-measurements of sparticle masses (case 2) in Fig. 4.2.2b. We successfully reconstruct the ATLAS SU3 parameters for m_0 and $m_{1/2}$, i.e., our credible regions closely envelope the ATLAS SU3 point, though large values of m_0 are permitted. Our reconstruction of $\tan\beta$ and A_0 is significantly worse than that of m_0 and $m_{1/2}$. Our resolution of the sign of A_0 is ambiguous, and we fail to reconstruct its magnitude. Our best-fit point is inaccurate — it lies away from the ATLAS SU3 point. This is an artefact of our algorithm, nested sampling, which is tailored for Bayesian rather than frequentist statistics. Our 1σ and 2σ credible regions and our posterior means agree well with those published in Ref. [209].

Fig. 4.2.2c shows credible regions including a likelihood from a WMAP-5 relic density pseudo-measurement (case 3). With respect to case 2 (Fig. 4.2.2b), m_0 is significantly squeezed, with $m_0 \gtrsim 150\,\text{GeV}$ truncated — if sfermion exchange in Fig. 3.3.1d is to reduce the relic density, sfermions must be light. The movement of our best-fit point is a reflection of the Monte-Carlo nature of the algorithm. Adding the WMAP-5's pseudo-measurement did not significantly improve the reconstruction of the CMSSM parameters, except for m_0. The resolution of A_0 and $\tan\beta$ remains poor; sfermion exchange, unlike stau-coannihilation or the pseudoscalar Higgs resonance, does not require particle mass differences to be fine-tuned. WMAP-5's impact is less than that in Ref. [209], because our theoretical error in the Ωh^2 calculation was larger than that in Ref. [209].

4.2.4 NUHM

Compared with the CMSSM, the NUHM has two additional parameters, m_{H_u} and m_{H_d}. These soft-breaking Higgs masses are not in the formulae for the masses of the sparticles that are measured in our scenario, but, in conjunction with $m_{1/2}$ and $\tan\beta$, determine μ via electroweak symmetry breaking conditions, which features in formulae in the mass matrices' off-diagonal elements.

Fig. 4.2.3 shows credible regions for the NUHM in our three likelihood cases, in a similar fashion to that for the CMSSM in Fig. 4.2.2. Fig. 4.2.3a shows *de facto*

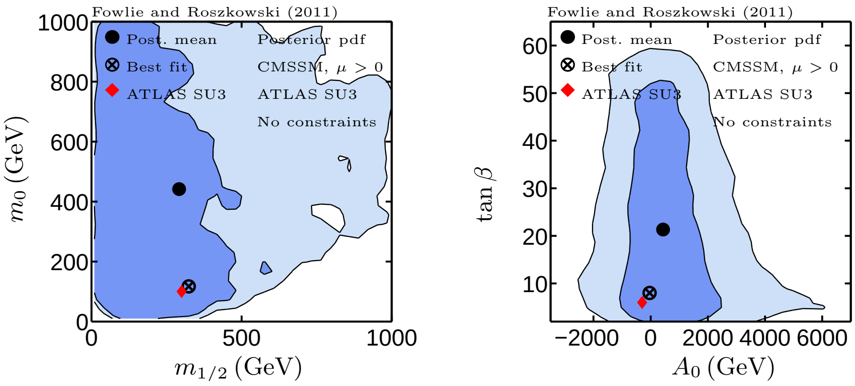

(a) *Likelihood from physicality conditions only (case 1).*

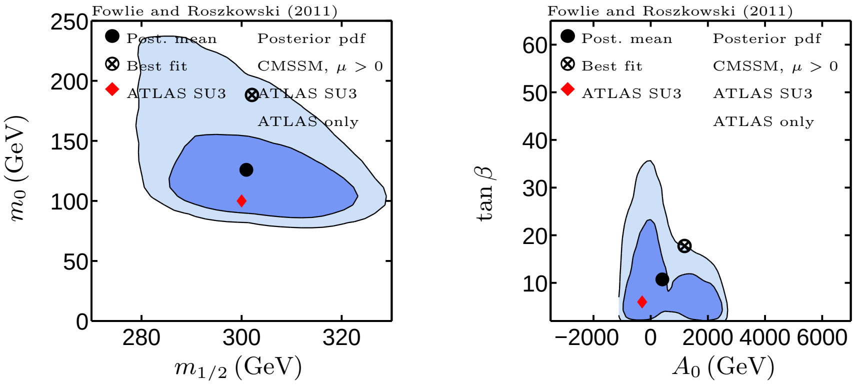

(b) *Likelihood from golden decay pseudo-measurements (case 2).*

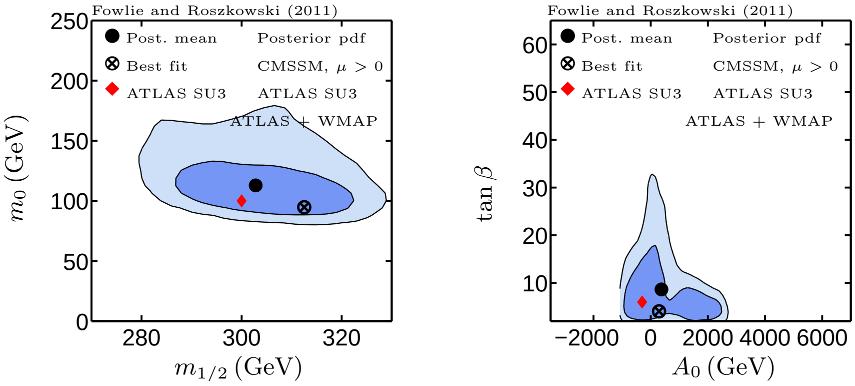

(c) *Likelihoods from golden decay and WMAP pseudo-measurements (case 3).*

Figure 4.2.2: *Bayesian* 1σ *(*2σ*) credible regions in dark (light) blue for the CMSSM with (a) physicality conditions only (case 1), (b) a likelihood from golden decay pseudo-measurements (case 2), and (c) likelihoods from golden decay and WMAP pseudo-measurements (case 3). Priors were logarithmic for* m_0 *and* $m_{1/2}$*, and linear otherwise. The red diamonds on the planes are the ATLAS SU3 values.*

priors for the NUHM (case 1). Similarly to the credible regions for the CMSSM in Fig. 4.2.2a, small $m_{1/2}$ and smaller $|A_0|$ are favoured. Unlike the CMSSM, however, small m_0 is disfavoured, because with large $m_{1/2}$, $\tilde{\tau}_1$ is the LSP, as in the CMSSM, and with small $m_{1/2}$, $\mu^2 < 0$.

The credible regions do not prefer particular $\tan\beta$ or m_{H_u}; however, smaller values of m_{H_d} are favoured, because its logarithmic prior is proportional to $1/m_{H_d}$. m_{H_u} is permitted to be as large as 1 TeV at 1σ, whereas $m_{H_d} \lesssim 0.5$ TeV at 1σ, because, via electroweak symmetry breaking conditions, it can reduce μ, preventing tachyonic sparticles and insuring that the neutralino is the LSP.

In Fig. 4.2.3b, the likelihood is from a golden decay measurement (case 2). A discernible difference between reconstruction in the NUHM and the CMSSM is that small $m_0 \lesssim 100$ GeV is permitted in the NUHM. Small $m_0 \lesssim 100$ GeV is compensated by large m_{H_u} and m_{H_d} via the RG equations. As in the CMSSM, $\tan\beta$ and A_0, are poorly reconstructed and the sign of A_0 is ambiguous. m_{H_d} and m_{H_u}, the NUHM's additional parameters, are poorly reconstructed. m_{H_d} is determined to within a narrower credible region than m_{H_u}, because its *de facto* prior was narrower than that for m_{H_u}.

The credible regions including a likelihood from a WMAP-5 pseudo-measurement of the relic density (case 3) are in Fig. 4.2.3c. As in the CMSSM in Fig. 4.2.2c, m_0 is squeezed, but its reconstruction remains poor in the NUHM. Reconstruction for $\tan\beta$, A_0, m_{H_d} and m_{H_u} is not improved relative to that in Fig. 4.2.3b, despite including WMAP-5.

In summary, parameter reconstruction in the NUHM for m_0 (with much lower values now allowed) is significantly poorer than it was in the CMSSM, though for $m_{1/2}$, A_0 and $\tan\beta$ the reconstruction is similar to that in the CMSSM. The reconstruction of m_{H_u} and m_{H_d}, the NUHM's additional parameters, is always poor, because the observables included in our likelihoods do not depend on the Higgs sector, within the relevant parameter space.

4.2.5 NUG

Compared with the CMSSM, the NUG has two additional parameters; the common gaugino mass is replaced by three independent gaugino soft-breaking masses for the bino (M_1), the wino (M_2) and the gluino (M_3). Unlike the NUHM's additional parameters, the NUG's additional gaugino masses heavily influence the

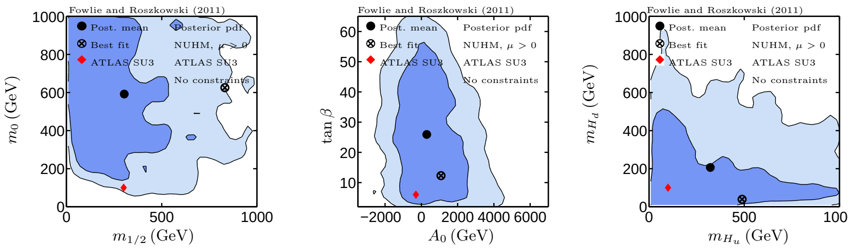

(a) *Likelihood from physicality conditions only (case 1).*

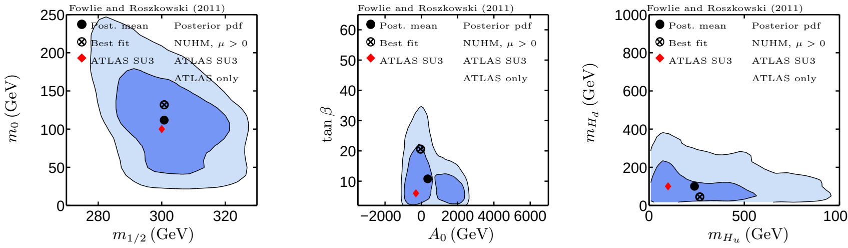

(b) *Likelihood from golden decay pseudo-measurements (case 2).*

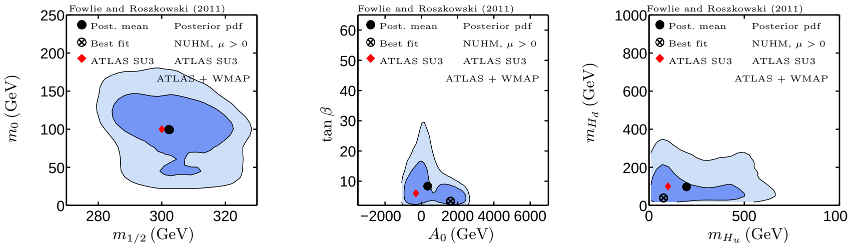

(c) *Likelihoods from golden decay and WMAP pseudo-measurements (case 3).*

Figure 4.2.3: *Bayesian credible regions for the NUHM, with a layout and legend identical to that in Fig. 4.2.2. Priors were logarithmic for soft-breaking masses and linear otherwise.*

masses of the sparticles that are measured in our scenario. Neutralino masses are proportional to M_1 and M_2, and sfermion masses are affected by gaugino masses via the RG.

Fig. 4.2.4 shows credible regions for the NUG in our three likelihood cases. The *de facto* priors (case 1) in Fig. 4.2.4a favour smaller M_1, M_2 and M_3, because of their logarithmic priors, and, for M_1 and M_2, to insure that χ is the LSP, which also disfavours the region in which M_1 and M_2 are both Large. As in the CMSSM, small absolute values of A_0 are favoured and there is no preference for $\tan\beta$. Large M_3 is disfavoured if m_0 is small. Large M_3 contributes in the RG to m_{H_u} and m_{H_d}, via gluino-stop two-loop diagrams, forcing μ large by the electroweak symmetry breaking condition in Eq. 1.66. With large μ, off-diagonal mass matrix elements are large, and sparticles are tachyonic or χ is not the LSP.

In Fig. 4.2.4b, the posterior includes a likelihood from golden decay pseudo-measurements (case 2). The reconstruction of m_0 in the NUG is significantly different from that in the CMSSM. Unlike in the CMSSM, small m_0 is permitted but large m_0 are forbidden.

The shape of the credible regions on the (M_3, m_0) plane is different from that on the $(m_{1/2}, m_0)$ plane in the CMSSM in Fig. 4.2.2b. The NUG favours small gaugino masses, because of their logarithmic priors, which, so that mass differences are compatible with the ATLAS SU3 predictions, requires light sleptons, and small m_0. As in the CMSSM, $\tan\beta$ is poorly reconstructed and the sign of A_0 is ambiguous.

An egregious prior effect is hampering reconstruction in the NUG. The NUG's priors favour small gaugino masses, and consequently light neutralinos. Because the neutralino is light, the squark and slepton must be light so that the mass differences are correct. This pushes the allowed m_0 values down, so that large values are not permitted and so that small values are favoured.

Fig. 4.2.4c shows the NUG's credible regions with the WMAP-5 pseudo-measurement (case 3). The reconstruction of M_1, M_2 and M_3 is greatly improved upon that without WMAP-5 in Fig. 4.2.4b. Whilst small m_0 was permitted in case 2, it is now forbidden. In fact, m_0 larger than that in case 2 is preferred. Surprisingly, the reconstruction of $\tan\beta$ in this case is worse than it was in case 2. WMAP-5 strengthens the likelihood, removing the prior effect that was hampering reconstruction. The credible regions are similar to those for the CMSSM in case 3 (Fig. 4.2.2c).

In summary, reconstruction in the NUG is poorer than it was in the CMSSM and the NUHM, and in no case were the credible regions independent of our choice of logarithmic or linear priors for the soft-breaking masses. The credible regions for M_1, M_2 and M_3 in the NUG were wide, whereas in the CMSSM, the credible regions for $m_{1/2}$ were tightly squeezed. Furthermore, small m_0, which was excluded in the CMSSM, was permitted in the NUG. The recovery of $\tan\beta$ and A_0 in the NUG was comparable to that in the CMSSM.

4.2.6 Direct detection

The lightest neutralino is the dark matter in our scenario; there is no additional subdominant component of the relic abundance. We consider direct detection of dark matter with the credible regions on the $\left(m_\chi, \sigma_p^{\mathrm{SI}}\right)$ planes of the CMSSM, NUHM, NUG and p12MSSM models (Fig. 4.2.5), with simulated golden decay and WMAP-5 likelihoods.

ATLAS SU3 is well recovered in the CMSSM (Fig. 4.2.5a), the NUHM (Fig. 4.2.5b) and the p12MSSM (Fig. 4.2.5d) but poorly recovered in the NUG (Fig. 4.2.5c). This results from the poor recovery of m_χ in the NUG, which resulted from its increased freedom. The recovery in the p12MSSM is worse than it is in the NUHM and CMSSM GUT models, but surprisingly, better than it is in the NUG. The credible regions for the p14MSSM (not shown) are similar to, though slightly larger than, those in the p12MSSM, and much smaller than those in the NUG.

4.2.7 Evidence

Fig. 4.2.6 compares reconstruction in the CMSSM, NUHM, NUG, p12MSSM and p14MSSM, by plotting the various Lagrangian parameters' posterior means and 2σ credible regions, with likelihoods from golden decay and WMAP-5 pseudo-measurements, and with logarithmic priors for soft-breaking masses, but linear priors otherwise.

The 2σ credible regions almost always include ATLAS SU3, and the posterior means are, in general, close to ATLAS SU3. The exception is that the 2σ credible region for $\tan\beta$ in the p12MSSM Fig. 4.2.6d omits ATLAS SU3, whilst in the p14MSSM it barely includes ATLAS SU3. Generally, $\tan\beta$ is overestimated with a wide credible region. A_0 is poorly reconstructed in all of the models, with credible regions spanning -1 TeV to 2 TeV.

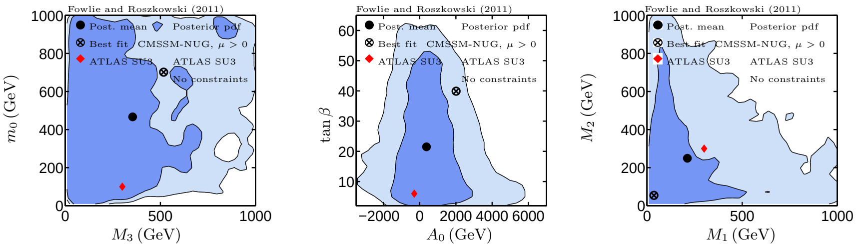

(a) *Likelihood from physicality conditions only (case 1).*

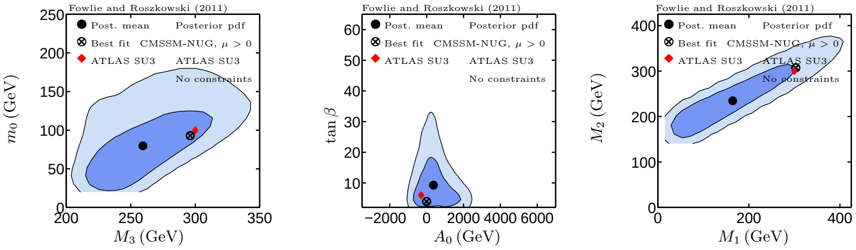

(b) *Likelihood from golden decay pseudo-measurements (case 2).*

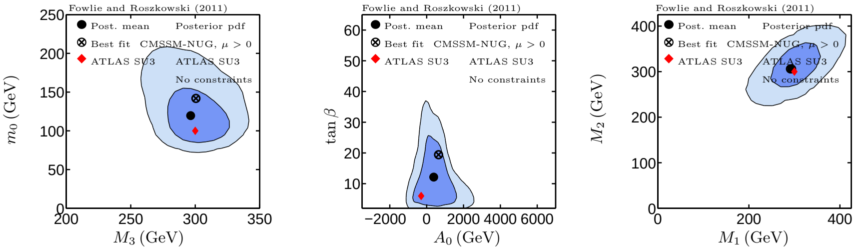

(c) *Likelihoods from golden decay and WMAP pseudo-measurements (case 3).*

Figure 4.2.4: *Bayesian credible regions for the NUG, with a layout and legend identical to that in Fig. 4.2.2. Priors were logarithmic for soft-breaking masses and linear otherwise.*

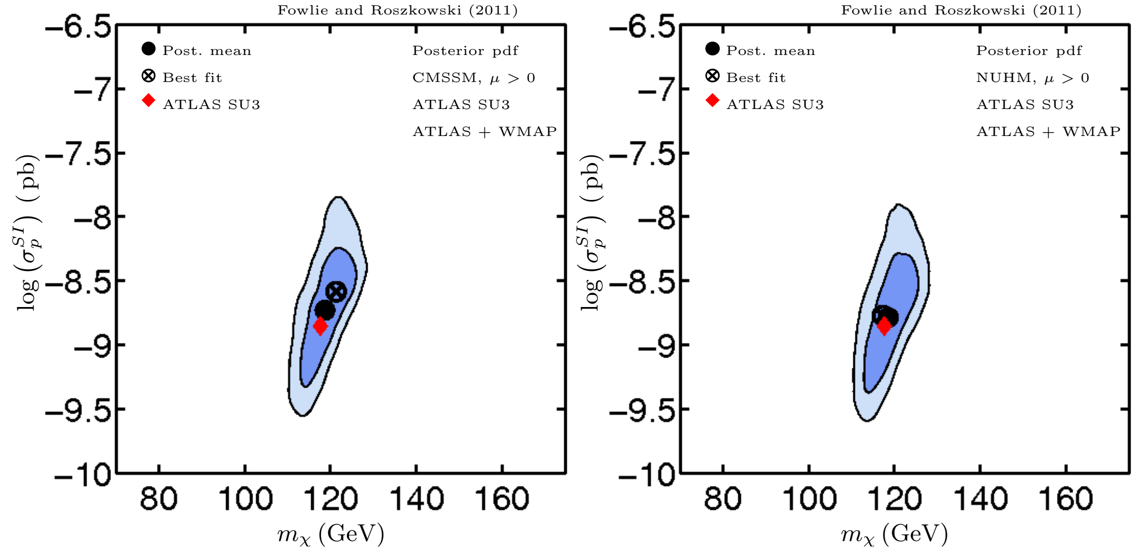

(a) *CMSSM.* **(b)** *NUHM.*

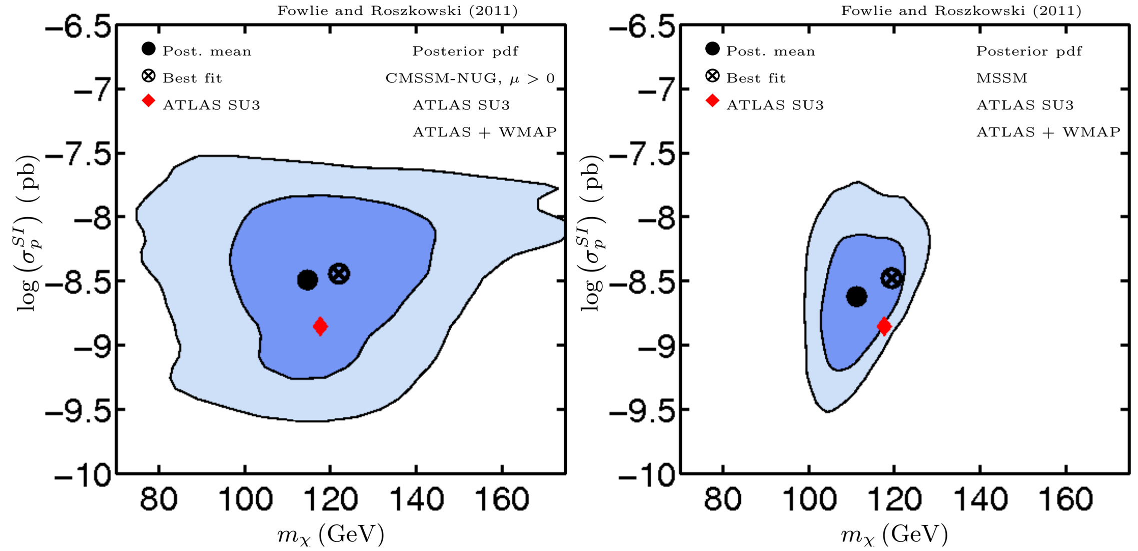

(c) *NUG.* **(d)** *MSSM.*

Figure 4.2.5: *Bayesian credible regions for the* $\left(m_\chi, \sigma_p^{SI}\right)$ *plane for (a) CMSSM, (b) NUG, (c) NUHM and (d) MSSM, with a likelihood from golden decay and WMAP pseudo-measurements (case 3). The legend is identical to that in Fig. 4.2.2. Priors were logarithmic for soft-breaking masses and linear otherwise.*

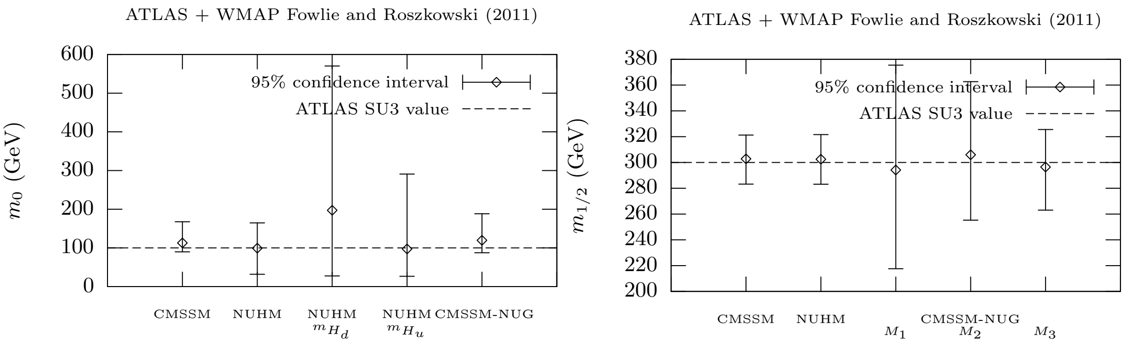

(a) *Common soft-breaking scalar mass in the CMSSM, NUG and NUHM, and the Higgs soft-breaking masses in the NUHM.*

(b) *Common soft-breaking gaugino mass in the CMSSM and NUHM, and the individual soft-breaking gaugino masses in the NUG.*

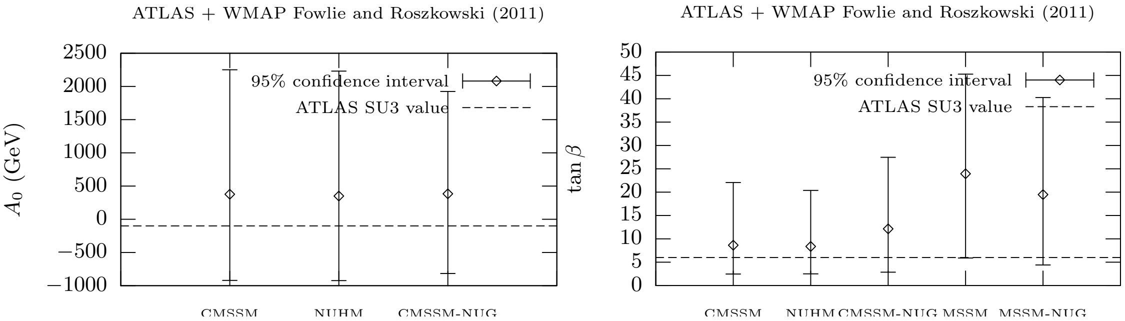

(c) *Common trilinear in the CMSSM, NUG and NUHM.*

(d) $\tan\beta$ *in the CMSSM, NUHM, NUG, p12MSSM and p14MSSM.*

Figure 4.2.6: *2σ Bayesian credible regions for Lagrangian parameters in the CMSSM, NUG, NUHM and, where possible, p12MSSM and p14MSSM, with a likelihood from golden decay and WMAP pseudo-measurements (case 3). Priors were logarithmic for soft-breaking masses and linear otherwise. ATLAS SU3 values are indicated by horizontal dashed lines and posterior means by unfilled diamonds.*

We investigated whether the Bayesian evidence (Sec. 2.4) decisively preferred a particular model, either the CMSSM, the NUHM or the NUG, in likelihood case 2 or case 3. Table 4.2.3 shows Bayes-factors (Eq. 2.17); ratios of the evidences in the CMSSM, NUHM and NUG.

By the Jeffreys' scale (Table 2.4.1), the difference in evidences for the CMSSM and the NUHM is "barely worth mentioning," though the NUHM is preferred. Because the likelihood functions were approximately independent of the NUHM's additional parameters, the evidence was approximately unaltered, because the prior pdfs are normalised to unity in Eq. 2.24. The evidence for the CMSSM and NUHM compared with the NUG is "very strong" in case 2 and "decisive" in case 3. The NUG is a complicated model in Fig. 2.4.1; its additional parameters broaden the CMSSM's predictions and dilute the evidence.

The Bayes-factors, however, were not entirely robust. We repeated our calculations, identically, except that we used linear priors, rather than logarithmic priors for the soft-breaking masses. A "substantial" preference for the CMSSM over the NUHM emerged in case 3, because prior probability for the NUHM's m_{H_u} and m_{H_d} parameters "piled-up" at large values. The NUG was still significantly disfavoured in all cases.

$\mathcal{Z}_{\text{Column}} / \mathcal{Z}_{\text{Row}}$	CMSSM	NUHM	NUG
ATLAS SU3 (case 2)			
CMSSM	1	1.06	0.02
NUHM	0.94	1	0.02
NUG	44.26	47.00	1
ATLAS SU3 + WMAP-5 (case 3)			
CMSSM	1	1.03	0.01
NUHM	0.97	1	0.01
NUG	167.34	172.43	1

Table 4.2.3: *Bayes-factors (Eq. 2.17), comparing the CMSSM, NUHM and NUG, with logarithmic priors for soft-breaking masses, and linear priors otherwise. The numbers are ratios of Bayesian evidences, with evidence of the model in the column heading in the numerator, and the evidence of the model in the row heading in the denominator. The ratios should be interpreted with the Jeffreys' scale (Table 2.4.1). A Bayes-factor of greater than one indicates that the model in the column heading is preferred over the model in the row heading.*

4.3 High-mass golden decay

The results in this section were published in Ref. [293].

Unfortunately, CMS excluded ATLAS SU3 from the null results of a multijet search in $35\,\text{pb}^{-1}$ of integrated luminosity [294]. Because the scenario in Sec. 4.2 was excluded, we considered a similar scenario with heavier soft-breaking masses, permitted by contemporary (Spring 2013) experimental results. Our first challenge was to find a CMSSM benchmark point that satisfied formidable experimental limits and with a mass hierarchy that permitted the golden decay.

We knew that if sleptons were to be lighter than the second neutralino, as is required for a golden decay, $m_{1/2} \gtrsim m_0$. Consequently, because we wanted to satisfy the neutralino relic density, we had to pick our benchmark point from the stau-coannihilation region. To find such a point, we used `Minuit` [295], which finds minima with iterative Newton-Raphson methods. We minimised a χ^2-function that vetoed points without the required mass hierarchy, and included contributions from PLANCK's relic density measurement [296], the CMS Higgs mass measurement [134], and the PDG top-quark pole mass [71].

In fact, we imposed stronger mass hierarchy requirements to avoid phase-space suppression of branching ratios in the golden decay and vetoed points for which $m_{\tilde{\tau}_1} - m_\chi < m_\tau$ to avoid long-lived staus that violate limits on long-lived charged particles [297]. By four-momentum conservation, for $\tilde{\tau}_1 \to \chi\tau$,

$$\begin{aligned} p^\mu_{\tilde{\tau}_1} &= p^\mu_\chi + p^\mu_\tau \\ m^2_{\tilde{\tau}_1} &> (m_\tau + m_\chi)^2 \\ m_{\tilde{\tau}_1} - m_\chi &> m_\tau . \end{aligned}$$

We fixed $m_{1/2} = 750\,\text{GeV}$, at that moment the lowest $m_{1/2}$ permitted by LHC searches [298], to maximise production cross sections, and minimised our χ^2-function with respect to m_0, A_0, $\tan\beta$ and M_t, resulting in the point in Table 4.3.1 with the mass spectrum in Table 4.3.2. We checked that our benchmark point was in agreement with experimental constraints, except δa_μ. We assume that the deviation from experiment in δa_μ is explained by other new physics or by uncertainties in the Standard Model prediction. The Higgs mass $m_h = 123.2\,\text{GeV}$ is reached by maximal stop-mixing, $X_t/M_{\text{SUSY}} = -2.1 \approx -\sqrt{6}$ and with a top pole mass,

$M_t = 175\,\text{GeV}$, heavier than that in PDG, $173.5 \pm 1\,\text{GeV}$ [71]. Unfortunately, our high-mass benchmark was later excluded by an ATLAS $0\ell + 2\text{-}6j + \not{E}_T$ search [299].

Having chosen a benchmark point, we simulated its golden decay at the LHC with `PYTHIA` [300] a Monte-Carlo event generator, with a number of events equivalent to $\sim 100\,\text{fb}^{-1}$ at $\sqrt{s} = 14\,\text{TeV}$. In the LHC's second phase, this integrated luminosity could be collected in $\sim$ 2 years [301], although the centre-of-mass energy is now planned to begin at $\sqrt{s} = 13\,\text{TeV}$. Our analysis was crude; we included no detector simulation (though we vetoed events in which decay products were outside the detector) and assumed that Standard Model backgrounds were negligible. We selected events with two opposite sign same flavour (OSSF) leptons, at least one jet, and sufficient missing energy, $\not{E}_T$.

From this Monte-Carlo, we binned events to obtain histograms (distributions) for the five invariant masses in Eq. 4.3. With `Root` [302], we fitted simple line-shapes, which described the expected endpoints' shapes, to the distributions with a least-squares method, with Poisson $\sqrt{N}$ statistical errors for the heights of each bin in the histogram. From the positions of the fitted line-shapes, we extracted the positions and statistical errors in the five endpoints in the distributions. Finally, with `Minuit`, we simultaneously fitted four sparticle masses to our five endpoints and statistical errors, by predicting the endpoints with Eq. 4.3 and minimising a multivariate Gaussian χ^2-function. We required five endpoints to break degenerate solutions for the four sparticle masses.

The covariance matrix resulting from this fit, defined $\sigma_{ij} = \sigma_{ji} = \text{E}(X_i)\text{E}(X_j) - \text{E}(X_i X_j)$ where $\text{E}(X)$ is the mean of X, was

$$\sigma = \begin{pmatrix} 1673.8 & 995.452 & 990.706 & 1507.58 \\ \cdot & 595.116 & 592.17 & 899.018 \\ \cdot & \cdot & 589.298 & 894.472 \\ \cdot & \cdot & \cdot & 1363.5 \end{pmatrix}, \tag{4.9}$$

in units $(\,\text{GeV})^2$ and in the basis $X_i = (\hat{m}_\chi, \hat{m}_{\tilde{\ell}}, \hat{m}_{\chi_2^0}, \hat{m}_{\tilde{q}})$. $m_{\tilde{\ell}}$ is the mass of the approximately degenerate first- and second-generation left-handed sleptons, which dominate the decay chain, and $m_{\tilde{q}}$ is the average of all squark masses, because the LHC cannot distinguish the squark in the decay chain. The non-zero off-diagonal covariance matrix elements indicate that the mass measurements are correlated. For insight, we diagonalise the inverse of this matrix to obtain the orthonormal

CMSSM parameter	Benchmark value	SM parameter	Benchmark value
$m_{1/2}$	750 GeV	M_t	175.0 GeV
m_0	228 GeV	$m_b(m_b)^{\overline{MS}}$	4.19 GeV
$\tan\beta$	8.82	α_s	0.1184
A_0	-2130 GeV	$1/\alpha_{\text{em}}(M_Z)^{\overline{MS}}$	127.916
$\text{sgn}\,\mu$	$+$		

Table 4.3.1: *High-mass benchmark CMSSM parameters with three significant figures and benchmark SM nuisance parameters. The SM nuisance parameters are the world-averages in [71], with the exception of M_t.*

Particle	Mass (GeV)						
χ	316.2	$\tilde{e}_L$	553.5	$\tilde{d}_L$	1546.2	h	123.2
χ_2^0	603.6	$\tilde{e}_R$	364.7	$\tilde{d}_R$	1479.1	H	1484.9
χ_3^0	1394.0	$\tilde{\nu}_e$	547.8	$\tilde{u}_L$	1546.2	A	1485.6
χ_4^0	1397.9	$\tilde{\tau}_1$	318.3	$\tilde{u}_R$	1485.2	$H^\pm$	1487.9
$\chi_1^\pm$	603.8	$\tilde{\tau}_2$	543.6	$\tilde{b}_1$	1277.9		
$\chi_2^\pm$	139.8	$\tilde{\nu}_\tau$	534.6	$\tilde{b}_2$	1463.6		
$\tilde{g}$	1675.1			$\tilde{t}_1$	821.5		
				$\tilde{t}_2$	1328.3		

Table 4.3.2: *The particle mass spectrum for our high-mass CMSSM benchmark, calculated with `SOFTSUSY` [72]. The first- and second-generation sparticles are approximately degenerate in mass.*

eigenvectors — the combinations of masses that can be independently measured, and their eigenvalues. The errors for each independent mass combination are

$$V\sigma^{-1}V^T \approx \mathrm{diag}\left[(0.2\,\mathrm{GeV})^{-2}, (1.6\,\mathrm{GeV})^{-2}, (1.9\,\mathrm{GeV})^{-2}, (64.9\,\mathrm{GeV})^{-2}\right], \quad (4.10)$$

and the eigenvectors are

$$\begin{aligned} V_{1i} &= 0.0 \cdot \hat{m}_\chi + 0.7 \cdot \hat{m}_{\tilde{\ell}} - 0.7 \cdot \hat{m}_{\chi_2^0} + 0.0 \cdot \hat{m}_{\tilde{q}} \approx \frac{1}{\sqrt{2}}(\hat{m}_{\tilde{\ell}} - \hat{m}_{\chi_2^0}) \quad (4.11)\\ V_{2i} &= 0.2 \cdot \hat{m}_\chi - 0.4 \cdot \hat{m}_{\tilde{\ell}} - 0.5 \cdot \hat{m}_{\chi_2^0} + 0.8 \cdot \hat{m}_{\tilde{q}}\\ V_{3i} &= -0.8 \cdot \hat{m}_\chi + 0.4 \cdot \hat{m}_{\tilde{\ell}} + 0.4 \cdot \hat{m}_{\chi_2^0} + 0.3 \cdot \hat{m}_{\tilde{q}}\\ V_{4i} &= 0.6 \cdot \hat{m}_\chi - 0.4 \cdot \hat{m}_{\tilde{\ell}} - 0.4 \cdot \hat{m}_{\chi_2^0} - 0.6 \cdot \hat{m}_{\tilde{q}}. \end{aligned}$$

It will later be of significance that the combination $(\hat{m}_{\tilde{\ell}} - \hat{m}_{\chi_2^0})$ has by far the smallest experimental uncertainty.

Similarly to Sec. 4.2, we investigated whether, in this scenario, one would be able to reconstruct CMSSM Lagrangian parameters from golden decay measurements. We investigated whether additional likelihoods for the Higgs mass and for the relic density would aid reconstruction. Our choices of priors was slightly moot; our likelihood ought to be informative enough to overcome different, sensible choices of prior. We choose linear priors for the CMSSM parameters, but expect our posterior to be independent of this choice. We choose fixed values for the Standard Model parameters, because their inclusion would be computationally expensive but have limited impact in our scenario. We fix these parameters to the weighted averages of their experimental values in PDG [71]. The prior ranges are listed in Table B.1 in Appendix B.

We consider three experiments: pseudo-measurements of sparticle masses via the golden decay, CMS measurements of the Higgs-like boson's mass [123], which we assume to be the lightest Higgs boson in the CMSSM, and the PLANCK measurement of the dark matter relic density [303], which we assume to be the relic density of CMSSM neutralinos. Our likelihood function for the golden decay, described in Sec. 4.2.1, is a multivariate Gaussian, reflecting the correlations in the sparticle mass measurements. Our likelihood functions for the Higgs mass and the relic density are Gaussians, though we include in quadrature theoretical errors in the CMSSM predictions of 3 GeV [121] and 10% [102,103], respectively:

$$\begin{aligned}\mathcal{L}_{\text{Higgs}} &= \exp\left[-\frac{(125.8\,\text{GeV} - m_h)^2}{2((0.6\,\text{GeV})^2 + (3\,\text{GeV})^2)}\right],\\ \mathcal{L}_{\text{PLANCK}} &= \exp\left[-\frac{(0.1186 - \Omega h^2)^2}{2(0.0031^2 + (0.1\Omega h^2)^2)}\right],\end{aligned} \tag{4.12}$$

where the means and standard deviations are those reported by CMS [123] and by PLANCK [303] respectively. Our benchmark point's Higgs mass of 123.2 GeV differs, within theory errors, from the CMS measurement [123] of 125.8 GeV. We, however, include in our likelihood the measured Higgs mass, rather than the benchmark. This is not a fault; it reflects the theoretical uncertainties in the Higgs mass and any biases that this might introduce.

In summary, we find CMSSM posterior density with three likelihoods;

1. Golden decay pseudo-measurements;
2. Golden decay pseudo-measurements and Higgs measurement;
3. Golden decay pseudo-measurements, Higgs measurement, and PLANCK relic density measurement;

and with linear priors for the CMSSM Lagrangian parameters. Our likelihoods are listed in Appendix A.

4.3.1 CMSSM $(m_0, m_{1/2})$ plane

Fig. 4.3.1 shows credible regions on the CMSSM's $(m_0, m_{1/2})$ plane, in all three likelihood cases, from left to right. Note the narrow scales shown; the parameters are reconstructed at 2σ to within $\lesssim$ 10%. Indeed, the reconstruction in case 1 is successful; a single, correct solution is recovered, which closely envelopes the benchmark point at 1σ. The major axis of the credible regions' oval shapes indicate positive correlation between m_0 and $m_{1/2}$. Recall that the $(\hat{m}_{\tilde{\ell}} - \hat{m}_{\chi_2^0})$ combination of masses was an approximate eigenvector of our inverse covariance matrix with a small 0.2 GeV uncertainty. If we apply the crude relations $m_{\tilde{\ell}} \approx \sqrt{m_0^2 + 0.6 m_{1/2}^2}$ and $m_{\chi_2^0} \approx 0.8 m_{1/2}$, we can understand that $(m_0 - m_{1/2})$ is well determined compared with $(m_0 + m_{1/2})$, and hence the positive correlation.* The major axis of the

---

* If we Taylor expand $\hat{m}_{\tilde{\ell}}$ with $m_{1/2} \gg m_0$, we find that $(\hat{m}_{\tilde{\ell}} - \hat{m}_{\chi_2^0}) \propto m_0^2/m_{1/2}$.

credible region is constrained, however, by the second and third eigenvectors in Eq. 4.11, which are dominated by m_χ and $m_{\tilde{q}}$ respectively and which have small experimental uncertainties. The fourth eigenvector in Eq. 4.11 is negligible, because it has an experimental error significantly larger than the other three eigenvectors.

The credible regions shrink successively as the data is added, though two orthogonal directions in the parameter space are visible. The major axis of the credible regions' oval shapes is only marginally shrunk by additional data, whereas the minor axis of the credible regions' oval shapes is squashed. In case 2, $\tan\beta$ is increased to saturate the tree-level bound on the Higgs mass (Eq. 1.37), which increases the split in the third-generation squark and slepton masses. In Fig. 4.3.1b, the lightest stau becomes lighter than the lightest neutralino in the left-hand side of the credible regions, which is forbidden, and hence this region is absent in Fig. 4.3.1b. Increases in Higgs mass from increasing $m_{1/2}$ and m_0 to increase stop masses are negligible. Indeed, varying $m_{1/2}$ by 50 GeV (10 GeV) of our benchmark point changes the Higgs mass by only 0.5 GeV (0.1 GeV), which is negligible compared with the 3 GeV theory error in m_h.

In case 3, when we add PLANCK's relic density measurement, we force $m_{\tilde{\tau}_1} \approx m_\chi$, so that staus and neutralinos coannihilate effectively and reduce the relic density to the PLANCK value. This further squashes the minor axis of the credible regions' oval shapes. This is rather unfortunate; PLANCK constrains the direction of parameter space that is already well constrained by the LHC golden decay, reducing the impact of this additional information.

The reconstruction, however, indicates some bias in the posterior mean as an estimator, in that as data is added, we approach the correct solution (the posterior mean is consistent), but that our distributions are not centred about the benchmark point. This is particularly apparent for m_0. If the posterior mean were an unbiased estimator, it would equal the benchmark point in all cases, and the credible regions would shrink around it as data was added.

4.3.2 CMSSM $(A_0, \tan\beta)$ plane

The CMSSM's $(A_0, \tan\beta)$ plane in Fig. 4.3.2 tells a similar story to that of the $(m_0, m_{1/2})$ plane in Fig. 4.3.1. The parameters are successfully reconstructed; our credible regions exhibit a single mode that closely envelopes the benchmark point. The unskewed shapes of the credible regions indicate little correlation between

$\tan\beta$ and A_0, though a slight positive correlation is visible. The reconstruction is, however, significantly worse than for $(m_0, m_{1/2})$, especially fractionally. The unified trilinear A_0 is initially, in case 1, determined to within $\sim 500\,\text{GeV}$ at 2σ. $\tan\beta$ is successfully constrained to $\tan\beta \lesssim 10$ at 2σ. Adding information from the Higgs mass, case 2 helps somewhat, with A_0 pushed slightly less negative and $\tan\beta$ pushed slightly higher, without exceeding $\tan\beta \lesssim 10$ at 2σ established in case 1. $\tan\beta$ is pushed higher to saturate the tree-level bound on the Higgs mass, $m_h \leq m_Z|\cos 2\beta|$. A_0 is pushed slightly less negative to tune stop-mixing so that $X_t/M_{\text{SUSY}} \approx -\sqrt{6}$, which maximises the Higgs mass.

Adding information from PLANCK dramatically improved parameter reconstruction on the CMSSM's $(A_0, \tan\beta)$ plane, especially for $\tan\beta$ which is determined to within ~ 1. The relic density is most sensitive in this region of the CMSSM to the stau mass, in contrast to the golden decay, which is sensitive to only the first- and second-generation sleptons. Because the τ-Yukawa coupling is significantly larger than the e- and μ-Yukawa couplings, the stau is sensitive to mixing between left- and right-handed states, which splits the stau mass eigenvalues. This mixing is proportional to $\tan\beta$, and hence $m_{\tilde{\tau}_1}$ can be driven smaller so that is approximately mass degenerate with m_χ by increasing $\tan\beta$. This enhances stau-coannihilation, thus decreasing the relic density to its measured PLANCK value. We again notice that the posterior mean is a biased estimator, in this case it is biased towards smaller values of $\tan\beta$.

4.3.3 Observables

Lastly, we investigate experimental quantities that would be of great interest in our scenario in which SUSY had been discovered. First, we consider dark matter direct detection experiments, which would attempt to verify that the neutralino was dark matter. We plot credible regions on the $\left(m_\chi, \sigma_p^{\text{SI}}\right)$ plane in Fig. 4.3.3. The plot shows little correlation between m_χ and σ_p^{SI}, and m_χ and σ_p^{SI} are both reasonably well-determined. σ_p^{SI} is determined at 2σ to within a decade. The resolution of σ_p^{SI} increases as data is added, especially PLANCK in case 3, but the resolution of m_χ is not much improved by the additional information. Nevertheless, the precision of the CMSSM direct detection predictions indicate that in our discovery scenario we would know that dark matter might be within reach of direct detection

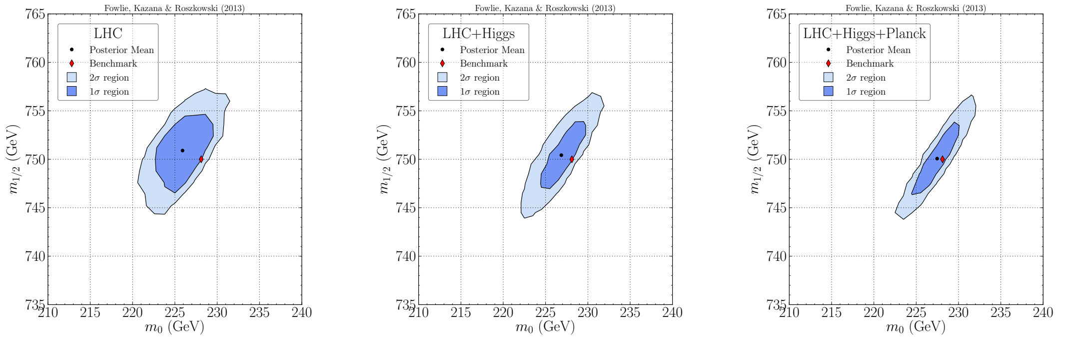

(a) *Likelihood from golden decay pseudo-measurements only (case 1).*

(b) *Likelihood from golden decay and Higgs measurements (case 2).*

(c) *Likelihoods from golden decay, Higgs and PLANCK relic density measurement (case 3).*

Figure 4.3.1: *Bayesian credible regions for the CMSSM's* $(m_0, m_{1/2})$ *plane in the high-mass benchmark scenario, adding the data one by one from left to right, with a legend identical to that in Fig. 4.2.2. Priors were logarithmic for soft-breaking masses and linear otherwise.*

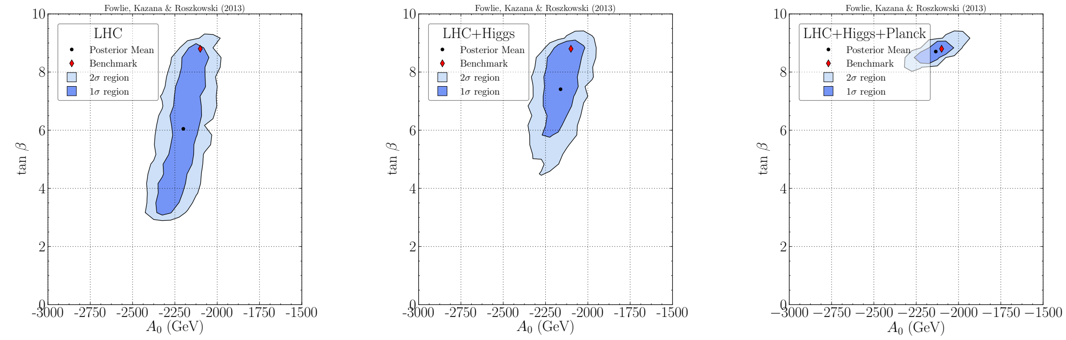

(a) *Likelihood from golden decay pseudo-measurements only (case 1).*

(b) *Likelihood from golden decay and Higgs measurements (case 2).*

(c) *Likelihoods from golden decay, Higgs and PLANCK relic density measurement (case 3).*

Figure 4.3.2: *Bayesian credible regions for the CMSSM's* $(A_0, \tan\beta)$ *plane in the high-mass benchmark scenario, adding the data one by one from left to right, with a legend identical to that in Fig. 4.2.2. Priors were logarithmic for soft-breaking masses and linear otherwise.*

experiments in the foreseeable future and be able to decide which experiments to build accordingly.

We consider the rare decay $\text{BR}\left(B_s \to \mu^+\mu^-\right)$, which, if it deviates from its Standard Model value, could indicate new physics. It would be an important measurement with which to understand new physics were it detected as in our discovery scenario. LHCb and CMS recently measured $\text{BR}\left(B_s \to \mu^+\mu^-\right)$ with statistical significance but limited precision; their combined result is $\text{BR}\left(B_s \to \mu^+\mu^-\right) = 2.9 \pm 0.7 \times 10^{-9}$ [304]. We found that one can make a precise CMSSM prediction for $\text{BR}\left(B_s \to \mu^+\mu^-\right)$ in case 1, with uncertainty $\sim 10^{-11}$ at 2σ. We investigated a parametric uncertainty from M_t by varying M_t within its experimental range and found that it results in an additional uncertainty of at least $\sim 10^{-10}$. Other parametric uncertainties from e.g., CKM matrix elements can be larger than but similar in magnitude to that from M_t [305]. Our posterior mean and mode for $\text{BR}\left(B_s \to \mu^+\mu^-\right)$ significantly differed from its nominal benchmark value, because of the unaccounted for experimental uncertainty in M_t. In summary, in our discovery scenario, the limiting factor for a precise CMSSM prediction for $\text{BR}\left(B_s \to \mu^+\mu^-\right)$ is not the sparticle mass spectrum, but parametric uncertainties in Standard Model nuisance parameters.

4.4 CMSSM with α_T 1 fb^{-1}

The results in this section were published in Ref. [211].

4.4.1 CMS α_T 35 pb^{-1}

In 2011, CMS published its first search for CMSSM squarks and gluinos in 35 pb^{-1} of integrated luminosity [294]. CMS discriminated Standard Model backgrounds from CMSSM signals or new physics signals with a sophisticated kinematic variable, α_T [306]. No statistically significant signal was observed, resulting in a 2σ exclusion contour on the CMSSM's $(m_0, m_{1/2})$ plane for fixed A_0 and $\tan\beta$ (Fig. 4.4.1b). We wanted to include a likelihood describing this experiment in the CMSSM's posterior density. Unfortunately, CMS published only a single 2σ exclusion contour, whereas we wanted a likelihood at each point in the CMSSM's parameter space. The likelihood function could not, *a priori*, be approximated from

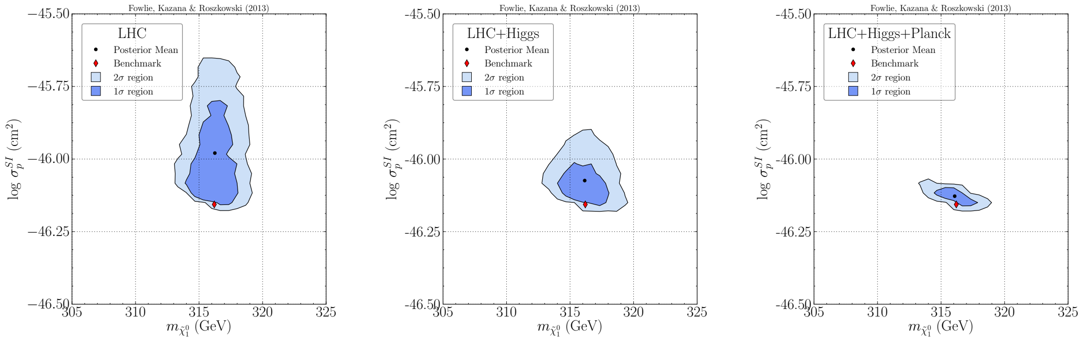

(a) *Likelihood from golden decay pseudo-measurements only (case 1).*

(b) *Likelihood from golden decay and Higgs measurements (case 2).*

(c) *Likelihoods from golden decay, Higgs and PLANCK relic density measurement (case 3).*

Figure 4.3.3: *Bayesian credible regions for the CMSSM's* $\left(m_\chi, \sigma_p^{SI}\right)$ *plane in the high-mass benchmark scenario, adding the data one by one from left to right, with a legend identical to that in Fig. 4.2.2. Priors were logarithmic for soft-breaking masses and linear otherwise.*

that single contour. CMS, in addition, published the numbers of observed and expected events in the search, and the details of their kinematic selections.

Inspired by Ref. [213], we attempted to replicate the CMS analysis, from the event level, and construct an approximate likelihood function. The α_T search strategy is based on dijet events, rather than a particular decay chain; it is an inclusive search. The α_T kinematic variable for a dijet event is

$$\alpha_T \equiv \frac{\min |\vec{p}_T|}{M_T}, \tag{4.13}$$

where we minimise over our two jets, $\vec{p}_T$ is the transverse momentum of a jet, and M_T is the transverse mass of the dijet system,

$$M_T^2 \equiv \left(\sum |\vec{p}_T|\right)^2 - \left(\sum \vec{p}_T\right)^2, \tag{4.14}$$

where we sum over our two jets. Quantities in our formulae are in the laboratory frame but are invariant under longitudinal boosts, unless indicated otherwise. In this dijet case, we find that

$$\alpha_T = \frac{1}{2}\sqrt{\frac{|\vec{p}_T|}{|\vec{q}_T|}}\frac{1}{|\sin\frac{\theta}{2}|}, \tag{4.15}$$

where the jet momenta are $\vec{p}_T$ and $\vec{q}_T$ with $|\vec{q}_T| > |\vec{p}_T|$ and θ is the angle between the dijets on the transverse plane.

We generalise this variable from a dijet to a multijet event, by clustering multijets into two pseudo-jets. The jets are divided into two pseudo-jets j_1 and j_2 in such a way that minimises

$$\Delta H_T = \left|\sum_{j_1} |\vec{p}_T| - \sum_{j_2} |\vec{p}_T|\right|. \tag{4.16}$$

Because of R-parity, sparticles should be produced in pairs, and we expect that a signal events to result in jets with a dijet topology.

The definition of transverse mass in our pseudo-dijet system identical to that in the genuine dijet system, except that we sum over all multijets. To rewrite Eq. 4.13, we introduce the variables

$$H_T \equiv \sum |\vec{p}_T|, \tag{4.17}$$

$$\not{H}_T \equiv |\sum \vec{p}_T|, \tag{4.18}$$

such that

$$\alpha_T = \frac{1 - \Delta H_T / H_T}{2\sqrt{1 - \not{H}_T^2 / H_T^2}}. \tag{4.19}$$

To understand the power of α_T, consider three cases

1. A perfectly measured QCD dijet event, in which dijets are back-to-back on the transverse plane. We measure that the jets have equal momentum, $|\vec{p}_T| = |\vec{q}_T|$, and that the jets are back-to-back on the transverse plane, $\theta = \pi$. With Eq. 4.15, we find
$$\alpha_T = \frac{1}{2}. \tag{4.20}$$
2. A mismeasured QCD dijet event. If we mismeasure transverse energy but correctly measure that the dijets are back-to-back on the transverse plane, we mismeasure that $|\vec{q}_T| = (1 + |\epsilon|)|\vec{p}_T|$ but correctly measure that $\theta = \pi$. With Eq. 4.15, we find
$$\alpha_T = \frac{1}{2}\frac{1}{\sqrt{1 + |\epsilon|}} < \frac{1}{2}. \tag{4.21}$$
3. A signal multijet event, with genuine missing momentum, in which the pseudo-dijets are not back-to-back on the transverse plane. Because we construct pseudo-dijets to minimise ΔH_T, the ratio of momenta in Eq. 4.15 ought to be ~ 1. This, in conjunction $\theta < \pi$, results in
$$\alpha_T > \frac{1}{2}. \tag{4.22}$$

We therefore select events with $\alpha_T > 0.55$ to discriminate against QCD backgrounds. In Eq. 4.15, if the ratio of momenta is unity, this corresponds to an angle between the dijets on the transverse plane of $\theta \lesssim 3\pi/4$. The α_T search is optimised if the squark production and decay has genuine dijet topology, so that $|\vec{p}_T| / |\vec{q}_T| \approx 1$ in Eq. 4.15. If gluinos are heavier than squarks, squark cascade decays via gluinos are forbidden and squarks decay dominantly to a neutralino and a jet, optimising α_T.

The $\not{H}_T$ variable is, however, vulnerable to "ignored" momentum; jets with $p_T < 50\,\text{GeV}$ are ignored. Background events might appear unbalanced and signal-like because of this "ignored" momentum. To minimise this vulnerability, we require

$$R = \frac{\not{H}_T}{\not{H}_T'} < 1.25, \tag{4.23}$$

where $\not{H}_T'$ is $\not{H}_T$ with a reduced transverse momentum veto. Only $\not{H}_T$ indicates whether the event was back-to-back — H_T and ΔH_T are sums of scalars, whereas $\not{H}_T$ is a sum of vectors. The kinematic variable R insures that θ in Eq. 4.15 is not mismeasured because of the $p_T < 50\,\text{GeV}$ veto.

To search for signal events which result from massive particles, and to increase the ratio of signal to background events, events must have $H_T > 350\,\text{GeV}$. The phase-space of the α_T search is (α_T, H_T). α_T describes the alignment of multijets clustered into two pseudo-jets; for new physics with genuine missing momentum, the pseudo-jets are not back-to-back. H_T describes the mass scale of the event; the mass scale of new physics ought to be higher than that of Standard Model backgrounds.

The Standard Model background consisted of a reducible QCD multijet background, with mismeasured $\not{E}_T$, and an irreducible electroweak background, with genuine $\not{E}_T$. The inclusive background was estimated in auxiliary counting experiments in "control regions" (regions in phase space in which no signal is expected). CMS estimated the number of background events in the signal region ($\alpha_T > 0.55$ and $H_T > 350\,\text{GeV}$) by extrapolating results from the control regions to the signal region. CMS observed $o = 13$ events in their signal region, which was consistent with their background estimate of $b = 9.3 \pm 0.9$.

The search was a counting experiment described by a Poisson, i.e., the events were independent and the likelihood of observing events was described by a Poisson distribution. The total number of expected events was a sum of expected contributions from supersymmetric processes and from Standard Model backgrounds. The expected number of SUSY events is a product of the efficiency (the fraction of events that survive the α_T selections, including detector efficiency), ϵ, the integrated luminosity, $\int L\,\mathrm{d}t$, and the total cross section for the production of supersymmetric particles at $\sqrt{s} = 7\,\text{TeV}$, σ,

$$s = \epsilon \times \sigma \times \int L\,\mathrm{d}t, \tag{4.24}$$

where ϵ and σ, and consequently s, are functions of $(m_0, m_{1/2})$.

The likelihood, $\mathcal{L}$ — the probability of observing o events given that we expected s supersymmetric events and b Standard Model background events — is a Poisson with mean $\lambda = s + b$,

$$\mathcal{L} = \frac{e^{-(s+b)} \, (s+b)^o}{o!}. \tag{4.25}$$

We neglected the error in the Standard Model background, though Eq. 4.25 includes statistical fluctuations in the background. If its experimental error was significant, Eq. 4.25 would be multiplied by a distribution describing the Standard Model background [307] and it would be included as a nuisance parameter. This is not the case for α_T with $35\,\text{pb}^{-1}$.

Calculating the likelihood at each trial point in the CMSSM's parameter space with this method is, however, impracticable, because simulating events with Monte-Carlo is time-consuming. The likelihood is, however, ultimately sensitive to only $(m_0, m_{1/2})$, because the masses of first- and second-generation squarks and the mass of the gluino, upon which α_T is based, are insensitive to $(A_0, \tan\beta)$. We calculated the likelihood on an 11×11 grid on the CMSSM's $(m_0, m_{1/2})$ plane from 0 to 500 GeV in 50 GeV steps, for fixed A_0 and $\tan\beta$. From this "likelihood map," we would interpolate or extrapolate a likelihood for any trial point in the CMSSM's parameter space, by constructing a quintic polynomial in the vicinity of the trial point [308].

We validated our likelihood map by comparing its 2σ $\Delta\chi^2$ contour (Eq. 2.11) with that published by CMS (Fig. 4.4.1). Our approximation and the official 2σ contour qualitatively agree, though differ by $\lesssim 100\,\text{GeV}$ in places. The contour is an approximate contour of squark mass in the CMSSM, though if squarks are too heavy to be produced, gluino production is important, which is suboptimal for α_T. Our approximation and the CMS 2σ contour differ because we did not include full detector simulation and we used leading order cross sections, rather than weighting our leading order with k-factors for the next-to-leading order. We also omitted systematics, e.g., parton distribution functions.

By the time we finished our likelihood map for α_T at $35\,\text{pb}^{-1}$, CMS published an α_T $1.1\,\text{fb}^{-1}$ exclusion on the CMSSM's $(m_0, m_{1/2})$ plane [309] that surpassed that with $35\,\text{pb}^{-1}$. This work, then, was a "warm-up" exercise. The methodology and expertise established would be utilised in later studies.

4.4.2 CMS α_T 1.1fb^{-1}

The CMS α_T 1.1 fb^{-1} null result [309] excluded $m_{1/2} \lesssim 600\,\text{GeV}$ for $m_0 \lesssim 500\,\text{GeV}$, and $m_{1/2} \lesssim 200\,\text{GeV}$ for $m_0 \gtrsim 500\,\text{GeV}$ in the CMSSM, for fixed $\tan\beta = 10$, $A_0 = 0$ (Fig. 4.4.2c). Light squarks and gluinos in the stau-coannihilation and focus-point regions that were favoured by previous experimental results, especially δa_μ, were excluded. It was imperative that we included this experiment in the CMSSM's posterior density.

We repeated our "warm-up" in Sec. 4.4.1, in which we constructed a likelihood from a similar α_T search with 35 pb^{-1}, for this new result. There were, however, complications; with 1.1 fb^{-1} of integrated luminosity, the expected number of events populated a distribution in H_T. To maximise the sensitivity of their experiment, CMS binned their events in eight H_T bins, and searched for SUSY in each bin.

We found selection efficiencies for each H_T bin on a uniform grid on the CMSSM's $(m_0, m_{1/2})$ plane. Our grids spanned $m_{1/2} = 50$-$1000\,\text{GeV}$ and $m_0 = 50$-$2000\,\text{GeV}$ in 50 GeV steps. The $325\,\text{GeV} < H_T < 375\,\text{GeV}$ "efficiency map" is shown in Fig. 4.4.2a. Our likelihood was now a product of Poisson distributions for each H_T bin — each bin was independent,

$$\mathcal{L} = \prod_i \frac{e^{-(s_i+b_i)}\,(s_i+b_i)^{o_i}}{o_i!}, \tag{4.26}$$

where $i = 1, \ldots, 8$ is the H_T bin and

$$s_i = \epsilon_i \times \sigma \times \int L\,\mathrm{d}t. \tag{4.27}$$

The cross section, σ, the efficiencies, ϵ_i, and, consequently, the likelihood, $\mathcal{L}$, were functions of $(m_0, m_{1/2})$.

We checked that, as expected, the likelihood was approximately independent of $(A_0, \tan\beta)$. We calculated a likelihood map on the $(m_0, m_{1/2})$ plane for $A_0 = 0$ and $\tan\beta = 10$ — this choice minimised the unphysical regions in the $(m_0, m_{1/2})$ plane. Our map spanned $m_{1/2} = 50$-$1000\,\text{GeV}$ and $m_0 = 50$-$2000\,\text{GeV}$ in a uniform grid with 50 GeV steps.

4.4.3 Scans

We found the posterior pdf for the CMSSM with the `MultiNest` algorithm, with five choices of likelihood function:

1. To validate our likelihood map and our computer codes, the α_T likelihood map and a likelihood from the experiments that constrain the Standard Model's nuisance parameters;
2. A likelihood function comprised of "non-LHC" experiments; all experiments excluding the α_T direct search and the XENON100 direct detection experiment, i.e., LEP and Tevatron sparticle and Higgs mass limits, experiments that constrain nuisance parameters, Ωh^2, $\sin^2\theta_{\text{eff}}$, M_W, δa_μ, $\text{BR}\,(b \to s\gamma)$, $\text{BR}\,(B_u \to \tau\nu)$, ΔM_{B_s} and $\text{BR}\,(B_s \to \mu^+\mu^-)$;
3. Likelihood from non-LHC experiments and our α_T likelihood map;
4. Likelihood from the XENON100 limit, non-LHC experiments and our α_T likelihood map;
5. Likelihood from the XENON100 limit, non-LHC experiments and our α_T likelihood map, but without a likelihood from δa_μ.

By adding XENON100 and α_T in steps, we would assess their impact. We repeated our calculations in case 4 for two choices of prior: linear and logarithmic priors for the soft-breaking masses, and linear priors for soft-breaking trilinear, $\tan\beta$, and nuisance parameters. Our priors are listed in Table B.3 in Appendix B and our likelihoods are listed in Appendix A.

Impact of α_T

With our preliminary likelihood function, case 1, in Fig. 4.4.2, we verified our approximation to the α_T likelihood. Our 2σ contour (Fig. 4.4.2b) was in superb agreement with the official CMS α_T $1.1\,\text{fb}^{-1}$ 2σ contour (Fig. 4.4.2c). This validated our α_T methodology.

Our case 2, with non-LHC likelihoods, elucidates the impact of the α_T search. In case 2 in Fig. 4.4.3a, the $(m_0, m_{1/2})$ plane has two discontiguous 1σ modes: a mode in the stau-coannihilation region at $m_0 \sim 100\,\text{GeV}$ and a mode in the h-resonance region at $m_0 \sim 1500\,\text{GeV}$. The 2σ mode at $m_0 \gtrsim 500\,\text{GeV}$, connected with the stau-coannihilation region, is the A-funnel region and the 2σ mode surrounding the h-resonance is the focus-point region. Because our posterior pdf on the $(m_0, m_{1/2})$ plane was bimodal, the posterior mean is between the two modes, outside of the 1σ credible region, though closer to the stau-coannihilation 1σ region. The best-fit point is in the stau-coannihilation region, in which δa_μ is poorly satisfied with loop contributions from light smuons.

The $(A_0, \tan\beta)$ plane (Fig. 4.4.3b) is similar to the $(m_0, m_{1/2})$ plane, in that it has two discontiguous 1σ modes. The mode at $\tan\beta \lesssim 30$ corresponds to the stau-coannihilation region, that at $\tan\beta \sim 30$ to the focus-point and h-resonance regions, and that at $\tan\beta \gtrsim 40$ to the A-funnel region. The credible regions on the $(m_0, m_{1/2})$ plane are determined by the dark matter annihilation mechanisms, as anticipated in Sec. 4.1.1. The behaviour on the $(A_0, \tan\beta)$ plane is, however, more complicated than that. The stau-coannihilation region is at $\tan\beta \lesssim 30$. Within the stau-coannihilation, this minimises destructive loop contributions from light stops to $\text{BR}\,(b \to s\gamma)$. The A-funnel region is at $\tan\beta \gtrsim 40$; large $\tan\beta$ decreases the pseudoscalar Higgs' mass so that $2m_\chi \sim m_A$. The h-resonance is insensitive to $\tan\beta$, though large $\tan\beta$ is preferred to maximise δa_μ. The focus point region occurs at fairly small μ, which occurs within our m_0 prior range if $\tan\beta$ is moderate. Because $\tan\beta$ is large, destructive loop contributions reduce $\text{BR}\,(b \to s\gamma)$ and it is smaller than its measurement in the A-funnel and focus-point regions.

The 1σ credible region spans $A_0 \gtrsim 0$. In the A-funnel, $A_0 > 0$ increases $\text{BR}\,(b \to s\gamma)$ via NLO chargino-stop contributions (Fig. 3.7.1c) proportional to A_t [310] and reduces m_A so that $m_A \simeq 2m_\chi$. In the h-resonance, $A_0 \sim 2\,\text{TeV}$ is favoured, because it increases $m_{\chi_1^\pm}$ so that it exceeds the LEP limit [311]. Furthermore, positive A_0 is favoured by physicality, especially if $\tan\beta \gtrsim 30$. Because the trilinear's RG equations are positive, positive A_0 at the GUT scale ran to the electroweak scale is smaller in magnitude than negative A_0 at the GUT scale ran to the electroweak scale. Positive A_0 seldom results in tachyonic scalars, even if $\tan\beta \gtrsim 30$.

Our case 3 includes α_T, and should be compared with case 2. As we expected from our likelihood map, α_T bites into the low-mass region of the CMSSM's $(m_0, m_{1/2})$ plane in Fig. 4.4.3c. Credible regions below the α_T 2σ contour in Fig. 4.4.3a disappear, and credible regions above the α_T 2σ contour are inflated, because the pdf must integrate to unity. The stau-coannihilation region increases from $m_{1/2} \gtrsim 300\,\text{GeV}$ to $m_{1/2} \gtrsim 600\,\text{GeV}$, and the A-funnel is inflated, especially from $m_0 \lesssim 1\,\text{TeV}$ to $m_0 \lesssim 1.5\,\text{TeV}$. The h-resonance region is eliminated by α_T. With heavier $m_{1/2}$, the resonance is impossible, because m_h increases logarithmically with $m_{1/2}$, whereas neutralino mass increases linearly. The focus-point region, however, remains, and is present at 1σ, rather than 2σ; however, so that $\mu \sim 0\,\text{GeV}$, m_0 is much heavier than before to compensate for the heavier $m_{1/2}$.

Case 3 for the $(A_0, \tan\beta)$ plane in Fig. 4.4.3d changes from case 2 in Fig. 4.4.3c because of correlations with $(m_0, m_{1/2})$, although our α_T likelihood map was independent of $(A_0, \tan\beta)$. The elimination of the h-funnel, which was insensitive to $\tan\beta$, simplifies the behaviour to two discontiguous 1σ modes. The small $\tan\beta$ mode is $\tan\beta \lesssim 20$, slightly smaller than before, because the h-resonance, with moderate $\tan\beta$, was excluded by α_T. The A-funnel is $\tan\beta \gtrsim 45$. The 2σ bridge between these modes is the focus-point region.

Impact of XENON100

In 2011, XENON100, a direct detection experiment, published a 90% exclusion contour the CMSSM's $\left(m_\chi, \sigma_p^{\text{SI}}\right)$ plane, which significantly improved previous limits from direct detection experiments [105]. We include a likelihood from XENON100 in case 4. We find that its impact is weak, but noticeable in Fig. 4.4.4. The null results of XENON100's search favour smaller scattering cross sections.

At leading order, two diagrams contribute to σ_p^{SI}: s-channel squarks and a t-channel CP-even Higgs. With α_T, however, squarks are massive and an s-channel squark is off-resonance. σ_p^{SI} is dominated by t-channel heavy Higgs exchange (similar to Fig. 3.3.1c) with a higgsino-bino-scalar vertex.

In Fig. 4.4.4a, compared with Fig. 4.4.3c, the focus-point region is reduced from 1σ to 2σ and the A-funnel shrinks. In the focus-point region, because $\mu \lesssim M_1$, the neutralino's composition is a higgsino/bino mixture. The focus-point's higgsino-like neutralino enhances σ_p^{SI} and is disfavoured by XENON100. In the A-funnel region, the neutralino's composition must have higgsino component, so that the A-funnel in Fig. 3.3.1c is permitted, and the pseudoscalar must be light, so that $2m_\chi \simeq m_A$. The A-funnel's light pseudoscalar enhances σ_p^{SI}, as $m_H \approx m_A$, and is disfavoured by XENON100. In the stau-coannihilation region, because the neutralino is bino-like and the heavy Higgs is heavy, as $\tan\beta$ is small, σ_p^{SI} is small.

Fig. 4.4.5 shows credible regions on the $\left(m_\chi, \sigma_p^{\text{SI}}\right)$ plane, with and without XENON100, to elucidate its impact. Without XENON100, in Fig. 4.4.5a, we see two 1σ modes inside a 2σ mode at $200\,\text{GeV} \lesssim m_\chi \lesssim 400\,\text{GeV}$, and a 2σ mode at $m_\chi \sim 100\,\text{GeV}$. The two 1σ modes are the stau-coannihilation region, with the smallest σ_p^{SI}, and the A-funnel. That the A-funnel appears at 1σ, rather than at 2σ as on the $(m_0, m_{1/2})$ plane, is a "volume effect" — the A-funnel's 2σ mode on the $(m_0, m_{1/2})$ plane has a large volume. The 2σ mode at $m_\chi \sim 100\,\text{GeV}$, above the XENON100 exclusion contour, is the focus-point, with the largest σ_p^{SI}. Once XENON100 is included in our likelihood, Fig. 4.4.5b, the A-funnel is reduced to 2σ and the focus-point region shrinks, because of their large σ_p^{SI}. Because of the appreciable theoretical error in the σ_p^{SI} calculation, the XENON100 exclusion contour was "smeared" in our likelihood function. Consequently, the focus-point region is not eliminated, despite lying above the XENON100 exclusion contour, and the A-funnel is affected, despite lying below the XENON100 exclusion contour.

Our credible regions suggest that, if they are to detect CMSSM dark matter, direct detection experiments ought to be sensitive to $\sigma_p^{\text{SI}} \lesssim 10^{-10}\,\text{pb}$. Furthermore, the neutralino's mass is $250\,\text{GeV} \lesssim m_\chi \lesssim 343\,\text{GeV}$ at 1σ, somewhat heavier than that of the peak sensitivity in direct detection experiments.

Mass spectra

Because this case, case 4, includes likelihoods from all relevant experiments, we review one-dimensional credible regions for sparticle masses in Table 4.4.1. For comparison, we include case 2. The credible region for the Higgs mass is marginally heavier than it was without α_T and XENON100, and remains close to the LEP lower limit, $m_h \gtrsim 112.2$ at 2σ. α_T and XENON100 increase squark masses from $\gtrsim 250\,\text{GeV}$ to $\gtrsim 400\,\text{GeV}$ at 2σ and gaugino masses dramatically. The lightest neutralino is heavier than $100\,\text{GeV}$ at 2σ and the gluino is $\gtrsim 1\,\text{TeV}$ at 2σ.

Prior dependence

We calculated the posterior density with two choices of sensible, non-informative priors, to check whether our results were robust. Comparing the credible regions on the $(m_0, m_{1/2})$ plane with linear priors in Fig. 4.4.6a to that with logarithmic priors in Fig. 4.4.4a, we see prior dependence. The credible regions are, however, qualitatively similar. With linear priors, the posterior pdf has three 1σ modes, whereas with logarithmic priors, it has one 1σ mode. The second and third mode, present at large $(m_0, m_{1/2})$, are absent with logarithmic priors, because logarithmic priors penalise large $(m_0, m_{1/2})$ with their $1/x$ dependence. With linear priors, new 2σ modes in the pdf arise in the A-funnel and focus-point regions, which were 1σ modes with logarithmic priors. The stau-coannihilation mode is unaffected.

Although our priors for $(A_0, \tan\beta)$ were unchanged, the posterior pdf on the $(A_0, \tan\beta)$ plane might change, because $(m_0, m_{1/2})$ are marginalised. Comparing the credible regions on the $(A_0, \tan\beta)$ plane with linear priors in Fig. 4.4.6b to that with logarithmic priors in Fig. 4.4.4b, we see little prior dependence. With linear priors, the 2σ mode at $\tan\beta \sim 50$ is enlarged. This mode corresponds to large $(m_0, m_{1/2})$, in the A-funnel and focus-point regions. This enlargement, then, is a result of a "volume effect" (Sec. 2.5).

This moderate prior dependence implies that our likelihood is too weak to overcome differences between sensible choices of priors, in spite of new experimental constraints from α_T and XENON100. Our α_T likelihood function on the $(m_0, m_{1/2})$ plane, above its 2σ contour, was approximately constant, and could not overcome sensible choices of priors (see Fig. 2.5.1).

Best-fit point

Our best-fit point (Sec. 2.3), *de jure*, should be independent of our priors. Because we found it, however, with a Monte-Carlo algorithm, it is a random variable with an error and with a weak dependence on the scanning algorithm, rather than an exact solution. For example, with logarithmic priors, our algorithm explores the low-mass region of the CMSSM's $(m_0, m_{1/2})$ plane in greater detail than the high-mass region.

Table 4.4.2 shows the CMSSM's best-fit points with non-LHC likelihoods only and with α_T and XENON100 likelihoods. In each likelihood case, our best-fit point is in the CMSSM's stau-coannihilation region. Our best-fit point with non-LHC likelihoods is in good agreement with best-fit points reported previously in Ref. [204,205,207,227], which is encouraging. Our p-value, 42%, is close to that reported in Ref. [229], 37%.

With α_T and XENON100 likelihoods, our best-fit point shifts to heavier $m_{1/2} \simeq 600\,\text{GeV}$, but is otherwise similar to that with non-LHC likelihoods. In contrast, in Ref. [229], the best-fit point moves radically to large $m_0 \approx 450\,\text{GeV}$ and $m_{1/2} \approx 780\,\text{GeV}$, and large $\tan\beta \approx 40$. Large errors, however, are reported for all parameters. The χ^2-function, however, contains plateaus (regions in which it is flat as a function of the CMSSM's parameters). Because χ^2 similar to χ^2_{Min} can be found for parameters different from those at the best-fit point, the location of the best-fit point is somewhat unstable with respect to minor changes in e.g., computer codes.

To show which experimental constraints were satisfied at our best-fit point, Table 4.4.3 shows a breakdown of the main contributions to the χ^2 at our best-fit point with α_T and XENON100 likelihoods. Because our α_T likelihood is a product of eight likelihoods, one for each H_T bin, its χ^2 is distributed with 8 degrees of freedom, and is expected to be ~ 8. The δa_μ likelihood contributes significantly to the total χ^2; our best-fit point cannot explain δa_μ. At our best-fit point, the hint in δa_μ is a statistical fluctuation, rather than new physics.

Fig. 4.4.7 shows that δa_μ requires that increases in $m_{1/2}$, caused by α_T, are compensated by increases in $\tan\beta$, which increases δa_μ at one-loop by Eq. 3.59, but necessitates an increase in m_0, so that the $\tilde{\tau}_1$ is not the LSP. Our best-fit point is, however, pulled in a different direction by $\text{BR}\,(b \to s\gamma)$ (Fig. 4.4.8); to enhance $\text{BR}\,(b \to s\gamma)$, we require small $\tan\beta$ in the stau-coannihilation region. In the stau-coannihilation region, δa_μ and $\text{BR}\,(b \to s\gamma)$ are affected by sparticle loops and are proportional to $\tan\beta$ and $\sim (\text{SM} - \tan\beta)^2$, respectively. That both must be enhanced causes tension [206]. This tension is exacerbated by α_T, because it suppresses sparticle loop contributions.

In Table 4.4.2, including likelihoods from α_T and XENON100 inevitably increased the total χ^2, from 16.53 to 22.21. The p-value, however, depends on the distributions of the additional α_T and XENON100 contributions to the χ^2. The χ^2 from α_T, a product of eight independent Poissons with moderate means, is approximately distributed as a χ^2 with eight degrees of freedom. Our p-value, in fact, increased from 42% to 61%, though neither p-value is significant. It is difficult to compare our p-value with that in Ref. [229], because Ref. [229] included different likelihoods. In Ref. [229], the p-value diminished from 37% to 15%.

To aid comparison with the frequentist analysis in Ref. [229], in Fig. 4.4.4c and Fig. 4.4.4d we show profile likelihood confidence intervals on the $(m_0, m_{1/2})$ and $(A_0, \tan\beta)$ planes. Our confidence intervals are qualitatively similar to our credible regions. The confidence interval for the A-funnel, however, on the $(m_0, m_{1/2})$ plane extends to $m_0 \sim 2\,\text{TeV}$ and connects with the focus point region at 2σ and on the $(A_0, \tan\beta)$ omits $\tan\beta \gtrsim 30$ at 1σ. Indicating that, on the $(m_0, m_{1/2})$ plane, fine-tuned points with small χ^2 exist, but are disfavoured by marginalisation, and that for $\tan\beta \gtrsim 30$, points with moderate χ^2 exist, but are favoured by marginalisation.

The confidence intervals on the CMSSM's $(m_0, m_{1/2})$ plane in Ref. [229] are qualitatively different from our confidence intervals; they are larger and extend from the stau-coannihilation region to heavier $(m_0, m_{1/2})$, but exclude the focus-point region. We speculate that this difference is caused by our different implementations of α_T and our different calculations for $\text{BR}\left(b \to s\gamma\right)$.

Dropping δa_μ

We remarked in Sec. 4.4.3 that δa_μ could not be interpreted as new physics at our best-fit point, because δa_μ was much smaller than its measurement. We, therefore, repeated our analysis without the δa_μ likelihood. Our credible regions were qualitatively similar to those with a δa_μ likelihood, suggesting that δa_μ is not dominant in determining credible regions, though the best-fit point increased in $m_{1/2}$.

4.5 CMSSM with Razor 4.4 fb^{-1} and Higgs discovery

The results in this section were published in Ref. [218].

The experimental constraints in our CMSSM analysis in Sec. 4.4 were quickly usurped: direct searches at the LHC with $4.4\,\text{fb}^{-1}$ [312], rather than $1.1\,\text{fb}^{-1}$, excluded heavier $(m_0, m_{1/2})$ in the CMSSM; LHCb's search for $B_s \to \mu^+\mu^-$ excluded $\text{BR}\left(B_s \to \mu^+\mu^-\right)$ that was ~ 3 times less than that which was previously permitted; and ATLAS and CMS reported tantalising hints of a Standard Model-like Higgs boson. We repeated our Bayesian analysis of the CMSSM with likelihoods describing these new experimental constraints.

4.5.1 CMS Razor 4.4 fb^{-1}

The Razor method [313,314] is similar to α_T (Sec. 4.4.1), in that it is an inclusive search for supersymmetry with a complicated kinematic variable that discriminates against Standard Model backgrounds. Razor searches for events in which sparticles are produced in pairs, and each sparticle decays to missing momentum and jets; it

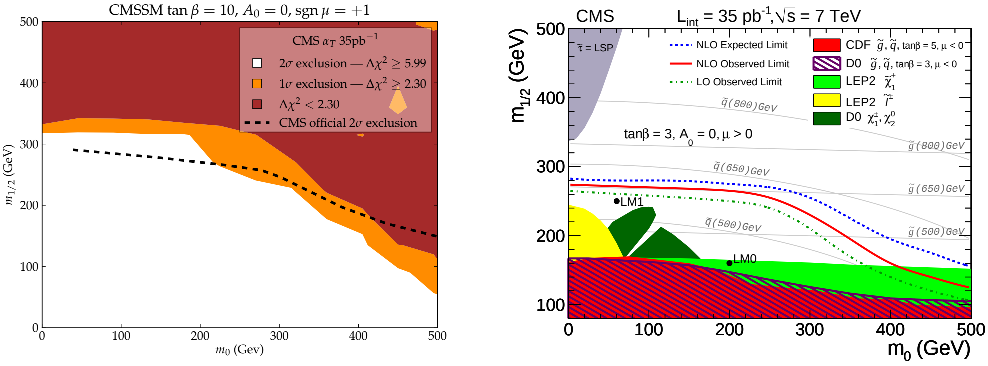

(a) *Approximation of CMS α_T 35 pb^{-1} confidence intervals for* tan $\beta = 10$ *and* $A_0 = 0$. *CMS excluded at* 2σ *below the black dashed line.*

(b) *CMS α_T 35 pb^{-1} result from Ref. [294].*

Figure 4.4.1: *Confidence intervals for CMS α_T with 35 pb^{-1}: Fig. 4.4.1a our approximation and Fig. 4.4.1b the official result.*

Mass	1σ	2σ	1σ	2σ
	Non-LHC (case 2)		Non-LHC + α_T + XENON100 (case 4)	
m_h	$(112.3, 116.5)$	$(110.1, 118.4)$	$(114.4, 117.8)$	$(112.2, 119.4)$
m_χ	$(56, 291)$	$(53, 356)$	$(250, 343)$	$(128, 390)$
$m_{\chi_1^\pm}$	$(110, 554)$	$(104, 676)$	$(475, 651)$	$(181, 738)$
$m_{\tilde{Q}_{1,2}}$	$(326, 808)$	$(254, 1172)$	$(434, 761)$	$(398, 1302)$
$m_{\tilde{g}}$	$(403, 1576)$	$(384, 1885)$	$(1380, 1825)$	$(879, 2043)$

Table 4.4.1: *One-dimensional credible regions, with an equal tail probability ordering rule (Eq. 2.13), for CMSSM sparticle masses with non-LHC (case 2) and non-LHC, α_T and XENON100 likelihoods (case 4), and with logarithmic priors. Masses are in GeV.*

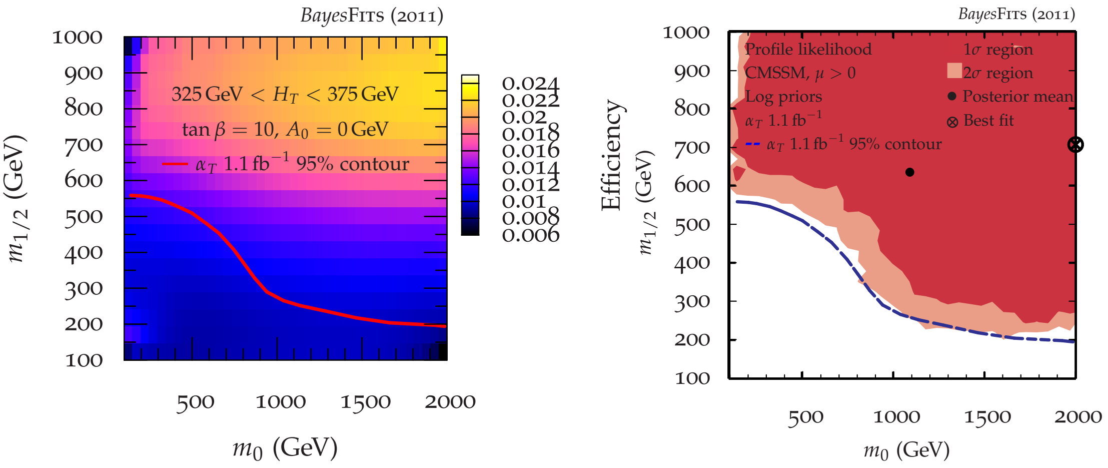

(a) *Approximation of the α_T selection efficiency for a dominant 325 GeV $< H_T <$ 375 GeV bin.*

(b) *Approximation to the α_T 1.1 fb^{-1} 1σ (2σ) confidence intervals in red (salmon). The blue dashed line is the official CMS 2σ exclusion contour.*

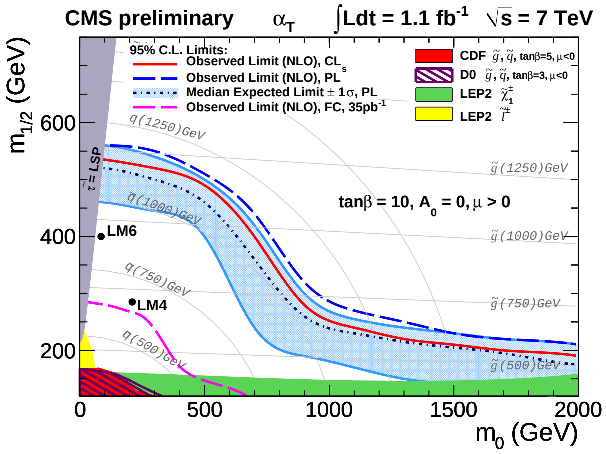

(c) *CMS α_T 1.1 fb^{-1} result from Ref. [309].*

Figure 4.4.2: *Approximations of CMS α_T 1.1 fb^{-1} (a) selection efficiency and (b) confidence intervals on the CMSSM$(m_0, m_{1/2})$ plane (case 1) for* tan β = 10 *and* $A_0 = 0$*, and (c) CMS's official α_T 1.1 fb^{-1} result.*

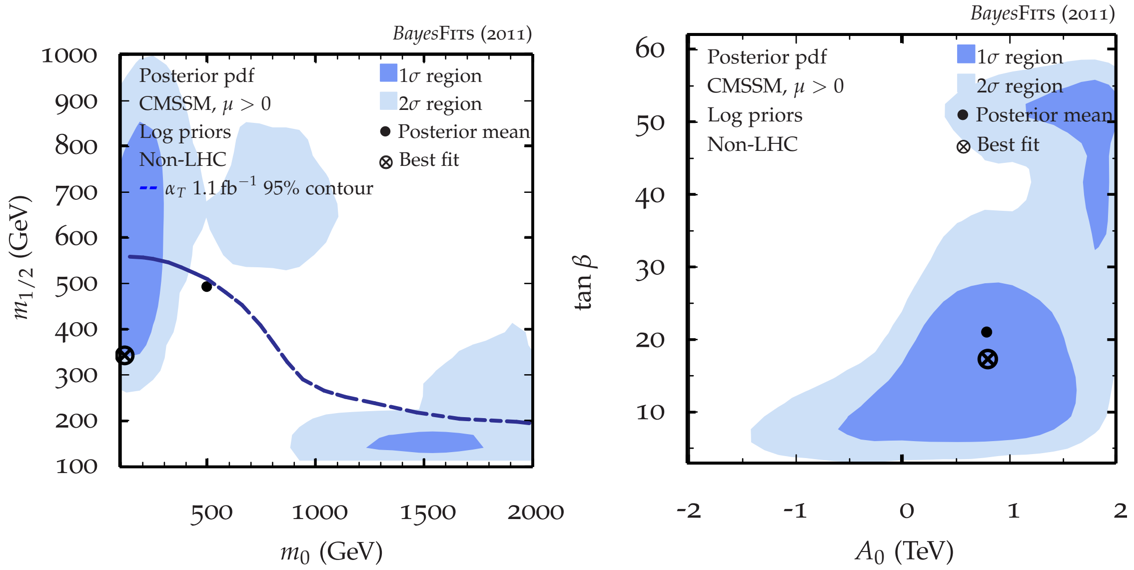

(a) *CMSSM$(m_0, m_{1/2})$ plane with non-LHC likelihoods (case 2). The α_T 2σ contour is marked, but our likelihood did no include α_T.*

(b) *CMSSM$(A_0, \tan\beta)$ plane with non-LHC likelihoods (case 2).*

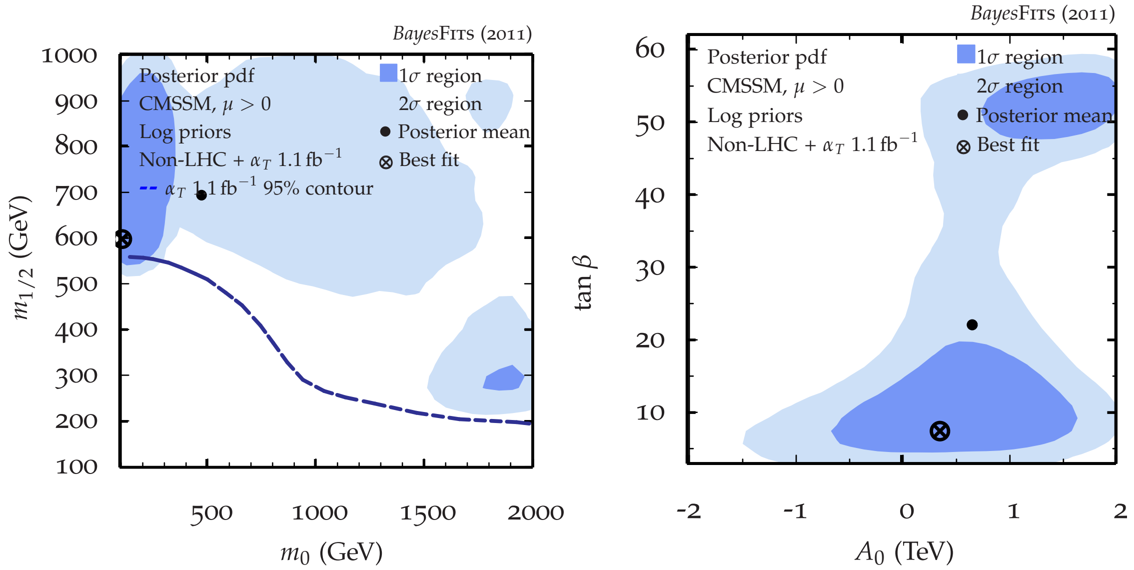

(c) *CMSSM$(m_0, m_{1/2})$ plane with non-LHC likelihoods and α_T (case 3).*

(d) *CMSSM$(A_0, \tan\beta)$ plane with non-LHC likelihoods and α_T (case 3).*

Figure 4.4.3: *Bayesian credible regions and confidence intervals for CMSSM parameters, with a likelihood from (a)-(b) non-LHC experiments (case 2) and (c)-(d) including α_T (case 3), and with logarithmic priors for soft-breaking masses and linear priors otherwise.*

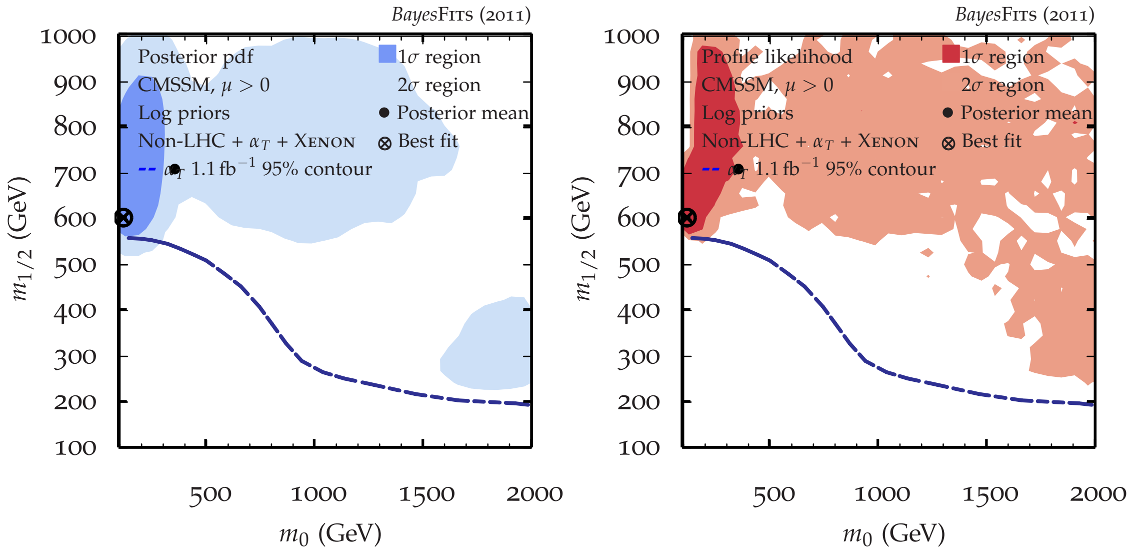

(a) *Credible regions for the CMSSM$(m_0, m_{1/2})$ plane.*

(b) *Confidence intervals for the CMSSM$(m_0, m_{1/2})$ plane.*

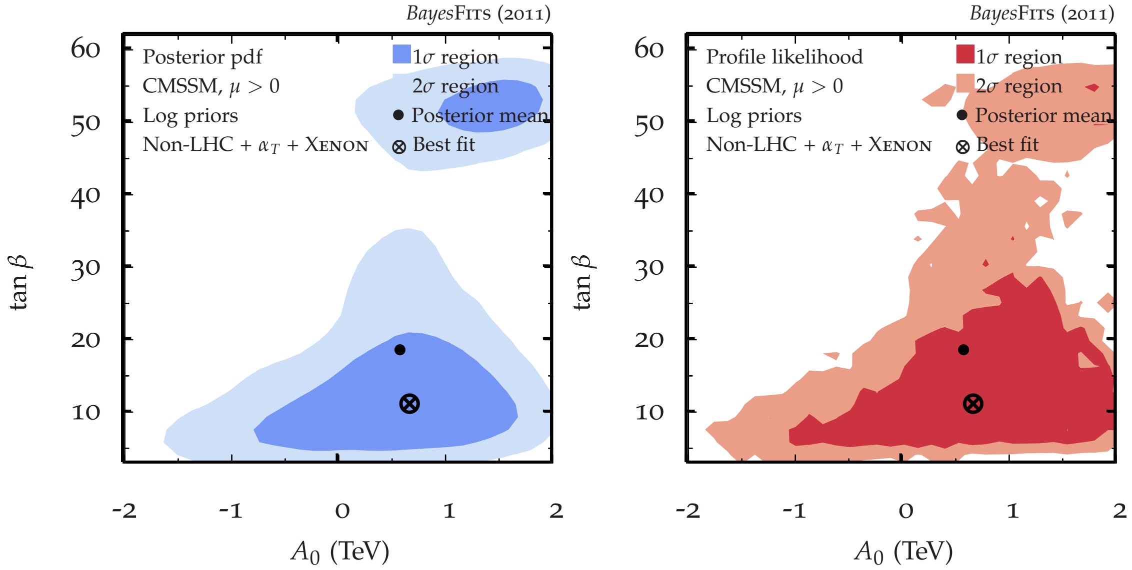

(c) *Credible regions for the CMSSM$(A_0, \tan\beta)$ plane.*

(d) *Confidence intervals for the CMSSM$(A_0, \tan\beta)$ plane.*

Figure 4.4.4: *Bayesian credible regions and confidence intervals for CMSSM parameters, with a likelihood from all experiments, including α_T and XENON100 (case 4), and with logarithmic priors for soft-breaking masses and linear priors otherwise.*

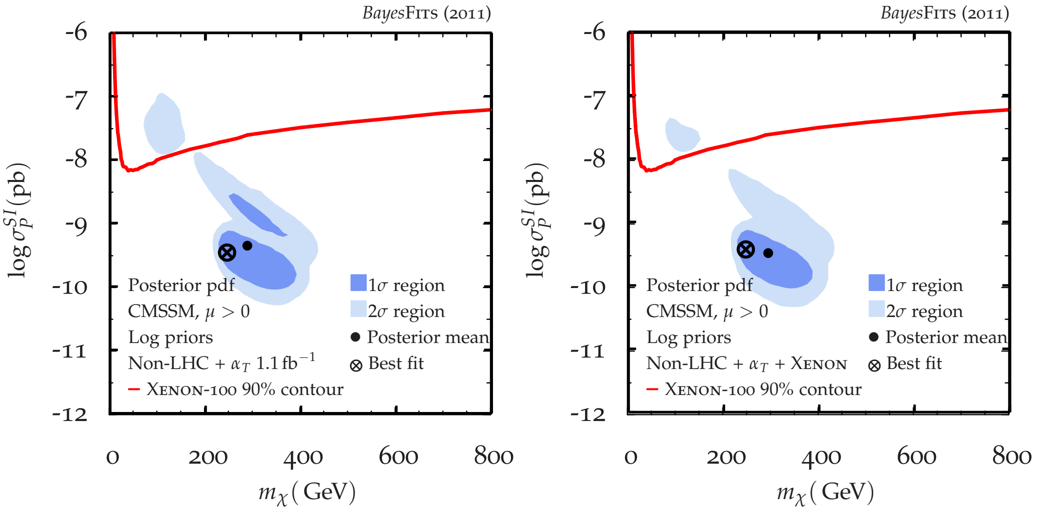

(a) *Likelihood from non-LHC experiments and* α_T *(case 3).*

(b) *Likelihood from non-LHC experiments,* α_T *and XENON100 (case 4).*

Figure 4.4.5: *Bayesian credible regions for direct detection of dark matter — the CMSSM's* $\left(m_\chi, \sigma_p^{SI}\right)$ *plane, with a likelihood from (a) non-LHC experiments and* α_T *(case 3), and (b) including XENON100 (case 4), and with logarithmic priors for soft-breaking masses and linear priors otherwise.*

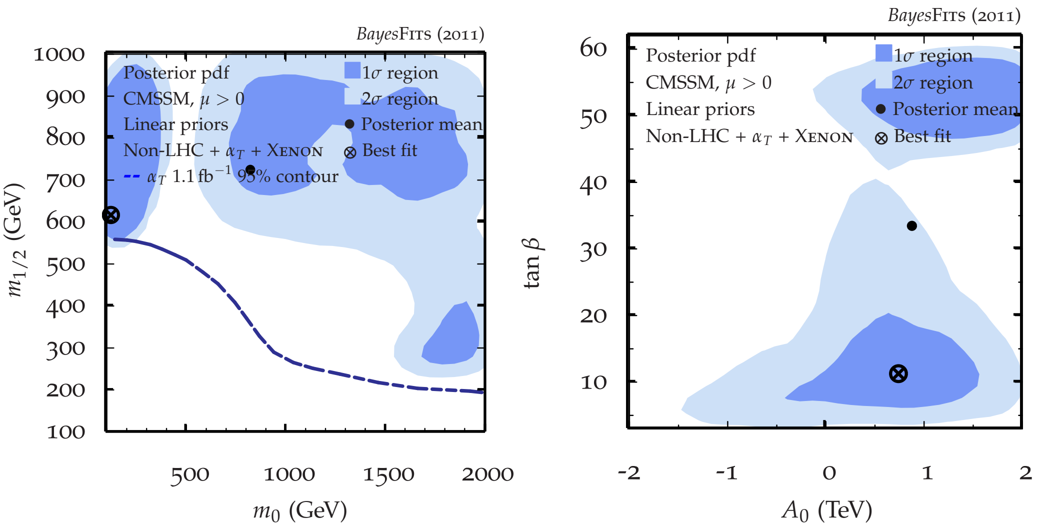

(a) $(m_0, m_{1/2})$ *plane.*

(b) $(A_0, \tan\beta)$ *plane.*

Figure 4.4.6: 1σ *(*2σ*) Bayesian credible regions in dark (light) blue for the CMSSM's (a)* $(m_0, m_{1/2})$ *plane and (b)* $(A_0, \tan\beta)$ *plane, with a likelihood from non-LHC experiments,* α_T*, and XENON100 (case 4), and with linear priors for all parameters.*

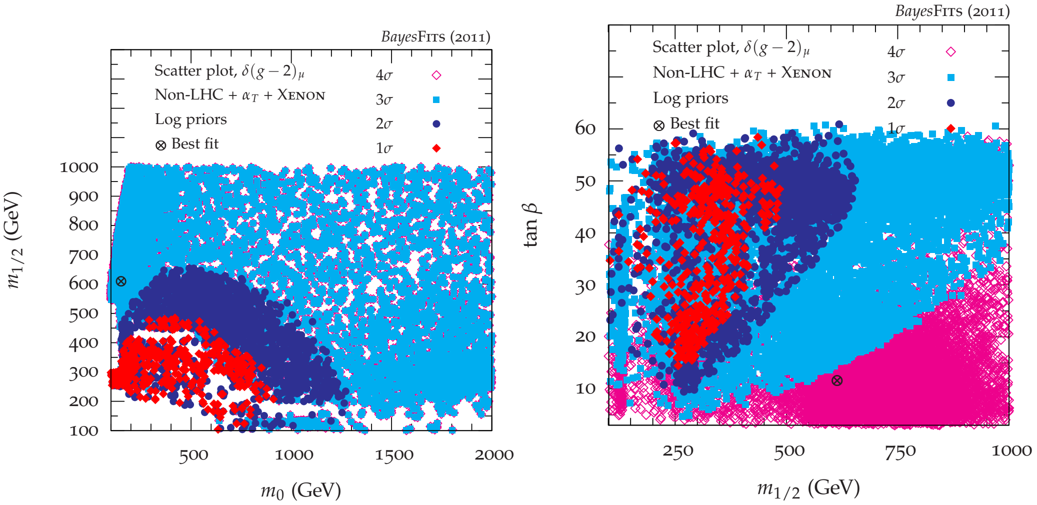

(a) $(m_0, m_{1/2})$ *plane.* **(b)** $(A_0, \tan\beta)$ *plane.*

Figure 4.4.7: *Points from nested sampling with appreciable posterior weight, coloured by their discrepancy with* δa_μ, *on the (a)* $(m_0, m_{1/2})$ *plane and (b)* $(m_{1/2}, \tan\beta)$ *plane.*

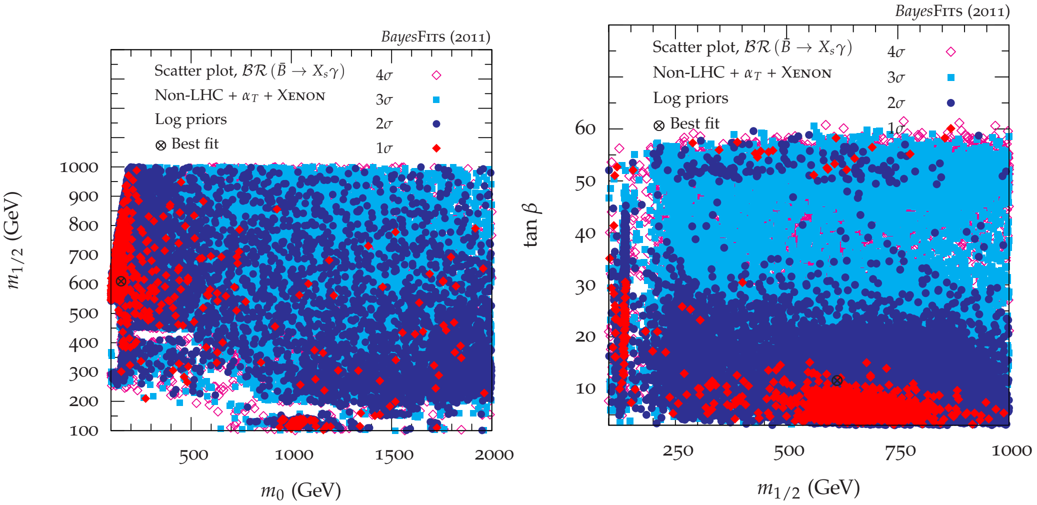

(a) $(m_0, m_{1/2})$ *plane.* **(b)** $(A_0, \tan\beta)$ *plane.*

Figure 4.4.8: *Points from nested sampling with appreciable posterior weight, coloured by their discrepancy with BR* $(b \to s\gamma)$, *on the (a)* $(m_0, m_{1/2})$ *plane and (b)* $(m_{1/2}, \tan\beta)$ *plane.*

	Non-LHC (case 2)		Non-LHC + α_T + XENON100 (case 4)	
Parameter	Best-fit	1σ credible region	Best-fit	1σ credible region
m_0	122	$(116, 1391)$	122	$(127, 741)$
$m_{1/2}$	343	$(142, 702)$	600	$(608, 820)$
A_0	806	$(236, 1514)$	677	$(82, 1283)$
$\tan\beta$	17	$(13, 22)$	11	$(9, 16)$
χ^2	16.53		22.21	
d.o.f.	16		25	
p-value	42%		61%	

Table 4.4.2: *Best-fit points and one-dimensional* 1σ *credible regions for the CMSSM's parameters, calculated with the equal tail probabilities ordering rule in Eq. 2.13, with two likelihood functions and with logarithmic priors. Masses are in GeV. Our best-fit parameters are, in some cases, excluded by our equal tail probability ordering rule, because the best-fitting parameters lie away from the median. We round to the nearest whole GeVor unit of* $\tan\beta$.

Constraint	χ^2
Ωh^2	0.01
m_h	1.32
$b \to s\gamma$	1.98
$\sin\theta_{\text{eff}}$	4.16
M_W	1.49
δa_μ	9.76
$B_u \to \tau\nu$	0.03
ΔM_{B_s}	0.25
α_T	3.42
Total	22.21
d.o.f.	25
p-value	61%

Table 4.4.3: *Breakdown of the main contributions to the* χ^2 *for our best-fit point in a scan with a likelihood from non-LHC experiments and the* α_T *and XENON100 limits (case 4) and with logarithmic priors. Note that all likelihoods are normalised to unity, including one for each* H_T *bin.*

is an inclusive search that includes simple and complicated decay chains. Observed jets are combined into two "megajets," similar to the pseudo-jets in α_T.

The Razor, however, utilises relativistic kinematics in a simple dijet topology, in which a pair of squarks is produced and each squark decays to a jet and a neutralino. We assume that the jets are massless. Unfortunately, from our laboratory frame, we cannot reconstruct the jet's four momentum in either the centre-of-momentum frame, in which the squarks are back-to-back, or in its parent squark's rest-frame. If we could reconstruct a jet's four momentum in its parent squark's rest frame, we could calculate the mass scale of the decay.

If we suppose that squarks are produced near their energy threshold, $\sqrt{s} \sim 2m_{\tilde{q}}$, the squarks are produced at rest. The centre-of-momentum frame and the squarks' rest frames coincide. In the squarks' rest-frames, the jets' momenta are equal in magnitude. We find a longitudinal boost such that squarks with arbitrary momentum four-vectors in the laboratory frame have equal energies in the boosted frame. This, then, is an approximate boost to the centre-of-momentum frame. We call this new frame the R-frame.

In a squark's rest-frame, we solve for the jet momenta and find

$$p_\mu = \frac{M_\Delta}{2}(1, \hat{u}), \tag{4.28}$$

where

$$M_\Delta \equiv \frac{m_{\tilde{q}}^2 - m_\chi^2}{m_{\tilde{q}}}. \tag{4.29}$$

Boosting from the squark's rest-frame back to the centre-of-momentum frame with $-\beta_{\text{CM}}$,

$$p_0^{\text{CM}} = \frac{M_\Delta}{2}\left[\gamma_{\text{CM}} + \gamma_{\text{CM}}\beta_{\text{CM}}\hat{u}\cdot\hat{v}\right]. \tag{4.30}$$

The dot-product between the jet's direction in the squark's rest frame and the boost direction to the centre-of-mass frame ought to average to zero, because the jet is emitted uniformly in angle.

In the laboratory frame, the jet momenta are,

$$p_\mu = (p_0, \vec{p}_T, p_z), \tag{4.31}$$

$$q_\mu = (q_0, \vec{q}_T, q_z). \tag{4.32}$$

Boosting from the laboratory frame to our as yet undefined R-frame with an arbitrary boost,

$$\Lambda^{\mu}{}_{\nu}p_{\mu} = p'_{\nu} = (\gamma p_0 - \gamma\beta p_z, \vec{p}_T, -\gamma\beta p_0 + \gamma p_z), \tag{4.33}$$

$$\Lambda^{\mu}{}_{\nu}q_{\mu} = q'_{\nu} = (\gamma q_0 - \gamma\beta q_z, \vec{q}_T, -\gamma\beta q_0 + \gamma q_z). \tag{4.34}$$

We require that the momenta are equal in magnitude — this defines our R-frame. Because the jets are massless, we require in fact that their energies are equal,

$$p'_0 = q'_0 \Rightarrow \tag{4.35}$$

$$\beta = \frac{q_0 - p_0}{q_z - p_z}. \tag{4.36}$$

Now, let us find the energy in this R-frame,

$$p'_0 = \sqrt{\frac{(q_z p_0 - p_z q_0)^2}{(q_z - p_z)^2 - (q_0 - p_0)^2}} \equiv \frac{M_R}{2}. \tag{4.37}$$

Because we assume that the centre-of-momentum frame and squarks' rest frames approximately coincide, we can approximate the energy in the centre-of-momentum frame (Eq. 4.30)

$$M_R \approx M_\Delta \gamma_{\text{CM}}. \tag{4.38}$$

In summary, with our manipulations and our approximation that squarks are produced near threshold, we approximated the Lorentz factor that boosts from the squark's rest frame to the centre-of-momentum frame times a function of sparticle masses.

We neglected, however, the angle between the jets — in a QCD background event, the jets ought to be back-to-back on the transverse plane. We include this information in a "transverse" variable,

$$M_T^2 = \frac{1}{2}\left[|\vec{\not{E}}_T|(|p_T| + |q_T|) - \vec{\not{E}}_T \cdot (\vec{p}_T + \vec{q}_T)\right], \tag{4.39}$$

which contains "back-to-backness" information in its dot-product which includes $\vec{p}_T \cdot \vec{q}_T$. For a signal-like events, with $\theta \approx 0$ and $|p_T|, |q_T| \lesssim M_\Delta/2$, the transverse variable $M_T \lesssim M_\Delta$ — the distribution of M_T has an endpoint at M_Δ and approximates M_Δ. For QCD background events, $\theta \approx \pi$ and $M_T \approx 0$.

Finally, we construct the dimensionless Razor variable,

$$R \equiv \frac{M_T}{M_R}, \tag{4.40}$$

which approximates $1/\gamma_{\text{CM}}$. The Razor phase-space is (R, M_T). R estimates the "boostedness" of the event — the reciprocal of the Lorentz factor between the squark's rest frame and the centre-of-momentum frame. For a signal like event, squarks are produced at threshold, almost at rest, and $R \sim 1$. M_T estimates the "back-to-backness" of the event and the mass scale of the event. We expect, then, that Razor is more powerful than α_T, because it includes "boostedness," "back-to-backness" and mass scale, whereas α_T omits "boostedness."

With a methodology identical to that in Sec. 4.4, we found a "likelihood map" for the Razor $4.4\,\text{fb}^{-1}$ search on the CMSSM's $(m_0, m_{1/2})$ plane. To validate our "likelihood map," we checked that our 2σ PL contour agreed with CMS's published 2σ contour (Fig. 4.5.1) — the agreement was superb.

4.5.2 Higgs likelihood

We considered two Higgs scenarios (see Sec. 3.4.2):

"Pessimistic:" Neither CMS or ATLAS achieved a significant result. We considered only their 95% CL_s exclusions, and constructed a box-car likelihood function by combining their exclusions with a theoretical error in the Higgs mass, resulting in

$$\begin{aligned}\mathcal{L}_{\text{Pre-LHC}} &= p\left(\text{LHC}|m_h^{\text{Calc}}\right) \qquad (4.41)\\ &= \text{erf}\left(m_h^{\text{Calc}} - 117.5\,\text{GeV}/\sqrt{2}\tau\right) - \text{erf}\left(m_h^{\text{Calc}} - 118.5\,\text{GeV}/\sqrt{2}\tau\right) + \\ &\quad \text{erf}\left(m_h^{\text{Calc}} - 122.5\,\text{GeV}/\sqrt{2}\tau\right) - \text{erf}\left(m_h^{\text{Calc}} - 127.5\,\text{GeV}/\sqrt{2}\tau\right),\end{aligned}$$

which is in Fig. 3.4.6.

"Optimistic:" Results were consistent with a Standard Model Higgs boson, with an insignificant, but appreciable, discrepancy with the background hypothesis. We supposed that a discovery was "around the corner," and constructed a likelihood for a pseudo-measurement of $m_h = 125 \pm 2\,\text{GeV}$. The mean is that which was hinted by ATLAS and CMS. We combined this hypothetical measurement with a theory error in the Higgs mass calculation via Eq. 3.5. Our likelihood in this hypothetical scenario was approximately that which was later realised by the ATLAS and CMS experiments, and, as such, we identified this scenario and its results with reality;

$$\mathcal{L}_{\text{Post-LHC}} = p\left(\text{LHC}|m_h^{\text{Calc}}\right) = \exp\left[-\frac{\left(125\,\text{GeV} - m_h^{\text{Calc}}\right)^2}{2\left(\tau^2 + \sigma^2\right)}\right]. \tag{4.42}$$

Although we always included a likelihood for the Higgs mass, we omitted experimental measurements of its couplings in our analysis.

4.5.3 Scans

We calculated the posterior pdf for the CMSSM with three likelihood functions:

1. Likelihood describing all experiments, including δa_μ and our "pessimistic" Higgs likelihood;
2. Likelihood describing all experiments, including δa_μ and our "optimistic" Higgs likelihood;
3. Likelihood describing all experiments, excluding δa_μ and our "optimistic" Higgs likelihood;

All experiments refers to experiments that constrain nuisance parameters, Ωh^2, $\sin^2\theta_{\text{eff}}$, M_W, δa_μ, $\text{BR}\,(b \to s\gamma)$, $\text{BR}\,(B_u \to \tau\nu)$, ΔM_{B_s}, $\text{BR}\,(B_s \to \mu^+\mu^-)$ and Razor. Our priors were identical in each case; we chose logarithmic priors in Table B.4 in Appendix B. Unless stated otherwise, we chose $\mu > 0$. Our likelihoods are listed in Appendix A.

4.5.4 Results

"Pessimistic" Higgs likelihood

We first inspect the $(m_0, m_{1/2})$ plane in case 1 — with our "pessimistic" Higgs likelihood, Razor $4.4\,\text{fb}^{-1}$ and likelihoods describing all experiments — in Fig. 4.5.2a, which should be compared with our previous result in Fig. 4.4.4, which included LEP's limit on the Higgs mass and α_T $1\,\text{fb}^{-1}$. Our result is similar to Fig. 4.4.4, in that it contains three 2σ modes corresponding to the stau-coannihilation, A-funnel and focus-point mechanisms of dark matter annihilation. Masses, however, are heavier in each mode, the A-funnel is at 1σ rather than 2σ, and the best-fit point is in the A-funnel region rather than the stau-coannihilation region. δa_μ cannot be satisfied in any mode; it is always smaller than its measurement with typical $\chi^2 \gtrsim 10$.

The stau-coannihilation region is heavier than it was because of the strict limit from Razor $4.4\,\text{fb}^{-1}$. Unlike in Fig. 4.4.4, the stau-coannihilation region is disconnected from the A-funnel at 2σ. Surprisingly, however, the 2σ mode that is ostensibly exclusively the A-funnel contains points at $m_0 \lesssim 1\,\text{TeV}$ that annihilate dark matter via an A-funnel and stau-coannihilation. These points, however, have $\tan\beta \gtrsim 30$ which is typical of the A-funnel. Within the stau-coannihilation region, achieving a heavy Higgs mass is difficult, because stops are relatively light at $\sim 1\,\text{TeV}$. The best-fit point in the stau-coannihilation region is at $m_{1/2} \sim 850\,\text{GeV}$ and is inside the first permitted window in Higgs mass at $m_h \sim 118.5\,\text{GeV}$. The dominant contributions to χ^2_{Min}, other than δa_μ, are Higgs, $\sin^2\theta_{\text{eff}}$ and $B_u \to \tau\nu$.

The A-funnel has heavier $(m_0, m_{1/2})$ than in Fig. 4.4.4 and is above rather than adjacent to the stau-coannihilation region. It is, furthermore, at 1σ rather than at 2σ. That it has heavier $(m_0, m_{1/2})$ is caused by our "pessimistic" Higgs likelihood and by $B_s \to \mu^+\mu^-$. Because our Higgs likelihood is stronger than that from LEP, stops, and thus $(m_0, m_{1/2})$, must be heavier to achieve a heavier Higgs. The LHCb upper limit on $\text{BR}\,(B_s \to \mu^+\mu^-)$ is especially relevant in the A-funnel, because $\tan\beta \sim 50$ and m_A is tuned to be light (see Eq. 3.45). Consequently, the A-funnel is pushed to heavier m_A to suppress $\text{BR}\,(B_s \to \mu^+\mu^-)$, and thus heavier $(m_0, m_{1/2})$. With large $(m_0, m_{1/2})$, stops are heavy at $\sim 3\,\text{TeV}$, and thus the best-fit Higgs mass is $\sim 122\,\text{GeV}$, in the heavier permitted interval. The dominant contributions to χ^2_{Min}, other than δa_μ, are Higgs, $\text{BR}\,(b \to s\gamma)$ and $B_u \to \tau\nu$.

The focus-point region is pushed to heavier m_0 and marginally heavier $m_{1/2} \sim 600\,\text{GeV}$ than in Fig. 4.4.4. The Razor limit excludes $m_{1/2} \lesssim 300\,\text{GeV}$ in the focus-point region, which was previously favoured. In the focus-point region, stops $\sim 2\,\text{TeV}$ are lighter than in the A-funnel, because, although m_0 is similar, $m_{1/2}$ is smaller in the focus-point region than in the A-funnel. Because achieving heavy

Higgs masses is difficult, the best-fit Higgs mass is $\sim 118\,\text{GeV}$. The dominant contributions to χ^2_{Min}, other than δa_μ, are Higgs, $B_u \to \tau\nu$, $\text{BR}\,(b \to s\gamma)$ and ΔM_{B_s}.

The $(A_0, \tan\beta)$ plane in case 1, which should be compared with our previous result in Fig. 4.4.4, is in Fig. 4.5.2b. There is a single 1σ mode at $\tan\beta \sim 50$ and a second 2σ mode at $\tan\beta \sim 15$. That at $\tan\beta \sim 50$ is the A-funnel region, which requires large $\tan\beta$ to reduce the pseudoscalar's mass and that at $\tan\beta \sim 15$ is the stau-coannihilation region. Unlike in Fig. 4.4.4, the stau-coannihilation region is at 2σ, because of its small volume on the marginalised $(m_0, m_{1/2})$ plane, but its shape is otherwise unchanged. Extreme A_0 is vetoed, because the stau would be the LSP, or else, if m_0 is simultaneously increased to insure that the stau is not the LSP, disfavoured by δa_μ. Within the A-funnel region, $A_0 \gtrsim 0$ is favoured, by physicality, $\text{BR}\,(b \to s\gamma)$ and by $m_A \approx 2m_\chi$.

Because of its small volume on the $(m_0, m_{1/2})$ plane, the focus-point is absent after marginalisation on the $(A_0, \tan\beta)$ plane, though it favours $\tan\beta \gtrsim 15$ and $0\,\text{TeV} \lesssim A_0 \lesssim 2.5\,\text{TeV}$ to achieve $\mu \sim 0$ in our prior ranges for $(m_0, m_{1/2})$.

"Optimistic" Higgs likelihood

In Fig. 4.5.2c we reconsider the CMSSM's $(m_0, m_{1/2})$ plane in case 2, with our "optimistic" Higgs likelihood. The credible regions marginally differ from Fig. 4.5.2a, case 1. Notably, the bottom of the stau-coannihilation region at $m_{1/2} \sim 600\,\text{GeV}$ is omitted at 1σ and the focus-point region is inflated to include heavier and, surprisingly, smaller $m_{1/2}$. The surprising inflation of the focus-point is caused by our $m_h \sim 125\,\text{GeV}$ likelihood function. With large m_0, achieving a heavier Higgs mass in the focus-point region is easier than in the stau-coannihilation region.

The $(A_0, \tan\beta)$ plane in Fig. 4.5.2d is similar to that in case 1, although intermediate $\tan\beta \sim 35$ is at 2σ, connecting the stau-coannihilation and A-funnel regions. Intermediate $\tan\beta$ is the focus-point region, inflated on the $(m_0, m_{1/2})$ plane, which favours $\tan\beta \gtrsim 15$. Furthermore, the stau-coannihilation region at $\tan \lesssim 30$ prefers heavier $A_0 \sim 2\,\text{TeV}$, especially at $\tan\beta \lesssim 10$, which increases the Higgs mass via maximal mixing.

Higgs mass

In case 2, our best-fit Higgs mass is $m_h = 123.3\,\text{GeV}$ in the A-funnel, which incurs a small $\chi^2 = 0.4$ penalty. The best-fit Higgs masses in the stau-coannihilation and focus-point regions are $m_h = 121.5\,\text{GeV}$ and $m_h = 122.0\,\text{GeV}$, respectively, which incur moderate, but insignificant, $\chi^2 = 1.5$ and $\chi^2 = 1.1$ penalties. Compared with case 1, m_h is increased by $\sim 1\,\text{GeV}$ in the A-funnel and by $\sim 3\,\text{GeV}$ in the stau-coannihilation and focus-point regions.

In our analysis, because nuisance parameters including M_t were sampled from their Gaussian priors, M_t discrepant from its measurement was not penalised in our likelihood function. The best-fit Higgs masses were achieved with a heavy top mass and are fine-tuned, because M_t is drawn from the tail of its Gaussian prior distribution. We investigate whether any mode increases Higgs mass via maximal stop mixing.

Stop mixing is examined on the (M_{SUSY}, X_t) plane in Fig. 4.5.3, with $X_t = A_t - \mu \cot\beta$. The 1σ mode at $M_{\text{SUSY}} \sim 1\,\text{TeV}$ is the stau-coannihilation, with mixing that is substantial but submaximal, $X_t / M_{\text{SUSY}} \lesssim \sqrt{6}$. Maximal mixing cannot be achieved by tuning X_t via $(A_0, \tan\beta)$ for a given $(m_0, m_{1/2})$, because X_τ must be tuned via $(A_0, \tan\beta)$ for $m_\chi \approx m_{\tilde{\tau}_1}$ in the stau-coannihilation region.

The mode at $M_{\text{SUSY}} \sim 3\,\text{TeV}$ is predominantly the A-funnel. Surprisingly, in spite of $\tan\beta \sim 50$ and moderate $A_0 \gtrsim 0$, the A-funnel achieves X_t similar to the stau-coannihilation region, because after RG flow to M_{SUSY}, A_t is negative and similar in magnitude to that in the stau-coannihilation region. Mixing is, however, less maximal than in the stau-coannihilation region, because M_{SUSY} is heavier than in the stau-coannihilation region. In the A-funnel, although decreasing A_0 to $\sim -2\,\text{TeV}$ increases the Higgs mass, it spoils $2m_\chi \approx m_A$. The focus-point region is connected with the A-funnel at $M_{\text{SUSY}} \sim 2.5\,\text{TeV}$ and $X_t \sim -0.5\,\text{TeV}$. In the focus-point, Higgs mass is comparable with that in the stau-coannihilation region, because although M_{SUSY} is heavier, stop mixing is submaximal. Stop mixing cannot be increased via A_0 without spoiling $\mu \sim 0$ in the focus-point.

Fig. 4.5.4 shows the posterior pdf and profile likelihood for the calculated Higgs mass. Remarkably, the posterior pdf excludes $m_h \gtrsim 123\,\text{GeV}$ at 2σ and favours $m_h \sim 121\,\text{GeV}$ with its mean and mode. The profile likelihood includes at 1σ Higgs masses $\gtrsim 123\,\text{GeV}$ that were excluded by the posterior pdf, indicating that whilst $\gtrsim 123\,\text{GeV}$ is possible, it must be fine-tuned, including by fine-tuning M_t. The 2σ confidence interval is, however, $m_h \lesssim 124\,\text{GeV}$ and the profile likelihood favours $m_h \sim 123\,\text{GeV}$, i.e., less than its measurement.

In summary, finding $m_h \sim 125\,\text{GeV}$ and satisfying other experimental constraints is difficult in the CMSSM with our prior ranges $m_0 \leq 4\,\text{TeV}$ and $m_{1/2} \leq$

2 TeV. Although our scan found m_h as heavy as $\sim 129\,\text{GeV}$, it was excluded at 2σ by a combination of experiments. At 2σ, we found $m_h \lesssim 123\,\text{GeV}$ and $m_h \lesssim 124\,\text{GeV}$ with our credible region and confidence interval, respectively. Note well, however, that m_h is the calculated rather than physical mass, with an appreciable theoretical error. $m_h \lesssim 123\,\text{GeV}$ could correspond to a physical Higgs mass of $\sim 125\,\text{GeV}$.

Dropping δa_μ and considering $\mu < 0$

In our results, as anticipated, the CMSSM cannot reproduce δa_μ close to its measurement in conjunction with other experimental constraints, with $\delta a_\mu \sim 10^{-10}$ rather than $\delta a_\mu \sim 30 \times 10^{-10}$ and, consequently, $\Delta\chi^2 \sim 10$. With an ensemble of measurements, there is an appreciable chance of obtaining a discrepant measurement. This disagreement could be a statistical fluctuation. With this interpretation, the true δa_μ is $\sim 10^{-10}$.

If, however, we insist that the discrepancy between the Standard Model prediction and measurement results from new physics, rather than fluctuations, we conclude that the CMSSM is not this new physics. If we suppose that more new physics exists that contributes to δa_μ, we should omit our δa_μ likelihood. Alternatively, if we suspect that the discrepancy results from an unidentified systematic error, we should omit our δa_μ likelihood. We investigate this case by dropping δa_μ from our likelihoods. With δa_μ omitted from our likelihood function, there was no motivation for exclusively picking $\mu > 0$, which was favoured by δa_μ. We separately considered $\mu > 0$ and $\mu < 0$, and marginalised $\operatorname{sgn}\mu$.

To marginalise $\operatorname{sgn}\mu$, we combined our separate scans with equal prior weight by concatenating our chains weighted by their evidences,

$$p = \frac{\mathcal{Z}_{\mu>0} p_{\mu>0} + \mathcal{Z}_{\mu<0} p_{\mu<0}}{\mathcal{Z}_{\mu>0} + \mathcal{Z}_{\mu<0}}. \tag{4.43}$$

The credible regions in our three cases — $\mu > 0$, $\mu < 0$ and $\operatorname{sgn}\mu$ marginalised — are shown in Fig. 4.5.5, with our "optimistic" Higgs likelihood function but without δa_μ (case 3). Our $\mu > 0$ results in Fig. 4.5.5a and Fig. 4.5.5b should be compared with our $\mu > 0$ results with δa_μ in Fig. 4.5.2c and Fig. 4.5.2d. The $(m_0, m_{1/2})$ planes are similar, though removing δa_μ shrinks the stau-coannihilation region and enlarges the focus-point and A-funnel regions. The stau-coannihilation, with its light sleptons, was favoured by δa_μ. Without δa_μ, its χ^2 is worse than it was relative to that of the A-funnel and focus-point regions. The A-funnel is pushed to heavier $(m_0, m_{1/2})$; δa_μ penalised heavier $(m_0, m_{1/2})$. The best-fit point moves to heavier $(m_0, m_{1/2})$ in the A-funnel. Surprisingly, the best-fit Higgs mass $m_h = 122.6\,\text{GeV}$ without δa_μ is lighter than that with δa_μ, $m_h = 123.3\,\text{GeV}$, resulting in a small $\Delta\chi^2 \sim 0.4$ penalty. This is probably because our `MultiNest` algorithm is tailored for Bayesian statistics and cannot reliably find the best-fit point. The posterior mean, credible regions and confidence intervals for m_h without δa_μ are $\sim 1\,\text{GeV}$ heavier than those with δa_μ. The χ^2 from $\sin^2\theta_{\text{eff}}$ is reduced by $\Delta\chi^2 \sim 1.1$, indicating slight tension between δa_μ and $\sin^2\theta_{\text{eff}}$. On the $(A_0, \tan\beta)$ plane, removing δa_μ shrinks the stau-coannihilation, especially at $A_0 \sim 0$, which corresponded to light smuons with small stau mixing.

The $\operatorname{sgn}\mu$ is particularly relevant in:

- Off-diagonal mass matrix elements of third-generation sfermions from F-terms, e.g., stop mixing,
$$X_t = A_t - \mu\cot\beta;$$
- Chargino-stop loop contributions to $b \to s\gamma$ in Fig. 3.7.1d and Fig. 3.7.1c, which are proportional μ because of mass insertions;
- Chargino-stop loop contributions to $B_s \to \mu^+\mu^-$ in Fig. 3.7.2c, which are proportional μ because of mass insertions;
- Higgsino-mixing in the neutralino and chargino mass matrix in Eq. 1.45 and Eq. 1.53, respectively;
- Higgsino-mixing in chargino-sneutrino and neutralino-slepton loop contributions to δa_μ, which are proportional μ because of mass insertions. In fact, $\delta a_\mu \propto \operatorname{sgn}\mu$.

With $\mu < 0$, the $(m_0, m_{1/2})$ plane in Fig. 4.5.5b is different from that with $\mu > 0$ in Fig. 4.5.5a. The stau-coannihilation and focus-point regions shrink, and the A-funnel inflates at smaller $(m_0, m_{1/2})$, almost connecting with the stau-coannihilation region. At $m_0 \sim 800\,\text{GeV}$, dark matter is annihilated by a combination of stau-coannihilation and A-funnel. With $\mu < 0$, loop contributions to $\text{BR}\,(B_s \to \mu^+\mu^-)$ are destructive, and a lighter pseudoscalar Higgs and thus smaller $(m_0, m_{1/2})$ is permitted. $\text{BR}\,(B_s \to \mu^+\mu^-)$ is particularly relevant in the

A-funnel, because $\tan\beta$ is large. With $\mu < 0$, the A-funnel inflates, and, to conserve the integral of the pdf, the stau-coannihilation and the focus-point regions shrink.

On the $(A_0, \tan\beta)$ plane with $\mu < 0$, the dominant 1σ mode is the A-funnel with $\tan\beta \lesssim 45$ smaller and A_0 smaller than with $\mu > 0$. With $\mu > 0$, the A-funnel preferred $A_0 \gtrsim 0$ to maximise $\mathrm{BR}\,(b \to s\gamma)$. With $\mu < 0$, loop contributions to $\mathrm{BR}\,(b \to s\gamma)$ are constructive and with $A_0 \gg 0$, $\mathrm{BR}\,(b \to s\gamma)$ is greater than its measurement. With $\mu < 0$ for points that were physical with $\mu > 0$, the pseudoscalar Higgs is often tachyonic, though can be made physical if $\tan\beta$ is decreased. The tiny 2σ mode at $A_0 \sim -2.5\,\mathrm{TeV}$ is the stau-coannihilation region. The stau-coannihilation regions favours negative A_0 to counter the opposite $\mathrm{sgn}\,\mu$, which cancels with A_τ and A_t in stau and stop mixing.

Without δa_μ, the Bayes-factor in Eq. 2.17 favours $\mu < 0$ by 2.5 to 1. With $\mu < 0$, CMSSM predictions for B-physics observables $B_s \to \mu^+\mu^-$ and $b \to s\gamma$ are less fine-tuned than with $\mu > 0$, though the agreement with experiment is similar. This preference, however, is "barely worth mentioning" on the Jeffreys' scale in Table 2.4.1. With $\mathrm{sgn}\,\mu$ marginalised, because its evidence is greater, $\mu < 0$ dominates credible regions on the $(m_0, m_{1/2})$ and $(A_0, \tan\beta)$ planes in Fig. 4.5.5e and Fig. 4.5.5f.

Best-fit point

The best-fit point in case 2 with $\mu > 0$ is in the A-funnel with $\chi^2 = 18.6$, though similar $\chi^2 = 18.7$ is achieved in the stau-coannihilation region. The minimum χ^2 in the focus-point region is $\chi^2 = 20.2$. The dominant contributions to the χ^2 are δa_μ, Razor, $b \to s\gamma$ and $\sin^2\theta_{\mathrm{eff}}$. In the stau-coannihilation and focus-point regions, χ^2 from m_h is substantial, whilst in the focus-point region, χ^2 from $\sin^2\theta_{\mathrm{eff}}$ is reduced. We inspect the χ^2 breakdown at our best-fit points with and without our δa_μ likelihood in Fig. 4.5.6. With δa_μ, the dominant contribution is that from δa_μ — it is poorly reproduced with either $\mathrm{sgn}\,\mu$ — and the minimum χ^2 with $\mu > 0$ is insignificantly smaller than that with $\mu < 0$. We see tension between δa_μ and $\sin^2\theta_{\mathrm{eff}}$; once δa_μ is removed, the χ^2 from $\sin^2\theta_{\mathrm{eff}}$ is reduced. Remarkably, once δa_μ is removed, the minimum χ^2 with $\mu < 0$ is insignificantly smaller than that with $\mu > 0$.

To calculate the CMSSM's p-value, we need to understand the distribution of our χ^2. Because the likelihood functions for Razor and $\mathrm{BR}\,(B_s \to \mu^+\mu^-)$ were not Gaussian, their contributions to the χ^2 are not χ^2-distributed. The Razor and $B_s \to \mu^+\mu^-$ searches would not be sensitive to our best-fit point; were the experiments repeated, the χ^2 would not change because of fluctuations in our best-fit point's signal, but fluctuations in the Standard Model backgrounds. We omit Razor and BR $(B_s \to \mu^+\mu^-)$ from our p-value calculation. Our best-fit point's χ^2 is 14.6 from 8 Gaussian likelihoods. Whilst we fitted 8 parameters, the 4 nuisance parameters weakly effect observables. Conservatively, we assume that we reduce the degrees of freedom from 8 to 4 by fitting the CMSSM's 4 parameters. The p-value, the probability of obtaining such a large χ^2 by chance, is 0.5%, which is significant. In the CMSSM 1 fb^{-1} study in Table 4.4.2, the CMSSM's p-value was 61%. We find, however, that our calculation is not robust — in Ref. [217], a similar analysis with a `MultiNest` scan tailored for frequentist statistics found p-value $= 21\%$, because it found a point in the stau-coannihilation that satisfied δa_μ. Our analysis focuses on Bayesian statistics. Because the best-fit point in Ref. [217] is fine-tuned for δa_μ, its posterior weight is negligible. We refrain from declaring that the CMSSM is excluded at 95%, despite our p-value.

Observables

We examine correlations between B-physics and δa_μ in Fig. 4.5.7. Fig. 4.5.7a indicates negative correlation [206], and thus tension, between $b \to s\gamma$ and δa_μ; increased BR $(b \to s\gamma)$ results in decreased δa_μ and *vice-versa*, though neither $b \to s\gamma$ nor δa_μ agrees with its measurement in our 1σ credible region. The 1σ credible region is predominantly the A-funnel and its 2σ tail extending to $\delta a_\mu \sim 5 \times 10^{-10}$ is predominantly the stau-coannihilation region. δa_μ in the stau-coannihilation region is bigger than that in the A-funnel region, because smuons are lighter in the stau-coannihilation region than in the A-funnel region. Because destructive chargino-stop loops in $b \to s\gamma$ are suppressed by their mass scale, $b \to s\gamma$ is largest in the A-funnel region. With $\mu > 0$, increasing $\tan\beta$ increases δa_μ in Eq. 3.59, but decreases $b \to s\gamma$ because it enhances destructive contributions in Eq. 3.41.

Fig. 4.5.7b indicates positive correlation and, as δa_μ must be enhanced, tension between $B_s \to \mu^+\mu^-$ and δa_μ, because their SUSY contributions are proportional to a positive power of $\tan\beta$ divided by a relevant SUSY mass scale (see Eq. 3.45 and Eq. 3.59). The 1σ credible region, with a steep gradient, corresponds the A-funnel region, in which $\tan\beta \sim 45$. Increasing BR $(B_s \to \mu^+\mu^-)$ corresponds to increasing $\tan\beta$ and decreasing m_A and thus $m_{1/2}$. The 2σ credible region, with a flatter gradient, is the stau-coannihilation region, in which $\tan\beta \sim 10$. Increasing δa_μ corresponds to decreasing $m_{1/2}$ and increasing $\tan\beta$.

We investigate B-physics by comparing $\operatorname{sgn}\mu = \pm 1$ in Fig. 4.5.7c and Fig. 4.5.7d. As anticipated, with $\mu > 0$ in Fig. 4.5.7c, $\mathrm{BR}\left(b \to s\gamma\right)$ is smaller than its measurement, but with $\mu < 0$ in Fig. 4.5.7d, it agrees with its measurement, because of constructive chargino-stop loops. With $\mu < 0$, $\mathrm{BR}\left(B_s \to \mu^+\mu^-\right)$ is safely below its experimental limit. By contrast, with $\mu > 0$, the 2σ credible region exceeds the experimental upper limit for $\mathrm{BR}\left(B_s \to \mu^+\mu^-\right)$. With each $\operatorname{sgn}\mu$, the A-funnel and stau-coannihilation regions separate. With $\mu > 0$, the 2σ tail at $\mathrm{BR}\left(b \to s\gamma\right) \sim 3 \times 10^{-4}$ is the stau-coannihilation region and the 2σ tail at $\mathrm{BR}\left(B_s \to \mu^+\mu^-\right) \sim \mathrm{BR}\left(B_s \to \mu^+\mu^-\right)_{\mathrm{EXP}}$ is the overlapping stau-coannihilation and A-funnel regions and with $\mu < 0$, the 2σ slither at $\mathrm{BR}\left(B_s \to \mu^+\mu^-\right) \sim 3 \times 10^{-9}$ is the stau-coannihilation region. In the stau-coannihilation region, SUSY contributions to $B_s \to \mu^+\mu^-$ are small and its predictions is $\mathrm{BR}\left(B_s \to \mu^+\mu^-\right) \sim 3 \times 10^{-9}$ with each $\operatorname{sgn}\mu$. In the A-funnel region, moderate SUSY contributions to $B_s \to \mu^+\mu^-$ flip sign with $\mu < 0$ and $\mathrm{BR}\left(B_s \to \mu^+\mu^-\right)$ is reduced with $\mu < 0$. With $\mu < 0$, $b \to s\gamma$ is largest in the overlapping stau-coannihilation and A-funnel regions, in which M_{SUSY} is moderate and $\tan\beta \sim 40$, resulting in substantial constructive chargino-stop loops.

Direct detection

Lastly, we consider direct detection in Fig. 4.5.8, which should be compared with the equivalent result in Sec. 4.4, Fig. 4.4.5. With $\mu > 0$ in Fig. 4.5.8a, the $\left(m_\chi, \sigma_p^{\mathrm{SI}}\right)$ plane has three modes. The mode at $\sigma_p^{\mathrm{SI}} \sim 10^{-8}$ is the focus-point, with Higgs exchange enhanced by the higgsino component of its mixed neutralino, that at $m_\chi \sim 300\,\mathrm{GeV}$ is the stau-coannihilation, and that at 1σ at $m_\chi \sim 700\,\mathrm{GeV}$ is the A-funnel. Compared with Sec. 4.4, σ_p^{SI} in the A-funnel is reduced, because the pseudoscalar Higgs is heavier, but σ_p^{SI} in the stau-coannihilation and focus-point is approximately unchanged. Although XENON100's direct detection 90% exclusion contour is plotted in Fig. 4.4.5a, we did not include it in our likelihood function. XENON100 appears to exclude the focus-point; however, our calculated σ_p^{SI} has significant theoretical uncertainties.

With $\mu < 0$, the credible regions and the behaviour on the $\left(m_\chi, \sigma_p^{\mathrm{SI}}\right)$ plane is different. In the focus-point, because $|\mu| \lesssim M_1$, $\operatorname{sgn}\mu$ is irrelevant. In the stau-coannihilation and A-funnel regions σ_p^{SI} with $\mu < 0$ is approximately three decades smaller than with $\mu > 0$. With $\mu < 0$, t-channel diagrams with light and heavy Higgs bosons cancel [315]. If $\mu < 0$ in the stau-coannihilation or A-funnel region, as is marginally favoured in our analysis, direction detection experiments would struggle to detect dark matter. With $\operatorname{sgn}\mu$ marginalised in Fig. 4.5.8b, five modes are present: the focus-point, and the stau-coannihilation and A-funnel regions with each $\operatorname{sgn}\mu$. The "v"-shape is the A-funnel with $\mu < 0$ at $m_\chi \gtrsim 600\,\text{GeV}$ and the overlapping stau-coannihilation and A-funnel regions with $\mu < 0$ at $m_\chi \lesssim 600\,\text{GeV}$. The tiny 2σ credible region at $m_\chi \sim 300\,\text{GeV}$ is the stau-coannihilation region with $\mu < 0$, which is deflated by the "volume effect." The stau-coannihilation region with $\mu > 0$ connects with the overlapping stau-coannihilation and A-funnel regions with $\mu < 0$ at $m_\chi \sim 250\,\text{GeV}$. That the best-fit point is excluded by the 2σ credible region indicates fine-tuning.

Surprisingly, in the A-funnel with $\mu < 0$, σ_p^{SI} increases with m_χ. In the A-funnel, $2m_\chi \sim m_A \sim m_H$. With lighter $2m_\chi \sim m_A$, heavy Higgs exchange dominates σ_p^{SI}. With $m_\chi \sim 600\,\text{GeV}$, light and heavy Higgs t-channel exchange cancel. With heavier $2m_\chi \sim m_A$, the heavy Higgs t-channel diagram is suppressed and cannot cancel the light Higgs t-channel diagram, which dominates σ_p^{SI}. From Ref. [315], if $\mu < 0$,

$$\sigma_p^{\text{SI}} \propto \left[\frac{|k_H|}{m_H^2} - |k_h| \right]^2, \tag{4.44}$$

where $k_{H,h}$ are numerical factors associated with heavy Higgs and light Higgs t-channel diagrams, respectively. This function exhibits the "v"-shape present on the $\left(m_\chi, \sigma_p^{\text{SI}}\right)$ plane for $\mu < 0$.

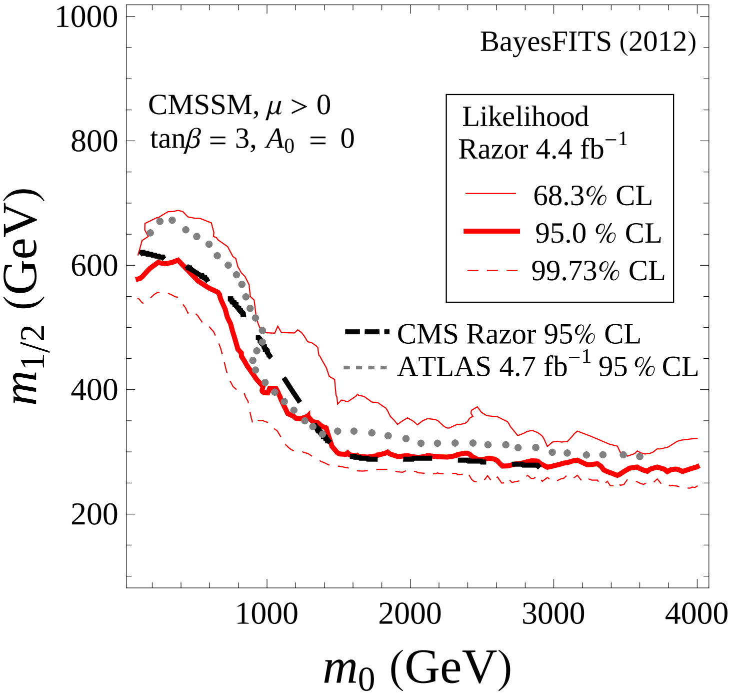

Figure 4.5.1: *Approximate CMS Razor confidence intervals (red lines) on the CMSSM's $(m_0, m_{1/2})$ plane. The black (grey) line is the 2σ confidence interval from CMS (ATLAS). The intervals are approximately independent of* $\tan\beta$, *A_0 and sgn μ.*

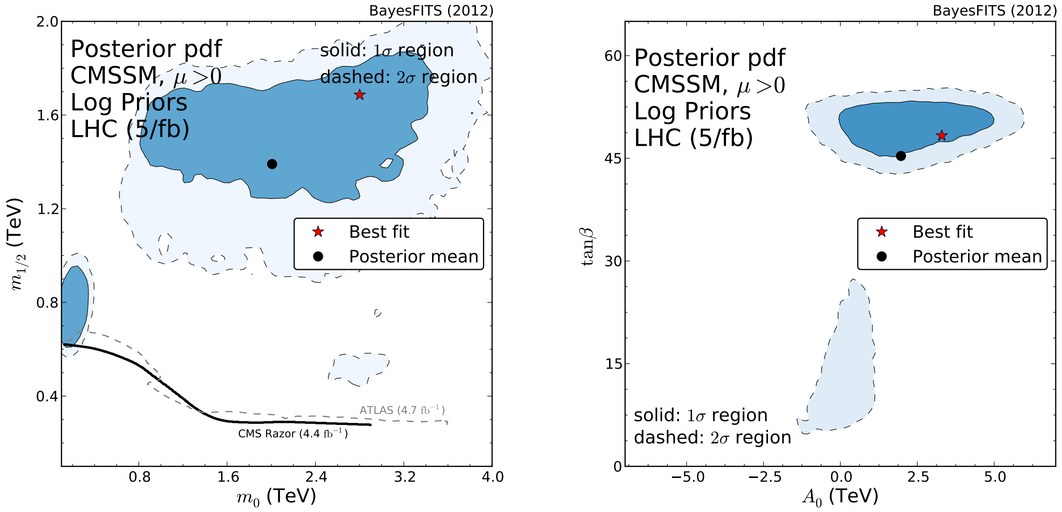

(a) $(m_0, m_{1/2})$ *with ATLAS and CMS Higgs experimental likelihoods (case 1).*

(b) $(A_0, \tan\beta)$ *with ATLAS and CMS Higgs experimental likelihoods (case 1).*

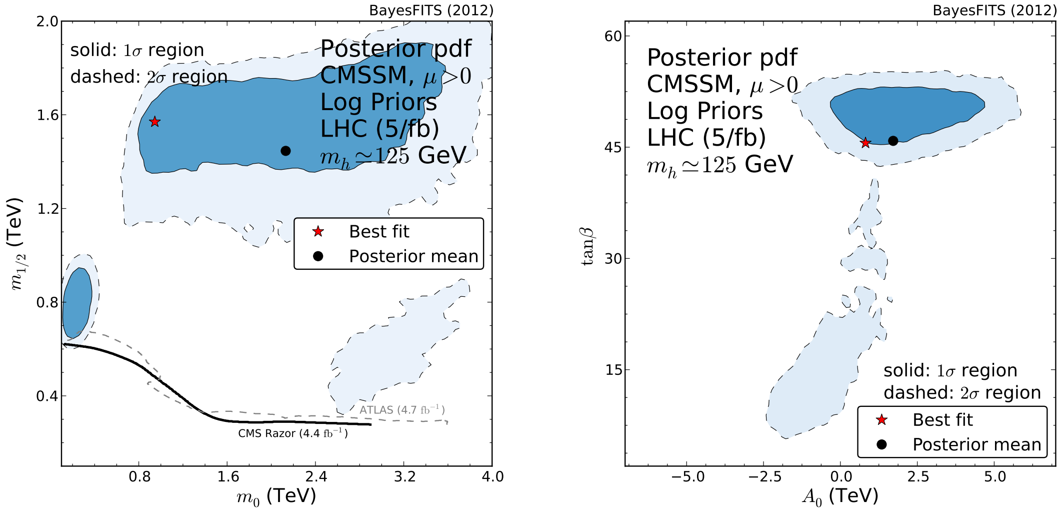

(c) $(m_0, m_{1/2})$ *with a hypothetical Higgs* $m_h = 125$ *GeV discovery likelihood (case 2).*

(d) $(A_0, \tan\beta)$ *with a hypothetical Higgs* $m_h = 125$ *GeV discovery likelihood (case 2).*

Figure 4.5.2: *1σ (2σ) Bayesian credible regions in dark (light) blue for the CMSSM with sgn* $\mu = 1$*. The posterior mean (best-fit point) is marked with a black circle (red star), and the CMS Razor (ATLAS) 2σ exclusion is marked with a full black (dashed grey) line. Logarithmic priors for soft-breaking masses and linear priors otherwise.*

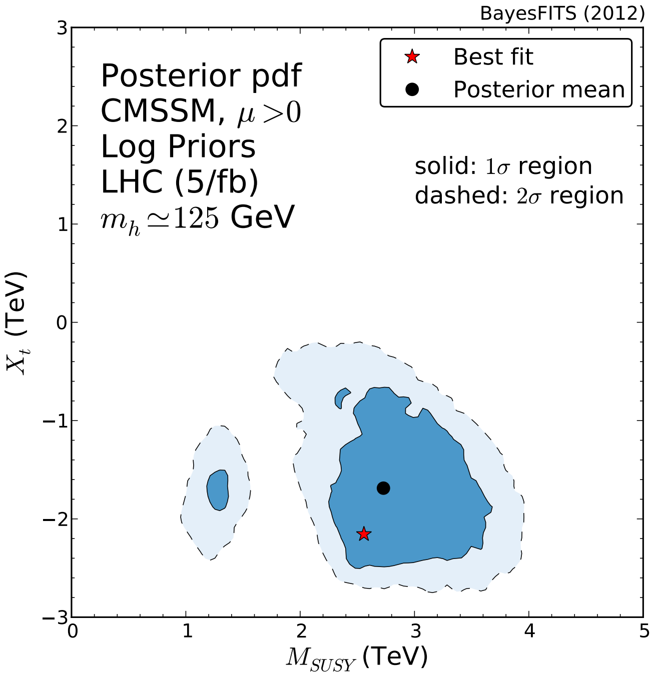

Figure 4.5.3: 1σ *(*2σ*) Bayesian credible regions in dark (light) blue for the CMSSM's* (M_{SUSY}, X_t) *plane in case 2, revealing stop mixing.*

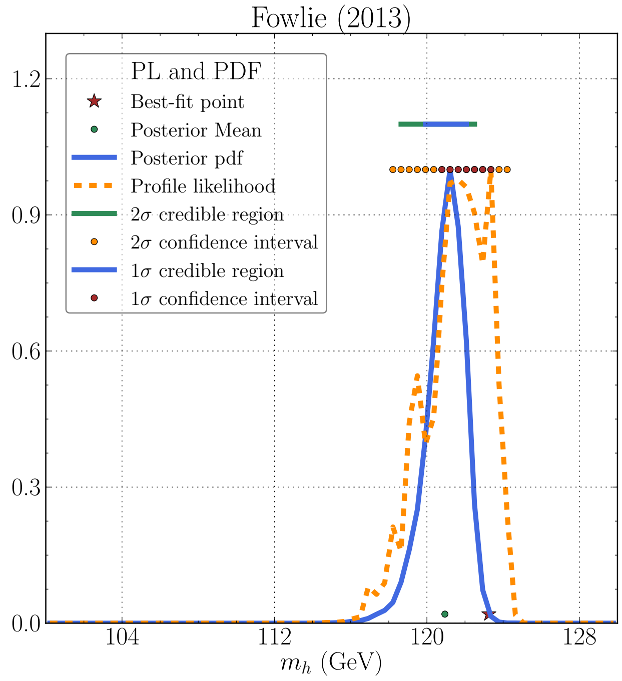

Figure 4.5.4: *Higgs mass in the sgn* $\mu = 1$ *CMSSM, with all likelihoods and an* $m_h = 125\,\text{GeV}$ *likelihood (case 2). Caveat:* m_h *is the calculated, rather than true, Higgs mass.*

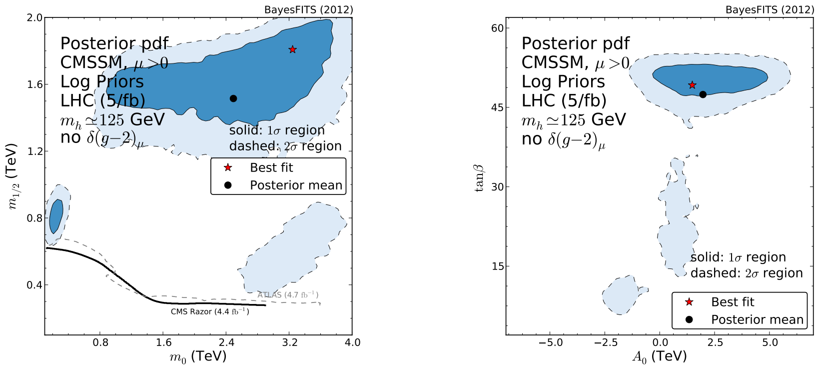

(a) $(m_0, m_{1/2})$ *and sgn* $\mu = 1$.

(b) $(A_0, \tan\beta)$ *and sgn* $\mu = 1$.

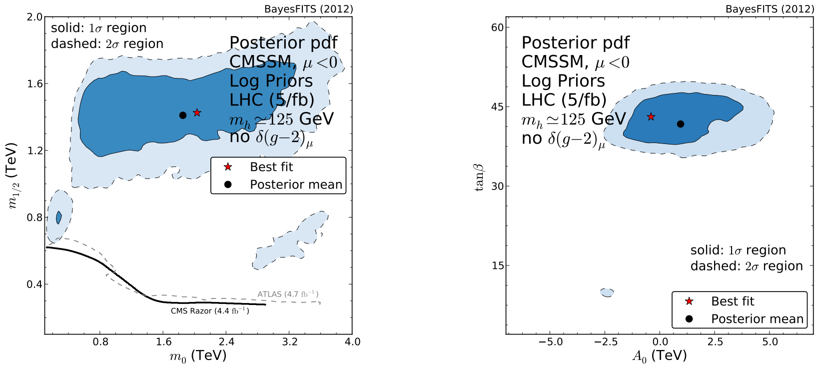

(c) $(m_0, m_{1/2})$ *and* $\mu < 0$.

(d) $(A_0, \tan\beta)$ *and* $\mu < 0$.

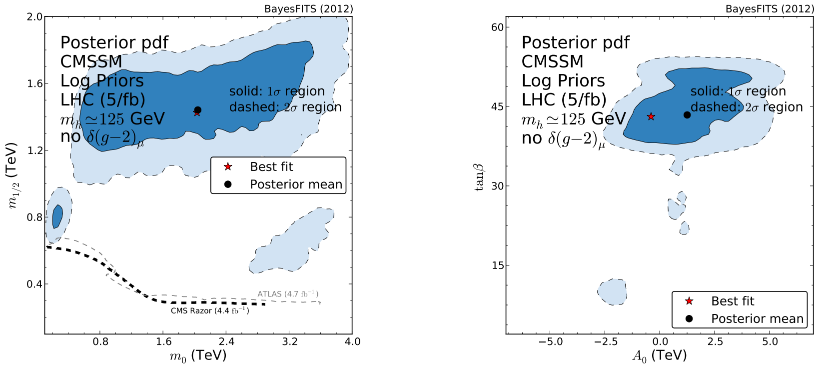

(e) $(m_0, m_{1/2})$ *and sgn* μ *marginalised.*

(f) $(A_0, \tan\beta)$ *and sgn* μ *marginalised.*

Figure 4.5.5: *1σ (2σ) Bayesian credible regions in dark (light) blue for the CMSSM with each sgn μ and with sgn μ marginalised. All likelihoods, except for δa_μ, and a $m_h = 125$ GeV likelihood were included (case 3). The posterior mean (best-fit point) is marked with a black circle (red star), and the CMS Razor (ATLAS) 2σ exclusion is marked with a full black (dashed grey) line. Logarithmic priors for soft-breaking masses and linear priors otherwise.*

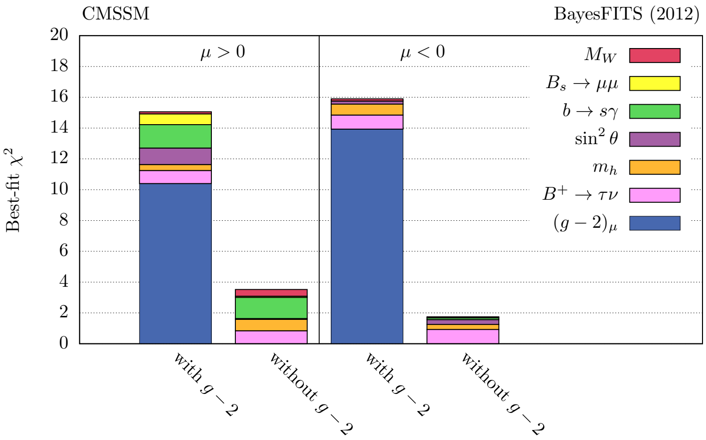

Figure 4.5.6: *Breakdown of the main contributions to the* χ^2 *at the CMSSM's best-fit points with and without a likelihood from* δa_μ *(case 2 and case 3), and with each sgn* μ*. Except for* δa_μ*, in each case all likelihoods and a* $m_h = 125$ *GeV likelihood were included.*

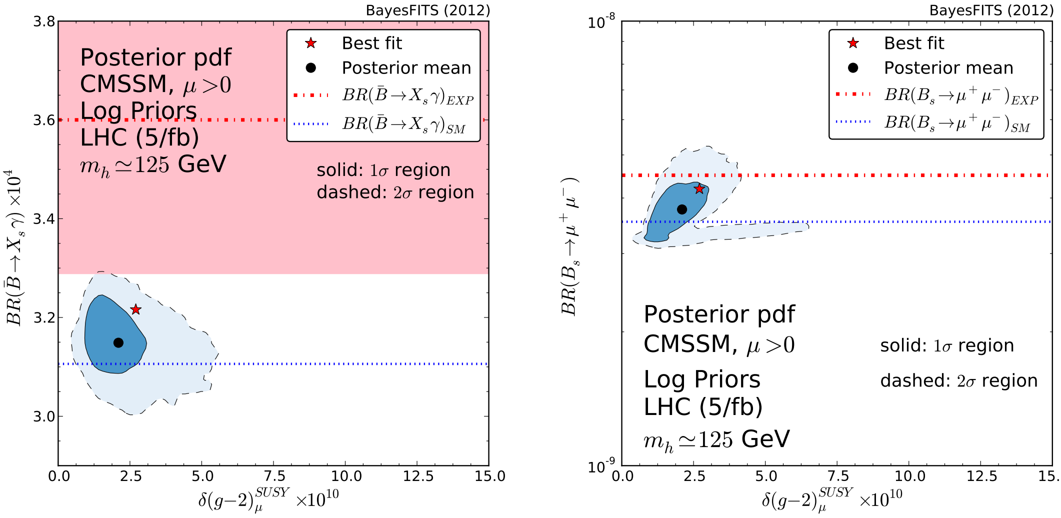

(a) $(\delta(g-2)_\mu, BR\,(b\to s\gamma))$ *with all likelihoods and an* $m_h = 125$ *GeV likelihood (case 2). The pink region is the* 1σ *experimental interval for* $BR\,(b\to s\gamma)$.

(b) $(\delta(g-2)_\mu, BR\,(B_s\to\mu^+\mu^-))$ *with all likelihoods and an* $m_h = 125$ *GeV likelihood (case 2).*

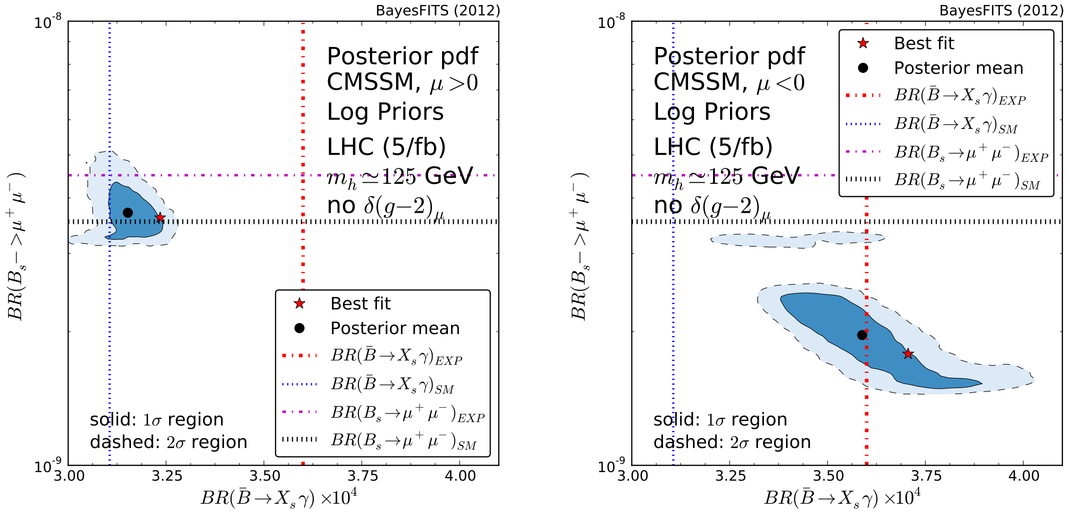

(c) $(BR\,(B_s\to\mu^+\mu^-)\,, BR\,(b\to s\gamma))$ *with all likelihoods except for* δa_μ *and an* $m_h = 125$ *GeV likelihood for* sgn $\mu = 1$ *(case 3).*

(d) $\mu < 0$*, but otherwise identical to (c).*

Figure 4.5.7: 1σ *(*2σ*) Bayesian credible regions in dark (light) blue for the CMSSM flavour and* δa_μ *observables, with logarithmic priors for soft-breaking masses and linear priors otherwise. The posterior mean (best-fit point) is marked with a black circle (red star). Standard Model predictions and experimental measurements are marked with dashed lines.*

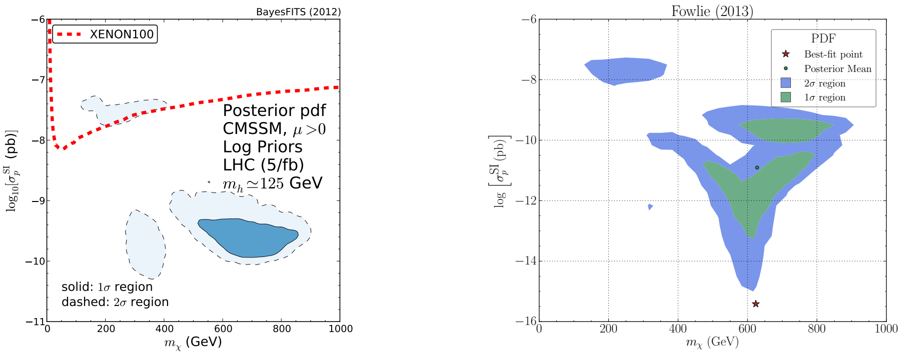

(a) *sgn* $\mu = 1$. **(b)** *sgn* μ *marginalised.*

Figure 4.5.8: 1σ *(*2σ*) Bayesian credible regions in dark (light) blue for the CMSSM direct detection* $\left(m_\chi, \sigma_p^{SI}\right)$ *plane with (a) sgn* $\mu = 1$ *and (b) sgn* μ *marginalised. All likelihoods, except for* δa_μ*, and a* $m_h = 125$ *GeV likelihood were included (case 3). Logarithmic priors for soft-breaking masses and linear priors otherwise. The* 90% *exclusion contour from XENON100 is marked with a red dashed line.*

Mass spectra

We examine the sparticle and Higgs masses in Fig. 4.5.9 in case 1 and case 2, and with each sgn μ without δa_μ in case 3. The favoured A-funnel region dominates credible regions for the sparticle masses. In case 1 in Fig. 4.5.9a, the entire spectrum is heavy with squarks and gluinos $\sim 2.5\,\text{TeV}$, sleptons $\sim 2\,\text{TeV}$, and electroweakinos $\sim 1\,\text{TeV}$. The credible regions, however, are typically $\gtrsim 1\,\text{TeV}$ at 2σ, because lighter masses are permitted in the stau-coannihilation and focus-point regions. In case 2 in Fig. 4.5.9b, remarkably, our 2σ credible regions permit electroweakinos lighter than in case 1, because the focus-point is enhanced in case 2. The 1σ credible regions and posterior means for the electroweakinos, however, are heavier, and the squarks, sleptons and Higgs are heavier.

Removing δa_μ with $\mu > 0$ in Fig. 4.5.9c has a negligible effect on sparticle masses, though squarks are marginally heavier than in Fig. 4.5.9b. With $\mu < 0$ in Fig. 4.5.9d, because the A-funnel was smaller on the $(m_0, m_{1/2})$ plane, the 1σ credible regions and posterior means are lighter than with $\mu > 0$, especially the heavy Higgs masses and the squark masses. Because the stau-coannihilation and focus-point regions were disfavoured with $\mu < 0$, however, the lower 1σ tails exclude light masses that were permitted in Fig. 4.5.9c.

4.6 pMSSM dark matter and collider signatures

The results in this section were published in Ref. [316].

In Sec. 4.5, we found that the CMSSM struggled to agree with LHC direct searches and Higgs searches, in conjunction with other experiments within our prior ranges. We, furthermore, wanted to investigate supersymmetric dark matter, without a particular pattern of soft-breaking masses. To relax the CMSSM, we investigated the MSSM, with soft-breaking parameters defined at the scale M_{SUSY}. Our model is the MSSM with degeneracies between soft-breaking masses, such that it captures dark matter and Higgs phenomenology and evades experimental limits, but remains tractable. Our p9MSSM, defined in Sec. 1.5.3, demands that $M_1 = 0.5 M_2$ at M_{SUSY}; this is unification at M_{GUT} evolved to the scale M_{SUSY} with the RG. Because $M_1 < M_2$, the lightest neutralino cannot be predominantly wino. We neglected wino-like neutralinos, because winos $\lesssim 3\,\text{TeV}$ annihilate to WW via a

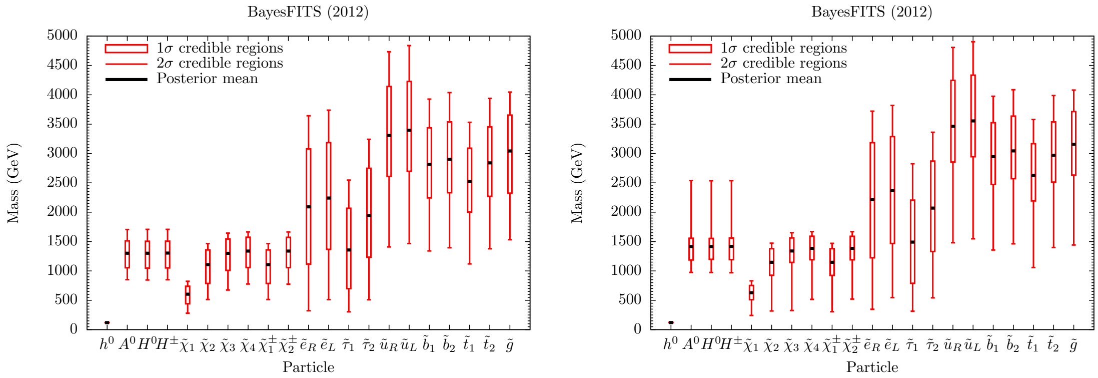

(a) *sgn $\mu = 1$ with all likelihoods and ATLAS and CMS Higgs experimental likelihoods (case 1).*

(b) *sgn $\mu = 1$ with all likelihoods and a hypothetical Higgs $m_h = 125\,\text{GeV}$ discovery likelihood.*

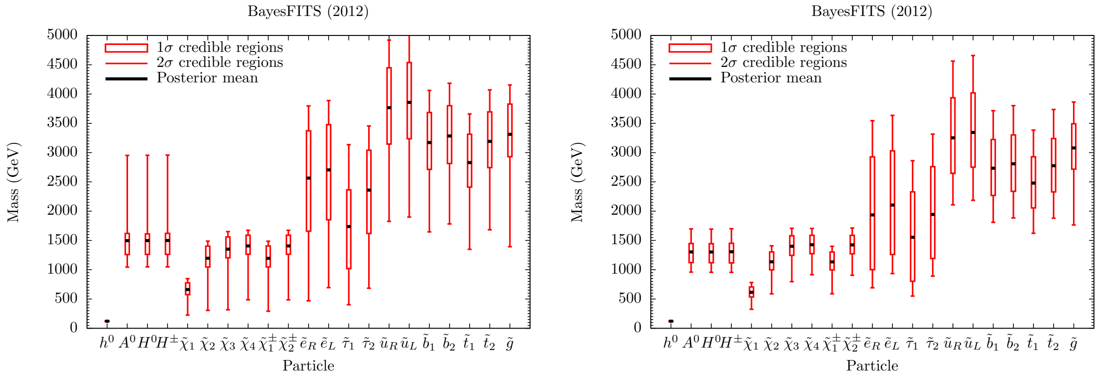

(c) *sgn $\mu = 1$ with all likelihoods and $m_h = 125\,\text{GeV}$, but without a likelihood from δa_μ (case 2).*

(d) *$\mu < 0$ with all likelihoods and $m_h = 125\,\text{GeV}$, but without a likelihood from δa_μ (case 3).*

Figure 4.5.9: *Credible regions (red candlesticks) and posterior means (black dashes) for CMSSM mass spectra, with logarithmic priors for soft-breaking masses and linear priors otherwise.*

t-channel wino-like chargino at a rate such that the relic density is smaller than its measurement and might be excluded by indirect detection experiments [317].

Because LHC direct searches strongly constrain only first and second-generation squark masses, we fixed first- and second-generation soft-breaking squark masses at 2.5 TeV, but permitted third-generation soft-breaking squark masses to vary to investigate Higgs phenomenology. Because sleptons cannot be lighter than the neutralino, we fixed first- and second-generation slepton masses to $M_1 + 50\,\text{GeV}$, in order to enhance δa_μ. We permitted the third-generation soft-breaking slepton mass to vary so that we might investigate stau-coannihilation with $m_\chi \approx m_{\tilde{\tau}_1}$. The trilinears are particularly relevant to the stau-coannihilation mechanism and the Higgs mass. We permitted the unified slepton trilinear and unified up-type trilinears to vary, but fixed unified down-type trilinears.

In the Higgs sector of our p9MSSM, we traded soft-breaking Higgs masses for m_A and M_Z via electroweak symmetry breaking conditions and fixed M_Z, leaving m_A, μ and $\tan\beta$. We investigated only $\operatorname{sgn}\mu = +1$. The soft-breaking masses in our p9MSSM are defined at the scale M_{SUSY}. The nuisance parameters $1/\alpha_{\text{em}}(M_Z)^{\overline{MS}}$ and α_s in our p9MSSM are less relevant than in the CMSSM, because the gauge couplings modify the RG evolution from the M_{SUSY} to M_{GUT} in the CMSSM. We fixed $1/\alpha_{\text{em}}(M_Z)^{\overline{MS}}$ and α_s, but varied M_t and $m_b(m_b)^{\overline{MS}}$.

In summary, our p9MSSM parameters are:

$$\begin{aligned}
M_1 &= 0.5 M_2, \\
m_{\tilde{L}_{1,2}} &= m_{\tilde{\bar{e}}_{1,2}} = M_1 + 50\,\text{GeV}, \\
m_{\tilde{L}_3} &= m_{\tilde{\bar{e}}_3}, \\
m_{\tilde{Q}_{1,2}} &= m_{\tilde{\bar{u}}_{1,2}} = m_{\tilde{\bar{d}}_{1,2}} = 2.5\,\text{TeV}, \\
m_{\tilde{Q}_3} &= m_{\tilde{\bar{u}}_3} = m_{\tilde{\bar{d}}_3}, \\
A_e &= A_\mu = A_\tau, \\
A_u &= A_c = A_t, \\
A_d &= A_s = A_b = -0.5\,\text{TeV},
\end{aligned} \tag{4.45}$$

and we have traded m_{H_u}, m_{H_d} and b for M_Z, $\tan\beta$ and m_A via electroweak symmetry breaking conditions. The ranges of parameters over which we scanned are in Table B.5 in Appendix B.

By contrast with our previous studies of the CMSSM, we investigated our p9MSSM with frequentist statistics, rather than Bayesian statistics. We worried that, with its extra parameters, with Bayesian statistics our p9MSSM would suffer from strongly increased prior dependence, and, rather than identify its best regions, we wanted only to establish that particular mechanisms of dark matter annihilation and sparticle masses could agree with experiment. We would, furthermore, struggle to cover our whole parameter space in detail. With frequentist statistics, we could concatenate chains from several `MultiNest` scans of the p9MSSM with linear and log priors. With Bayesian statistics, combining samples requires that each sample is correctly weighted.

We scanned our p9MSSM with the parameter ranges in Table B.5 in Appendix B and considered four likelihood cases, by adding experiments one by one to our likelihood:

1. "Basic" likelihoods: likelihoods from α_T, LEP sparticle mass limits, m_h, Ωh^2, $b \to s\gamma$, $B_s \to \mu^+\mu^-$, $B_u \to \tau\nu$, ΔM_{B_s}, $\sin^2\theta_{\text{eff}}$, M_W, $m_b(m_b)^{\overline{MS}}$ and M_t;
2. "Basic" likelihoods plus a likelihood from XENON100;
3. "Basic" likelihoods plus a likelihood from δa_μ.
4. "Basic" likelihoods, plus a likelihood from XENON100 and a likelihood from δa_μ.

The likelihood functions are in Table A.1, Table A.2, Table A.3 and Table A.5 in Appendix A.

CMS updated their α_T search with $11.7\,\text{fb}^{-1}$ and included b-tagged jets to improve their search's sensitivity to third-generation squarks [318]. We calculated selection efficiencies for this search and cross sections for our p9MSSM points "on the fly" in our scan, if the search might be sensitive to our trial point. Our likelihood was a product of Poissons, similar to that in Sec. 4.4 and Sec. 4.5. If the search was not sensitive to our trial point, its likelihood was unity. The search was sensitive to $\sim 1\%$ of points.

We wished to include the CMS $3\ell + \not{E}_T$ search for direct production of neutralinos and charginos in $9.2\,\text{fb}^{-1}$ [319]. Because electroweak production searches, however, might be sensitive to $\sim 25\%$ of our points, we could not include it "on the fly," because our computer time was limited. We instead simulated electroweak production for a random $\sim 2\%$ subset of our points, with a similar methodology to that in Sec. 4.4 and Sec. 4.5.

Predicting σ_p^{SI} in direct detection experiments in the MSSM is complicated by hadronic uncertainties (Sec. 3.3.4) in the π-nucleon σ-term,

$$\Sigma_{\pi N} = \frac{1}{2}\left(m_u + m_d\right)\left(\langle N|\bar{u}u|N\rangle + \langle N|\bar{d}d|N\rangle\right), \tag{4.46}$$

which is independent of whether the nucleon N is a proton or a neutron. $\Sigma_{\pi N}$ is measured in low-energy pion-nucleon scattering in pion-hydrogen collisions. If $\Sigma_{\pi N}$ is varied within its 2σ confidence interval, σ_p^{SI} varies by an order of magnitude [110]. Intriguingly, a reanalysis of CHAOS [320] pion-nucleon scattering in Ref. [321] found

$$\Sigma_{\pi N} = 43 \pm 12\,\mathrm{MeV}, \tag{4.47}$$

which disagrees at $\sim 2.5\sigma$ with a previous estimate [322] of

$$\Sigma_{\pi N} = 66 \pm 6\,\mathrm{MeV}. \tag{4.48}$$

We included $\Sigma_{\pi N}$ as a nuisance parameter in our p9MSSM. We constructed our Poisson likelihood function for XENON100 from their event data [323]. We separately considered the measurements in Eq. 4.47 and Eq. 4.48 in conjunction with XENON100 by convoluting our likelihood function by a Gaussian for $\Sigma_{\pi N}$ via Eq. 3.5.

To investigate dark matter in our p9MSSM, we predicted quantities relevant to indirect detection experiments (see Sec. 3.3.5). Indirect detection experiments search for products from dark matter annihilation. The pertinent quantity is the dark matter annihilation rate in the zero temperature limit.

4.6.1 Results

Basic likelihoods

We present our results on the (M_2, μ) plane, because from it one can deduce the approximate mass and composition of the lightest neutralino. We discard points with $\Delta\chi^2 > 5.99$ in case 1, i.e., points that are excluded at 2σ by experiments in case 1. We approximately identify mechanisms by which dark matter is annihilated:

***h*-resonance,** in which $0.45 m_h < m_\chi < 0.50 m_h$, present in the CMSSM in Sec. 4.4. Because the lightest Higgs has such a narrow width, we omit $m_\chi \gtrsim m_h/2$.

***Z*-resonance,** in which $0.45 M_Z < m_\chi < 0.55 M_Z$, absent in the CMSSM.

***A*-funnel,** in which $0.45 m_A < m_\chi < 0.55 m_A$, present in the CMSSM. The A-funnel definition differs from that for the h-resonance, because the pseudoscalar's width is appreciable.

Stau-coannihilation, in which $m_{\tilde{\tau}_1} < 1.1 m_\chi$, present in the CMSSM.

$\tilde{\chi}_1^\pm$-coannihilation, in which $m_{\chi_1^\pm} < 1.1 m_\chi$, absent in the CMSSM. Because the chargino annihilates slower than the neutralino, $\tilde{\chi}_1^\pm$-coannihilation can increase the relic density.

$\tilde{f}$-coannihilation, in which $m_{\tilde{f}} < 1.1 m_\chi$, with $\tilde{f}$ any sfermion other than a stau. Absent in the CMSSM.

Mixed neutralino, in which the neutralino's higgsino component is greater than 0.2 ($Z_{13}^2 + Z_{14}^2 > 0.2$) and the neutralino annihilates predominantly via a t-channel higgsino-like chargino to WW in Fig. 3.3.1b. This annihilation mechanism is in the focus-point region in the CMSSM.

These definitions are somewhat arbitrary and, strictly, ought to refer to the dominant contribution to neutralino annihilation in $\langle \sigma v \rangle_{T_{\text{F.O.}}}$. These mechanisms are not mutually exclusive; a point could annihilate dark matter by a combination of mechanisms. In fact, because heavy neutralinos struggle to annihilate fast enough to reduce the relic density, a combination of mechanisms might be required to reduce the relic density of heavy neutralinos.

The categorised points are scattered on the (M_2, μ) plane in Fig. 4.6.1 and separately in Fig. 4.6.2. We observe that for much of the (M_2, μ) plane, there were no points with $\Delta\chi^2 < 5.99$; the points lie on an "L"-shape. We examine the plane from $M_2 = 0\,\text{GeV}$. With $M_2 \lesssim 100\,\text{GeV}$ or $\mu \lesssim 100\,\text{GeV}$, the chargino is lighter than LEP's limit that $m_{\chi_1^\pm} > 94\,\text{GeV}$.

The h/Z-resonance is $M_2 \sim 100\,\text{GeV}$ for all $\mu \gtrsim 50\,\text{GeV}$, in which, because m_h or $M_Z \approx 2 m_\chi$, neutralinos annihilate via an s-channel light Higgs/Z-boson resonance, the vertex for which is bino-higgsino-Higgs/bino-bino-gauge boson.

Whilst the neutralino must have a higgsino component for the h-resonance, it is predominantly bino-like, with no visible upper limit for μ.

At $M_2 \sim 200\,\text{GeV}$, adjacent to the h-resonance, is a strip points that annihilate dark matter via $\tilde{f}$-coannihilation and bulk mechanisms, despite the sfermions being $\sim 30\,\text{GeV}$ heavier than the neutralino. If the sfermions were degenerate with the neutralino, neutralinos and sfermions would coannihilate at a rate such that the relic density would be less than that measured by WMAP and PLANCK, because the neutralino is light. With $M_2 \lesssim 200\,\text{GeV}$, LEP limits on sfermion masses forbid $m_\chi \simeq m_{\tilde{f}}$. With our p9MSSM, although soft-breaking slepton masses are $50\,\text{GeV}$ heavier than M_1, negative diagonal D-terms result in degenerate neutralinos and right-handed sleptons.

The stau-coannihilation and $\tilde{f}$-coannihilation region is $M_2 \gtrsim 200\,\text{GeV}$; $M_2 \sim 300\,\text{GeV}$ for all μ is exclusively coannihilation. With $300\,\text{GeV} \lesssim M_2 \lesssim 500\,\text{GeV}$, the condition $m_\chi \approx m_{\tilde{f}}$ and correct relic density is achieved for any μ, by tuning the soft-breaking stau mass and third-generation slepton trilinear. The coannihilation regions end at $M_2 \simeq 600\,\text{GeV}$, because, with such heavy neutralinos, coannihilation is insufficient to annihilate dark matter. The coannihilation is predominantly slepton, because squarks must be heavy to evade LHC searches.

In the low-mass region in Fig. 4.6.1b, with $\mu \sim M_2$, there is a mixed neutralino region, which includes unclassified points. There is a gap with no points at $\mu \sim 150\,\text{GeV}$, because the relic density is smaller than its measured value. That the mixed region at $\mu \sim 100\,\text{GeV}$ exists is puzzling; why is the relic density as big as it is, given that the neutralino is mixed and that $\mu \sim 150\,\text{GeV}$ is forbidden? With $\mu \sim 100\,\text{GeV}$ and $\mu \sim M_2$, $m_\chi < M_W$ and the chargino is heavier than the LEP limit (see Fig. 4.6.1b). With $m_\chi < M_W$, higgsino-like annihilation to WW is off-shell and dark matter is annihilated by chargino coannihilation or by bulk mechanisms. With heavier M_2, achieving higgsino-like neutralinos with $m_\chi < M_W$ and charginos heavier than LEP's limit is impossible.

The ridge in the mixed region in Fig. 4.6.1b at $M_2 \simeq 400\,\text{GeV}$ is at $m_\chi < M_t$, at which point, because bulk sfermion exchange to $\bar{t}t$ is forbidden, μ may be smaller than would otherwise be permitted. Bulk exchange favours heavy fermion final states because it is helicity suppressed.

On the diagonal $\mu \approx 0.5 M_2 = M_1$ strip, beginning at $M_2 \sim 500\,\text{GeV}$, a combination of mechanisms annihilate dark matter. This is not surprising; within the MSSM, heavy neutralinos struggle to annihilate fast enough to reduce the relic density. In fact, $\mu \approx 0.5 M_2 = M_1$ naturally combines annihilation mechanisms. With $\mu \sim M_1$, the neutralino's composition is a bino-higgsino admixture (Fig. 4.6.2f).

The A-funnel with $m_A \approx 2 m_\chi$ begins at $m_A \simeq M_2 \simeq 500\,\text{GeV}$ (Fig. 4.6.2b); such heavy m_A is required to suppress $\text{BR}\left(B_s \to \mu^+\mu^-\right)$. All neutralinos in the A-funnel have a significant higgsino component. Without a higgsino component, A-funnel annihilation is impossible (Fig. 4.6.2b), because it is a bino-higgsino-pseudoscalar Higgs vertex. The A-funnel region is limited to the $\mu \approx 0.5 M_2 = M_1$ strip to insure that the neutralino is mixed.

As well as A-funnel annihilation, t-channel higgsino-like chargino exchange annihilates dark matter to WW on the $\mu \approx 0.5 M_2 = M_1$ strip, because the neutralino is mixed. With $\mu \lesssim M_2$, the higgsino fraction of the neutralino is such that the relic density is less than its measurement, resulting in the region with no points with $\Delta\chi^2 < 5.99$ in Fig. 4.6.1a. The diagonal strip flattens at $M_2 \sim 2\,\text{TeV}$ and mixed solutions exist with $\mu \sim 1\,\text{TeV}$ for $2\,\text{TeV} \lesssim M_2 \lesssim 4\,\text{TeV}$. With such large μ, the neutralino and chargino masses are degenerate. The chargino is "parasitic" rather than "symbiotic" [92] — it annihilates slower than the neutralino and increases the relic density, such that the relic density is not reduced below its measured value. Neutralino-chargino degeneracy determines the location on the (M_2, μ) plane of the mixed region. If it were possible to decouple chargino masses from higgsino-like neutralino masses, the mixed region would not occur at $\mu \approx 0.5 M_2 = M_1$, but at $\mu \gtrsim 0.5 M_2 = M_1$.

One might wonder; is there a maximum neutralino mass in our model, above which it is impossible to sufficiently annihilate dark matter? With case 1, $m_\chi < 1840\,\text{GeV}$ at 2σ, though this might result from our scanning ranges. Because the soft-breaking stau mass is $\leq 2000\,\text{GeV}$, after mixing, the lightest stau might be $\lesssim 1900\,\text{GeV}$. Because the neutralino must be our LSP, this would limit $m_\chi \lesssim 1900\,\text{GeV}$. Could an arbitrarily heavy neutralino sufficiently annihilate? Naïvely, one might expect that if its composition was solely higgsino, the neutralino could be $m_\chi \gg 2\,\text{TeV}$. With $\mu \ll M_1, M_2$, $m_\chi \simeq m_{\chi_1^\pm}$. The light $\chi_1^\pm$, however, increases the relic density, because the chargino annihilates slower than the neutralino. Charginos are "parasitic" rather than "symbiotic" [92]. A-funnel annihilation, however, could be sufficient for $m_\chi \gg 2\,\text{TeV}$. We find points with heavy neutralinos and $\mu \approx 0.5 M_2 = M_1$ in the A-funnel in Fig. 4.6.2a. Their scarcity in Fig. 4.6.2a might be because it is difficult to find points with heavy neutralinos in the A-funnel that satisfy all of the experimental constraints, i.e., solutions in the A-funnel with heavy neutralinos exist but are "fine-tuned." It might be impossible to satisfy all of the experimental constraints with $m_\chi \gtrsim 2\,\text{TeV}$ in the A-funnel [324].

There is, furthermore, coannihilation with sfermions on the $\mu \approx 0.5M_2 = M_1$ strip. The masses of neutralinos and sfermions are often degenerate (Fig. 4.6.2d and Fig. 4.6.2e). Because with $m_\chi \gtrsim 500\,\text{GeV}$ coannihilation alone cannot sufficiently annihilate dark matter, with $m_\chi \gtrsim 500\,\text{GeV}$ coannihilation appears only in conjunction with other mechanisms, which naturally occur on the diagonal $\mu \approx 0.5M_2 = M_1$ strip.

Hadronic uncertainties

We confirm in Fig. 4.6.3 that $\Sigma_{\pi N}$ significantly affects σ_p^{SI}; however, with Eq. 4.48 from Ref. [322], propagating the 1σ error from $\Sigma_{\pi N}$, the error in σ_p^{SI} is less than an order of magnitude, which was our previous estimate. With Eq. 4.47 from Ref. [321], σ_p^{SI} is ~ 3 times smaller than that with Eq. 4.48 from Ref. [322]. This result is independent of neutralino mass and composition.

Direct and indirect detection

We examine direct detection on the $\left(m_\chi, \sigma_p^{\text{SI}}\right)$ plane in Fig. 4.6.4. Because squarks are heavy, the t-channel Higgs exchange dominates σ_p^{SI}. σ_p^{SI} varies by ~ 5 orders of magnitude in our p9MSSM points with $\Delta\chi^2 < 5.99$. The h/Z-resonance is a vertical strip at $m_\chi \sim 75\,\text{GeV}$; σ_p^{SI} increases with the neutralino's higgsino component, which increases as μ decreases. The stau-coannihilation and $\tilde{f}$-coannihilation region at $m_\chi \sim 250\,\text{GeV}$ is similar. The mixed neutralino region is at $m_\chi \sim 1\,\text{TeV}$. σ_p^{SI} is largest in the A-funnel and mixed neutralino regions.

We examine indirect detection on the $(m_\chi, \langle\sigma v\rangle_{T\to 0})$ plane in Fig. 4.6.5. The quantity $\langle\sigma v\rangle_{T\to 0}$ is the neutralino annihilation rate at zero temperature, relevant now, in the late Universe. $\langle\sigma v\rangle_{T\to 0}$ is not zero in the zero temperature limit; it is the convolution of a cross section with a statistical weight is approximately a Dirac function at $s = 4m_\chi^2$ in Eq. 3.16. The plane exhibits similar behaviour to the $\left(m_\chi, \sigma_p^{\text{SI}}\right)$ plane in Fig. 4.6.4; we observe distinct mechanisms of dark matter annihilation, with $\langle\sigma v\rangle_{T\to 0}$ varying most in the h-resonance and coannihilation regions. The $\tilde{f}$-coannihilation and stau-coannihilation regions, however, bifurcate at $\langle\sigma v\rangle_{T\to 0} \sim 10^{-28}\,\text{pb}$. At zero temperature, $\sqrt{s} = 2m_\chi$ and only $L = 0$, $S = 0$ partial wave annihilation is possible, which is "helicity suppressed" (see Sec. 3.3.2).

Because of this "helicity suppression," bulk sfermion exchange $\chi\chi \to \bar{f}f$, significant if the sfermion is light, is proportional to m_f^2. Because the tau is much heavier than the electron and muon leptons, $\langle\sigma v\rangle_{T\to 0}$ with bulk stau exchange is larger than that with bulk selectron or smuon exchange. $\langle\sigma v\rangle_{T\to 0}$ is largest in the A-funnel, which avoids "helicity suppression" via a pseudoscalar Yukawa coupling, and in the mixed neutralino region, which avoids "helicity suppression" because its final state is WW, rather than fermions.

Naïvely, from an order of magnitude calculation, we might expect that $\langle\sigma v\rangle_{T\to 0} \sim 10^{-26}\mathrm{cm}^3\mathrm{s}^{-1}$ for $\Omega_\chi h^2 \sim 0.1$ [88]. We find, however, that $\langle\sigma v\rangle_{T\to 0}$ is ~ 5 orders of magnitude smaller than that in the h-resonance and coannihilation regions. In the coannihilation regions, the explanation is trivial. Our $\langle\sigma v\rangle_{T\to 0}$ includes only annihilation. Our relic density calculation, of course, includes coannihilation. In the h-resonance, the explanation is that the pertinent quantity in the relic density calculation is the thermally averaged annihilation cross section, rather than that in the zero temperature limit. As a function of $\sqrt{s}$, $\langle\sigma v\rangle_{T_{\mathrm{F.O.}}}$ spikes at $\sqrt{s} = m_h$. Thermally averaged over the spike at $\sqrt{s} = m_h$, the annihilation cross section is $\sim 10^{-26}\mathrm{cm}^3\mathrm{s}^{-1}$. The h/Z resonance cannot contribute to $\langle\sigma v\rangle_{T\to 0}$, because a CP-even resonance is forbidden in the $S = 0$ partial wave. The mixed neutralino region parallel to the h/Z-resonance at $m_\chi \sim 200\,\mathrm{GeV}$ is the $\mu \sim 100\,\mathrm{GeV}$ solution in Fig. 4.6.1b, for which chargino coannihilation is relevant, because of the WW threshold. Because WW is off-shell at $T = 0$, it cannot contribute to $\langle\sigma v\rangle_{T\to 0}$.

Including XENON100

We examine the impact of XENON100's 90% exclusion contour on the $\left(m_\chi, \sigma_p^{\mathrm{SI}}\right)$ plane (case 2) in Fig. 4.6.6 with separate determinations of $\Sigma_{\pi N}$. With Eq. 4.47 from Ref. [321] ($\Sigma_{\pi N} \simeq 43\,\mathrm{MeV}$), XENON100's impact is small — it excludes a fraction of $m_\chi \sim 100\,\mathrm{GeV}$ higgsino/gaugino mixed neutralino solutions with $250\,\mathrm{GeV} \lesssim m_\chi \lesssim 750\,\mathrm{GeV}$ (see Fig. 4.6.4), for which σ_p^{SI} via Higgs exchange is largest. By contrast, with Eq. 4.48 from Ref. [322] ($\Sigma_{\pi N} \simeq 66\,\mathrm{MeV}$), XENON100 excludes mixed neutralinos with $m_\chi \lesssim 1\,\mathrm{TeV}$. With each determination of $\Sigma_{\pi N}$, the majority of points with $\Delta\chi^2 < 5.99$ in case 1 are unaffected by XENON100. If realised, however, projected exclusion limits from XENON100 and from LUX would exclude most points with mixed neutralinos and a fraction of the coannihilation and h-

resonance regions, though small σ_p^{SI} in the coannihilation and h-resonance regions would be unaffected.

Including δa_μ

Because δa_μ is enhanced by chargino, neutralino, smuon and smuon-neutrino loop contributions, including δa_μ in our likelihood function (case 3) ought to limit their masses. Because the neutralino must be the LSP, δa_μ constrains m_χ via $m_{\tilde{\mu}}$. The points that survive case 3 with $\Delta\chi^2 < 5.99$ are scattered on the (M_2, μ) plane in Fig. 4.6.7. δa_μ is devastating; it excludes $M_2 \gtrsim 1200\,\text{GeV}$, including the A-funnel and $\chi_1^\pm$-coannihilation regions, and disfavours $\mu \gtrsim 2\,\text{TeV}$, including the h/Z-resonance and bulk regions. With light neutralinos, for $\mu \gtrsim 2\,\text{TeV}$ in the h/Z-resonance and bulk regions, δa_μ is larger than its measurement. For $M_2 \gtrsim 1200\,\text{GeV}$, δa_μ is suppressed by heavy sparticles.

We examine the relevant sparticle masses in Fig. 4.6.8. The $\left(m_{\tilde{\mu}_R}, m_\chi\right)$ plane in Fig. 4.6.8a demonstrates that δa_μ excludes $m_{\tilde{\mu}_R} \gtrsim 500\,\text{GeV}$ at 2σ. In conjunction with our likelihood functions (case 3), δa_μ permits narrow bands of points at 2σ. The band closest to the unphysical region with $m_{\tilde{\mu}_R} \approx m_\chi$ is $\tilde{f}$-coannihilation with a slepton. The lightest permitted neutralino masses at $m_\chi \sim 100\,\text{GeV}$ are the h/Z resonance and the bulk regions. The "hook" feature at $m_\chi \lesssim 100\,\text{GeV}$ and $m_{\tilde{\mu}_R} \simeq 200\,\text{GeV}$ is the region in which $m_\chi < M_W$ in Fig. 4.6.1b. The remainder is mixed neutralino solutions with $\mu \approx 0.5 M_2$. The $\left(m_{\tilde{\nu}_\mu}, m_{\chi_1^\pm}\right)$ plane in Fig. 4.6.8b is similar. δa_μ excludes $m_{\tilde{\nu}_\mu} \gtrsim 500\,\text{GeV}$ at 2σ. The strip closest to the unphysical region is the h/Z-resonance and bulk region at $m_{\tilde{\nu}_\mu} \lesssim 100\,\text{GeV}$ and the coannihilation regions at $m_{\tilde{\nu}_\mu} \gtrsim 100\,\text{GeV}$. The second strip is the mixed region. Triangular regions of the planes are unphysical, because χ was not the LSP.

Electroweak search

With $\sim 10^6$ points, including LHC searches at the event level was impracticable with our computers. Instead, we included the CMS electroweak search for $3\ell + \not{E}_T$ at the event level for a subset of $\sim 2\%$ of randomly chosen points with $\Delta\chi^2 < 5.99$ in case 1. Because this search constrains m_χ, it might be in tension with δa_μ. We plot $(m_\chi, \delta a_\mu)$ in Fig. 4.6.9. We find that, whilst δa_μ requires $m_\chi \lesssim 500\,\text{GeV}$, the electroweak search requires $m_\chi \gtrsim 200\,\text{GeV}$. The exact limit from the electroweak search depends on the chargino mass and chargino and neutralino compositions.

There exists an interval $200\,\text{GeV} \lesssim m_\chi \lesssim 500\,\text{GeV}$ that is in agreement with δa_μ, the electroweak search and with the likelihoods in case 1.

Minimum χ^2

We identify the minimum χ^2 in four cases: basic likelihoods (case 1), basic and δa_μ likelihoods (case 3), basic and XENON100 likelihoods (case 2), and basic, δa_μ and XENON100 likelihoods (case 4). The χ^2_{Min} with all likelihoods is ~ 6.4 from 9 Gaussian likelihoods, XENON100, the electroweak search and α_T, with 13 fitted parameters. The model cannot span the whole observable space, else the χ^2_{Min} would be zero, because the number of fitted parameters is greater than the number of constraints. Whilst this χ^2_{Min} is ostensibly improbable, we cannot calculate a p-value because there are, ostensibly, less than one degrees of freedom.

We breakdown the contributions to the χ^2_{Min} in Fig. 4.6.10. $B_u \to \tau\nu$ and ΔM_{B_s} are significant $\chi^2 \sim 2$ contributions. Electroweak precision observables, Higgs mass, $\Omega_\chi h^2$, $b \to s\gamma$ and $B_s \to \mu^+\mu^-$ are negligible contributions. Whilst the χ^2 from δa_μ is substantial in case 1, in case 3, in which it is minimised, it is negligible, though the χ^2 from electroweak precision observables increases. Including XENON100 and δa_μ further increases the contribution from electroweak precision observables. That χ^2 from $B_u \to \tau\nu$ was significant was surprising; $\text{BR}\,(B_u \to \tau\nu)$ in our p9MSSM ought to be similar to that in the Standard Model, because the charged Higgs is heavy (see Eq. 3.51). We found that our Standard Model prediction for $\text{BR}\,(B_u \to \tau\nu)$ with `SuperIso` [281,282], $\sim 0.8 \times 10^{-4}$, was considerably smaller than that of the CKM-fitter collaboration [184], $1.68 \pm 0.31 \times 10^{-4}$.

Neutralino, Higgs and sparticle mass spectrum

We examine sparticle mass spectra with the best-fit and confidence intervals with our four likelihood functions in Fig. 4.6.11. The best-fit lightest neutralino in case 1 is $m_\chi = 1050\,\text{GeV}$, with $m_\chi \in (51\,\text{GeV}, 1211\,\text{GeV})$ at 1σ and $m_\chi \in (51\,\text{GeV}, 1840\,\text{GeV})$ at 2σ. With XENON100 in case 2, because intermediate neutralino masses are forbidden, the neutralino's 1σ confidence interval has disconnected modes in the coannihilation and mixed regions. The lightest and heaviest permitted masses at 1σ are $(60\,\text{GeV}, 1184\,\text{GeV})$. The best-fit mass, however, is in the heavy mixed region with $m_\chi = 1049\,\text{GeV}$. With δa_μ in case 3, the neutralino must be light. The best-fit is $m_\chi = 296\,\text{GeV}$ and $m_\chi \in (78\,\text{GeV}, 357\,\text{GeV})$ at 1σ. The heaviest permitted mass at 2σ is $m_\chi \leq 474\,\text{GeV}$.

Unlike in the CMSSM in Sec. 4.5.4, the calculated Higgs mass is sufficiently heavy — $m_h \sim 126\,\text{GeV}$ in each mode, achieved with heavy stops with large mixing. The lightest Higgs is, however, only approximately Standard Model-like, with couplings strengths that deviate from those in the Standard Model by ±20%, illustrated in Fig. 4.6.12. Positive deviations are especially prevalent in the bulk and h/Z-resonance regions, whereas negative deviations are prevalent for all annihilation mechanisms. Because m_A cannot be arbitrarily light in A-funnel, the Higgs is Standard Model-like in the A-funnel. If $m_A \gg M_Z$, the Higgs' tree-level couplings to Standard Model fields is Standard Model-like. Couplings can, however, be affected by sparticle loops, especially stau and chargino loops in triangle diagrams.

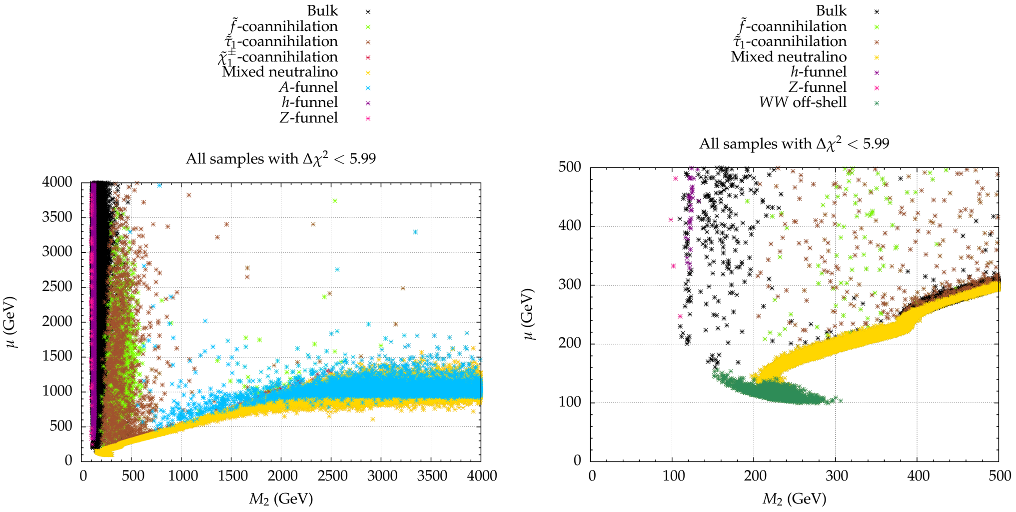

(a) *Full range.* **(b)** *Low-mass region.*

Figure 4.6.1: *Scatter of p9MSSM points permitted at 2σ in case 1 on the (M_2, μ) plane, coloured by possible dark matter annihilation mechanisms. The colour scheme and definitions are those in Fig. 4.6.2: h-resonance is yellow, A-funnel red, stau-coannihilation green, $\chi_1^{\pm}$-coannihilation blue, $\tilde{f}$-coannihilation magenta, mixed neutralino cyan and unclassified black. The categories are not mutually exclusive.*

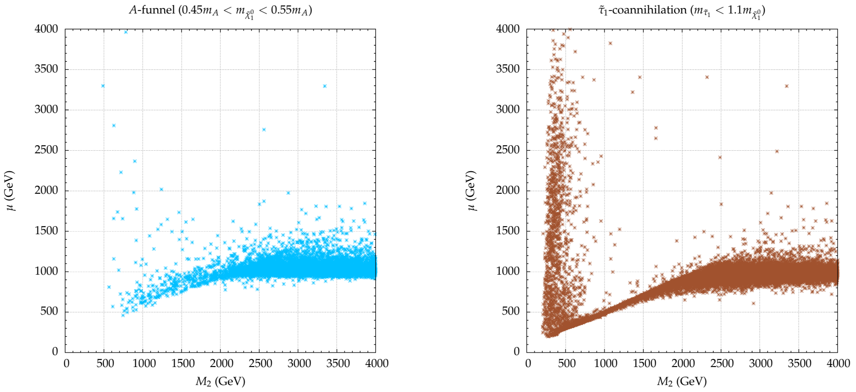

(a) *A-funnel.* **(b)** *Stau-coannihilation.*

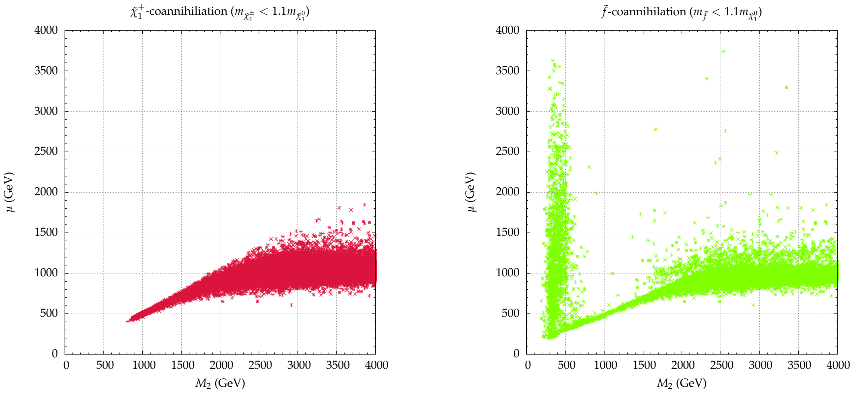

(c) *$\chi_1^{\pm}$-coannihilation.* **(d)** *$\tilde{f}$-coannihilation.*

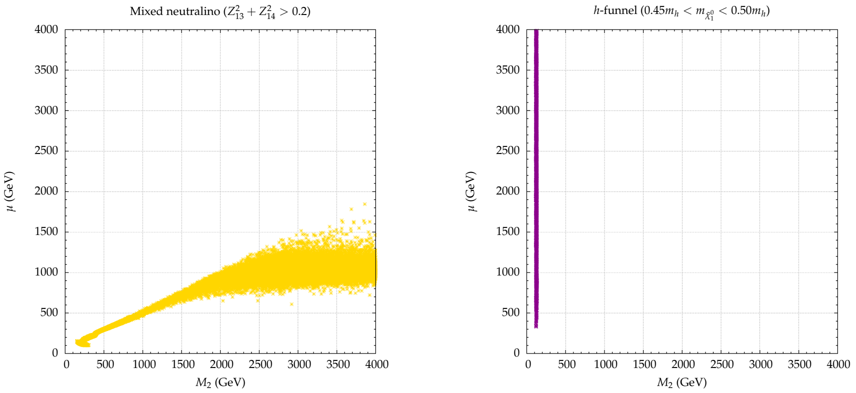

(e) *Mixed neutralino.* **(f)** *h-resonance.*

Figure 4.6.2: *Scatter of p9MSSM points permitted at 2σ in case 1 on the (M_2, μ) plane, split by possible dark matter annihilation mechanisms.*

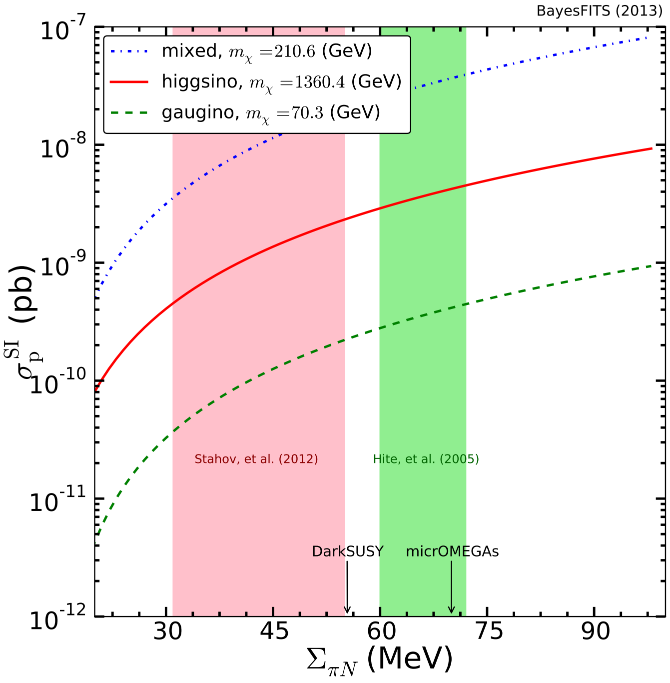

Figure 4.6.3: *The spin-independent neutralino-proton scattering cross-section against π-nucleon σ-term, $\Sigma_{\pi N}$, for gaugino, higgsino and mixed neutralino composition. The pink (green) band is the 1σ interval for $\Sigma_{\pi N}$ from Ref. [321] (Ref. [322]). The arrows on the abscissa mark the default values of $\Sigma_{\pi N}$ in* `MicrOMEGAs` *and* `DarkSUSY`*.*

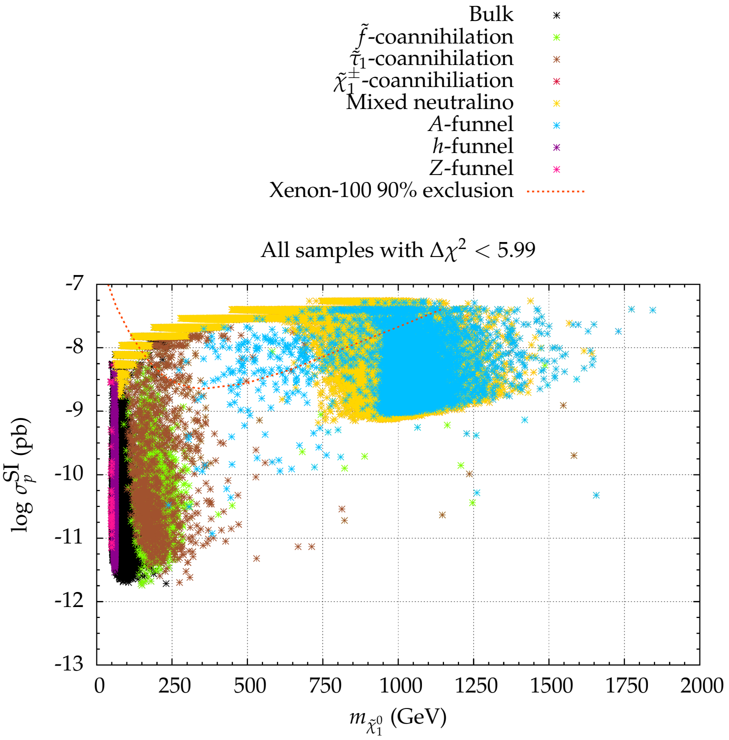

Figure 4.6.4: *p9MSSM predictions for direct detection. p9MSSM points with $\Delta\chi^2 < 5.99$ in case 1 are scattered on the $\left(m_\chi, \sigma_p^{SI}\right)$ plane, split by possible dark matter mechanisms.*

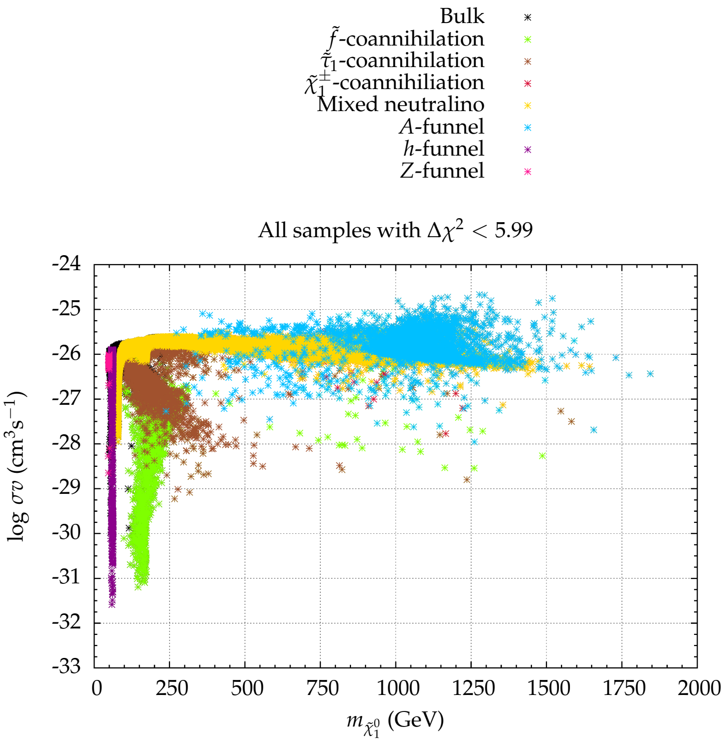

Figure 4.6.5: *p9MSSM predictions for indirect detection. p9MSSM points with $\Delta\chi^2 < 5.99$ in case 1 are scattered on the $(m_\chi, \langle\sigma v\rangle_{T\to 0})$ plane, split by possible dark matter mechanisms.*

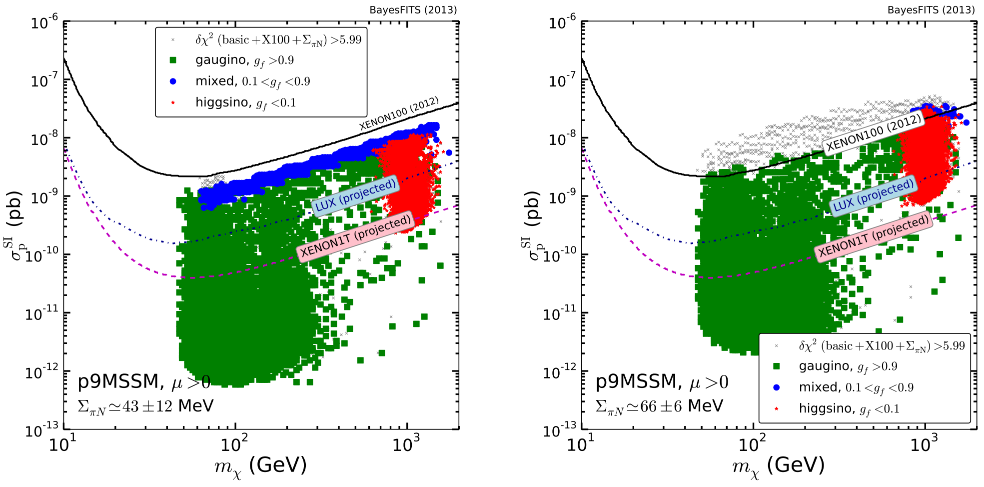

(a) *$\left(m_\chi, \sigma_p^{SI}\right)$ plane with $\Sigma_{\pi N} \simeq 43$ MeV [321].*

(b) *$\left(m_\chi, \sigma_p^{SI}\right)$ plane with $\Sigma_{\pi N} \simeq 66$ MeV [322].*

Figure 4.6.6: *Points permitted by XENON100 direct detection in case 2 scattered on the p9MSSM's $\left(m_\chi, \sigma_p^{SI}\right)$ and (M_2, μ) planes.*

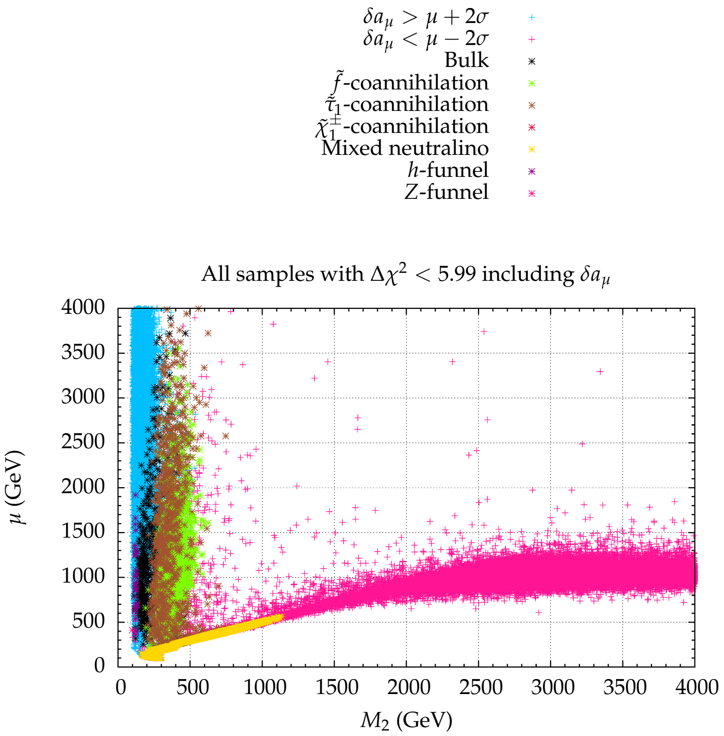

Figure 4.6.7: *Points permitted by δa_μ (case 3) scattered on the p9MSSM's (M_2, μ) plane, coloured by their dark matter annihilation mechanism. The blue and pink crossed are excluded by δa_μ.*

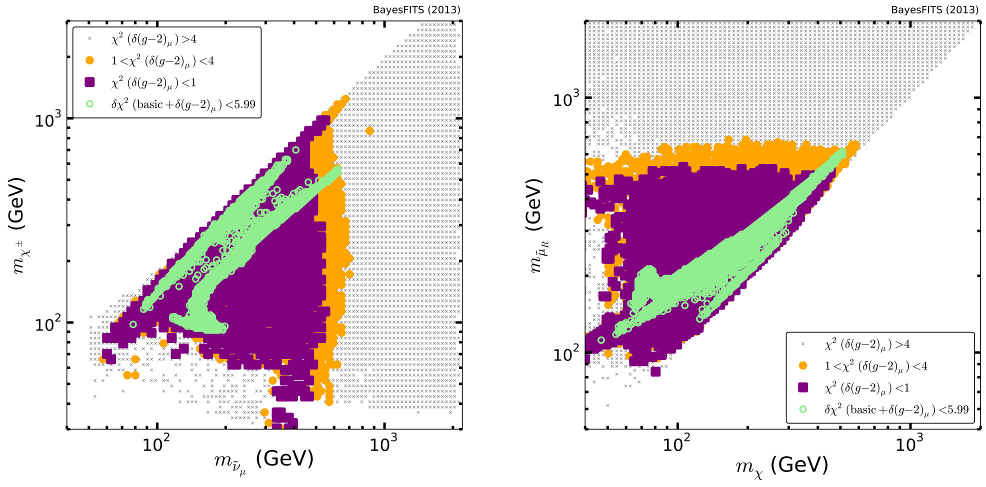

(a) $(m_{\tilde{\mu}_R}, m_\chi)$ *plane.*

(b) $\left(m_{\tilde{\nu}_\mu}, m_{\chi_1^\pm}\right)$ *plane.*

Figure 4.6.8: *All points scattered on the p9MSSM's $(m_{\tilde{\mu}_R}, m_\chi)$ and $\left(m_{\tilde{\nu}_\mu}, m_{\chi_1^\pm}\right)$ planes. Purple (orange) points agree with δa_μ alone at 1σ (2σ). Green points are within the 2σ confidence interval in case 3, which includes δa_μ and other experiments.*

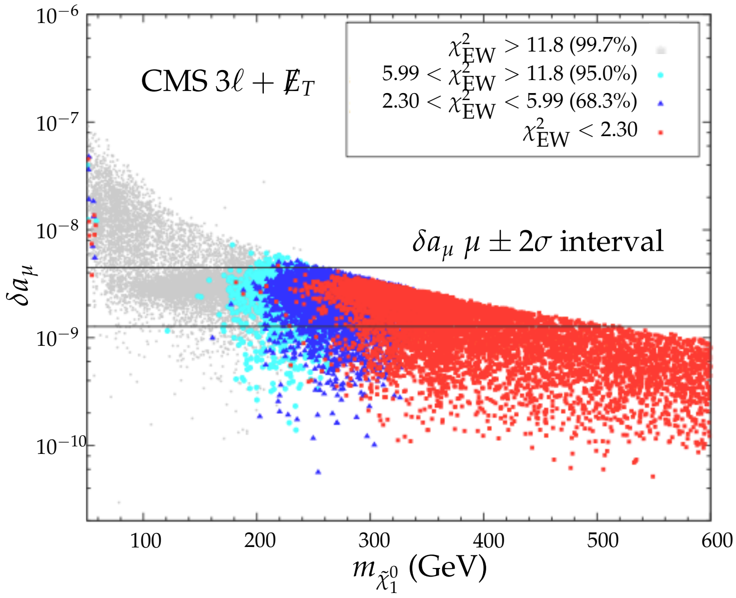

Figure 4.6.9: *Selection of p9MSSM points with $\Delta\chi^2 < 5.99$ in case 1 scattered on the $(\delta a_\mu, m_\chi)$ plane coloured by their agreement with the CMS $3\ell + \not{E}_T$ electroweak search. The horizontal lines enclose the 2σ experimental confidence interval for δa_μ.*

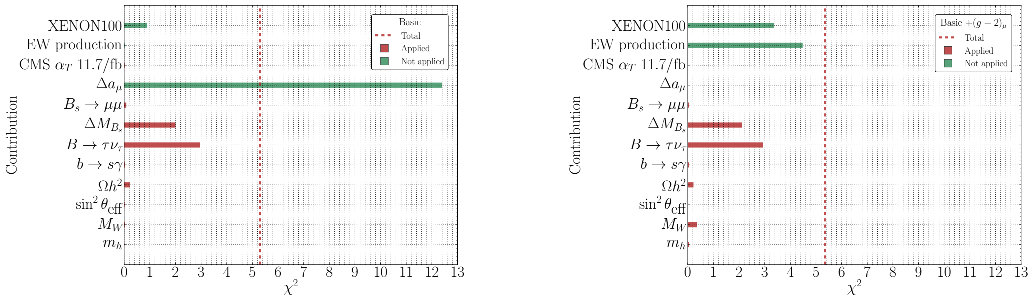

(a) *Basic likelihoods only (case 1).*

(b) *Basic and δa_μ likelihoods (case 3).*

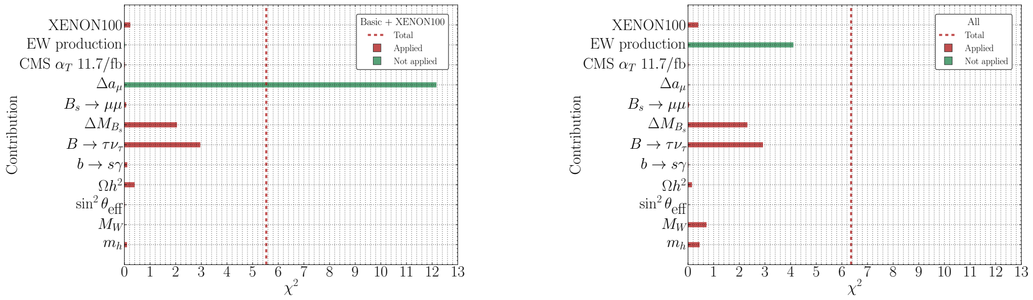

(c) *Basic and XENON100 likelihoods (case 2).*

(d) *Basic, δa_μ and XENON100 likelihoods (case 4).*

Figure 4.6.10: *Breakdown of the χ^2 at the best-fit point in the p9MSSM in four cases: (a) basic likelihoods (case 1), (b) basic and δa_μ likelihoods (case 3), (c) basic and XENON100 likelihoods (case 2), and (a) basic, δa_μ and XENON100 likelihoods (case 4). Whilst in each plot all contributions are plotted, only specific contributions were minimised in each case. Contributions that were (were not) minimised are shown with red (green) bars. The total χ^2 in each case is marked with a vertical dashed red line.*

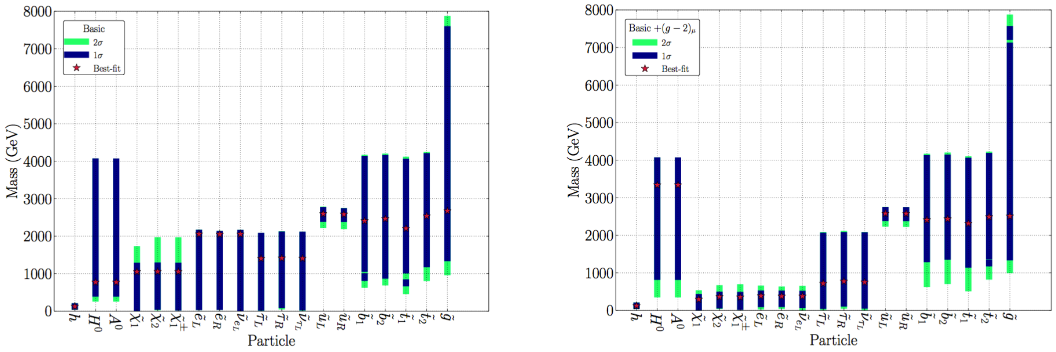

(a) *Basic likelihoods only (case 1).*

(b) *Basic and δa_μ likelihoods (case 3).*

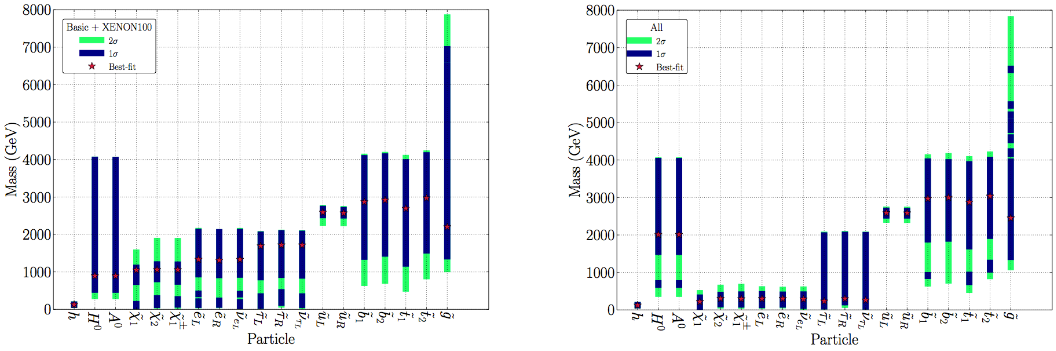

(c) *Basic and XENON100 likelihoods (case 2).*

(d) *Basic, δa_μ and XENON100 likelihoods (case 4).*

Figure 4.6.11: *Best-fitting mass spectra in the p9MSSM for four likelihood combinations identical to those in Fig. 4.6.10. 1σ (2σ) confidence intervals are shown with blue (green) bars and best-fitting mass spectra with red stars.*

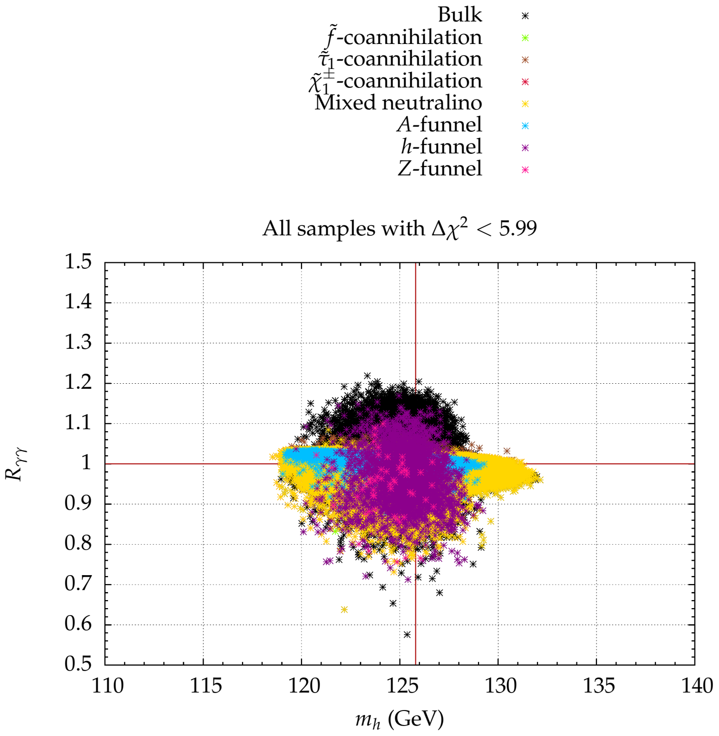

Figure 4.6.12: *Higgs coupling strength to $\gamma\gamma$ against mass for points with $\Delta\chi^2 < 5.99$ in case 1. The Standard Model is axiomatically $R_{\gamma\gamma} = 1$.*

Chapter 5

Conclusions

I began by introducing pertinent theory; in Chap. 1 I reviewed supersymmetry and explained that low-scale supersymmetry is motivated by experimental and theoretical puzzles. I introduced tractable, unified models, including the CMSSM, the predictions of which I would compare with experiment with Bayesian statistics, which I reviewed in Chap. 2. I reviewed the relevant experiments in Chap. 3, including Higgs searches, dark matter, B-physics, the muon's anomalous magnetic moment and electroweak precision observables.

I presented my findings — Bayesian analyses of supersymmetric models' parameter spaces — in Chap. 4. I investigated constrained and phenomenological supersymmetric models, including the CMSSM, and included several experimental constraints, including future experiments and the strongest contemporary experimental constraints.

In Sec. 4.2, I investigated a benchmark scenario in which sparticles were measured at the LHC via a "golden decay." Our Bayesian analysis demonstrated that, although we could recover the CMSSM's Lagrangian parameters, we would struggle to recover the Lagrangian parameters of relaxed NUHM, NUG and pMSSM models, and struggle to discriminate between patterns of soft-breaking masses, even with additional information from dark matter measurements. We, furthermore, investigated *de facto* priors in the CMSSM, NUHM, NUG and pMSSM by including only physicality conditions.

We updated our "golden decay" analysis to a heavy benchmark point in Sec. 4.3. By replicating CMS methodologies to simulate the "golden decay" at the event level in Monte-Carlo, we found a covariance matrix describing hypothetical sparticle mass measurements. We investigated parameter reconstruction in the CMSSM, finding that whilst we could recover soft-breaking masses, we struggled to recover the soft-breaking trilinear, even with additional information from dark matter and Higgs measurements.

In Sec. 4.4, we included the strongest available experimental constraints in a Bayesian analysis of the CMSSM. This required that we build a likelihood function describing the CMS α_T $1.1\,\text{fb}^{-1}$ search for supersymmetry with Monte-Carlo simulations. We found that the Bayesian credible regions of the CMSSM's parameter space were dramatically shifted to heavier masses by the CMS α_T search, but that the CMSSM remained simultaneously compatible with all experimental constraints. The stau-coannihilation mechanism of dark matter annihilation was favoured.

The CMS α_T $1.1\,\text{fb}^{-1}$ search was surpassed by the CMS Razor $5\,\text{fb}^{-1}$ search. We again built a likelihood function at the event-level with Monte-Carlo simulations. We included, *inter alia*, the CMS Razor search, an updated $B_s \to \mu^+\mu^-$ upper limit and, significantly, the Higgs discovery in our Bayesian analysis of the CMSSM in Sec. 4.5. We found that the credible regions favoured the A-funnel, rather than the stau-coannihilation region, with heavy sparticle masses, but that the CMSSM preferred Higgs masses lighter than that which was measured. Because with such heavy sparticles δa_μ could not be satisfied, we omitted it from our likelihood function and investigated each $\operatorname{sgn}\mu = \pm 1$. Remarkably, we found that, without δa_μ, $\operatorname{sgn}\mu = -1$ was insignificantly preferred. Whilst the agreement with the data was poor, we declined to declare that the CMSSM was excluded, because our likelihood functions were non-Gaussian and because our algorithm was optimised for Bayesian, rather than frequentist, analysis.

In Sec. 4.6, we investigated a tractable p9MSSM, focusing on dark matter, including its relic density, direct detection and indirect detection. We found that a broad range of neutralino masses and compositions could agree with relic density measurements via a variety of annihilation mechanisms, and that the cross sections relevant to direct and indirect detection varied by orders of magnitude. We investigated the impact of uncertainties in direct detection by repeating our analysis with a different assumption for hadronic uncertainties.

In summary, having reviewed supersymmetry, pertinent experiments and Bayesian statistics and algorithms, I applied Bayesian statistics to constrained and phenomenological supersymmetric models in benchmark scenarios and with the strongest contemporary experimental constraints, building likelihood functions at the event-level in Monte-Carlo. I presented in detail the results: credible regions of the models' parameter spaces, the models' predictions, particularly for dark matter direct detection experiments, and agreement with data.

I was fortunate that our analyses coincided with the early years of the LHC, a watershed moment in particle physics. We published timely, noteworthy analyses, and it was a personally enjoyable, challenging time. The results in Sec. 4.5 in particular were conducted around the discovery of the Higgs boson, an exciting moment with frenzied activity in our community. Although there was no sign of supersymmetry, there were rumours, especially in the CMS α_T $1.1\,\text{fb}^{-1}$ search in Sec. 4.5. I conclude with my personal thoughts on the status of SUSY. LHC experiments, including the discovery of the Higgs boson, are in concordance that the scale of supersymmetry breaking must be heavier than that which was expected; however, the motivations for introducing supersymmetry in Sec. 1.1 are unspoiled, and even the CMSSM is simultaneously compatible with all experiments. "Naturalness," however, is a problem in MSSM-type models. As I hinted in Sec. 2.1, I believe that "naturalness" is statistical in nature rather than an aesthetic criterion. If supersymmetry is discovered, I suspect that a mechanism "naturally" generates $\mu \sim M_\text{SUSY}$, probably spontaneously, as in the next-to-minimal MSSM, or, if not, that "naturalness" incorporates problems beyond that which we usually consider, e.g., the cosmological constant, or even beyond that which we know. I believe that it is most likely that $M_\text{SUSY} \lesssim 10\,\text{TeV}$, so that supersymmetry can explain dark matter and insure gauge coupling unification, though neither is strictly necessary. I hope that the LHC $\sqrt{s} = 13\,\text{TeV}$ phase will definitively settle the matter, but perhaps we will be left to speculate for a while longer.

Appendix A

Experimental constraints

Sparticle	Mass limit	Alternative hierarchy	Theory error	Function	Reference
LEP sparticle mass 95% limits					
χ	> 50		5%	Lower limit Error Function	[163,325,326]
$\chi_1^{\pm}$	> 103.5	> 92.4	*v.s.*	*v.s.*	[325,326]
$\tilde{e}_R$	> 100	> 73	*v.s.*	*v.s.*	*v.s.*
$\tilde{\mu}_R$	> 95	> 73	*v.s.*	*v.s.*	*v.s.*
$\tilde{\tau}_1$	> 87	> 73	*v.s.*	*v.s.*	*v.s.*
$\tilde{t}_1$	> 95	> 65	*v.s.*	*v.s.*	*v.s.*
$\tilde{b}_1$	> 95	> 59	*v.s.*	*v.s.*	*v.s.*
Tevatron sparticle mass 95% limits					
$\tilde{\nu}$	> 94	> 43	5%	Lower limit Error Function	[327] ([328])
$\tilde{q}$	> 375		*v.s.*	*v.s.*	[329]
$\tilde{g}$	> 289		*v.s.*	*v.s.*	*v.s.*
LEP Higgs mass and coupling 95% limits					
h	> 114.4		3	Lower limit Error Function	[111]
ζ_h^2	$< f(m_h)$		0	Upper limit Step Function	*v.s.*

Table A.1: *LEP and Tevatron indirect limits on sparticle masses and the Higgs mass and Z-boson coupling. Masses are in GeV. The alternative hierarchies are detailed in Ref. [71].*

Observable	ATLAS SU3	CMSSM 1 fb^{-1}	CMSSM 4.4 fb^{-1}+Higgs	p9MSSM	High mass
Non-LHC					
Ωh^2	$0.2332 \pm 0.0062 \pm 10\%$ [330]*	$0.1120 \pm 0.0056 \pm 10\%$ [86]	*Id.*	$0.1199 \pm 0.0027 \pm 10\%$ [303]	*Id.*
$\sin\theta_{\text{eff}}$		$0.23116 \pm 0.00013 \pm 0.00015$ [328]†	*Id.*	$0.23146 \pm 0.00012 \pm 0.00015$ [71]	
$M_W(\,\text{GeV})$		$80.399 \pm 0.023 \pm 0.015$ [328]	*Id.*	*Id.*	
$\delta a_\mu \times 10^{10}$		$30.5 \pm 8.6 \pm 1.0$ [199,328]	$28.7 \pm 8.0 \pm 1.0$ [328]	*Id.*	
$\text{BR}\,(b \to s\gamma) \times 10^4$		$3.60 \pm 0.23 \pm 0.21$ [328]	*Id.*	$3.43 \pm 0.22 \pm 0.21$ [173,174]	
$\text{BR}\,(B_u \to \tau\nu) \times 10^{-4}$		$1.66 \pm 0.66 \pm 0.38$ [189]	*Id.*	*Id.*	
$\Delta M_{B_s}(\,\text{ps}^{-1})$		$17.77 \pm 0.12 \pm 2.40$ [328]	*Id.*	$17.719 \pm 0.043 \pm 2.400$ [71]	
Nuisance					
$1/\alpha_{\text{em}}(M_Z)^{\overline{MS}}$	127.955 [331]	127.916 ± 0.015 [328]	*Id.*	127.916 [71]	*Id.*
$M_t(\,\text{GeV})$	172.6 [331]	172.9 ± 1.1 [328]	*Id.*	173.5 ± 1.0 [71]	173.5 [71]
$m_b(m_b)^{\overline{MS}}(\,\text{GeV})$	4.20 [331]	4.19 ± 0.12 [328]	*Id.*	4.18 ± 0.03 [71]	4.18 [71]
α_s	0.1176 [331]	0.1184 ± 0.0006 [328]	*Id.*	0.1184 [71]	*Id.*

Table A.2: *Experimental measurements (cf. limits) in likelihoods in the five studies in Chap. 4, with experimental (statistical and systematic combined) and theoretical errors. The likelihoods for these observables were Gaussian. If an entry is Id., see left. If an entry is blank, that measurement was not included in the study. If a measurement has no errors, it was fixed to its mean.*

**The mean Ωh^2 is the Ωh^2 in our hypothetical ATLAS SU3 scenario, whilst the experimental error is that achieved by WMAP.*

†*Value applied is for the wrong renormalisation scheme, which was corrected only in later work.*

	Status	Experimental result	Likelihood function
ATLAS SU3	Upper limit	BR $(B_s \to \mu^+\mu^-) < 1.5 \times 10^{-8} \pm 14\%$ [180]	Not applied
CMSSM 1 fb^{-1}	*v.s.*	*v.s.*	Upper limit Error Function
CMSSM 4.4 fb^{-1}+Higgs	*v.s.*	BR $(B_s \to \mu^+\mu^-) < 4.5 \times 10^{-9} \pm 14\%$ [181]	*v.s.*
p9MSSM	Significant measurement	BR $(B_s \to \mu^+\mu^-) = 3.2^{+1.5}_{-1.2} \times 10^{-9} \pm 10\%$ [182]	Two half-Gaussians
High mass	*v.s.*	*v.s.*	Not applied

Table A.3: *Likelihood functions for BR $(B_s \to \mu^+\mu^-)$ in the five studies in Chap. 4. The error function is described in the text. Where two errors are shown, the errors are experimental (combined statistical and systematic) and theoretical, respectively. Where one error is shown, the error is theoretical.*

	LHC	$\int \mathcal{L}\,\mathrm{d}t$	$\sqrt{s}$	Likelihood function
ATLAS SU3	ATLAS simulated golden decay	$1\,\mathrm{fb}^{-1}$	7 TeV	Multivariate Gaussian
CMSSM $1\,\mathrm{fb}^{-1}$	CMS α_T [309]	$1.1\,\mathrm{fb}^{-1}$	7 TeV	Poisson — map on $(m_0, m_{1/2})$ plane
CMSSM $4.4\,\mathrm{fb}^{-1}$+Higgs	CMS Razor [312]	$4.4\,\mathrm{fb}^{-1}$	7 TeV	*v.s.*
p9MSSM	CMS α_T [318]	$11.7\,\mathrm{fb}^{-1}$	8 TeV	Poisson — subset of points
	CMS $3\ell + \not{E}_T$ [319]	$9.2\,\mathrm{fb}^{-1}$	8 TeV	Poisson — subset of points
High mass	Simulated golden decay	$100\,\mathrm{fb}^{-1}$	14 TeV	Multivariate Gaussian

Table A.4: *Likelihood functions for LHC SUSY searches in the five studies in Chap. 4. The likelihood maps are explained in detail in Chap. 4.*

	Status	Experimental result	Theory error	Likelihood function
ATLAS SU3	LEP limits [111]	$m_h > 114.4\,\text{GeV}$	2 GeV	Not applied
CMSSM 1 fb^{-1}	*v.s.*	*v.s.*	*v.s.*	Lower limit Error function
CMSSM 4.4 fb^{-1}+Higgs	Strong- ATLAS [127] and CMS [124] limits	$m_h \in (117.5\,\text{GeV}, 118.5\,\text{GeV})$ $(122.5\,\text{GeV}, 127.5\,\text{GeV})$	*v.s.*	Box-car function
	and hints at $\sim 3\sigma$	$m_h = 125 \pm 2\,\text{GeV}$	*v.s.*	Gaussian
p9MSSM	CMS [123] discovery	$m_h = 125.8 \pm 0.6\,\text{GeV}$	3 GeV	*v.s.*
High mass	*v.s.*	*v.s.*	*v.s.*	*v.s.*

Table A.5: *Likelihood functions for Higgs mass in the five studies in Chap. 4. The box-car functions and error function are described in the text. Where two errors are shown, the errors are experimental (combined statistical and systematic) and theoretical, respectively. Where one error is shown, the error is theoretical.*

Appendix B

Priors

Parameter	Prior range	Scale
CMSSM		
m_0	100, 4000	Linear
$m_{1/2}$	100, 2000	Linear
A_0	-4000, 4000	Linear
$\tan\beta$	3, 62	Linear
$\operatorname{sgn}\mu$	$+1$	Fixed
Nuisance		
M_t	173.5	Fixed
$m_b(m_b)^{\overline{MS}}$	4.19	Fixed
$\alpha_s(M_Z)^{\overline{MS}}$	0.1184	Fixed
$1/\alpha_{\text{em}}(M_Z)^{\overline{MS}}$	127.944	Fixed

Table B.1: *Priors in ourHigh mass study in Sec. 4.3. Mass parameters and trilinear couplings are in GeV.*

Parameter	Prior range	Scale
CMSSM		
m_0	25, 1000	Log/linear
$m_{1/2}$	25, 1000	Log/linear
A_0	$-7000, 7000$	Linear
$\tan\beta$	2, 65	Linear
$\operatorname{sgn}\mu$	$+1$	Fixed
NUHM, CMSSM plus soft-breaking Higgs masses		
m_{H_d}, m_{H_d}	25, 1000	Log/linear
NUG, CMSSM plus soft-breaking gaugino masses		
M_1, M_2, M_3	25, 1000	Log/linear
p12MSSM		
M_2, $A_{u,c,t}$, $A_{d,s,b}$, $A_{e,\mu,\tau}$	1, 1000	Log/linear
m_A, μ, $m_{\tilde{L}_{1,2,3}}$, $m_{\tilde{\tilde{e}}_{1,2,3}}$, $m_{\tilde{Q}_{1,2,3}}$, $m_{\tilde{\tilde{u}}_{1,2,3}}$, $m_{\tilde{\tilde{d}}_{1,2,3}}$	100, 1000	Log/linear
$\tan\beta$	2, 60	Linear
p14MSSM: p12MSSM plus soft-breaking gaugino masses		
M_1, M_2, M_3	1, 1000	Log/linear
Nuisance		
M_t	163.7, 178.1	Linear
$m_b(m_b)^{\overline{MS}}$	3.92, 4.48	Linear
$\alpha_s(M_Z)^{\overline{MS}}$	0.1096, 0.1256	Linear
$1/\alpha_{\text{em}}(M_Z)^{\overline{MS}}$	127.846, 127.99	Linear

Table B.2: *Priors in our ATLAS SU3 study in Sec. 4.2. Mass parameters and trilinear couplings are in GeV. Note that a mistake in Ref. [286] is corrected.*

Parameter	Prior range	Scale
CMSSM		
m_0	100, 2000	Log
$m_{1/2}$	100, 1000	Log
A_0	$-2000, 2000$	Linear
$\tan\beta$	3, 62	Linear
$\mathrm{sgn}\,\mu$	$+1$	Fixed
Nuisance		
M_t	163.7, 178.1	Linear
$m_b(m_b)^{\overline{MS}}$	3.92, 4.48	Linear
$\alpha_s(M_Z)^{\overline{MS}}$	0.1096, 0.1256	Linear
$1/\alpha_{\text{em}}(M_Z)^{\overline{MS}}$	127.846, 127.99	Linear

Table B.3: *Priors for the CMSSM's parameters and for the Standard Model's nuisance parameters in our CMSSM $1 fb^{-1}$ study in Sec. 4.4. Masses are in GeV.*

Parameter	Prior range	Scale
CMSSM		
m_0	100, 4000	Log
$m_{1/2}$	100, 1000	Log
A_0	$-7000, 7000$	Linear
$\tan\beta$	3, 62	Linear
$\mathrm{sgn}\,\mu$	$+1$ and -1	Fixed
Nuisance		
M_t	172.9 ± 1.1	Gaussian
$m_b(m_b)^{\overline{MS}}$	4.19 ± 0.12	Gaussian
$\alpha_s(M_Z)^{\overline{MS}}$	0.1184 ± 0.0007	Gaussian
$1/\alpha_{\text{em}}(M_Z)^{\overline{MS}}$	127.916 ± 0.015	Gaussian

Table B.4: *Priors for the CMSSM's parameters and for the Standard Model's nuisance parameters in our CMSSM $4.4 fb^{-1}$+Higgs study in Sec. 4.5. Masses are in GeV.*

Parameter	Range	Scale
p9MSSM		
M_1	$M_1 = 0.5M_2$	Dependent on M_2
M_2	10, 4000	Linear and log combined
M_3	700, 8000	Linear and log combined
$m_{\tilde{Q}_{1,2}}$	2500	Fixed
$m_{\tilde{Q}_3}$	300, 4000	Linear and log combined
$m_{\tilde{L}_{1,2}}$	$m_{\tilde{L}_{1,2}} = M_1 + 50$	Dependent on M_1
$m_{\tilde{L}_3}$	100, 2000	Linear and log combined
A_t	-7000, 7000	Linear
A_τ	-7000, 7000	Linear
A_b	-500	Fixed
m_A	200, 4000	Linear and log combined
μ	10, 4000	Linear and log combined
$\tan\beta$	3, 62	Linear
Nuisance		
M_t	173.5 ± 1.0	Gaussian
$m_b(m_b)^{\overline{MS}}$	4.18 ± 0.03	Gaussian

Table B.5: *Scanning ranges for our p9MSSM and Standard Model nuisance parameters in our p9MSSM study in Sec. 4.6. All masses are in GeV. Note that because the p9MSSM study was frequentist rather than Bayesian, these ranges are not priors. "Combined" indicates that chains with each scale were concatenated.*

Bibliography

[1] S. Glashow, *"Partial Symmetries of Weak Interactions,"* Nucl.Phys. 22 (1961) 579.
Cited on page: 1.

[2] A. Salam, *"Weak and Electromagnetic Interactions,"* Elementary Particle Theory: Relativistic Groups and Analyticity, edited by N. Svartholm, pp. 367–377, Aspenäsgården, Göteborg, Sweden, 1968, The Nobel Symposium 8.

Cited on page: 1.

[3] S. Weinberg, *"A Model of Leptons,"* Phys.Rev.Lett. 19 (1967) 1264.
Cited on page: 1.

[4] S. Novaes, *"Standard model: An Introduction,"* IFT-P-010-2000, (1999), arXiv:hep-ph/hep-ph/0001283.
Cited on page: 1.

[5] J. Wess and B. Zumino, *"Supergauge Transformations in Four-Dimensions,"* Nucl.Phys. B70 (1974) 39.
Cited on pages: 1 and 7.

[6] D. Volkov and V. Akulov, *"Is the Neutrino a Goldstone Particle?,"* Phys.Lett. B46 (1973) 109.
Cited on page: 1.

[7] Y. Golfand and E. Likhtman, *"Extension of the Algebra of Poincaré Group Generators and Violation of p Invariance,"* JETP Lett. 13 (1971) 323.
Cited on page: 1.

[8] J.L. Feng, *"Naturalness and the Status of Supersymmetry,"* UCI-TR-2013-01, (2013) 13, arXiv:hep-ph/1302.6587.
Cited on page: 1.

[9] L. Susskind, *"Dynamics of Spontaneous Symmetry Breaking in the Weinberg-Salam Theory,"* SLAC-PUB-2142, Phys.Rev. D20 (1979) 2619.
Cited on page: 1.

[10] S. Weinberg, *"Implications of Dynamical Symmetry Breaking,"* PRINT-75-0804 (HARVARD), Phys.Rev. D13 (1976) 974.
Cited on page: 1.

[11] E. Gildener, *"Gauge Symmetry Hierarchies,"* Print-76-0529 (HARVARD), Phys.Rev. D14 (1976) 1667.
Cited on page: 1.

[12] C.T. Hill and E.H. Simmons, *"Strong dynamics and electroweak symmetry breaking,"* FERMILAB-PUB-02-045-T, BUHEP-01-09, Phys.Rept. 381 (2003) 235, arXiv:hep-ph/hep-ph/0203079.
Cited on page: 3.

[13] N. Arkani-Hamed, S. Dimopoulos and G. Dvali, *"The Hierarchy problem and new dimensions at a millimeter,"* SLAC-PUB-7769, SU-ITP-98-13, Phys.Lett. B429 (1998) 263, arXiv:hep-ph/9803315.
Cited on page: 3.

[14] K.A. Meissner and H. Nicolai, *"Conformal Symmetry and the Standard Model,"* Phys.Lett. B648 (2007) 312, arXiv:hep-th/0612165.
Cited on page: 3.

[15] G. Bertone, *"Particle dark matter: Observations, models and searches,"* (Cambridge University Press, 2010), ISBN: 0521763681.
Cited on page: 3.

[16] M. Drees and G. Gerbier, *"Mini-Review of Dark Matter: 2012,"* (2012), arXiv:hep-ph/1204.2373.
Cited on page: 3.

[17] K. Garrett and G. Duda, *"Dark Matter: A Primer,"* Adv.Astron. 2011 (2011) 968283, arXiv:hep-ph/1006.2483.
Cited on page: 3.

[18] A.H. Peter, *"Dark Matter: A Brief Review,"* (2012), arXiv:astro-ph.CO/1201.3942.
Cited on page: 3.

[19] S. van den Bergh, *"The Early history of dark matter,"* Publ.Astron.Soc.Pac. (1999), arXiv:astro-ph/astro-ph/9904251.
Cited on page: 3.

[20] A.G. Bergmann, V. Petrosian and R. Lynds, *"Gravitational lens models of arcs in clusters,"* Astrophys.J. 350 (1990) 23.
Cited on page: 4.

[21] **MACHO Collaboration**, C. Alcock et al., *"The MACHO project: Microlensing results from* 5.7 *years of LMC observations,"* Astrophys.J. 542 (2000) 281, arXiv:astro-ph/astro-ph/0001272.
Cited on page: 4.

[22] **WMAP Collaboration**, G. Hinshaw et al., *"Nine-Year Wilkinson Microwave Anisotropy Probe (WMAP) Observations: Cosmological Parameter Results,"* (2012), arXiv:astro-ph.CO/1212.5226.
Cited on pages: 4 and 59.

[23] D. Clowe et al., *"A direct empirical proof of the existence of dark matter,"* SLAC-PUB-12078, Astrophys.J. 648 (2006) L109, arXiv:astro-ph/astro-ph/0608407.
Cited on page: 4.

[24] H. Georgi and S. Glashow, *"Unity of All Elementary Particle Forces,"* Phys.Rev.Lett. 32 (1974) 438.
Cited on page: 5.

[25] T. Cheng and L. Li, *"Gauge Theory Of Elementary Particle Physics,"* (Oxford University Press, 1984), ISBN: 9780198519614.
Cited on page: 5.

[26] M. Dine, *"Supersymmetry and String Theory: Beyond the Standard Model,"* (Cambridge University Press, 2007), ISBN: 0521858410.
Cited on pages: 5, 11, 59, and 60.

[27] S.R. Coleman and J. Mandula, *"All Possible Symmetries of the S Matrix,"* Phys.Rev. 159 (1967) 1251.
Cited on page: 5.

[28] A. Salam and J. Strathdee, *"Supergauge Transformations,"* IC/74/11, Nucl.Phys. B76 (1974) 477.
Cited on page: 11.

[29] N. Polonsky, *"Supersymmetry: Structure and phenomena. Extensions of the standard model,"* MIT-CTP-3164, Lect.Notes Phys. M68 (2001) 1, arXiv:hep-ph/0108236.
Cited on pages: 3, 11, 12, and 82.

[30] M.A. Luty, *"2004 TASI lectures on supersymmetry breaking,"* (2005) 495, arXiv:hep-th/0509029.
Cited on page: 12.

[31] S. Dimopoulos and H. Georgi, *"Softly Broken Supersymmetry and* $SU(5)$*,"* HUTP-81/A022, Nucl.Phys. B193 (1981) 150.
Cited on page: 12.

[32] M. Drees and S.P. Martin, *"Implications of SUSY model building,"* MAD-PH-879, MADPH-95-879, UM-TH-95-02, (1995), arXiv:hep-ph/9504324.
Cited on page: 12.

[33] H.E. Haber, *"Introductory low-energy supersymmetry,"* SCIPP-92-33, C92-06-03.1, (1993), arXiv:hep-ph/9306207.
Cited on page: 12.

[34] X. Tata, *"Supersymmetry: Where it is and how to find it,"* UH-511-833-95, C95-06-04.1, (1995), arXiv:hep-ph/9510287.
Cited on page: 12.

[35] H. Baer et al., *"Low-energy supersymmetry phenomenology,"* SLAC-PUB-9981, FSU-HEP-950401, LBL-37016, UH-511-822-95, CERN-PPE-95-45, CERN-PPE-95-045, (1995), arXiv:hep-ph/9503479.
Cited on page: 12.

[36] J.A. Bagger, *"Weak scale supersymmetry: Theory and practice,"* JHU-TIPAC-96008, (1996), arXiv:hep-ph/9604232.
Cited on page: 12.

[37] J.D. Lykken, *"Introduction to supersymmetry,"* FERMILAB-PUB-96-445-T, (1996) 85, arXiv:hep-th/9612114.
Cited on page: 12.

[38] M.E. Peskin, *"The Experimental investigation of supersymmetry breaking,"* SLAC-PUB-7133, C95-08-21.3, Prog.Theor.Phys.Suppl. 123 (1996) 507, arXiv:hep-ph/9604339.
Cited on page: 12.

[39] M. Dine, *"Supersymmetry phenomenology (with a broad brush),"* SCIPP-96-73, (1996) 813, arXiv:hep-ph/9612389.
Cited on page: 12.

[40] M. Drees, *"An Introduction to supersymmetry,"* APCTP-05, KEK-TH-501, C96-06-04.1, (1996), arXiv:hep-ph/9611409.
Cited on pages: 2 and 12.

[41] S.P. Martin, *"A Supersymmetry primer,"* (1997), arXiv:hep-ph/9709356.
Cited on pages: 7, 8, 12, 18, 29, and 72.

[42] I. Aitchison, *"Supersymmetry in Particle Physics. An Elementary Introduction,"* (Cambridge University Press, 2007), ISBN: 0521880238.
Cited on pages: 7 and 12.

[43] D. Kazakov, *"Supersymmetry on the Run: LHC and Dark Matter,"* Nucl.Phys.Proc.Suppl. 203-204 (2010) 118, arXiv:hep-ph/1010.5419.
Cited on page: 12.

[44] A. Gladyshev and D. Kazakov, *"IS (Low Energy) SUSY STILL ALIVE?,"* (2012), arXiv:hep-ph/1212.2548.
Cited on page: 12.

[45] T. Falk, K.A. Olive and M. Srednicki, *"Heavy sneutrinos as dark matter,"* UMN-TH-1306-94, UCSBTH-94-29, Phys.Lett. B339 (1994) 248, arXiv:hep-ph/9409270.
Cited on page: 15.

[46] S.S. AbdusSalam et al., *"Benchmark Models, Planes, Lines and Points for Future SUSY Searches at the LHC,"* CERN-PH-TH-2011-224, DAMTP-2011-69, DESY-11-090, FTPI-MINN-11-22, KCL-PH-TH-2011-30, LCTS-2011-15, LPT-ORSAY-11-76, TTK-11-41, UMN-TH-3012-11, Eur.Phys.J. C71 (2011) 1835, arXiv:hep-ph/1109.3859.
Cited on page: 26.

[47] J.E. Kim and H.P. Nilles, *"The μ Problem and the Strong CP-Problem,"* UGVA-DPT 1983/10-410, Phys.Lett. B138 (1984) 150.
Cited on page: 26.

[48] U. Ellwanger, C. Hugonie and A.M. Teixeira, *"The Next-to-Minimal Supersymmetric Standard Model,"* LPT-ORSAY-09-76, CFTP-09-032, LPTA-09-066, Phys.Rept. 496 (2010) 1, arXiv:hep-ph/0910.1785.
Cited on pages: 26 and 27.

[49] M. Maniatis, *"The Next-to-Minimal Supersymmetric extension of the Standard Model reviewed,"* HD-THEP-09-9, Int.J.Mod.Phys. A25 (2010) 3505, arXiv:hep-ph/0906.0777.
Cited on pages: 26 and 27.

[50] R. Peccei and H.R. Quinn, *"Constraints Imposed by CP Conservation in the Presence of Instantons,"* ITP-572-STANFORD, Phys.Rev. D16 (1977) 1791.
Cited on page: 27.

[51] M. Cvetic et al., *"Electroweak breaking and the μ problem in supergravity models with an additional $U(1)$,"* UPR-0737-T, IEM-FT-150-97, Phys.Rev. D56 (1997) 2861, arXiv:hep-ph/9703317.
Cited on page: 27.

[52] S. King, S. Moretti and R. Nevzorov, *"Theory and phenomenology of an exceptional supersymmetric standard model,"* SHEP-05-32, Phys.Rev. D73 (2006) 035009, arXiv:hep-ph/0510419.
Cited on page: 27.

[53] L. Ryder, *"Quantum Field Theory,"* (Cambridge University Press, 1985), ISBN: 9780521237642.
Cited on page: 27.

[54] F. James, *"Statistical Methods in Experimental Physics,"* second ed., (World Scientific, 2006), ISBN: 9789812567956.
Cited on page: 30.

[55] P. Gregory, *"Bayesian Logical Data Analysis for the Physical Sciences,"* first ed., (Cambridge University Press, 2005), ISBN: 052184150X.
Cited on page: 30.

[56] J. Bernardo and M. Juárez, *"Bayesian Statistics 7,"* (Oxford University Press, 2003) , chap. *"Intrinsic Estimation,"* pp. 465–476, last retrieval Sept. 2013: `http://www.uv.es/~bernardo/BernardoJuarez.pdf`.
Cited on page: 39.

[57] H. Jeffreys, *"Theory of probability,"* third ed., (Clarendon Press Oxford, 1961), ISBN: 0198531931.
Cited on page: 42.

[58] P.V. Spade and C. Panaccio, *"William of Ockham,"* The Stanford Encyclopedia of Philosophy, edited by E.N. Zalta, The Metaphysics Research Lab, Stanford University, 2011, last retrieval Sept. 2013: `http://plato.stanford.edu/archives/fall2011/entries/ockham/`.
Cited on page: 40.

[59] A. Grinbaum, *"Which fine-tuning arguments are fine?,"* (2009), arXiv:physics.hist-ph/0903.4055.
Cited on page: 40.

[60] R. Barbieri and G. Giudice, *"Upper Bounds on Supersymmetric Particle Masses,"* CERN-TH-4825/87, Nucl.Phys. B306 (1988) 63.
Cited on page: 40.

[61] J.R. Ellis et al., *"Observables in Low-Energy Superstring Models,"* CERN-TH-4350-86, Mod.Phys.Lett. A1 (1986) 57.
Cited on page: 40.

[62] I. Murray and Z. Ghahramani, *"A note on the evidence and Bayesian Occam's razor,"* Gatsby Computational Neuroscience Unit, University College London, GCNU-TR 2005-003, last retrieval Sept. 2013: `http://mlg.eng.cam.ac.uk/zoubin/papers/05occam/`.
Cited on page: 40.

[63] D. MacKay, *"Bayesian Methods for Adaptive Models,"* Ph.D. thesis, California Institute of Technology, 1991, last retrieval Sept. 2013: `http://resolver.caltech.edu/CaltechETD:etd-01042007-131447`.
Cited on pages: 40 and 42.

[64] W.H. Jeffereys and J.O. Burger, *"Sharpening Occam's Razor on a Bayesian Strop,"* Department of Statistics, Purdue University, 91-44C, last retrieval Sept. 2013: `http://quasar.as.utexas.edu/papers/ockham`.
Cited on page: 41.

[65] R.M. Neal, *"Probabilistic Inference Using Markov Chain Monte Carlo Methods,"* Department of Computer Science, University of Toronto, last retrieval Sept. 2013: `http://www.cs.toronto.edu/~radford/ftp/review.pdf`.
Cited on page: 45.

[66] N. Metropolis et al., *"Equation of State Calculations by Fast Computing Machines,"* JCHP 21 (1953) 1087.
Cited on page: 45.

[67] C. Robert and G. Casella, *"Introducing Monte Carlo Methods with R,"* first ed., (Springer Verlag, 2009) , chap. *"Metropolis-Hastings Algorithms,"* pp. 167–197, ISBN: 1441915753.
Cited on page: 45.

[68] J. Skilling, *"Nested sampling for general Bayesian computation,"* Bayesian Analysis 1 (2006) 833, last retrieval Sept. 2013: `http://projecteuclid.org/euclid.ba/1340370944`.
Cited on pages: 47, 49, and 50.

[69] F. Feroz, M. Hobson and M. Bridges, *"MultiNest: an efficient and robust Bayesian inference tool for cosmology and particle physics,"* Mon.Not.Roy.Astron.Soc. 398 (2009) 1601, arXiv:astro-ph/0809.3437.
Cited on page: 47.

[70] F. Feroz and M. Hobson, *"Multimodal nested sampling: an efficient and robust alternative to MCMC methods for astronomical data analysis,"* Mon.Not.Roy.Astron.Soc. 384 (2008) 449, arXiv:astro-ph/0704.3704.
Cited on page: 47.

[71] **Particle Data Group**, J. Beringer et al., *"Review of Particle Physics,"* Phys.Rev. D86 (2012) 010001.
Cited on pages: 53, 55, 78, 82, 88, 91, 92, 115, 116, 117, 118, 191, and 192.

[72] B.C. Allanach, *"SOFTSUSY: a program for calculating supersymmetric spectra,"* CERN-TH-2001-102, Comput.Phys.Commun. 143 (2002) 305, arXiv:hep-ph/0104145.
Cited on pages: 56, 96, and 117.

[73] **CDF and DØ Collaborations**, T. Aaltonen et al., *"Combination of the top-quark mass measurements from the Tevatron collider,"* FERMILAB-PUB-12-336-E-TD, Phys.Rev. D86 (2012) 092003, arXiv:hep-ex/1207.1069.
Cited on page: 55.

[74] **CMS Collaboration**, S. Chatrchyan et al., *"Measurement of the $t\bar{t}$ production cross section and the top quark mass in the dilepton channel in pp collisions at $\sqrt{s} = 7$ TeV,"* CERN-PH-EP-2011-055, CMS-TOP-11-002, JHEP 1107 (2011) 049, arXiv:hep-ex/1105.5661.
Cited on page: 55.

[75] A.H. Hoang and I.W. Stewart, *"Top Mass Measurements from Jets and the Tevatron Top-Quark Mass,"* MIT-CTP-3966, MPP-2008-93, Nucl.Phys.Proc.Suppl. 185 (2008) 220, arXiv:hep-ph/0808.0222.
Cited on page: 55.

[76] **Belle Collaboration**, C. Schwanda et al., *"Measurement of the Moments of the Photon Energy Spectrum in $b \to s\gamma$ Decays and Determination of $|V_{cb}|$ and m_b at Belle,"* Phys.Rev. D78 (2008) 032016, arXiv:hep-ex/0803.2158.
Cited on page: 57.

[77] **CLEO Collaboration**, A. Mahmood et al., *"Measurement of lepton momentum moments in the decay $\bar{B} \to X\ell\bar{\nu}$ and determination of heavy quark expansion parameters and $|V_{cb}|$,"* CLNS-02-1810, CLEO-02-16, Phys.Rev. D67 (2003) 072001, arXiv:hep-ex/0212051.
Cited on page: 57.

[78] **BaBar Collaboration**, B. Aubert et al., *"Measurement and interpretation of moments in inclusive semileptonic decays $\bar{B} \to X_c\ell\bar{\nu}$,"* SLAC-PUB-13735, BaBar-PUB-09-004, Phys.Rev. D81 (2010) 032003, arXiv:hep-ex/0908.0415.
Cited on page: 57.

[79] **DELPHI Collaboration**, J. Abdallah et al., *"Study of b-quark mass effects in multijet topologies with the DELPHI detector at LEP,"* CERN-PH-EP-2007-011, Eur.Phys.J. C55 (2008) 525, arXiv:hep-ex/0804.3883.
Cited on page: 57.

[80] **ALEPH Collaboration**, R. Barate et al., *"Measurement of the Z resonance parameters at LEP,"* CERN-EP-99-104, Eur.Phys.J. C14 (2000) 1.
Cited on page: 58.

[81] **L3 Collaboration**, M. Acciarri et al., *"Measurements of cross-sections and forward backward asymmetries at the Z resonance and determination of electroweak parameters,"* CERN-EP-2000-022, Eur.Phys.J. C16 (2000) 1, arXiv:hep-ex/0002046.
Cited on page: 58.

[82] **OPAL Collaboration**, G. Abbiendi et al., *"Precise determination of the Z resonance parameters at LEP: 'Zedometry',"* CERN-EP-2000-148, OPAL-PR-328, Eur.Phys.J. C19 (2001) 587, arXiv:hep-ex/0012018.
Cited on page: 58.

[83] **DELPHI Collaboration**, P. Abreu et al., *"Cross-sections and leptonic forward backward asymmetries from the Z^0 running of LEP,"* CERN-EP-2000-037, Eur.Phys.J. C16 (2000) 371.
Cited on page: 58.

[84] H. Goldberg, *"Constraint on the Photino Mass from Cosmology,"* NUB-2592, Phys.Rev.Lett. 50 (1983) 1419.
Cited on page: 59.

[85] J.R. Ellis et al., *"Supersymmetric Relics from the Big Bang,"* SLAC-PUB-3171, Nucl.Phys. B238 (1984) 453.
Cited on page: 59.

[86] **WMAP Collaboration**, E. Komatsu et al., *"Seven-Year Wilkinson Microwave Anisotropy Probe (WMAP) Observations: Cosmological Interpretation,"* Astrophys.J.Suppl. 192 (2011) 18, arXiv:astro-ph.CO/1001.4538.
Cited on pages: 59 and 192.

[87] **Planck Collaboration**, F. Villa et al., *"The Planck Telescope,"* AIP Conf.Proc. 616 (2002) 224, arXiv:astro-ph/astro-ph/0112173.
Cited on pages: 59 and 64.

[88] G. Bertone, D. Hooper and J. Silk, *"Particle dark matter: Evidence, candidates and constraints,"* FERMILAB-PUB-04-047-A, Phys.Rept. 405 (2005) 279, arXiv:hep-ph/0404175.
Cited on pages: 59, 67, and 174.

[89] G. Jungman, M. Kamionkowski and K. Griest, *"Supersymmetric dark matter,"* SU-4240-605, UCSD-PTH-95-02, IASSNS-HEP-95-14, CU-TP-677, Phys.Rept. 267 (1996) 195, arXiv:hep-ph/9506380.
Cited on pages: 59 and 60.

[90] J. Edsjo and P. Gondolo, *"Neutralino relic density including coannihilations,"* UUITP-11-97, MPI-PHT-97-27, Phys.Rev. D56 (1997) 1879, arXiv:hep-ph/9704361.
Cited on page: 60.

[91] J. Edsjo et al., *"Accurate relic densities with neutralino, chargino and sfermion coannihilations in mSUGRA,"* NSF-ITP-03-03, CWRU-P1-03, JCAP 0304 (2003) 001, arXiv:hep-ph/0301106.
Cited on page: 60.

[92] S. Profumo, *"TASI 2012 Lectures on Astrophysical Probes of Dark Matter,"* (2013), arXiv:hep-ph/1301.0952.
Cited on pages: 61 and 172.

[93] G. Belanger et al., *"MicrOMEGAs: A Program for calculating the relic density in the MSSM,"* LAPTH-881-01, Comput.Phys.Commun. 149 (2002) 103, arXiv:hep-ph/0112278.
Cited on pages: 61 and 96.

[94] N.F. Bell et al., *"Electroweak Bremsstrahlung in Dark Matter Annihilation,"* Phys.Rev. D78 (2008) 083540, arXiv:hep-ph/0805.3423.
Cited on page: 62.

[95] T.J. Weiler, *"On the likely dominance of WIMP annihilation to fermion pair+W/Z (and implication for indirect detection),"* AIP Conf.Proc. 1534 (2012) 165, arXiv:hep-ph/1301.0021.
Cited on page: 62.

[96] J.L. Feng, K.T. Matchev and D. Sanford, *"Focus Point Supersymmetry Redux,"* UCI-TR-2011-28, Phys.Rev. D85 (2012) 075007, arXiv:hep-ph/1112.3021.
Cited on page: 62.

[97] K.L. Chan, U. Chattopadhyay and P. Nath, *"Naturalness, weak scale supersymmetry and the prospect for the observation of supersymmetry at the Tevatron and at the CERN LHC,"* Phys.Rev. D58 (1998) 096004, arXiv:hep-ph/9710473.
Cited on page: 62.

[98] M. Drees and M.M. Nojiri, *"The Neutralino relic density in minimal $N = 1$ supergravity,"* SLAC-PUB-5860, DESY-92-101, Phys.Rev. D47 (1993) 376, arXiv:hep-ph/9207234.
Cited on page: 63.

[99] H. Baer et al., *"Exploring neutralino dark matter resonance annihilation via $bA, bH \to b\mu^+\mu^-$ at the LHC,"* Phys.Rev. D84 (2011) 095029, arXiv:hep-ph/1106.5055.
Cited on page: 63.

[100] J.R. Ellis et al., *"Calculations of neutralino-stau coannihilation channels and the cosmologically relevant region of MSSM parameter space,"* CERN-TH-99-146, MADPH-99-1117, TPI-MINN-99-28, UMN-TH-1801-99, Astropart.Phys. 13 (2000) 181, arXiv:hep-ph/9905481.
Cited on page: 64.

[101] L. Page, *"The map satellite mission to map the CMB anisotropy,"* (2000), arXiv:astro-ph/0012214.
Cited on page: 64.

[102] B.C. Allanach et al., *"Uncertainties in the prediction of the relic density of supersymmetric dark matter,"* LAPTH-CONF-1063-04, LAPTH-CONF-1063-04 (2004) 961, arXiv:hep-ph/0410049.
Cited on pages: 64, 96, and 119.

[103] B.C. Allanach et al., *"Uncertainties in relic density calculations in mSUGRA,"* LAPTH-1026-04, LAPTH-1026-04 (2004), arXiv:hep-ph/0402161.
Cited on pages: 64, 96, and 119.

[104] L. Baudis, *"Direct dark matter detection: the next decade,"* Phys.Dark Univ. 1 (2012) 94, arXiv:astro-ph.IM/1211.7222.
Cited on page: 65.

[105] **XENON100 Collaboration**, E. Aprile et al., *"Dark Matter Results from* 100 *Live Days of XENON*100 *Data,"* Phys.Rev.Lett. 107 (2011) 131302, arXiv:astro-ph.CO/1104.2549.
Cited on pages: 65 and 132.

[106] **DAMA and LIBRA Collaborations**, R. Bernabei et al., *"First results from DAMA/LIBRA and the combined results with DAMA/NaI,"* ROM2F-2008-07, Eur.Phys.J. C56 (2008) 333, arXiv:astro-ph/0804.2741.
Cited on page: 65.

[107] **DAMA and LIBRA Collaborations**, R. Bernabei et al., *"New results from DAMA/LIBRA,"* Eur.Phys.J. C67 (2010) 39, arXiv:astro-ph.GA/1002.1028.
Cited on page: 65.

[108] R. Bernabei et al., *"DAMA/LIBRA results and perspectives,"* (2013), arXiv:astro-ph.GA/1301.6243.
Cited on page: 65.

[109] **XENON100 Collaboration**, E. Aprile, *"The search for dark matter with XENON,"* (2011).
Cited on page: 65.

[110] J.R. Ellis, K.A. Olive and C. Savage, *"Hadronic Uncertainties in the Elastic Scattering of Supersymmetric Dark Matter,"* CERN-PH-TH-2008-005, UMN-TH-2631-08, FTPI-MINN-08-02, Phys.Rev. D77 (2008) 065026, arXiv:hep-ph/0801.3656.
Cited on pages: 65 and 169.

[111] **LEP Working Group for Higgs boson searches, ALEPH, DELPHI, L3 and OPAL Collaborations**, R. Barate et al., *"Search for the standard model Higgs boson at LEP,"* CERN-EP-2003-011, Phys.Lett. B565 (2003) 61, arXiv:hep-ex/0306033.
Cited on pages: 67, 69, 191, and 195.

[112] **CDF, D∅, Tevatron New Physics Group and Higgs Working Group Collaborations**, *"Updated Combination of CDF and D∅ Searches for Standard Model Higgs Boson Production with up to* $10.0\,fb^{-1}$ *of Data,"* FERMILAB-CONF-12-318-E, CDF-NOTE-10884, D0-NOTE-6348, (2012), arXiv:hep-ex/1207.0449.
Cited on page: 67.

[113] H. Flacher et al., *"Revisiting the Global Electroweak Fit of the Standard Model and Beyond with Gfitter,"* CERN-OPEN-2008-024, DESY-08-160, Eur.Phys.J. C60 (2009) 543, arXiv:hep-ph/0811.0009.
Cited on page: 67.

[114] **ALEPH, CDF, D∅, DELPHI, L3, OPAL, SLD, LEP Electroweak Working Group, Tevatron Electroweak Working Group, SLD Electroweak Working Group and Heavy Flavour Group Collaborations**, *"Precision Electroweak Measurements and Constraints on the Standard Model,"* SLAC-PUB-14301, CERN-PH-EP-2008-020, FERMILAB-TM-2420-E, LEPEWWG-2008-01, TEVEWWG-2008-01, ALEPH-2008-001-PHYSICS-2008-001, CDF-NOTE-9610, D0-NOTE-5802, DELPHI-2008-001-PHYS-950, L-NOTE-2834, OPAL-PR428, (2008), arXiv:hep-ex/0811.4682.
Cited on page: 67.

[115] J.R. Ellis, M.K. Gaillard and D.V. Nanopoulos, *"A Historical Profile of the Higgs Boson,"* KCL-PH-TH-2012-04, LCTS-2012-01, CERN-PH-TH-2012-009, LBNL, UCB-PTH-12-01, ACT-1-12, MIFPA-12-01, (2012), arXiv:hep-ph/1201.6045.
Cited on page: 67.

[116] **ALEPH Collaboration**, R. Barate et al., *"Observation of an excess in the search for the standard model Higgs boson at ALEPH,"* CERN-EP-2000-138, Phys.Lett. B495 (2000) 1, arXiv:hep-ex/0011045.
Cited on page: 69.

[117] **DELPHI Collaboration**, P. Abreu et al., *"Search for the standard model Higgs boson at LEP in the year 2000,"* CERN-EP-2001-004, Phys.Lett. B499 (2001) 23, arXiv:hep-ex/0102036.
Cited on page: 69.

[118] **L3 Collaboration**, M. Acciarri et al., *"Higgs candidates in* e^+e^- *interactions at* $\sqrt{s} = 206.6$ *GeV,"* CERN-EP-2000-140, Phys.Lett. B495 (2000) 18, arXiv:hep-ex/0011043.
Cited on page: 69.

[119] **OPAL Collaboration**, G. Abbiendi et al., *"Search for the standard model Higgs boson in e^+e^- collisions at $\sqrt{s}$ approximately = 192 GeV - 209 GeV,"* CERN-EP-2000-156, Phys.Lett. B499 (2001) 38, arXiv:hep-ex/0101014.
Cited on page: 69.

[120] **LHC Higgs Cross Section Working Group**, S. Dittmaier et al., *"Handbook of LHC Higgs Cross Sections: 1. Inclusive Observables,"* CERN-2011-002, (2011), arXiv:hep-ph/1101.0593.
Cited on page: 71.

[121] B.C. Allanach et al., *"Precise determination of the neutral Higgs boson masses in the MSSM,"* MPP-2004-50, LAPTH-1046-04, PM-04-13, ZU-TH-08-04, IFIC-04-21, JHEP 0409 (2004) 044, arXiv:hep-ph/0406166.
Cited on pages: 70, 96, and 119.

[122] **ATLAS Collaboration**, G. Aad et al., *"Observation of a new particle in the search for the Standard Model Higgs boson with the ATLAS detector at the LHC,"* CERN-PH-EP-2012-218, Phys.Lett. B716 (2012) 1, arXiv:hep-ex/1207.7214.
Cited on page: 70.

[123] **CMS Collaboration**, S. Chatrchyan et al., *"Observation of a new boson at a mass of 125 GeV with the CMS experiment at the LHC,"* CMS-HIG-12-028, CERN-PH-EP-2012-220, Phys.Lett. B716 (2012) 30, arXiv:hep-ex/1207.7235.
Cited on pages: 70, 118, 119, and 195.

[124] **CMS Collaboration**, S. Chatrchyan et al., *"Combined results of searches for the standard model Higgs boson in pp collisions at $\sqrt{s} = 7$ TeV,"* CMS-HIG-11-032, CERN-PH-EP-2012-023, Phys.Lett. B710 (2012) 26, arXiv:hep-ex/1202.1488.
Cited on pages: 70, 74, 75, and 195.

[125] **ATLAS Collaboration**, *"An update to the combined search for the Standard Model Higgs boson with the ATLAS detector at the LHC using up to 4.9 fb^{-1} of pp collision data at $\sqrt{s} = 7$ TeV,"* ATLAS-CONF-2012-019, ATLAS-COM-CONF-2012-039, (2012).
Cited on page: 70.

[126] **ATLAS Collaboration**, G. Aad et al., *"Combined search for the Standard Model Higgs boson in pp collisions at $\sqrt{s} = 7$ TeV with the ATLAS detector,"* CERN-PH-EP-2012-167, Phys.Rev. D86 (2012) 032003, arXiv:hep-ex/1207.0319.
Cited on page: 70.

[127] **ATLAS Collaboration**, G. Aad et al., *"Combined search for the Standard Model Higgs boson using up to 4.9 fb^{-1} of pp collision data at $\sqrt{s} = 7$ TeV with

the ATLAS detector at the LHC," CERN-PH-EP-2012-019, Phys.Lett. B710 (2012) 49, arXiv:hep-ex/1202.1408.
Cited on pages: 70, 74, 75, and 195.

[128] **ATLAS Collaboration**, *"Combination of Higgs Boson Searches with up to* $4.9\,fb^{-1}$ *of pp Collisions Data Taken at a center-of-mass energy of 7 TeV with the ATLAS Experiment at the LHC,"* ATLAS-CONF-2011-163, ATLAS-COM-CONF-2011-195, (2011).
Cited on page: 70.

[129] **CMS Collaboration**, *"Combination of Higgs Searches,"* CMS-PAS-HIG-11-022, (2011).
Cited on page: 70.

[130] **CMS Collaboration**, *"Combined Standard Model Higgs boson searches with up to 2.3 inverse femtobarns of pp collision data at* $\sqrt{s} = 7$ *TeV at the LHC,"* CMS-PAS-HIG-11-023, (2011).
Cited on page: 70.

[131] **CMS Collaboration**, *"Combination of SM Higgs Searches,"* CMS-PAS-HIG-11-032, (2011).
Cited on page: 70.

[132] **CMS Collaboration**, *"Observation of a new boson with a mass near* 125 *GeV,"* CMS-PAS-HIG-12-020, (2012).
Cited on page: 70.

[133] A. Djouadi, *"The Anatomy of electro-weak symmetry breaking. I: The Higgs boson in the standard model,"* LPT-ORSAY-05-17, Phys.Rept. 457 (2008) 1, arXiv:hep-ph/0503172.
Cited on page: 72.

[134] **CMS Collaboration**, *"Combination of standard model Higgs boson searches and measurements of the properties of the new boson with a mass near* 125 *GeV,"* CMS-PAS-HIG-12-045.
Cited on pages: 72 and 115.

[135] G. Belanger et al., *"Higgs Couplings at the End of 2012,"* LAPTH-061-12, LPSC12350, LPT-ORSAY-12-119, (2012), arXiv:hep-ph/1212.5244.
Cited on page: 74.

[136] D. Carmi et al., *"Higgs After the Discovery: A Status Report,"* LPT-ORSAY-12-77, JHEP 1210 (2012) 196, arXiv:hep-ph/1207.1718.
Cited on page: 74.

[137] T. Plehn and M. Rauch, *"Higgs Couplings after the Discovery,"* KA-TP-31-2012, SFB-CPP-12-51, Europhys.Lett. 100 (2012) 11002, arXiv:hep-ph/1207.6108.
Cited on page: 74.

[138] **ATLAS Collaboration**, *"An update of combined measurements of the new Higgs-like boson with high mass resolution channels,"* CERN, ATLAS-CONF-2012-170.
Cited on page: 74.

[139] J.F. Gunion, Y. Jiang and S. Kraml, *"Could two NMSSM Higgs bosons be present near* 125 *GeV?,"* Phys.Rev. D86 (2012) 071702, arXiv:hep-ph/1207.1545.
Cited on page: 74.

[140] **CMS Collaboration**, *"Combination of standard model Higgs boson searches and measurements of the properties of the new boson with a mass near* 125 *GeV,"* CERN, CMS-PAS-HIG-13-005.
Cited on pages: 76 and 77.

[141] S. Heinemeyer, *"Electroweak Precision Physics from Low to High Energies,"* (2007), arXiv:hep-ph/0710.3022.
Cited on page: 76.

[142] S. Heinemeyer, W. Hollik and G. Weiglein, *"Electroweak precision observables in the minimal supersymmetric standard model,"* CERN-PH-TH-2004-224, DCPT-04-162, IPPP-04-81, MPP-2004-145, Phys.Rept. 425 (2006) 265, arXiv:hep-ph/0412214.
Cited on pages: 76, 78, and 93.

[143] J. Haestier et al., *"Two-loop contributions to electroweak precision observables in the MSSM,"* DCPT-05-68, IPPP-05-34, LCWS-2005-0611, eConf C050318 (2005) 0611, arXiv:hep-ph/0506259.
Cited on page: 76.

[144] **DELPHI Collaboration**, J. Abdallah et al., *"Measurement of the Mass and Width of the W Boson in* e^+e^- *Collisions at* $\sqrt{s} = 161$ *GeV -* 209 *GeV,"* CERN-PH-EP-2007-026, Eur.Phys.J. C55 (2008) 1, arXiv:hep-ex/0803.2534.
Cited on page: 76.

[145] **OPAL Collaboration**, G. Abbiendi et al., *"Measurement of the mass and width of the W boson,"* OPAL-PR-410, CERN-PH-EP-2005-038, Eur.Phys.J. C45 (2006) 307, arXiv:hep-ex/0508060.
Cited on page: 76.

[146] **L3 Collaboration**, P. Achard et al., *"Measurement of the mass and the width of the W boson at LEP,"* CERN-PH-EP-2005-043, Eur.Phys.J. C45 (2006) 569, arXiv:hep-ex/0511049.
Cited on page: 76.

[147] **ALEPH Collaboration**, S. Schael et al., *"Measurement of the W boson mass and width in e^+e^- collisions at LEP,"* CERN-PH-EP-2006-004, Eur.Phys.J. C47 (2006) 309, arXiv:hep-ex/0605011.
Cited on page: 76.

[148] **CDF Collaboration**, T. Aaltonen et al., *"Precise measurement of the W-boson mass with the CDF II detector,"* FERMILAB-PUB-12-061-E, Phys.Rev.Lett. 108 (2012) 151803, arXiv:hep-ex/1203.0275.
Cited on page: 76.

[149] **D∅ Collaboration**, V.M. Abazov, *"Measurement of the W Boson Mass with the D∅ Detector,"* FERMILAB-PUB-12-056-PPD, Phys.Rev.Lett. 108 (2012) 151804, arXiv:hep-ex/1203.0293.
Cited on page: 76.

[150] S. Heinemeyer and G. Weiglein, *"The MSSM in the light of precision data,"* DCPT-03-84, IPPP-03-42, LMU-14-03, (2003) 147, arXiv:hep-ph/0307177.
Cited on page: 78.

[151] A. Olshevsky, P. Ratoff and P. Renton, *"How effective is the weak mixing angle?,"* Z.Phys. C60 (1993) 643.
Cited on page: 78.

[152] **UA1 Collaboration**, R. Batley, *"Missing Energy Results from the UA*1 *Experiment,"* CERN-EP/86-181, C86/06/30, (1986).
Cited on page: 79.

[153] **LEP SUSY Working Group, ALEPH, DELPHI, L3 and OPAL Collaborations**, *"Combined LEP Selectron/Smuon/Stau Results,* 183-208 *GeV,"* LEPSUSYWG/04-01.1, last retrieval Sept. 2013: `http://lepsusy.web.cern.ch/lepsusy/www/sleptons_summer04/slep_final.html`.
Cited on page: 79.

[154] **LEP SUSY Working Group, ALEPH, DELPHI, L3 and OPAL Collaborations**, *"Combined LEP stop and sbottom Results* 183-208 *GeV,"* LEPSUSYWG/04-02.1, last retrieval Sept. 2013: `http://lepsusy.web.cern.ch/lepsusy/www/squarks_summer04/stop_combi_208_final.html`.
Cited on page: 79.

[155] **LEP SUSY Working Group, ALEPH, DELPHI, L3 and OPAL Collaborations**, *"Combined LEP Chargino Results, up to* 208 *GeV for large*

m_0," LEPSUSYWG/01-03.1, last retrieval Sept. 2013: `http://lepsusy.web.cern.ch/lepsusy/www/inos_moriond01/charginos_pub.html`.
Cited on page: 79.

[156] **LEP SUSY Working Group, ALEPH, DELPHI, L3 and OPAL Collaborations**, *"Combined LEP Chargino Results, up to* 208 *GeV for low DM,"* LEPSUSYWG/02-04.1, last retrieval Sept. 2013: `http://lepsusy.web.cern.ch/lepsusy/www/inoslowdmsummer02/charginolowdm_pub.html`.
Cited on page: 79.

[157] **LEP SUSY Working Group, ALEPH, DELPHI, L3 and OPAL Collaborations**, *"Combined Lower Bound of the Neutralino Mass in a Constrained MSSM model,"* LEPSUSYWG/04-07.1, last retrieval Sept. 2013: `http://lepsusy.web.cern.ch/lepsusy/www/lsp_cmssm_summer04/cMSSM_final.html`.
Cited on page: 79.

[158] **CDF Collaboration**, T. Aaltonen et al., *"Search for the supersymmetric partner of the top quark in $p\bar{p}$ collisions at $\sqrt{s} = 1.96$ TeV,"* FERMILAB-PUB-10-347-E, Phys.Rev. D82 (2010) 092001, arXiv:hep-ex/1009.0266.
Cited on pages: 79 and 80.

[159] **CDF Collaboration**, T. Aaltonen et al., *"Search for Supersymmetry in $p\bar{p}$ Collisions at $\sqrt{s} = 1.96$ TeV Using the Trilepton Signature of Chargino-Neutralino Production,"* FERMILAB-PUB-08-306-E, Phys.Rev.Lett. 101 (2008) 251801, arXiv:hep-ex/0808.2446.
Cited on pages: 79 and 80.

[160] **DØ Collaboration**, V. Abazov et al., *"Search for associated production of charginos and neutralinos in the trilepton final state using $2.3 fb^{-1}$ of data,"* FERMILAB-PUB-09-003-E, Phys.Lett. B680 (2009) 34, arXiv:hep-ex/0901.0646.
Cited on pages: 79 and 80.

[161] **DØ Collaboration**, V. Abazov et al., *"Search for squarks and gluinos in events with jets and missing transverse energy using $2.1 fb^{-1}$ of $p\bar{p}$ collision data at $\sqrt{s} = 1.96$ TeV,"* FERMILAB-PUB-07-668-E, Phys.Lett. B660 (2008) 449, arXiv:hep-ex/0712.3805.
Cited on pages: 79 and 80.

[162] S. Ask, *"A Review of the supersymmetry searches at LEP,"* (2003), arXiv:hep-ex/0305007.
Cited on page: 79.

[163] **ALEPH Collaboration**, A. Heister et al., *"Absolute mass lower limit for the lightest neutralino of the MSSM from e^+e^- data at $\sqrt{s}$ up to* 209 *GeV,"* CERN-EP-2003-077, Phys.Lett. B583 (2004) 247.
Cited on pages: 79 and 191.

[164] B.C. Allanach, S. Kraml and W. Porod, *"Theoretical uncertainties in sparticle mass predictions from computational tools,"* CERN-TH-2003-029, LAP-TH-963-03, ZU-TH-03-03, JHEP 0303 (2003) 016, arXiv:hep-ph/0302102.

Cited on page: 80.

[165] S. Lammel, *"Supersymmetry at the Tevatron?,"* FERMILAB-CONF-98-055-E, (1998) 393, arXiv:hep-ex/9802010.
Cited on page: 80.

[166] **DØ and CDF Collaborations**, T. Nunnemann, *"Searches for the Higgs boson and supersymmetry at the Tevatron,"* Frascati Phys.Ser. 44 (2007) 475, arXiv:hep-ex/0710.0248.
Cited on page: 80.

[167] M.S. Carena et al., *"The Search for supersymmetry at the Tevatron collider,"* ANL-HEP-PR-97-98, Rev.Mod.Phys. 71 (1999) 937, arXiv:hep-ex/9712022.
Cited on page: 80.

[168] M. Neubert, *"Introduction to B physics,"* CLNS-00-1660, (2000) 244, arXiv:hep-ph/0001334.
Cited on page: 82.

[169] M. Wick and W. Altmannshofer, *"A Reconsideration of the $b \to s\gamma$ Decay in the Minimal Flavor Violating MSSM,"* AIP Conf.Proc. 1078 (2009) 348, arXiv:hep-ph/0810.2874.
Cited on pages: 82 and 84.

[170] **CLEO Collaboration**, S. Chen et al., *"Branching fraction and photon energy spectrum for $b \to s\gamma$,"* CLNS-01-1751, CLEO-01-16, Phys.Rev.Lett. 87 (2001) 251807, arXiv:hep-ex/0108032.
Cited on page: 82.

[171] **BaBar Collaboration**, B. Aubert et al., *"Measurement of the branching fraction and photon energy moments of $B \to X_s\gamma$ and $A_{CP}(B \to X_{s+d}\gamma)$,"* SLAC-PUB-12002, BaBar-PUB-06-037, Phys.Rev.Lett. 97 (2006) 171803, arXiv:hep-ex/0607071.
Cited on page: 82.

[172] **Belle Collaboration**, A. Limosani et al., *"Measurement of Inclusive Radiative B-meson Decays with a Photon Energy Threshold of* 1.7 *GeV,"*

BELLE-PREPRINT-2009-16, KEK-PREPRINT-2009-14, Phys.Rev.Lett. 103 (2009) 241801, arXiv:hep-ex/0907.1384.
Cited on page: 82.

[173] **Heavy Flavor Averaging Group**, Y. Amhis et al., *"Averages of b-hadron, c-hadron, and tau-lepton properties as of early 2012,"* SLAC-R-1002, (2012), arXiv:hep-ex/1207.1158.
Cited on pages: 83 and 192.

[174] **Heavy Flavor Averaging Group**, *"Compilation of B Semi-leptonic and Radiative Branching Fractions,"* (2012), last retrieval Sept. 2013: `http://www.slac.stanford.edu/xorg/hfag/rare/2012/radll/OUTPUT/HTML/radll_table3.html`.
Cited on pages: 83 and 192.

[175] M. Misiak et al., *"Estimate of BR $(\bar{B} \to X_s \gamma)$ at $\mathcal{O}(\alpha_s^2)$,"* IFT-18-2006, CERN-PH-TH-2006-184, YERPHI-1608-6, FREIBURG-THEP-06-13, DFTT-20-2006, SFB-CPP-06-45, TTP06-26, ZU-TH-22-06, SLAC-PUB-12117, DESY-06-168, Phys.Rev.Lett. 98 (2007) 022002, arXiv:hep-ph/0609232.
Cited on page: 83.

[176] A. Arbey et al., *"Supersymmetry confronts $B_s \to \mu^+\mu^-$: Present and future status,"* CERN-PH-TH-2012-346, (2012), arXiv:hep-ph/1212.4887.
Cited on page: 83.

[177] A. Djouadi, *"The Anatomy of electro-weak symmetry breaking. II. The Higgs bosons in the minimal supersymmetric model,"* LPT-ORSAY-05-18, Phys.Rept. 459 (2008) 1, arXiv:hep-ph/0503173.
Cited on page: 83.

[178] A.J. Buras et al., *"$\Delta M_{d,s}$, $B^0_{d,s} \to \mu^+\mu^-$ and $B \to X_s\gamma$ in supersymmetry at large $\tan\beta$,"* TUM-HEP-479-02, IFT-02-34, Nucl.Phys. B659 (2003) 3, arXiv:hep-ph/0210145.
Cited on page: 85.

[179] A.J. Buras et al., *"On the Standard Model prediction for BR $(B_{s,d} \to \mu^+\mu^-)$,"* FLAVOUR(267104)-ERC-20, LAPTH-032-12, CERN-PH-TH-2012-210, Eur.Phys.J. C72 (2012) 2172, arXiv:hep-ph/1208.0934.
Cited on page: 85.

[180] **LHCb Collaboration**, R. Aaij et al., *"Search for the rare decays $B^0_s \to \mu^+\mu^-$ and $B^0 \to \mu^+\mu^-$,"* CERN-PH-EP-2011-029, Phys.Lett. B699 (2011) 330, arXiv:hep-ex/1103.2465.
Cited on pages: 85 and 193.

[181] **LHCb Collaboration**, R. Aaij et al., *"Strong constraints on the rare decays $B_s \to \mu^+\mu^-$ and $B^0 \to \mu^+\mu^-$,"* CERN-PH-EP-2012-072, LHCB-PAPER-2012-007, Phys.Rev.Lett. 108 (2012) 231801, arXiv:hep-ex/1203.4493.
Cited on pages: 85 and 193.

[182] **LHCb Collaboration**, R. Aaij et al., *"First Evidence for the Decay $B_s^0 \to \mu^+\mu^-$,"* CERN-PH-EP-2012-335, LHCB-PAPER-2012-043, Phys.Rev.Lett. 110 (2013) 021801, arXiv:hep-ex/1211.2674.
Cited on pages: 85 and 193.

[183] S. Stone, *"New physics from flavour,"* SU-HEP-1-2012, (2012), arXiv:hep-ph/1212.6374.
Cited on page: 87.

[184] J. Charles et al., *"Predictions of selected flavour observables within the Standard Model,"* LPT-ORSAY-11-53, Phys.Rev. D84 (2011) 033005, arXiv:hep-ph/1106.4041.
Cited on pages: 87 and 176.

[185] **BaBar Collaboration**, R. Barlow, *"Experimental status of $B \to \tau\nu$ and $B \to \ell\nu(\gamma)$,"* (2011), arXiv:hep-ex/1102.1267.
Cited on page: 87.

[186] **CLEO Collaboration**, T. Browder et al., *"A Search for $B \to \tau\bar{\nu}$,"* SLAC-REPRINT-2000-071, CLNS-00-1674, CLEO-00-10, Phys.Rev.Lett. 86 (2001) 2950, arXiv:hep-ex/0007057.
Cited on page: 87.

[187] **Belle Collaboration**, K. Abe et al., *"Search for $B \to \tau\bar{\nu}$ at BELLE,"* BELLE-CONF-0428, ICHEP04-11-0675, (2004), arXiv:hep-ex/0408144.
Cited on page: 87.

[188] **BaBar Collaboration**, B. Aubert et al., *"Measurement of the Semileptonic Decays $\bar{B} \to D\tau^-\bar{\nu}_\tau$ and $\bar{B} \to D^*\tau^-\bar{\nu}_\tau$,"* SLAC-PUB-13532, BaBar-PUB-08-047, Phys.Rev. D79 (2009) 092002, arXiv:hep-ex/0902.2660.
Cited on page: 87.

[189] **Heavy Flavor Averaging Group**, D. Asner et al., *"Averages of b-hadron, c-hadron, and τ-lepton Properties,"* (2010), arXiv:hep-ex/1010.1589.
Cited on pages: 87 and 192.

[190] J.L. Rosner and M. Gronau, *"B_s Decays and Mixing,"* PoS BEAUTY2011 (2011) 045, arXiv:hep-ph/1105.1923.
Cited on page: 88.

[191] U. Nierste, *"B Mixing in the Standard Model and Beyond,"* TTP12-051, (2012), arXiv:hep-ph/1212.5805.
Cited on page: 88.

[192] M. Talby, *"B_s^0 mixing and decays at the Tevatron,"* FERMILAB-CONF-07-356-E, eConf C070512 (2007) 015, arXiv:hep-ex/0707.1007.
Cited on page: 88.

[193] **CDF Collaboration**, A. Abulencia et al., *"Observation of $B_s^0 - \bar{B}_s^0$ Oscillations,"* FERMILAB-PUB-06-344-E, Phys.Rev.Lett. 97 (2006) 242003, arXiv:hep-ex/0609040.
Cited on page: 88.

[194] **LHCb Collaboration**, R. Aaij et al., *"Measurement of the $B_s^0 - \bar{B}_s^0$ oscillation frequency Δm_s in $B_s^0 \to D_s^-(3)\pi$ decays,"* LHCB-PAPER-2011-010, CERN-PH-EP-2011-194, Phys.Lett. B709 (2012) 177, arXiv:hep-ex/1112.4311.

Cited on page: 88.

[195] **UTfit Collaboration**, M. Bona et al., *"The Unitarity Triangle Fit in the Standard Model and Hadronic Parameters from Lattice QCD: A Reappraisal after the Measurements of Δm_s and BR $(B \to \tau\nu_\tau)$,"* JHEP 0610 (2006) 081, arXiv:hep-ph/0606167.
Cited on page: 88.

[196] D. Stockinger, *"The Muon Magnetic Moment and Supersymmetry,"* EDINBURGH-2006-22, J.Phys. G34 (2007) R45, arXiv:hep-ph/0609168.
Cited on pages: 91 and 92.

[197] **Muon $(g-2)$ Collaboration**, G. Bennett et al., *"Final Report of the Muon E821 Anomalous Magnetic Moment Measurement at BNL,"* Phys.Rev. D73 (2006) 072003, arXiv:hep-ex/0602035.
Cited on page: 91.

[198] F. Jegerlehner and A. Nyffeler, *"The Muon $g-2$,"* HU-EP-09-07, HRI-P-09-02-001, RECAPP-HRI-2009-003, Phys.Rept. 477 (2009) 1, arXiv:hep-ph/0902.3360.
Cited on page: 91.

[199] J.P. Miller, E. de Rafael and B.L. Roberts, *"Muon $(g-2)$: Experiment and theory,"* PREPRINT-CPT-P07-2007, Rept.Prog.Phys. 70 (2007) 795, arXiv:hep-ph/0703049.
Cited on pages: 92 and 192.

[200] A. Czarnecki and W.J. Marciano, *"The Muon anomalous magnetic moment: A Harbinger for 'new physics',"* ALBERTA-THY-03-01, BNL-HET-01-4, Phys.Rev. D64 (2001) 013014, arXiv:hep-ph/0102122.
Cited on page: 92.

[201] B.C. Allanach and C.G. Lester, *"Multi-dimensional mSUGRA likelihood maps,"* DAMTP-2005-64, Phys.Rev. D73 (2006) 015013, arXiv:hep-ph/0507283.
Cited on page: 95.

[202] B.C. Allanach, *"Naturalness priors and fits to the constrained minimal supersymmetric standard model,"* DAMTP-2006-5, Phys.Lett. B635 (2006) 123, arXiv:hep-ph/0601089.
Cited on page: 95.

[203] B.C. Allanach, C.G. Lester and A.M. Weber, *"The Dark side of mSUGRA,"* DAMTP-2006-75, MPP-2006-122, CAVENDISH-HEP-2006-024, JHEP 0612 (2006) 065, arXiv:hep-ph/0609295.
Cited on page: 95.

[204] R. Ruiz de Austri, R. Trotta and L. Roszkowski, *"A Markov chain Monte Carlo analysis of the CMSSM,"* JHEP 0605 (2006) 002, arXiv:hep-ph/0602028.
Cited on pages: 45, 85, 95, 96, and 134.

[205] B.C. Allanach et al., *"Natural priors, CMSSM fits and LHC weather forecasts,"* DAMTP-2007-18, CAVENDISH-HEP-2007-03, MPP-2007-36, JHEP 0708 (2007) 023, arXiv:hep-ph/0705.0487.
Cited on pages: 95 and 134.

[206] L. Roszkowski, R. Ruiz de Austri and R. Trotta, *"Implications for the Constrained MSSM from a new prediction for $b \to s\gamma$,"* JHEP 0707 (2007) 075, arXiv:hep-ph/0705.2012.
Cited on pages: 95, 135, and 154.

[207] R. Trotta et al., *"The Impact of priors and observables on parameter inferences in the Constrained MSSM,"* JHEP 0812 (2008) 024, arXiv:hep-ph/0809.3792.
Cited on pages: 83, 87, 88, 95, and 134.

[208] F. Feroz et al., *"Bayesian Selection of sign μ within mSUGRA in Global Fits Including WMAP5 Results,"* JHEP 0810 (2008) 064, arXiv:hep-ph/0807.4512.
Cited on page: 95.

[209] L. Roszkowski, R. Ruiz de Austri and R. Trotta, *"Efficient reconstruction of CMSSM parameters from LHC data: A Case study,"* Phys.Rev. D82 (2010) 055003, arXiv:hep-ph/0907.0594.
Cited on pages: 95, 101, and 104.

[210] F. Feroz et al., *"Are BR* $(\bar{B} \to X_s\gamma)$ *and* $(g-2)_\mu$ *consistent within the Constrained MSSM?,"* (2009), arXiv:hep-ph/0903.2487.
Cited on page: 95.

[211] A. Fowlie et al., *"Bayesian Implications of Current LHC and XENON*100 *Search Limits for the Constrained MSSM,"* Phys.Rev. D85 (2012) 075012, arXiv:hep-ph/1111.6098.
Cited on pages: 95 and 123.

[212] B.C. Allanach et al., *"The impact of the ATLAS zero-lepton, jets and missing momentum search on a CMSSM fit,"* JHEP 1106 (2011) 035, arXiv:hep-ph/1103.0969.
Cited on page: 95.

[213] B.C. Allanach, *"Impact of CMS Multi-jets and Missing Energy Search on CMSSM Fits,"* Phys.Rev. D83 (2011) 095019, arXiv:hep-ph/1102.3149.
Cited on pages: 95 and 125.

[214] C. Strege et al., *"Updated global fits of the cMSSM including the latest LHC SUSY and Higgs searches and XENON*100 *data,"* IFT-UAM-CSIC-11-99, FTUAM-11-66, JCAP 1203 (2012) 030, arXiv:hep-ph/1112.4192.
Cited on page: 95.

[215] G. Bertone et al., *"Global fits of the cMSSM including the first LHC and XENON*100 *data,"* IFT-UAM-CSIC-11-52, FTUAM-11-50, JCAP 1201 (2012) 015, arXiv:hep-ph/1107.1715.
Cited on page: 95.

[216] F. Feroz et al., *"Challenges of Profile Likelihood Evaluation in Multi-Dimensional SUSY Scans,"* JHEP 1106 (2011) 042, arXiv:hep-ph/1101.3296.
Cited on page: 95.

[217] C. Strege et al., *"Global Fits of the cMSSM and NUHM including the LHC Higgs discovery and new XENON*100 *constraints,"* (2012), arXiv:hep-ph/1212.2636.
Cited on pages: 95 and 154.

[218] A. Fowlie et al., *"The CMSSM Favoring New Territories: The Impact of New LHC Limits and a* 125 *GeV Higgs,"* Phys.Rev. D86 (2012) 075010, arXiv:hep-ph/1206.0264.
Cited on pages: 95 and 136.

[219] L. Roszkowski, E.M. Sessolo and Y.L.S. Tsai, *"Bayesian Implications of Current LHC Supersymmetry and Dark Matter Detection Searches for the Constrained MSSM,"* Phys.Rev. D86 (2012) 095005, arXiv:hep-ph/1202.1503.
Cited on pages: 95 and 96.

[220] S. Akula, P. Nath and G. Peim, *"Implications of the Higgs Boson Discovery for mSUGRA,"* Phys.Lett. B717 (2012) 188, arXiv:hep-ph/1207.1839.
Cited on page: 95.

[221] M.E. Cabrera, J.A. Casas and R. Ruiz de Austri, *"The health of SUSY after the Higgs discovery and the XENON*100 *data,"* (2012), arXiv:hep-ph/1212.4821.
Cited on page: 95.

[222] K. Kowalska, L. Roszkowski and E.M. Sessolo, *"Two ultimate tests of constrained supersymmetry,"* (2013), arXiv:hep-ph/1302.5956.
Cited on page: 95.

[223] L. Roszkowski et al., *"Global fits of the Non-Universal Higgs Model,"* Phys.Rev. D83 (2011) 015014, arXiv:hep-ph/0903.1279.
Cited on page: 95.

[224] O. Buchmueller et al., *"Prediction for the Lightest Higgs Boson Mass in the CMSSM using Indirect Experimental Constraints,"* CERN-PH-EP-2007-037, Phys.Lett. B657 (2007) 87, arXiv:hep-ph/0707.3447.
Cited on page: 95.

[225] O. Buchmueller et al., *"Predictions for Supersymmetric Particle Masses using Indirect Experimental and Cosmological Constraints,"* CERN-PH-TH-2008-181, JHEP 0809 (2008) 117, arXiv:hep-ph/0808.4128.
Cited on page: 95.

[226] O. Buchmueller et al., *"Likelihood Functions for Supersymmetric Observables in Frequentist Analyses of the CMSSM and NUHM1,"* CERN-PH-TH-2009-124, Eur.Phys.J. C64 (2009) 391, arXiv:hep-ph/0907.5568.
Cited on page: 95.

[227] O. Buchmueller et al., *"Frequentist Analysis of the Parameter Space of Minimal Supergravity,"* CERN-PH-TH-2010-169, DCPT-10-196, DESY-10-211, IPPP-10-98, FTPI-MINN-10-34, KCL-PH-TH-2010-34, UMN-TH-2928-10, Eur.Phys.J. C71 (2011) 1583, arXiv:hep-ph/1011.6118.
Cited on pages: 95 and 134.

[228] O. Buchmueller et al., *"Higgs and Supersymmetry,"* KCL-PH-TH-2011-40, LCTS-2011-21, CERN-PH-TH-2011-305, DCPT-11-168, DESY-11-242, IPPP-11-84, FTPI-MINN-11-31, UMN-TH-3023-11, Eur.Phys.J. C72 (2012) 2020, arXiv:hep-ph/1112.3564.
Cited on page: 95.

[229] O. Buchmueller et al., *"Supersymmetry in Light of* $1/fb$ *of LHC Data,"* KCL-PH-TH-2011-28, LCTS-2011-14, CERN-PH-TH-2011-220, DCPT-11-108,

DESY-11-161, IPPP-11-54, FTPI-MINN-11-23, UMN-TH-3013-11, Eur.Phys.J. C72 (2012) 1878, arXiv:hep-ph/1110.3568.
Cited on pages: 95, 134, 135, and 136.

[230] O. Buchmueller et al., *"Supersymmetry and Dark Matter in Light of LHC 2010 and Xenon100 Data,"* CERN-PH-TH-2011-129, DCPT-11-62, DESY-11-119, IPPP-11-31, FTPI-MINN-11-12, KCL-PH-TH-2011-12, LCTS-2011-01, UMN-TH-3002-11, Eur.Phys.J. C71 (2011) 1722, arXiv:hep-ph/1106.2529.
Cited on page: 95.

[231] O. Buchmueller et al., *"Implications of Initial LHC Searches for Supersymmetry,"* DESY-10-249, CERN-PH-TH-2010-321, KCL-PH-TH-2011-04, Eur.Phys.J. C71 (2011) 1634, arXiv:hep-ph/1102.4585.
Cited on page: 95.

[232] O. Buchmueller et al., *"The CMSSM and NUHM1 in Light of* 7 *TeV LHC,* $B_s \to \mu^+\mu^-$ *and XENON*100 *Data,"* KCL-PH-TH-2012-26, LCTS-2012-13, CERN-PH-TH-2012-164, DCPT-12-82, DESY-12-115, IPPP-12-41, FTPI-MINN-12-20, UMN-TH-3106-12, Eur.Phys.J. C72 (2012) 2243, arXiv:hep-ph/1207.7315.
Cited on page: 95.

[233] M.W. Cahill-Rowley et al., *"More Energy, More Searches, but the pMSSM Lives On,"* SLAC-PUB-15273, (2012), arXiv:hep-ph/1211.1981.
Cited on page: 95.

[234] U. Haisch and F. Mahmoudi, *"MSSM: Cornered and Correlated,"* CERN-PH-TH-2012-270, JHEP 1301 (2013) 061, arXiv:hep-ph/1210.7806.
Cited on page: 95.

[235] S.S. AbdusSalam, *"LHC-7 supersymmetry search interpretation within the pMSSM,"* (2012), arXiv:hep-ph/1211.0999.
Cited on page: 95.

[236] M.W. Cahill-Rowley et al., *"The Higgs Sector and Fine-Tuning in the pMSSM,"* SLAC-PUB-15076, Phys.Rev. D86 (2012) 075015, arXiv:hep-ph/1206.5800.
Cited on page: 95.

[237] R. Benbrik et al., *"Confronting the MSSM and the NMSSM with the Discovery of a Signal in the two Photon Channel at the LHC,"* DESY-12-114, Eur.Phys.J. C72 (2012) 2171, arXiv:hep-ph/1207.1096.
Cited on page: 95.

[238] M. Carena et al., *"The pMSSM Interpretation of LHC Results Using Rernormalization Group Invariants,"* ANL-HEP-PR-12-26, EFI-12-06,

FERMILAB-PUB-12-132-PPD-T, Phys.Rev. D86 (2012) 075025, arXiv:hep-ph/1205.5903.
Cited on page: 95.

[239] S. Antusch et al., *"Naturalness of the Non-Universal MSSM in the Light of the Recent Higgs Results,"* MPP-2012-120, SISSA-22-2012-EP, JHEP 01 (2013) 187, arXiv:hep-ph/1207.7236.
Cited on page: 95.

[240] K. Hagiwara, J.S. Lee and J. Nakamura, *"Properties of* 125 *GeV Higgs boson in non-decoupling MSSM scenarios,"* JHEP 1210 (2012) 002, arXiv:hep-ph/1207.0802.
Cited on page: 95.

[241] M. Carena et al., *"MSSM Electroweak Baryogenesis and LHC Data,"* ANL-HEP-PR-12-47, BI-TP-2012-22, EFI-12-15, FERMILAB-PUB-12-375-T, UAB-FT-706, JHEP 1302 (2013) 001, arXiv:hep-ph/1207.6330.
Cited on page: 95.

[242] F. Mahmoudi, A. Arbey and M. Battaglia, *"Light neutralino dark matter in MSSM,"* CERN-PH-TH-2012-308, (2012), arXiv:hep-ph/1211.2795.
Cited on page: 95.

[243] F. Mahmoudi et al., *"Implications of LHC Higgs and SUSY searches for MSSM,"* CERN-PH-TH-2012-307, (2012), arXiv:hep-ph/1211.2794.
Cited on page: 95.

[244] J.L. Feng and D. Sanford, *"A Natural* 125 *GeV Higgs Boson in the MSSM from Focus Point Supersymmetry with A-Terms,"* UCI-TR-2012-12, Phys.Rev. D86 (2012) 055015, arXiv:hep-ph/1205.2372.
Cited on page: 95.

[245] A. Arbey et al., *"An update on the constraints on the phenomenological MSSM from the new LHC Higgs results,"* CERN-PH-TH-2012-316, LPT-ORSAY-12-111, Phys.Lett. B720 (2013) 153, arXiv:hep-ph/1211.4004.
Cited on page: 95.

[246] A. Arbey, M. Battaglia and F. Mahmoudi, *"Light Neutralino Dark Matter in the pMSSM: Implications of LEP, LHC and Dark Matter Searches on SUSY Particle Spectra,"* CERN-PH-TH-2012-123, Eur.Phys.J. C72 (2012) 2169, arXiv:hep-ph/1205.2557.
Cited on page: 95.

[247] P. Lodone, *"Supersymmetry phenomenology beyond the MSSM after* 5/*fb of LHC data,"* Int.J.Mod.Phys. A27 (2012) 1230010, arXiv:hep-ph/1203.6227.
Cited on page: 95.

[248] F. Brümmer, *"The MSSM after two years of LHC running,"* DESY-PROC-2012-02/179, (2012) 641.
Cited on page: 95.

[249] M. Carena et al., *"Light Stau Phenomenology and the Higgs $\gamma\gamma$ Rate,"* ANL-HEP-PR-12-27, EFI-12-7, FERMILAB-PUB-12-195-PPD-T, JHEP 1207 (2012) 175, arXiv:hep-ph/1205.5842.
Cited on page: 95.

[250] A. Arbey et al., *"The Higgs sector of the phenomenological MSSM in the light of the Higgs boson discovery,"* CERN-PH-TH-2012-185, JHEP 1209 (2012) 107, arXiv:hep-ph/1207.1348.
Cited on page: 95.

[251] G. Belanger et al., *"PAMELA and FERMI-LAT limits on the neutralino-chargino mass degeneracy,"* CERN-PH-TH-2012-214, SACLAY-T12-054, LAPTH-040-12, JCAP 1211 (2012) 028, arXiv:hep-ph/1208.5009.
Cited on page: 95.

[252] F. Brümmer, S. Kraml and S. Kulkarni, *"Anatomy of maximal stop mixing in the MSSM,"* DESY-12-064, LPSC12121, JHEP 1208 (2012) 089, arXiv:hep-ph/1204.5977.
Cited on page: 95.

[253] F. Mahmoudi, *"Supersymmetry in the LHC era. Interplay between flavour physics, cosmology and collider physics,"* Ph.D. thesis, Blaise Pascal University, 2012.
Cited on page: 95.

[254] V. Barger, M. Ishida and W.Y. Keung, *"Flavor-Tuned* 125 *GeV SUSY Higgs Boson at the LHC: MSSM and NATURAL SUSY TESTS,"* Phys.Rev. D87 (2013) 015003, arXiv:hep-ph/1207.0779.
Cited on page: 95.

[255] M. Cahill-Rowley et al., *"SUSY Without Prejudice at the* 7 *and* 8 *TeV LHC: Gravitino LSPs,"* SLAC-PUB-15272, (2012), arXiv:hep-ph/1211.7106.
Cited on page: 95.

[256] S.S. AbdusSalam and D. Choudhury, *"Higgs boson discovery versus sparticles prediction: Impact on the pMSSM's posterior samples from a Bayesian global fit,"* (2012), arXiv:hep-ph/1210.3331.
Cited on page: 95.

[257] M.W. Cahill-Rowley et al., *"The New Look pMSSM with Neutralino and Gravitino LSPs,"* SLAC-PUB-14922, Eur.Phys.J. C72 (2012) 2156, arXiv:hep-ph/1206.4321.
Cited on page: 95.

[258] W. Altmannshofer et al., *"Indirect Probes of the MSSM after the Higgs Discovery,"* EFI-12-30, FERMILAB-PUB-12-590-T, MCTP-12-28, JHEP 1301 (2013) 160, arXiv:hep-ph/1211.1976.
Cited on page: 95.

[259] J.A. Conley et al., *"Supersymmetry Without Prejudice at the LHC,"* SLAC-PUB-14094, ANL-HEP-PR-10-15, NUHEP-TH-10-06, BONN-TH-2010-03, Eur.Phys.J. C71 (2011) 1697, arXiv:hep-ph/1009.2539.
Cited on page: 95.

[260] G. Belanger et al., *"Light Neutralino Dark Matter in the MSSM and Its Implication for LHC Searches for Staus,"* JHEP 1212 (2012) 076, arXiv:hep-ph/1206.5404.
Cited on page: 95.

[261] P. Bechtle et al., *"MSSM Interpretations of the LHC Discovery: Light or Heavy Higgs?,"* DESY-12-200, BONN-TH-2012-028, (2012), arXiv:hep-ph/1211.1955.

Cited on page: 95.

[262] T. Kitahara and T. Yoshinaga, *"Stau with Large Mass Difference and Enhancement of the Higgs to Diphoton Decay Rate in the MSSM,"* UT-13-06, (2013), arXiv:hep-ph/1303.0461.
Cited on page: 95.

[263] M. Carena et al., *"MSSM Higgs Boson Searches at the LHC: Benchmark Scenarios after the Discovery of a Higgs-like Particle,"* ANL-HEP-PR-13-12, EFI-13-2, DESY-13-024, FERMILAB-PUB-13-041-T, (2013), arXiv:hep-ph/1302.7033.
Cited on page: 95.

[264] M. Carena et al., *"Light Stops, Light Staus and the* 125 *GeV Higgs,"* ANL-HEP-PR-13-14, EFI-13-3-, FERMILAB-PUB-13-065-T, MCTP-13-07, (2013), arXiv:hep-ph/1303.4414.
Cited on page: 95.

[265] S. Heinemeyer, *"Higgs/Electroweak in the SM and the MSSM,"* (2013), arXiv:hep-ph/1301.7197.
Cited on page: 95.

[266] A. Dighe et al., *"Testing Times for Supersymmetry: Looking Under the Lamp Post,"* TIFR-TH-13-05, (2013), arXiv:hep-ph/1303.0721.
Cited on page: 95.

[267] T. Han, Z. Liu and A. Natarajan, *"Dark Matter and Higgs Bosons in the MSSM,"* PITT-PACC-1303, (2013), arXiv:hep-ph/1303.3040.
Cited on page: 95.

[268] C. Boehm et al., *"Naturalness of Light Neutralino Dark Matter in pMSSM after LHC, XENON100 and Planck Data,"* MAN-HEP-2013-05, (2013), arXiv:hep-ph/1303.5386.
Cited on page: 95.

[269] A. Djouadi and J. Quevillon, *"The MSSM Higgs sector at a high M_{SUSY}: reopening the low* $\tan\beta$ *regime and the search for heavy Higgsses,"* LPT-ORSAY-13-26, (2013), arXiv:hep-ph/1304.1787.
Cited on page: 95.

[270] D. Hooper et al., *"Closing Supersymmetric Resonance Regions With Direct Detection Experiments,"* FERMILAB-PUB-13-077-A, (2013), arXiv:hep-ph/1304.2417.
Cited on page: 95.

[271] S. Mohanty, S. Rao and D. Roy, *"Reconciling the Muon $g-2$ and Dark Matter Relic Density with the LHC Results in Nonuniversal Gaugino Mass Models,"* (2013), arXiv:hep-ph/1303.5830.
Cited on page: 95.

[272] S. Scopel, N. Fornengo and A. Bottino, *"Embedding the* 125 *GeV Higgs boson measured at the LHC in an effective MSSM: possible implications for neutralino dark matter,"* (2013), arXiv:hep-ph/1304.5353.
Cited on page: 95.

[273] S. Zheng and Y. Yu, *"Electroweak Precision Tests On the MSSM and NMSSM Constrained at the LHC,"* (2013), arXiv:hep-ph/1303.1900.
Cited on page: 95.

[274] A. Pierce, *"Implications of the Higgs Boson and the LHC for the MSSM,"* MCTP-13-05, (2013), arXiv:hep-ph/1303.1142.
Cited on page: 95.

[275] B.C. Allanach, *"Theoretical uncertainties in sparticle mass predictions,"* SNOWMASS-2001-P319, eConf C010630 (2001) P319, arXiv:hep-ph/0110227.

Cited on page: 96.

[276] B.C. Allanach, S. Kraml and W. Porod, *"Comparison of SUSY mass spectrum calculations,"* (2002) 904, arXiv:hep-ph/0207314.
Cited on page: 96.

[277] M. Frank et al., *"The Higgs Boson Masses and Mixings of the Complex MSSM in the Feynman-Diagrammatic Approach,"* DCPT-06-160, IPPP-06-80, MPP-2006-158, PSI-PR-06-14, JHEP 0702 (2007) 047, arXiv:hep-ph/0611326.
Cited on page: 96.

[278] G. Degrassi et al., *"Towards high precision predictions for the MSSM Higgs sector,"* DCPT-02-126, IPPP-02-63, LMU-11-02, MPI-PHT-2002-73 RM3-TH-02-19, Eur.Phys.J. C28 (2003) 133, arXiv:hep-ph/0212020.
Cited on page: 96.

[279] S. Heinemeyer, W. Hollik and G. Weiglein, *"The Masses of the neutral CP-even Higgs bosons in the MSSM: Accurate analysis at the two loop level,"* KA-TP-17-1998, DESY-98-194, CERN-TH-98-405, Eur.Phys.J. C9 (1999) 343, arXiv:hep-ph/9812472.
Cited on page: 96.

[280] S. Heinemeyer, W. Hollik and G. Weiglein, *"FeynHiggs: A Program for the calculation of the masses of the neutral CP even Higgs bosons in the MSSM,"* KA-TP-16-1998, DESY-98-193, CERN-TH-98-389, Comput.Phys.Commun. 124 (2000) 76, arXiv:hep-ph/9812320.
Cited on page: 96.

[281] F. Mahmoudi, *"SuperIso v2.3: A Program for calculating flavor physics observables in Supersymmetry,"* Comput.Phys.Commun. 180 (2009) 1579, arXiv:hep-ph/0808.3144.
Cited on pages: 96 and 176.

[282] F. Mahmoudi, *"SuperIso: A Program for calculating the isospin asymmetry of $B \to K^* \gamma$ in the MSSM,"* Comput.Phys.Commun. 178 (2008) 745, arXiv:hep-ph/0710.2067.
Cited on pages: 96 and 176.

[283] R. Ruiz de Austri, R. Trotta and F. Feroz, *"B-Decay,"* last retrieval Sept. 2013: `http://www.ft.uam.es/personal/rruiz/superbayes/index.php?page=html/bdecay.htm`.
Cited on page: 96.

[284] R. Ruiz de Austri, R. Trotta and F. Feroz, *"SuperBayeS: Supersymmetry Parameters Extraction Routines for Bayesian Statistics,"* last retrieval Sept. 2013: `http://www.ft.uam.es/personal/rruiz/superbayes/`.
Cited on page: 96.

[285] A. Fowlie, *"SuperPy,"* (2013), last retrieval Sept. 2013: `https://github.com/innisfree/superpy`.
Cited on page: 96.

[286] A. Fowlie and L. Roszkowski, *"Reconstructing ATLAS SU3 in the CMSSM and relaxed phenomenological supersymmetry models,"* version 1, (2011), arXiv:hep-ph/1106.5117v1.
Cited on pages: 96, 197, and 230.

[287] B.C. Allanach et al., *"The Snowmass points and slopes: Benchmarks for SUSY searches,"* SLAC-PUB-9134, BNL-HET-02-6, CERN-TH-2002-020, DCPT-02-16, DESY-02-022, FERMILAB-CONF-02-011-T, HEPHY-PUB-751, IPPP-02-08, PM-01-69, UCD-2002-01, UFIFT-HEP-02-2, UMN-TH-2043-02, ZU-TH-3-02, SNOWMASS-2001-P125, Eur.Phys.J. C25 (2002) 113, arXiv:hep-ph/0202233.
Cited on page: 96.

[288] **ATLAS Collaboration**, G. Aad et al., *"Expected Performance of the ATLAS Experiment — Detector, Trigger and Physics,"* SLAC-R-980, CERN-OPEN-2008-020, (2009), arXiv:hep-ex/0901.0512.
Cited on pages: 98 and 101.

[289] B. Gjelsten, D. Miller and P. Osland, *"Measurement of SUSY masses via cascade decays for SPS 1a,"* ATL-PHYS-2004-029, EDINBURGH-2004-12, JHEP 0412 (2004) 003, arXiv:hep-ph/0410303.
Cited on pages: 98 and 100.

[290] C.G. Lester, *"Model independent sparticle mass measurements at ATLAS,"* Ph.D. thesis, Cambridge University, Geneva, 2001.
Cited on page: 100.

[291] B.C. Allanach and M.J. Dolan, *"Supersymmetry With Prejudice: Fitting the Wrong Model to LHC Data,"* IPPP-11-38, DCPT-11-76, Phys.Rev. D86 (2012) 055022, arXiv:hep-ph/1107.2856.
Cited on page: 102.

[292] **WMAP Collaboration**, J. Dunkley et al., *"Five-Year Wilkinson Microwave Anisotropy Probe (WMAP) Observations: Likelihoods and Parameters from the WMAP data,"* Astrophys.J.Suppl. 180 (2009) 306, arXiv:astro-ph/0803.0586.
Cited on page: 102.

[293] A. Fowlie, L. Roszkowski and M. Kazana, (2013), version 2 of Ref. [286], in preparation.
Cited on page: 115.

[294] **CMS Collaboration**, V. Khachatryan et al., *"Search for Supersymmetry in pp Collisions at 7 TeV in Events with Jets and Missing Transverse Energy,"* CERN-PH-EP-2010-084, CMS-SUS-10-003, Phys.Lett. B698 (2011) 196, arXiv:hep-ex/1101.1628.
Cited on pages: 115, 123, and 137.

[295] F. James and M. Roos, *"Minuit: A System for Function Minimization and Analysis of the Parameter Errors and Correlations,"* CERN-DD-75-20, Comput.Phys.Commun. 10 (1975) 343.
Cited on page: 115.

[296] **Planck Collaboration**, P. Ade et al., *"Planck 2013 results. I. Overview of products and scientific results,"* (2013), arXiv:astro-ph.CO/1303.5062.
Cited on page: 115.

[297] M. Citron et al., *"The End of the CMSSM Coannihilation Strip is Nigh,"* KCL-PH-TH-2012-46, LCTS-2012-32, CERN-PH-TH-2012-331, UMN-TH-3127-12, FTPI-MINN-12-38, –UMN–TH–3127-12, FTPI–MINN–12-38, (2012), arXiv:hep-ph/1212.2886.
Cited on page: 115.

[298] **ATLAS Collaboration**, *"Search for squarks and gluinos with the ATLAS detector using final states with jets and missing transverse momentum and* $5.8\,fb^{-1}$ *of* $\sqrt{s} = 8$ *TeV proton-proton collision data,"* ATLAS-CONF-2012-109, ATLAS-COM-CONF-2012-140, (2012).
Cited on page: 115.

[299] **ATLAS Collaboration**, *"Search for squarks and gluinos with the ATLAS detector in final states with jets and missing transverse momentum and* $20.3\,fb^{-1}$ *of* $\sqrt{s} = 8$ *TeV proton-proton collision data,"* CERN, ATLAS-CONF-2013-047.
Cited on page: 116.

[300] T. Sjostrand, S. Mrenna and P.Z. Skands, *"A Brief Introduction to PYTHIA 8.1,"* CERN-LCGAPP-2007-04, LU-TP-07-28, FERMILAB-PUB-07-512-CD-T, Comput.Phys.Commun. 178 (2008) 852, arXiv:hep-ph/0710.3820.
Cited on page: 116.

[301] **CMS Collaboration**, *"Technical Proposal for the Upgrade of the CMS detector through 2020,"* CERN, CERN-LHCC-2011-006. LHCC-P-004, last retrieval Sept. 2013: `http://cds.cern.ch/record/1355706`.
Cited on page: 116.

[302] I. Antcheva et al., *"ROOT: A C++ framework for petabyte data storage, statistical analysis and visualization,"* FERMILAB-PUB-09-661-CD, Comput.Phys.Commun. 180 (2009) 2499.
Cited on page: 116.

[303] **Planck Collaboration**, P. Ade et al., *"Planck 2013 results. XVI. Cosmological parameters,"* (2013), arXiv:astro-ph.CO/1303.5076.
Cited on pages: 118, 119, and 192.

[304] **CMS and LHCb collaborations**, *"Combination of results on the rare decays* $B^0_{(s)} \to \mu^+\mu^-$ *from the CMS and LHCb experiments,"* CERN, CMS-PAS-BPH-13-007. CERN-LHCb-CONF-2013-012, last retrieval Sept. 2013: `http://cds.cern.ch/record/1564324`.
Cited on page: 123.

[305] A.J. Buras et al., *"Probing New Physics with the $B_s \to \mu^+\mu^-$- Time-Dependent Rate,"* FLAVOUR(267104)-ERC-35, NIKHEF-2013-007, (2013), arXiv:hep-ph/1303.3820.
Cited on page: 123.

[306] L. Randall and D. Tucker-Smith, *"Dijet Searches for Supersymmetry at the LHC,"* Phys.Rev.Lett. 101 (2008) 221803, arXiv:hep-ph/0806.1049.
Cited on page: 123.

[307] F. Loparco and M. Mazziotta, *"A Bayesian approach to evaluate confidence intervals in counting experiments with background,"* Nucl.Instrum.Meth. A646 (2011) 167, arXiv:physics.data-an/1105.3041.
Cited on page: 128.

[308] H. Akima, *"A Method of Bivariate Interpolation and Smooth Surface Fitting for Irregularly Distributed Data Points,"* ACM Trans. Math. Softw. 4 (1978) 148, last retrieval Sept. 2013: `http://doi.acm.org/10.1145/355780.355786`.
Cited on page: 128.

[309] **CMS Collaboration**, *"Search for supersymmetry in all-hadronic events with α_T,"* CMS-PAS-SUS-11-003, (2011).
Cited on pages: 128, 129, 138, and 194.

[310] M.S. Carena et al., *"$b \to s\gamma$ and supersymmetry with large $\tan\beta$,"* FERMILAB-PUB-00-242-T, CERN-TH-2000-295, SCIPP-00-34, ANL-HEP-PR-00-104, EFI-2000-35, Phys.Lett. B499 (2001) 141, arXiv:hep-ph/0010003.
Cited on page: 131.

[311] U. Chattopadhyay et al., *"Probing the light Higgs pole resonance annihilation of dark matter in the light of XENON100 and CDMS-II observations,"* Phys.Rev. D82 (2010) 075013, arXiv:hep-ph/1006.3045.
Cited on page: 131.

[312] **CMS Collaboration**, *"Search for supersymmetry with the razor variables at CMS,"* CERN, CMS-PAS-SUS-12-005.
Cited on pages: 136 and 194.

[313] **CMS Collaboration**, S. Chatrchyan et al., *"Inclusive search for squarks and gluinos in pp collisions at $\sqrt{s} = 7$ TeV,"* CERN-PH-EP-2011-099, Phys.Rev. D85 (2012) 012004, arXiv:hep-ex/1107.1279.
Cited on page: 136.

[314] C. Rogan, *"Kinematical variables towards new dynamics at the LHC,"* CALT-68-2790, (2010), arXiv:hep-ph/1006.2727.
Cited on page: 136.

[315] P. Grothaus, M. Lindner and Y. Takanishi, *"Naturalness of Neutralino Dark Matter,"* JHEP 1307 (2013) 094, arXiv:hep-ph/1207.4434.
Cited on page: 156.

[316] A. Fowlie et al., *"Dark matter and collider signatures of the MSSM,"* (2013), arXiv:hep-ph/1306.1567.
Cited on page: 165.

[317] T. Cohen et al., *"Wino Dark Matter Under Siege,"* MCTP-13-19, MIT-CTP-4482, SLAC-PUB-15664, (2013), arXiv:hep-ph/1307.4082.
Cited on page: 167.

[318] **CMS Collaboration**, S. Chatrchyan et al., *"Search for supersymmetry in hadronic final states with missing transverse energy using the variables* α_T *and b-quark multiplicity in* pp *collisions at* $\sqrt{s} = 8$ *TeV,"* CMS-SUS-12-028, CERN-PH-EP-2013-037, (2013), arXiv:hep-ex/1303.2985.
Cited on pages: 168 and 194.

[319] **CMS Collaboration**, *"Search for direct EWK production of SUSY particles in multilepton modes with 8 TeV data,"* CMS-PAS-SUS-12-022.
Cited on pages: 168 and 194.

[320] H. Denz et al., *"*$\pi^{\pm}p$ *differential cross sections at low energies,"* JLAB-PHY-05-455, Phys.Lett. B633 (2006) 209, arXiv:nucl-ex/0512006.
Cited on page: 169.

[321] J. Stahov, H. Clement and G. Wagner, *"Evaluation of the Pion-Nucleon Sigma Term from CHAOS data,"* (2012), arXiv:nucl-th/1211.1148.
Cited on pages: 169, 173, 174, 180, and 182.

[322] G.E. Hite, W.B. Kaufmann and R.J. Jacob, *"New evaluation of the* $\pi N \Sigma$ *term,"* Phys.Rev. C71 (2005) 065201.
Cited on pages: 169, 173, 174, 180, and 182.

[323] **XENON100 Collaboration**, E. Aprile et al., *"Dark Matter Results from 225 Live Days of XENON100 Data,"* Phys.Rev.Lett. 109 (2012) 181301, arXiv:astro-ph.CO/1207.5988.
Cited on page: 169.

[324] Y.G. Kim et al., *"Upper and lower limits on neutralino WIMP mass and spin independent scattering cross-section, and impact of new* $(g-2)_\mu$ *measurement,"* JHEP 0212 (2002) 034, arXiv:hep-ph/hep-ph/0208069.
Cited on page: 173.

[325] **ALEPH Collaboration**, A. Heister et al., *"Search for scalar leptons in* e^+e^- *collisions at center-of-mass energies up to 209 GeV,"* CERN-EP-2001-086, Phys.Lett. B526 (2002) 206, arXiv:hep-ex/0112011.
Cited on page: 191.

[326] **L3 Collaboration**, P. Achard et al., *"Search for scalar leptons and scalar quarks at LEP,"* CERN-EP-2003-059, Phys.Lett. B580 (2004) 37, arXiv:hep-ex/0310007.
Cited on page: 191.

[327] **DELPHI Collaboration**, J. Abdallah et al., *"Searches for supersymmetric particles in e^+e^- collisions up to* 208 *GeV and interpretation of the results within the MSSM,"* CERN-EP-2003-007, Eur.Phys.J. C31 (2003) 421, arXiv:hep-ex/0311019.
Cited on page: 191.

[328] **Particle Data Group**, K. Nakamura et al., *"Review of particle physics,"* FERMILAB-PUB-10-665-PPD, J.Phys. G37 (2010) 075021.
Cited on pages: 191 and 192.

[329] **D∅ Collaboration**, M. Shamim, *"Searches for Squarks and Gluinos with D∅ Detector,"* FERMILAB-CONF-07-550-E, (2007), arXiv:hep-ex/0710.2897.
Cited on page: 191.

[330] **WMAP Collaboration**, G. Hinshaw et al., *"Five-Year Wilkinson Microwave Anisotropy Probe (WMAP) Observations: Data Processing, Sky Maps, and Basic Results,"* Astrophys.J.Suppl. 180 (2009) 225, arXiv:astro-ph/0803.0732.
Cited on page: 192.

[331] **Particle Data Group**, W. Yao et al., *"Review of Particle Physics,"* J.Phys. G33 (2006) 1.
Cited on page: 192.